

Copyright

by

Hye In Ahn

2010

**The Thesis Committee for Hye In Ahn
Certifies that this is the approved version of the following thesis:**

**Mineralogy and Geochemistry of the Non-sulfide Zn Deposits in the
Sierra Mojada district, Coahuila, Mexico**

**APPROVED BY
SUPERVISING COMMITTEE:**

Supervisor:

J. Richard Kyle

Philip C. Bennett

H. Albert Gilg

**Mineralogy and Geochemistry of the Non-sulfide Zn Deposits in the
Sierra Mojada district, Coahuila, Mexico**

by

Hye In Ahn, B.S.

Thesis

Presented to the Faculty of the Graduate School of

The University of Texas at Austin

in Partial Fulfillment

of the Requirements

for the Degree of

Master of Science in Geological Sciences

The University of Texas at Austin

August, 2010

Dedication

Dedicated to my family.

Acknowledgements

I would like to show my gratitude to many people for their help with achieving my research goals. I am heartily thankful to Dr. J. Richard Kyle for his encouragement and guides throughout my time in graduate school. He has given me great advice and support to accomplish my research project and I especially thank him for giving me the opportunity to study geology in the United States. Thanks to Dr. Philip Bennett for providing me additional knowledge on geochemistry. I would like to thank Dr. H. Albert Gilg for giving me advice and knowledge on stable isotopes and general issues in non-sulfide Zn deposits. Acquiring carbon and isotope data would have been impossible without him. Thanks to Dr. Kitty Miliken and Dr. Donggao Zhao for guiding me to use the electron microbeam facilities in the Jackson School of Geosciences. I would like to thank Dr. Nathan Miller for providing me great help and advice on my LA-ICP-MS project. Thanks to Dr. Larry Mack for Pb isotope analyses. I would like to thank Dr. Peter Eichhubl for allowing me to use the fluid inclusion lab at the Bureau of Economic Geology, the University of Texas at Austin, and thank Dr. Andras Fall for his advice and help on fluid inclusion analyses. I'm grateful to Dr. Dan Breecker for sharing his knowledge and advice on stable isotopes and geochemistry. Thanks to Dr. Robert Folk for giving me his knowledge on microorganisms and SEM imaging.

I owe my gratitude to Metalline Mining Company for giving me an opportunity to work on the Sierra Mojada district. I would like to especially thank for allowing me to access to the mines and providing me financial support. Thanks to Dr. Roger Kolvoord for sharing his knowledge and experience during the visit to Sierra Mojada for collecting samples in 2008 and for offering additional advice on my project. I would like to thank

all other people at Sierra Mojada for their generous help while I was there. Also, this project would not have been possible without student research grants from the Society of Economic Geologists. Additional thanks to the Geology Foundation of the Jackson School of Geosciences for providing generous support to make this project possible.

I would like to thank my fellow students in Jackson School. It was a precious opportunity that I met a lot of good friends in a new place. They are willing to share their professional and personal advice with me.

Thanks to my family and friends in Korea. They have believed in me and given me continuous support while I am far away from home.

August, 2010

Abstract

Mineralogy and Geochemistry of the Non-sulfide Zn Deposits in the Sierra Mojada district, Coahuila, Mexico

Hye In Ahn, MSGeoSci.

The University of Texas at Austin, 2010

Supervisor: J. Richard Kyle

The Sierra Mojada district consists of multiple types of mineral concentrations ranging from polymetallic sulfide deposits, “non-sulfide Zn” (NSZ) deposits, and a Pb carbonate deposit hosted by Upper Jurassic to Lower Cretaceous carbonates. This study focuses on the two non-sulfide Zn deposits, the Smithsonite Manto and the Iron Oxide Manto, that occur south of the San Marcos fault. The Smithsonite Manto shows karst features, including internal sediments interbanded with smithsonite (ZnCO_3). The Iron Oxide Manto consists of strata-bound zones dominantly of hemimorphite ($\text{Zn}_4\text{Si}_2\text{O}_7(\text{OH})_2 \cdot \text{H}_2\text{O}$) that fills pores in Fe-oxides. The mineralogy of the NSZ mineralization consists of smithsonite, hemimorphite and Zn clays (sauconite) associated mainly with calcite and Mn-Fe-oxides. Zn clays are abundant in the Smithsonite Manto, but no Zn clays have been found in the Iron Oxide Manto. This project attempts to constrain the

origin of the NSZ concentrations through petrographic and mineralogical study of major Zn-bearing minerals, and their carbon and oxygen stable isotopes and Pb isotope geochemistry.

Smithsonite in the Smithsonite Manto occurs as botryoidal aggregates consisting of scalenohedral or rhombohedral microcrystals and banded colloform or massive smithsonite in open spaces, whereas smithsonite in the Iron Oxide Manto occurs as rhombic microcrystals grown in pore spaces or finely intergrown with Fe-oxides. Both Fe-poor and Fe-rich smithsonite are found in the Iron Oxide Manto. Under optical-CL, smithsonite displays complex growth zoning that can be related to variable trace element content. Trace elements semiquantitatively analyzed using LA-ICP-MS show that most blue luminescent smithsonite has lower Mn contents than pink to bright red luminescent zones in smithsonite.

Preliminary fluid inclusion petrography in hemimorphite and calcite suggests that fluid composition can be related to precipitation of NSZ minerals from freshwater to slightly saline waters. Calculated salinities for two phase (liquid +vapor) and single phase (liquid) inclusions in hemimorphite range between 0.0 and 1.6 wt. % NaCl equivalent, and salinities of inclusions in calcite were between 0.0 and 1.1 wt. % NaCl equivalent.

The oxygen isotope values for smithsonite are relatively constant (avg. $\delta^{18}\text{O}_{\text{VSMOW}} = 21.9 \pm 0.5\text{‰}$), whereas $\delta^{13}\text{C}_{\text{VPDB}}$ values range from -8.4 to -1.1 ‰. The oxygen isotope values in late calcite are within the same range of smithsonite, whereas the average values of the carbon isotope are lower by 5 ‰. Formational temperature of smithsonite is calculated to be between 26 ~ 40 °C using the modern groundwater composition at Cuatro Ciénegas. Similar Pb isotopic compositions of smithsonite and cerussite to galena suggest the source of metals in the NSZ deposits presumably originate from the sulfide deposits.

Table of Contents

List of Tables	xii
List of Figures	xiii
Chapter 1. Introduction	1
Geographic Location and Climate	1
History of the Sierra Mojada District and Exploration	1
Previous Studies	3
Non-sulfide Zn Overview	4
Geologic Setting.....	4
Geochemical Processes of Formation of Non-sulfide Zn Minerals.....	6
Chapter 2. Regional and District Geology	14
Regional Geology	14
Geology of the Sierra Mojada District.....	15
Mineral Deposits of the District.....	16
Sierra Mojada Non-sulfide Zn Mineralization.....	17
Sampling and Methodology.....	18
Chapter 3. Mineralogy and Geochemistry of the Smithsonite Manto	24
Petrography and SEM Study of Major Minerals	25
Morphological Characteristics of Zn-bearing minerals	25
Major Element Analyses of Carbonates	31
Methodology	31
Results.....	32
Conclusion	34
Chapter 4. Petrography and Mineralogy of the Iron Oxide Manto.....	56
Sampling and Methods	56
Host Rock Description and Petrography.....	56
Mineralogy of Major Minerals.....	58
Hemimorphite	58

Smithsonite	59
Calcite	60
Other secondary minerals	60
Conclusion	61
Chapter 5. Stable Carbon and Oxygen Isotopes of Carbonates	74
Analytical Method	74
Results.....	75
Calcite	75
Smithsonite	76
Discussion.....	77
Carbon isotopes.....	78
Oxygen isotopes.....	79
Chapter 6. Pb Isotope Compositions.....	88
Methods.....	88
Results and Discussion	88
Chapter 7. CL Investigations and Trace Element Distribution in Smithsonite.....	92
Introduction.....	92
Purpose.....	95
Methods.....	96
Results.....	96
Semiquantitative Elemental Analysis of Smithsonite.....	97
Method	97
Results.....	98
Conclusions.....	98
Chapter 8. Reconnaissance Fluid Inclusions Studies.....	104
Methods and Procedures	104
Results.....	105
Chapter 9. Discussion	109
Paragenetic Sequence.....	109

Mineralizing Fluids and Source of Metals.....	110
Chapter 10. Conclusions.....	113
Appendix A: Sample Description.....	115
Appendix B. Petrography.....	120
Appendix C. SEM-EDS Analyses.....	128
Appendix D. Microprobe Analyses.....	136
Appendix E. Pb Isotope Analyses.....	162
Appendix F. CL and LA-ICP-MS.....	166
Appendix G. Fluid Inclusion Microthermometry.....	171
References.....	173
Vita.....	179

List of Tables

Table 2.1. Abbreviations.....	23
Table 3.1. Morphological types of smithsonite.....	40
Table 3.2. Quantitative WDS results for banded, colloform smithsonite.....	50
Table 3.3. Quantitative WDS results for scalenohedral smithsonite.....	52
Table 3.4. Quantitative WDS results for matrix smithsonite.....	53
Table 3.5. Quantitative WDS results for late-stage calcite.....	54
Table 4.1. WDS results of smithsonite and calcite.....	71
Table 5.1. Carbon and Oxygen stable isotope values of carbonates.....	83
Table 6.1. Pb isotope compositions of galena, cerussite, and smithsonite.....	90
Table 8.1. Sample description and microthermometry data of fluid inclusions.....	106

List of Figures

Figure 1.1. Location map of the Sierra Mojada district.....	10
Figure 1.2. Distribution of non-sulfide Zn deposits around the world.....	11
Figure 1.3. Three models of formation of supergene non-sulfide Zn deposits.....	12
Figure 1.4. The stability fields of non-sulfide Zn minerals.....	13
Figure 2.1. Regional geology of Mexico.....	20
Figure 2.3. Overview of the Sierra Mojada region.....	21
Figure 2.4. Ore bodies and mines of the Sierra Mojada district.....	22
Figure 3.1. Hand samples from the Smithsonite Manto.....	36
Figure 3.2. Photomicrographs of NSZ minerals.....	37
Figure 3.3. Scalenohedral smithsonite.....	38
Figure 3.4. Typical smithsonite ores and SEM images.....	39
Figure 3.5. Occurrences of hemimorphite in the Smithsonite Manto.....	41
Figure 3.6. Characteristics of Aurora limestone.....	42
Figure 3.7. Occurrences of late-stage calcite.....	43
Figure 3.8. Occurrences of Zn clays.....	45
Figure 3.9. Alteration of smithsonite and hemimorphite into Zn clays.....	46
Figure 3.10. Occurrences of Zn clays and Mn minerals.....	47
Figure 3.11. Other associated minerals in the Smithsonite Manto.....	48
Figure 3.12. Occurrences of botryoidal, colloform smithsonite.....	49
Figure 3.13. Scalenohedral smithsonite.....	51
Figure 3.14. Matrix smithsonite.....	53
Figure 3.15. Textural types of smithsonite and minor element compositions.....	55
Figure 4.1. Hemimorphite and smithsonite ores in the Iron Oxide Manto.....	63
Figure 4.2. Occurrences of Fe-oxides.....	64
Figure 4.3. SE images and EDS spectra of Fe-oxides.....	65
Figure 4.4. Occurrences of pore-filling hemimorphite in the Iron Oxide Manto.....	66
Figure 4.5. Altered hemimorphite and late-stage calcite.....	67
Figure 4.6. Smithsonite in the Iron Oxide Manto.....	69
Figure 4.7. Smithsonite in the Iron Oxide Manto.....	70
Figure 4.8. Barite and Mn-bearing minerals.....	72
Figure 4.9. Textural types of smithsonite and minor element compositions.....	73
Figure 5.1. Samples for the C-O isotope measurements.....	81
Figure 5.2. Diagrams of carbon and oxygen isotope composition of calcite.....	82
Figure 5.3. Carbon and oxygen stable isotope values of smithsonite.....	85
Figure 5.4. Comparison of the C-O isotope values.....	86
Figure 5.5. Oxygen equilibrium curves between smithsonite and water.....	87
Figure 6.1. A plot of $^{207}\text{Pb}/^{204}\text{Pb}$ versus $^{206}\text{Pb}/^{204}\text{Pb}$	91
Figure 6.2. A plot of $^{208}\text{Pb}/^{204}\text{Pb}$ versus $^{206}\text{Pb}/^{204}\text{Pb}$	91
Figure 7.1. CL images of carbonates and hemimorphite.....	100
Figure 7.2. CL images of smithsonite.....	101
Figure 7.3. CL images of smithsonite, calcite, and hemimorphite.....	102
Figure 7.4. A plot of the ratio of the Mn over Zn signals in smithsonite.....	103
Figure 8.1. Primary inclusions in hemimorphite.....	107

Figure 8.2. Fluid inclusions in calcite and hemimorphite..... 108
Figure 9.1. Paragenetic sequence of NSZ minerals and other common minerals. 112

Chapter 1. Introduction

GEOGRAPHIC LOCATION AND CLIMATE

The Sierra Mojada district (latitude 27.2 °N, longitude 103.6 °W) is located in the west central part of the state of Coahuila, Mexico, near the border of the state of Chihuahua (Figure 1). The Sierra Madre Oriental Mountain range trends northwest to southeast across Coahuila. The district can be reached most directly from the city of Torreón, which is the most populated city in the state, approximately 250 km south of the district. Sierra Mojada is the names for both a town and mountain ranges (Horn, 1912). The elevation of the district is between 1200 and 1500 m with the crest of the Sierra Mojada range at more than 2400 m above sea level. Local climate is arid or semi-arid conditions. In the town of Sierra Mojada, winter is dry and most precipitation occurs during summer mostly in July as heavy rainfalls. Mean annual rainfalls at Sierra Mojada is 439 mm (Wallén, 1955), and evaporation is nearly as same as precipitation (Riley, 1930).

HISTORY OF THE SIERRA MOJADA DISTRICT AND EXPLORATION

Historical information on the Sierra Mojada district could be accessed from Chism (1887), Malcolmson (1902), Horn (1912), Shaw (1923), and Riley (1936), and the Metalline mining website (www.metalin.com). The Sierra Mojada District was discovered in 1879 as an early high grade silver district. High grade silver with lead carbonates was first mined in the Lead Manto, which was mined from discovery through the 1950's. A manto, the Spanish work for blanket, is used to describe morphology of ore bodies that are stratabound horizontal tabular bodies. The district extends over 6 km east-west and 1.5 km north-south. The discovery of copper silver ore deposits in the San Jose

Mine in 1906 led to new exploration in the north side of the San Marcos fault. The San Marcos fault is an east-trending regional fault crossing through the Sierra Mojada district, and it is locally called the Sierra Mojada fault. The Iron Oxide Manto and the Smithsonite Manto were discovered in the 1920's. In the 1960s, a deposit with zinc silicates and carbonates was discovered below the Lead Manto.

Since 1997, Metalline Mining Company has held concessions in the district. Metalline started the drilling program in the La Nortena area and in the oxide Zn zones in the San Salvador and Encantada mines, where high grade ores were intersected in both mineral systems (Metalline: www.metalin.com). In 2001, Metalline Mining Company signed a joint venture with North Limited of Australia for a feasibility study of the district. North Limited of Australia worked on mapping, channel sampling in underground workings, and creating vertical cross sections compiled north to south at 10 m intervals along the 1500 m strike length of the San Salvador-Encantada-Froteriza zinc manto, which is now called the Iron Oxide Manto. In the beginning of 2000, channel sampling was performed in the Smithsonite Manto below the Red Zinc Manto. In October, 2000, the joint venture with the North Limited of Australia was terminated due to the different corporate priorities (Metalline: www.metalin.com). In November 2001, Metalline Mining Company signed a joint venture agreement with Minas Peñoles S.A. for a feasibility study. They continued to explore and evaluated the non-sulfide Zn resources through surface and underground drilling, mapping, and channel sampling in the San Salvador, Encantada, and Fronteriza mines. The joint venture agreement was terminated in December 2003. In January 2004, Metalline began a diamond drilling program of 30,000 m in the San Salvador, Encantada, and Fronteriza mines (Metalline: www.metalin.com). In late 2009, Metalline Mining and Dome Ventures Corp. joined forces to continue exploration of the Sierra Mojada district.

PREVIOUS STUDIES

Geologic occurrences of metal deposits in northeastern Mexico are widely studied in literature (Titley 1997, and Megaw et al., 1998). Recent studies on metal deposits in northeastern Mexico include Tritlla et al. (2007) and González-Sánchez et al. (2009). Specific studies on the Sierra Mojada district are available through the company consulting report by Hodder (2001) and information on the website of the Metalline Mining Company (www.metalin.com). Older studies include Chism (1887), Malcolmson (1902), Horn (1912), Shaw (1923), and Riley (1936), but these studies are mostly related to Ag-, Cu-, Pb- polymetallic deposits and none of these involves the non-sulfide Zn deposits. Low-temperature deposits in northern Mexico have been considered to originate from adjacent magmatic activities. The Sierra Mojada district traditionally is classified as one of the high-temperature carbonate-replacement type deposits of the Mexican belts (Megaw et al., 1988). However, there is no evidence of high temperature mineral assemblages and alteration features in the district, and the regional setting shows no close relationship with the polymetallic carbonate-hosted deposits in northern Mexico. Evidence of intrusive activity has not been found in the ore-hosting sequences or near the district, and the lack of high-temperature mineral assemblages has been used in recent studies to promote the origin of the deposits through low-temperature basin-related processes (Tritlla et al., 2007; Gonzalez et al., 2009). The origin of the non-sulfide Zn deposits is believed to represent secondary processes with metals being transported by groundwater after oxidation of primary Zn-sulfide deposits.

NON-SULFIDE ZN OVERVIEW

Geologic Setting

With the development of solvent-extraction electro-winning (SXEW) processes, non-sulfide Zn ores have drawn both economic and academic attention in recent years. Non-sulfide Zn deposits around the world have been considerably reviewed and classified in literature (Large 2001, Boni et al. 2003, Borg et al. 2003, Hitzman et al. 2003). An advantage of non-sulfide Zn over Zn sulfides includes lack of undesirable elements, such as Pb and S and an effective recovery of ores by SXEW (Boni, 2003) without causing hazardous effects on environment. Most supergene Zn deposits occur near major deformational belts due to the favorable weathering history (Hitzman et al., 2003) (Figure 1.2.). Most of known non-sulfide Zn deposits occur in carbonate rocks due to the highly reactive nature of the host rocks.

Major minerals commonly associated with non-sulfide Zn deposits are hemimorphite ($\text{Zn}_4\text{Si}_2\text{O}_7(\text{OH})_2 \cdot \text{H}_2\text{O}$), smithsonite (ZnCO_3), sauconite ($\text{Na}_{0.3}\text{Zn}_3(\text{Si},\text{Al})_4\text{O}_{10}(\text{OH})_2 \cdot 4(\text{H}_2\text{O})$), willemite (Zn_2SiO_4), hydrozincite ($\text{Zn}_5(\text{CO}_3)_2(\text{OH})_6$), zincite (ZnO), anglesite (PbSO_4), cerussite (PbCO_3), and franklinite (ZnFe_2O_4). Non-sulfide Zn deposits mostly include economic Zn minerals, such as smithsonite, hemimorphite, and hydrozincite (Boni, 2003).

Large (2001) divided non-sulfide Zn deposits into supergene and hypogene deposits. Later, Hitzman et al. (2003) classified these into several subtypes. Hypogene deposits can be subdivided into: structurally controlled deposits, consisting of veins and irregular pipes and stratiform non-sulfide zinc deposits. They are not necessarily originated from oxidation of sulfides. Hypogene deposits are dominant by Zn silicates and oxides, and mainly consist of willemite, minor sphalerite, franklinite, zincite, and manganese-rich minerals. The structurally controlled type formed by fluid mixing of S-

poor, reduced Zn-rich hydrothermal solutions and an oxidizing fluid along the fault consists of irregular pipes and veins (Hitzman et al., 2003). Willemite may replace sphalerite, but it can be intergrown or overgrown sphalerite (Hitzman et al., 2003). Hydrothermal willemite-dominant deposits are rare around the world because they require specific geochemical constraints (Brugger et al., 2003). Stratiform hypogene non-sulfide Zn deposits are manganese-rich. Formation of these deposits is also from mixing of two fluids between reduced Zn-rich, S-poor hydrothermal fluids and S-poor oxidizing waters (Hitzman et al., 2003).

Supergene non-sulfide zinc deposits are more common than hypogene non-sulfide Zn deposits and can be formed either from oxidation of sulfides or non-sulfide Zn deposits (Hitzman et al., 2003). Hitzman et al. (2003) subdivided supergene Zn deposits into three types: direct replacement, wall-rock replacement, and residual and karst-fill deposits (Figure 1.3). The major Zn minerals of these supergene deposits are smithsonite, hemimorphite, hydrozincite, and sauconite. In the most common weathering conditions of 25 °C and neutral pH, smithsonite is the most stable mineral (Hitzman et al., 2003).

In direct replacement supergene deposits, hemimorphite and smithsonite directly replace sphalerite in original sulfide deposits that usually contain galena, copper and iron sulfides. As there is subsequent weathering of sulfide bodies during supergene processes, the deposits show different replacement mineral assemblages. Their mineralogy is complex. Direct replacement deposits can be formed from Mississippi Valley-types or carbonate-replacement-types, and so their resulting mineralogy is different from each other.

Wall-rock replacement supergene deposits form near groundwater flow gradient from the primary sulfide bodies and direct-replacement deposits. Acid is generated from the oxidation of the sulfide body; the acidic Zn-bearing groundwater moves into

carbonate host rocks, and Zn carbonates, such as smithsonite, can be precipitated as the solution is neutralized. As a result of metal separation due to different metal mobilities, the major Zn mineral is cryptocrystalline smithsonite (Boni, 2003).

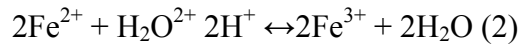
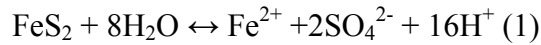
Residual and karst-fill deposits form from the accumulation of secondary Zn minerals in karstic depressions or cavity fills. They are usually formed in tectonically uplifted areas and also wet tropical climates which can accelerate the formation of a karst system (Hitzman et al., 2003). Since Zn can be easily separated from other metals in wet, heavy rainfall areas, this type of deposit might form high-grade smithsonite within those cavities (Hitzman et al., 2003).

Some of non-sulfide zinc deposits show a more hybrid nature of their genesis, mixing these three supergene deposit types. There are several important factors for generating economic non-sulfide Zn deposits: wall rock composition, fluid pathways (determining the location of ore bodies), climate, effective trap area, and topographic changes, such as tectonic uplifts by decreasing groundwater movement that can move Zn out of the sulfide bodies (Hitzman et al., 2003). Reactive carbonate rocks provide an effective trap site of metals from acidic oxidizing metal-bearing fluids. The composition of carbonate wall rocks plays an important role on deciding what kind of Zn-bearing minerals will precipitate. Smithsonite and hydrozincite usually precipitate in wall rocks with low impurities, whereas hemimorphite and sauconite tend to precipitate in siliciclastic or impure carbonates, or near siliceous soils (Hitzman et al., 2003).

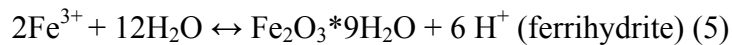
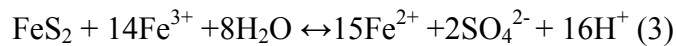
Geochemical Processes of Formation of Non-sulfide Zn Minerals

Geochemical characteristics of Pb and Zn mineral deposits are discussed in Takahashi (1960), Sangameshwar and Barnes (1983), Williams (1991), and Reichert and Borg (2008). The oxidation of pyrite, following hydrolyzation of ferric iron (Fe^{3+}), and Fe-bearing sphalerite are the most important factors of ore genesis in non-sulfide Zn

deposits because this processes lower the pH of groundwater in contact with the sulfide bodies (Reichert and Borg, 2008). The general reactions of the pyrite oxidation and the oxidation of ferrous iron (Fe^{2+}) followed as (Williams, 1990):

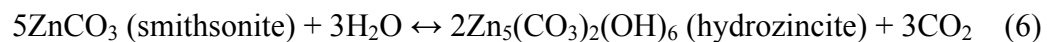


This released ferric iron (Fe^{3+}) involves the generation of acid and release of protons in reactions 3, 4 and 5, and released acids react with carbonates ultimately causing the constant removal of protons that drives the equations to the right due to the consumption of H^+ ions (Reichert and Borg, 2008). The reactions are (from Reichert and Borg, 2008).



The released bicarbonate and carbonates may react with metal ions and precipitate secondary minerals (Reichert and Borg, 2008).

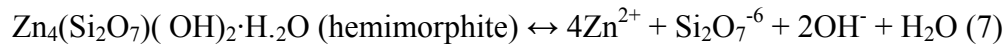
High P_{CO_2} (g) increases the stability of smithsonite within a certain pH interval due to the raised activity of $\text{HCO}_3^-(\text{aq})$ and $\text{CO}_3^{2-}(\text{aq})$ in the aqueous fluids, and the minimum $\log P_{\text{CO}_2}(\text{g})$ of 0.4 kPa is required for smithsonite precipitation, which is higher than atmospheric or arid soil $\text{P}_{\text{CO}_2}(\text{g})$ (Reichert and Borg, 2008). If $\log P_{\text{CO}_2}(\text{g})$ is greater than 0.4 kPa, the reaction would go to the left, and smithsonite will precipitate instead of hydrozincite in reaction 6 (Reichert and Borg, 2008):



In the unsaturated zone, closer to the atmosphere, hydrozincite would be more stable than smithsonite because the stability of smithsonite requires higher P_{CO_2} than atmospheric CO_2 or P_{CO_2} (Reaction 6 and Figure 1.4B). Because smithsonite is the least

soluble mineral compared to other NSZ minerals, such as hemimorphite and hydrozincite, under 25 °C and neutral conditions, typical of weathering environments, it is the most abundant mineral in supergene deposits (Hitzman et al., 2003).

Hemimorphite is commonly formed from the oxidation of sphalerite when silica is present. The precipitation of Zn silicates, including hemimorphite, depends on the availability of silica in solution, which is greater under acidic to slightly basic pH conditions. The abundance of hemimorphite can indicate acidic and slightly reducing genetic conditions (Hitzman et al., 2003).



The equation for hemimorphite dissolution by Takahashi (1960) is shown in a reaction 7. In an experimental study done by McPhail et al. (2003), hemimorphite is less soluble at temperatures between 20 and 80 °C than willemite (Zn_2SiO_4). Willemite can form from both supergene and hydrothermal environments. Willemite in supergene conditions may precipitate over hemimorphite in saturated oxidizing fluids having some specific composition through slightly elevated temperature and pressure (Pough, 1941 and Markham, 1960).

Figure 1.4A shows the stability fields for hemimorphite, smithsonite, hydrozincite, and Zn hydroxide in silica-saturated solution at 25 °C indicating possible maximum stability fields of hemimorphite. The stability fields of hemimorphite and hydrozincite can be changed by different P_{CO_2} (g) values and the chemistry of mineral assemblages in equilibrium with aqueous fluids (Reichert and Borg, 2008). Hydrozincite and smithsonite are less stable under acidic conditions than hemimorphite (Figure 1.4B). Hemimorphite is stable under acidic conditions and low carbonate activities produced by sulfide weathering (Hitzman et al., 2003). If the solution is undersaturated with silica, the area of hemimorphite stability is reduced to more acidic side (Takahashi, 1960). Hemimorphite

is believed to be stable with many other non-sulfide Zn minerals, but sauconite would be more stable under the basic pH condition (McPhail et al., 2003).

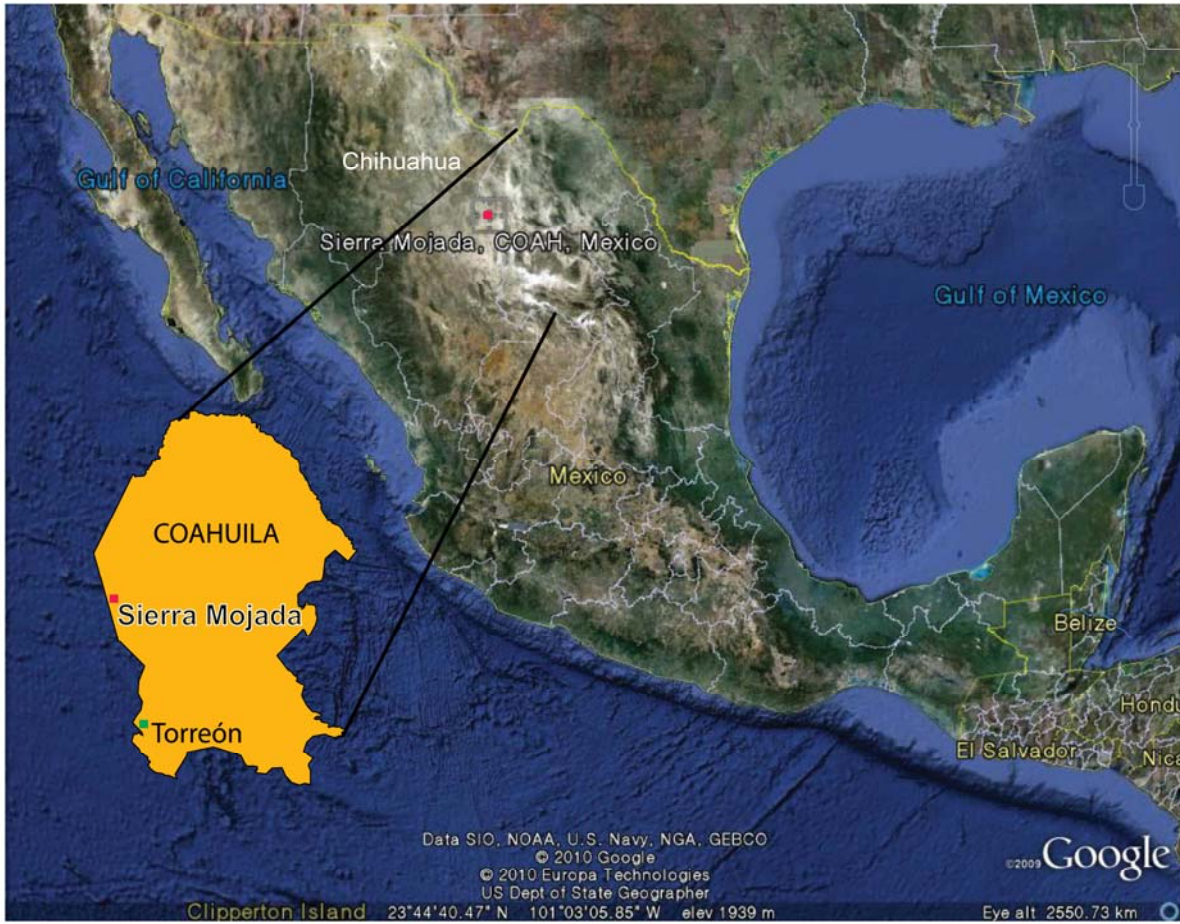


Figure 1.1. Location map of the Sierra Mojada district.

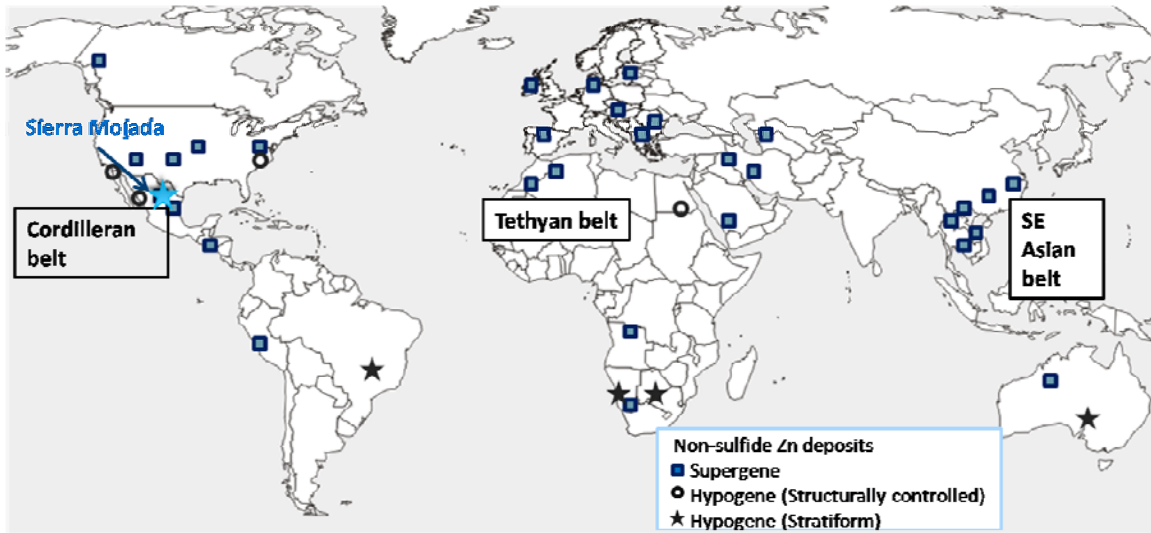


Figure 1.2. Distribution of non-sulfide Zn deposits around the world.

Modified after Hitzman et al. (2003) and Boni (2003).

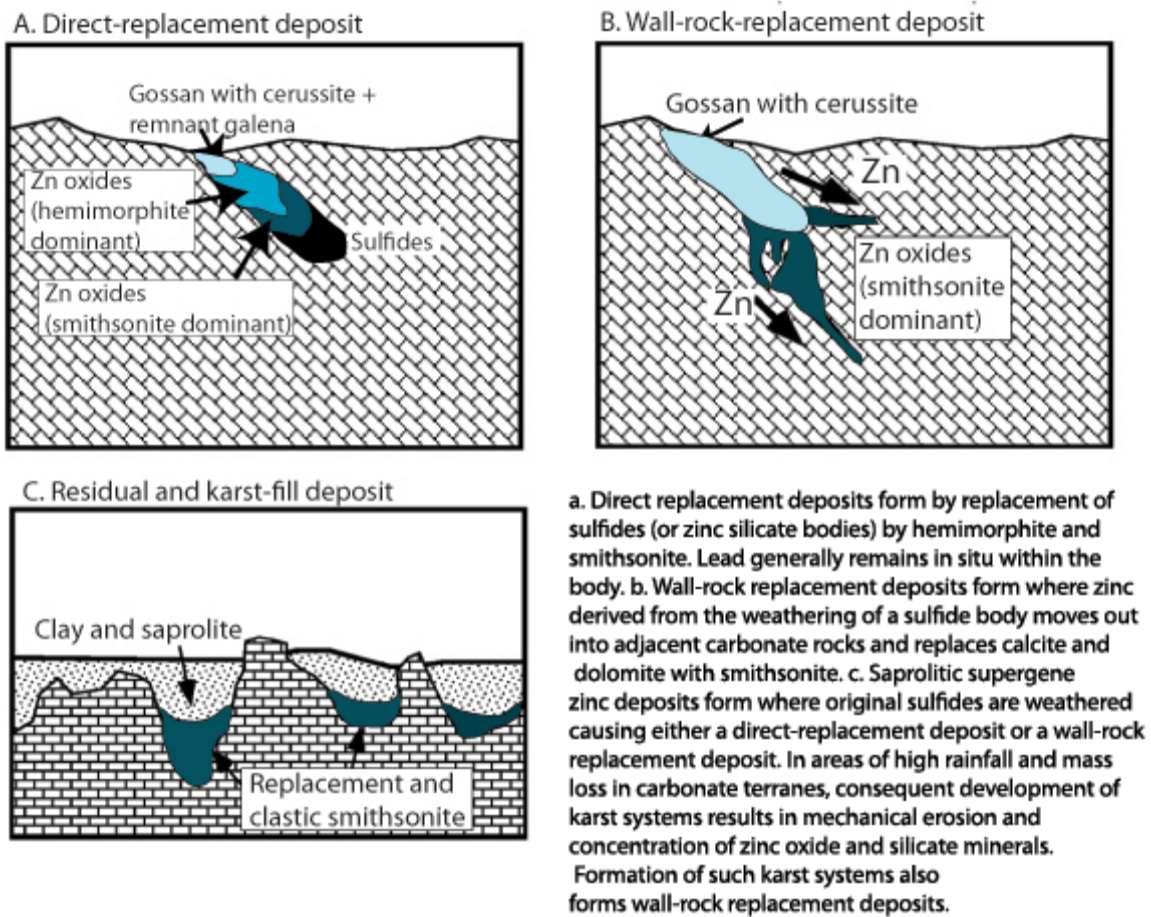


Figure 1.3. Three models of formation of supergene non-sulfide Zn deposits.

Modified after Hitzman et al. (2003).

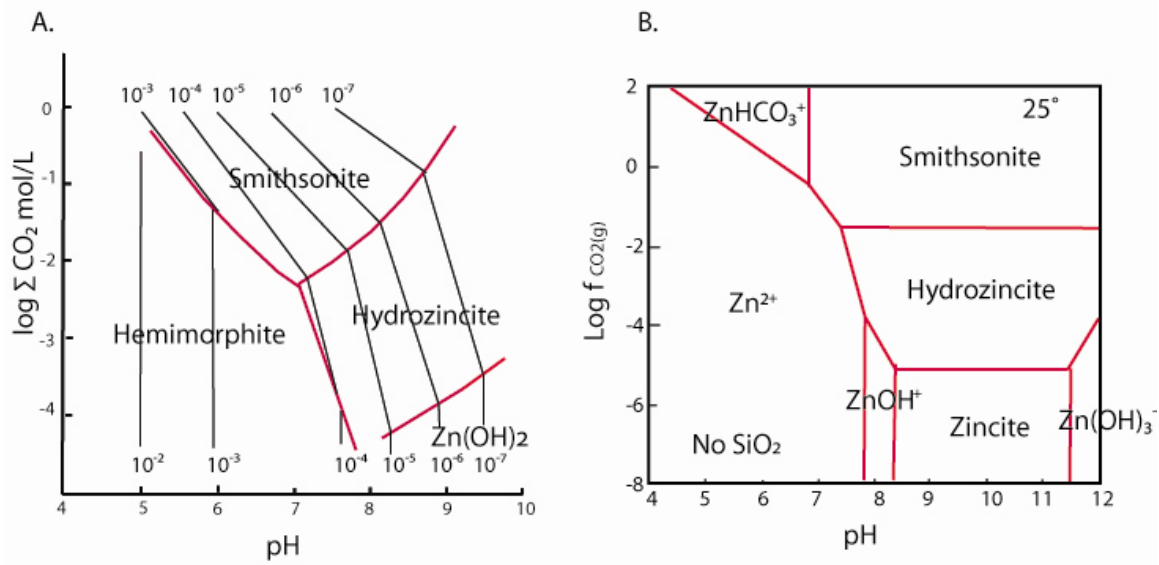


Figure 1.4. The stability fields of non-sulfide Zn minerals.

A. Possible maximum stability field of hemimorphite in silica-saturated solutions at 25°C . Contour lines indicating Zn mol/L in solution. After Takahashi (1960) **B.** Stabilities of Zn minerals with “Zn species” = 10^{-5} and atmospheric CO_2 of $10^{-3.5}$. Assuming no silica. After McPhail et al. (2003).

Chapter 2. Regional and District Geology

REGIONAL GEOLOGY

Northeastern Mexico has undergone a complex set of geologic events, starting from the Ouachita-Marathon orogenic event during the Permian and Triassic, followed by Jurassic rifting, and then by the early Mesozoic opening of the Gulf of Mexico and passive margin development through the late Cretaceous (Goldhammer, 1991). Laramide deformation occurred during the Late Cretaceous through the Early Tertiary. The Laramide deformational features in Mexico show different styles of deformation mechanisms from region to region (Chávez et al., 2008). Northeast-southwest Laramide compression developed the Mexican thrust belt, where most high-temperature carbonate-hosted deposits occur, but the margins of the Mexican thrust belt were less folded than the center, where the Sierra Mojada district lies (Megaw et al., 1988).

The Sabinas Basin is located in the states of Coahuila and Nuevo Leon, and the basin is originated from a rifting event during the opening of the Gulf of Mexico (de Antunano, 2001). Figure 2.1 illustrates general geology and a tectonic map of Mexico and the Sierra Mojada district is located on the southern edge of Sabinas basin. The northern margin of the Coahuila block is bound by the San Marcos fault (Goldhammer, 1991). The San Marcos Fault is the regional basement structure in northeast Mexico with the length of at least 300 km separating the Coahuila block from the Coahuila fold belt, and the fault is believed to have been reactivated at least four times from the Late Jurassic extension to the Pliocene-Quaternary (Chávez-Cabello et al., 2007).

The basement of the region is Late Paleozoic, heterogeneous rocks that accumulated on the North American Precambrian craton during the Appalachian-Ouachita-Marathon orogeny (Campa and Coney, 1983). Basement is unconformably

overlain by Middle Jurassic terrestrial red beds and evaporite (Campa and Coney, 1983). The Chihuahua, Coahuila, and Sierra Madre are the largest terranes in northeastern Mexico (Megaw et al., 1988). The Sierra Mojada district occurs within the Coahuila terrane, where Mesozoic limestone, dolomite, shaly limestone, red beds, and evaporite stratigraphic sections occur (Megaw et al., 1988). The Coahuila terrane is bound by the Sierra Madre terrane to the west and to the Maya terrane on the south, which belongs to the front of the Late Cretaceous-Early Tertiary Laramide thrust zone (Hodder, 2001).

GEOLOGY OF THE SIERRA MOJADA DISTRICT

The Sierra Mojada district is located on the southern edge of the Sabinas Basin, a rift basin of carbonate and clastic sedimentary rocks formed during Late Jurassic and Cretaceous tectonic extension. The structure of the Sierra Mojada district was controlled by Laramide folding (Megaw et al, 1988). The Sierra Mojada mountains entirely consist of limestone (Malcolmson, 1901).

The two secondary Zn ore deposits are hosted by the Cretaceous marine carbonate sequence south of the San Marcos fault that transverses the Sierra Mojada district. The stratigraphy and structure of the district is currently being studied by S. Gryger (in progress). The following discussion will refer to current local stratigraphic terminology used by Metalline Mining (www.metalline.com). The marine carbonates, and sandstone and shale of the Menchaca and La Casita Formations at Upper Jurassic and Lower Cretaceous sequence is underlain by Lower Cretaceous red beds of the San Marcos Formation. The marine carbonate rocks of Early and Middle Cretaceous age of Cupido, La Pena, Aurora, and Georgetown Formations overlie the San Marcos Formation. The Aurora Formation is characterized by massive beds, dipping south, with rudists and large bivalves and the Menchaca Formation of shale and sandstone units, dipping north, is

medium bedded including foraminifera and small bivalves without rudists (Metalline, www.metanlin.com).

The general topography of the region and possible groundwater flow gradients (Figure 2.3). The district is located at a relatively high elevation of 1200 m in a region where the highest location is 2400 m. The entire water table is now below known Zn ore bodies in the district, even for the deepest mine at 1135 m. Closed drainage basins are prevalent in the region. Usually wells in carbonate rocks around the mine area are non-productive, but wells away from the mine area become artesian in the carbonate sequence with the static water table around 1000 and 1020 m elevation (R. Kolvoord, written comment). The water is nearly neutral (6.7-7.4 pH) with a warm temperature around 26 and 27 °C, and is of the sulfate-bicarbonate-chloride type (R. Kolvoord, written commun.).

The time of ore mineralization in most carbonate-hosted deposits in the Mexican belts is assumed to be mid-Tertiary, after the Laramide aged Mexican thrust belt (Megaw et al., 1988), but the exact time of mineralization for the Sierra Mojada district has not yet been confirmed. The host carbonates in the Mexican belt are thick-bedded, porous stones of diagenetic origin (Megaw et al., 1988). Hodder (2001) suggested that the timing of mineralization may be post-Laramide thrusting, but before mid-Tertiary thermal inversion of the Sabinas Basin based on the evidence from metal concentrations on Mesa La Blanca that are separated by a reverse fault.

MINERAL DEPOSITS OF THE DISTRICT

In the Sierra Mojada district, there are three major deposits: polymetallic (Zn-Pb-Cu-Ag) sulfides and two non-sulfide Zn deposits called the Smithsonite Manto and the Iron Oxide Manto (Figure 2.4A). Much of the historic production was from the Lead

Carbonate Manto which is largely mined out. Polymetallic Zn-bearing sulfide concentrations and the Lead Carbonate Manto are present as separate zones from two NSZ mantos (Figure 2.4). Classification of carbonate-replacement ore deposits in Mexico, which is primarily based on morphology and mineralogy, can be in the form of chimneys and mantos (Megaw et al., 1988). The orebodies in the district share similar morphologies with other carbonate-hosted deposits in Mexico (Hodder, 2001). Mineralization of the district is mainly separated by the San Marcos fault, locally called the Sierra Mojada fault (Figure 2.3A). To the north of the fault, massive polymetallic sulfides occur at lower elevations in the Menchaca Formation. These sulfides are the stratigraphically lowest and structurally highest ore in the district (R. Kolvoord, written comment). South of the Sierra Mojada fault mineralization comprises of non-sulfide Zn and Ag-rich Pb carbonate mantos in the Aurora and La Pena Formations (Metalline: www.metalin.com).

Beneath the Lead Manto, the Iron Oxide Manto consists of strata-bound bodies of Fe-oxide rich material with Zn-bearing silicates and carbonates within a dolomitic horizon at the base of the Aurora Formation (Hodder, 2001). Below this zone non-sulfide Zn mineralization of the Smithsonite Manto hosted in Cretaceous marine carbonate sequence is located in the basal Aurora Formation and extends to the La Pena Formation. Smithsonite Manto shows a more chimney-like form with smithsonite. Karst features and cavity-fills are observed in underground exposures.

SIERRA MOJADA NON-SULFIDE ZN MINERALIZATION

The two main non-sulfide Zn deposits, the Smithsonite Manto and the Iron Oxide Manto, occur south of the San Marcos fault in younger strata at lower elevations. The non-sulfide Zn ores at the Sierra Mojada district consist of stratigraphically constrained Zn carbonates and silicates. The most important non-sulfide Zn minerals are smithsonite,

hemimorphite, and sauconite. Mn-oxides intermixed with Zn clays and smithsonite is common. Late-stage calcite is abundant in both Zn deposits with minor amount of barite and Fe oxides, and traces of chert.

These ore zones are spatially separate from each other and from the polymetallic manto. Non-sulfide Zn mineralization in the district shows various ore textures and the vertical and horizontal bands that consist of several layers of Zn minerals ranging on a scale from a few centimeters to meters. In the Smithsonite Manto, the Zn minerals occupy secondary porosity in the host carbonates, including karst features and internal sediments cemented by and intermixed with Zn-rich zones. Smithsonite occurs as layers or brecciated cavity-fills. Hemimorphite shows different types of mineralization. It has locally replaced or occurs as fracture-filling in smithsonite, although locally smithsonite and hemimorphite appear to have grown together. Also, it is observed that hemimorphite cemented some cave-fill sediments and breccias with later stage calcite cement. The Iron Oxide Manto is stratabound with pore-filling of hemimorphite and smithsonite in Fe-rich dolostone, including local cave-fill deposits. Hemimorphite and smithsonite in the Iron Oxide manto are hosted by dolomitic goethitic or hematitic oxide matrix. In many cases, hemimorphite is coated by late-stage calcite.

SAMPLING AND METHODOLOGY

The main objective of this project is characterization of secondary Zn minerals in two different mantos (the Smithsonite Manto and the Iron Oxide Manto) and to constraint the environment of formation. This part of this project focuses on morphological characterization and geochemical variations of secondary minerals, the possible presence of primary sulfides, and relationships between Zn carbonates and Zn silicates in the carbonate setting. Samples are collected from underground exposures in the Smithsonite and the Iron Oxide Mantos. Lists and detailed descriptions of samples are shown in

Appendix A. Oriented samples of Zn carbonates, Zn silicates, and associated minerals and a few sulfide samples in mineralized strata were studied using a polarized microscope, a scanning electron microscope (SEM) with an energy-dispersive X-ray detector (EDS), an electron microprobe (EPMA), cathodoluminescence (CL), and a laser ablation-inductively coupled plasma-mass spectrometry (LA-ICP-MS). Carbon and oxygen isotopes of smithsonite and calcite analyzed by Dr. H. Albert Gilg, at Technische Universität München, Germany.

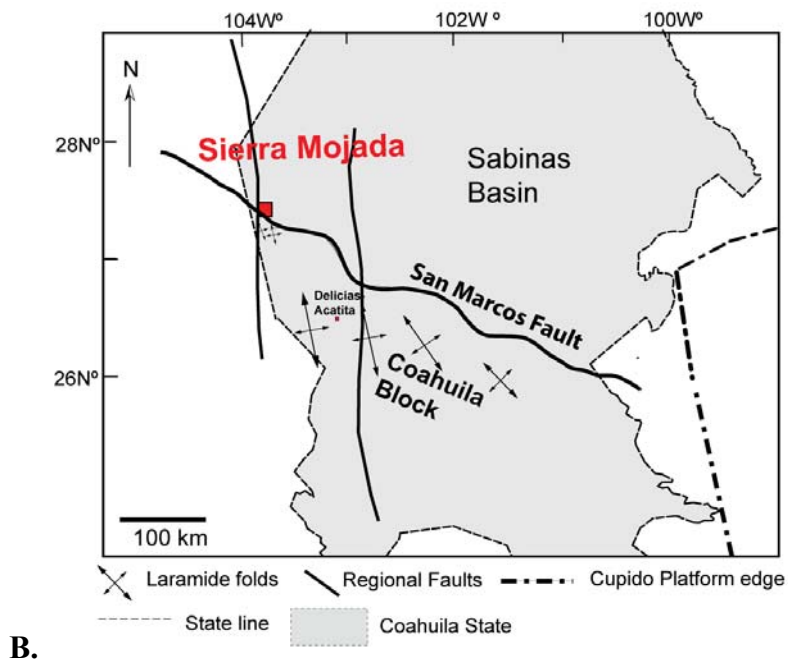
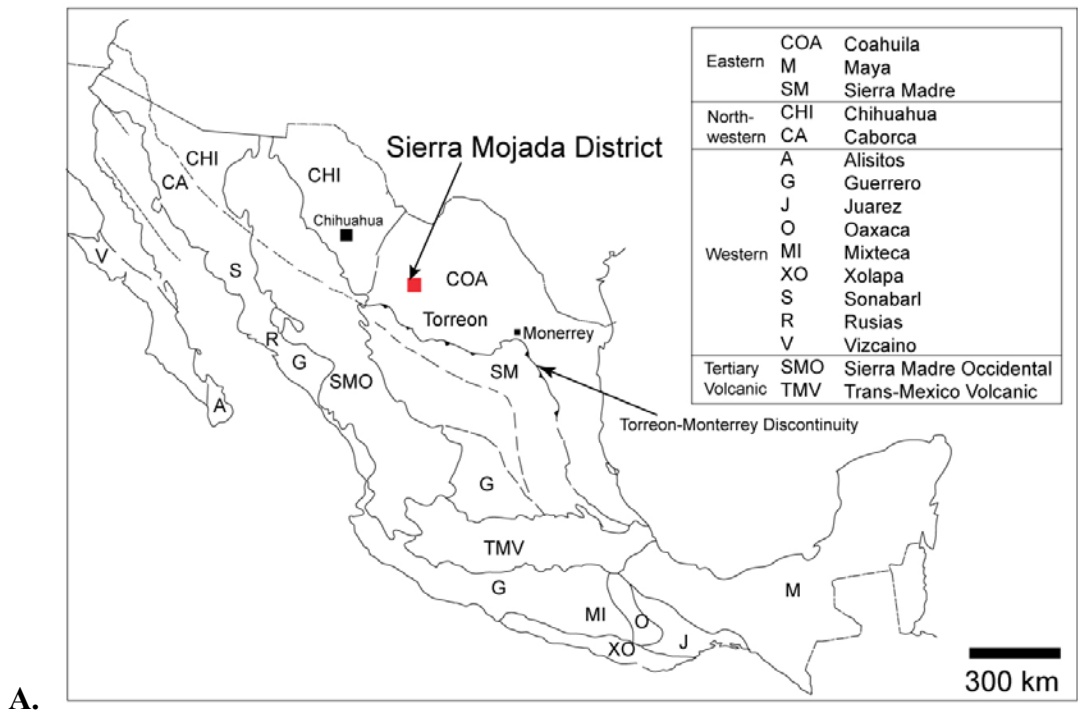


Figure 2.1. Regional geology of Mexico.

A. Regional geology of Mexico. Modified after Campa and Coney (1983). **B.** Tectonic map of northeast Mexico and contiguous U.S. Modified after Goldhammer et al. (1991).

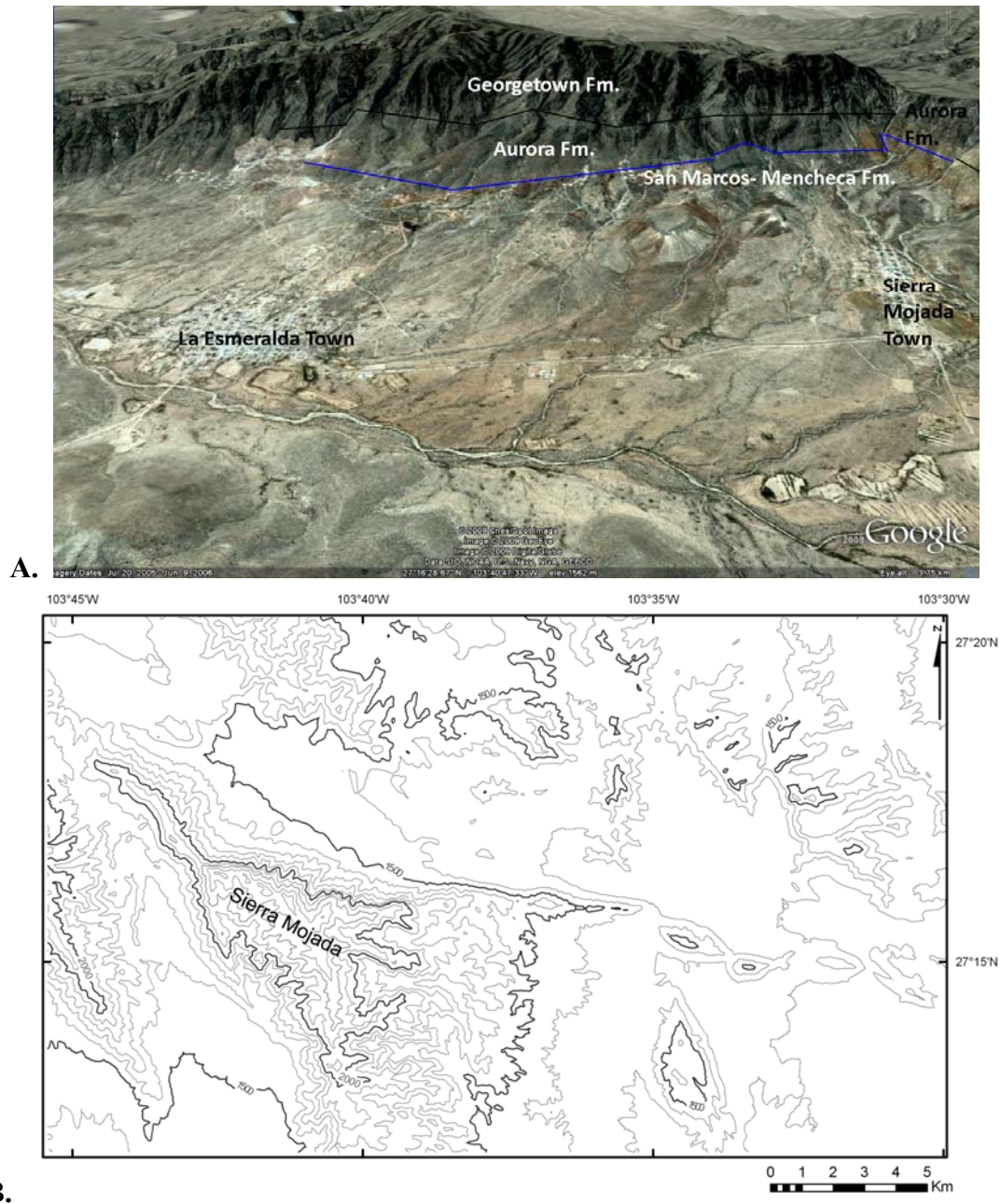


Figure 2.3. Overview of the Sierra Mojada region.

A. View of the longitudinal section of the district and the San Marcos fault looking southwest. The blue line refers to the traces of the San Marcos fault. Modified after Metalline: www.metalin.com. **B.** Topographic map of the Sierra Mojada region. Created from 1-Arc Second National Elevation Dataset (NED) from the National Map Seamless Server: seamless.usgs.gov.

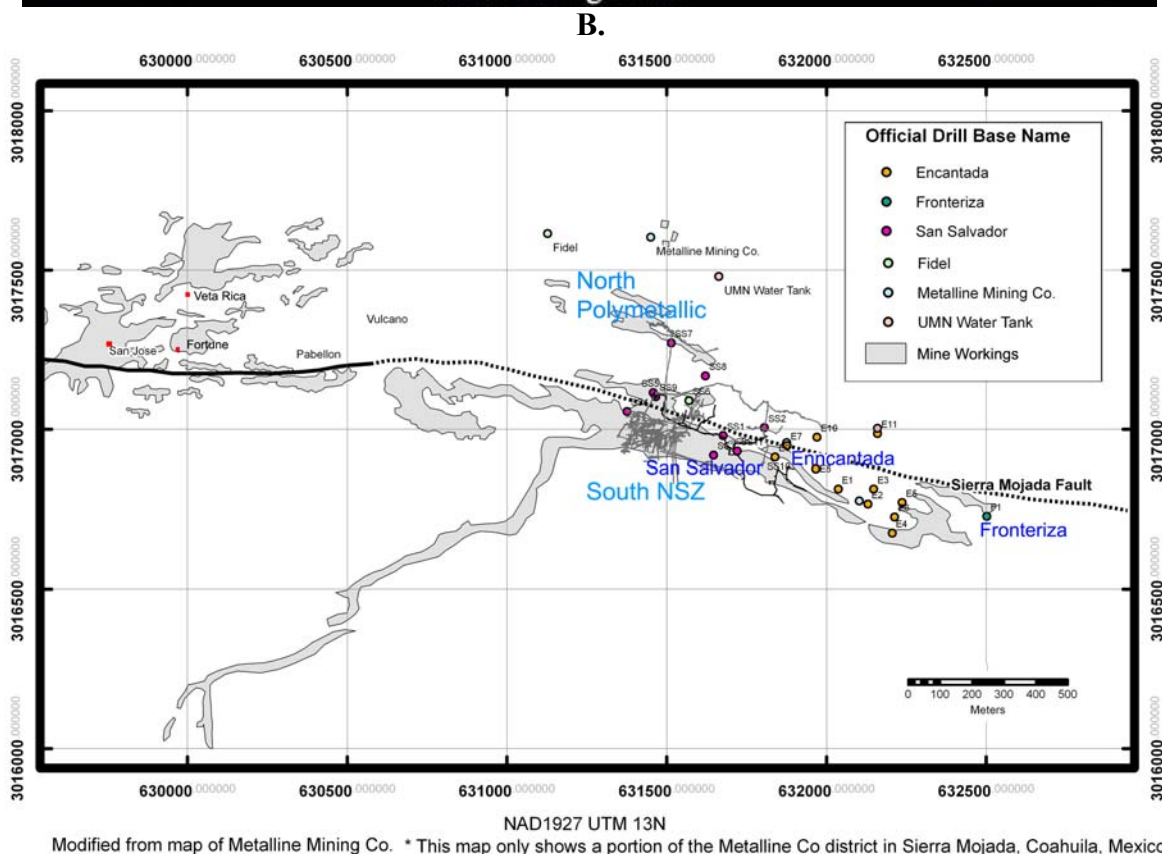
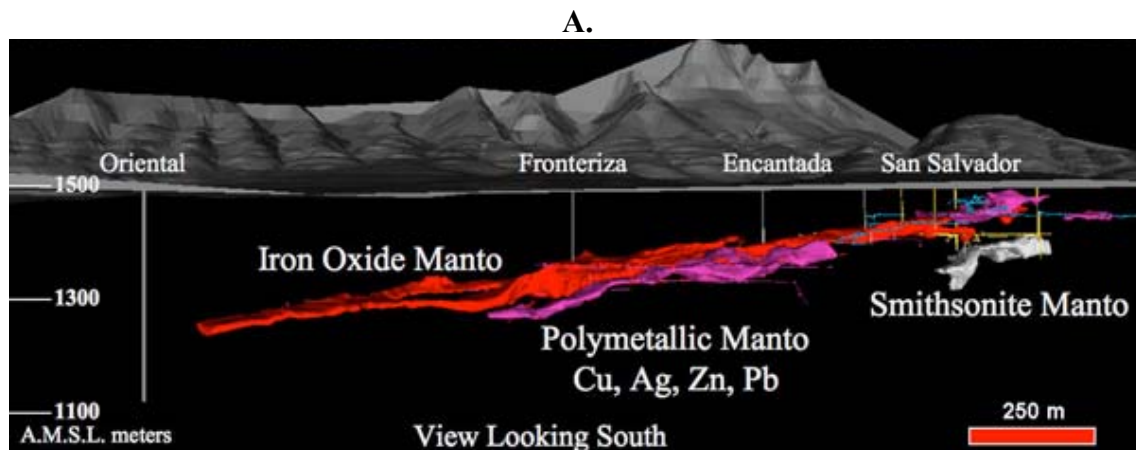


Figure 2.4. Ore bodies and mines of the Sierra Mojada district.

A. A 3-D block model of ore bodies, including the Iron Oxide Manto, Smithsonian Manto, and Polymetallic Manto. From Metalline Mining: www.metalin.com. B. Mines, workings and stopes. Modified after Metalline Mining: www.metalin.com.

Table 2.1. Abbreviations.

A. Mineral abbreviations identified within the Smithsonite Manto and the Iron Oxide Manto

Minerals	Chemical Formula	Abbreviation
Anhydrite	CaSO ₄	an
Argentite	Ag ₂ S	ag
Barite	BaSO ₄	ba
Calcite	CaCO ₃	ca
Cerussite	PbCO ₃	ce
Galena	PbS	ga
Gypsum	CaSO ₄ ·2H ₂ O	gy
Covellite	CuS	cv
Dolomite	CaMg(CO ₃) ₂	do
Hemimorphite	Zn ₄ Si ₂ O ₇ (OH) ₂ ·H ₂ O	hm
Quartz	SiO ₂	qz
Sauconite	Na _{0.3} Zn ₃ (Si,Al) ₄ O ₁₀ (OH) ₂ ·4H ₂ O	sc
Smithsonite	ZnCO ₃	ss
Sphalerite	ZnS	sp
Tennantite	Cu ₁₂ As ₄ S ₁₃	tn

B. Other abbreviations commonly used in this report

Abbreviation	Term
BEI	Backscattered electron imaging
BSE	Backscattered electron
CL	Cathodoluminescence
CPS	Counts per second
EDS	Energy-dispersive X-ray Analysis
EPMA	Electron Microprobe analysis
Fm	Formation
IOM	Iron Oxide Manto
keV	Kilo electron volts
LA-ICP-MS	Laser Ablation Inductively Coupled Plasma-Mass Spectrometry
NSZ	Non-sulfide Zn
PPL	Plane polarized light
SE	Secondary electrons
SEI	Secondary electron imaging
SEM	Scanning Electron Microscope
SMF	San Marcos Fault
SMj	Sierra Mojada
SSM	Smithsonite Manto
WDS	Wavelength-dispersive spectrometer
XPL	Cross polarized light

Chapter 3. Mineralogy and Geochemistry of the Smithsonite Manto

The non-sulfide Zn ores are hosted by the thin-bedded Cretaceous Aurora Formation and by the upper part of the La Pena Formation. The Aurora formation consists of thick massive beds of platform and reef limestone with large rudistid bivalves. The La Pena formation, conformably overlain by the Aurora formation, is thin-bedded limestone with shale partings. The Smithsonite Manto shows chimney-like morphology (Figure 2.4A). It also shows karst features with internal sediments cemented by or intermixed with smithsonite, hemimorphite, or calcite. It spans an area between 1300 and 1400 m elevation, and samples were collected near the bottom about 1300 m elevation. Hand sample analyses are performed on a total of 34 hand specimens, and approximately 46 thin sections are made in order to perform petrographic analyses. Selected samples are analyzed with SEM/EDS and microprobe analyses. Botryoidal smithsonite with minor amounts of hemimorphite in vuggy cave-fills is commonly found (Figure 3.1A), and vertical bandings of smithsonite are locally observed (Figure 3.1D) in the Smithsonite Manto. Laminated cave-fill detritus cemented with Zn-bearing minerals is observed locally (Figure 3.1B) in underground exposures. Banded or pendulant smithsonite is also common. Smithsonite is more abundant than hemimorphite. White-banded smithsonite alternating with sauconite can be mainly observed (Figure 3.1C). Sulfide minerals are very rare in this ore body. The principal Zn-bearing minerals are smithsonite, hemimorphite, and sauconite.

PETROGRAPHY AND SEM STUDY OF MAJOR MINERALS

Morphological Characteristics of Zn-bearing minerals

Hand specimen observation, petrography, and SEM/EDS are used to characterize Zn minerals, including smithsonite, hemimorphite, and Zn clays, and other associated minerals.

Smithsonite

Smithsonite samples are characterized by their mineral habits. There was an effort to compare morphological types of smithsonite in the Sierra Mojada district to those of smithsonite in other non-sulfide Zn deposits in literature. Micromorphologies of smithsonite in Sardinia (Boni et al., 2003) and in Irish Midlands (Balassone et al., 2008) are divided into six types. Table 3.1 shows morphological types of smithsonite in other supergene deposits and in the Sierra Mojada district. Type I smithsonite consists of distinctly idiomorphic, rhombohedral crystals that commonly showed zonings, and range in size from 50 to 600 μm . It was found in vugs and cavities. The surface of the type I smithsonite does not show corrosion. The type II is polycrystalline microaggregates with curved faces ranging in size from 20 to 400 μm . This type is found as coatings over irregular vugs in earthy, grayish smithsonite. It is of tiny, subhedral crystals. Type III smithsonite is called “rice grains,” which consisted of both single large elongated crystal and microcrystalline aggregates. Type IV smithsonite is botryoidal aggregates of platy smithsonite. Type V smithsonite is a kind of type IV smithsonite without platy surfaces showing less distinctive crystal terminations. The average size of a mass of type V ranges from 100 to 300 μm across. Type VI consists of vuggy to drusy scalenohedral crystals.

Various morphological types of smithsonite have been observed in pore spaces, fractures, and vugs in samples collected for this project. The size of open space ranges

from micrometers to a few centimeters. Study of smithsonite morphologies reveals some mineral habits are comparable to those described in the literature. It includes rhombohedral (type I) and scalenohedral (type VI) crystals. However, their occurrences did not exactly match to the descriptions in the literatures.

Smithsonite in the Smithsonite Manto shows four major morphologies: scalenohedral, rhombohedral, matrix smithsonite, and massive crystals of banded, colloform smithsonite. The most common type of smithsonite in pores and vugs is aggregates of dog-tooth (scalenohedral) smithsonite growing on microcrystalline smithsonite and sauconite matrix (Figure 3.3). It occurs as either a cluster on smithsonite and sauconite matrix (Figure 3.3A) or scalenohedral crusts on smithsonite bands (5 mm to 1 cm) (Figure 3.1A). The length of each scalenohedral crystals ranges from 50 to 400 μm . Aggregates of dog-tooth smithsonite consist of several dog-tooth smithsonite microcrystals (Figures 3.3). Some of them seem to be corroded at the edge, while most scalenohedral smithsonite shows a euhedral crystal surface (Fig. 3.3C and E). Also, the matrix of Zn clays and Mn oxides of globular concretions locally are intergrown with smithsonite (Figure 3.4F). Some smithsonite shows sharp edges and others show slightly rounded edges (Figure 3.3F) and it would belong to a variation of aggregates of scalenohedral smithsonite.

Rhombohedral smithsonite crystals occurs as aggregates of botryoidal smithsonite (Figures 3.4A~D). The clusters of rhombic smithsonite crystals appear to grow on massive smithsonite substrate (Figure 3.4A), and some of them are zoned (Figure 3.4D). On the mineral surface, they are encrusted by Zn clays, Mn oxides, and occasionally Fe oxides.

Banded, colloform smithsonite with a thickness ranging from 5 mm to 10 cm is common in vugs. In hand specimen, it shows white, ivory, yellow, pale gray, pale green

and pale purple colors. It is usually banded. In microscopic scale, it shows massive or microcrystalline surface without distinct zonation (Figures 3.4F).

In morphological classifications, scalenohedral crystals growing on microcrystalline smithsonite substrate or infillings of open space can be classified as type VI smithsonite as it shared similar characteristics with those of Coppola et al. (2008). Rhombohedral smithsonites may be classified as type I smithsonite in agreement with Boni et al. (2003) and Balassone et al. (2008), but rhombic smithsonite in the SMj district appeared corroded (Figure 3.4D and F).

Hemimorphite

Hemimorphite is the second most common supergene Zn mineral in the Smithsonite Manto. It is closely associated with smithsonite, calcite, and sauconite. It usually occurs as distinct euhedral (tabular) crystals (Figure 3.5). On the basis of petrographic and morphological observation, hemimorphite is divided into two different types: hemimorphite-A and hemimorphite-B. Hemimorphite-A occurs as subhedral to euhedral crystals replacing or intergrown with smithsonite and filling fractures in non-sulfide Zn bodies (Figures 3.2C, 3.5C and D). It shows fan-shaped mineral habits under a petrographic microscope, which appears to have partially replaced banded smithsonite along a certain layers of smithsonite or along fractures in smithsonite (Figure 3.2C). This fan-shaped or sheaf-like hemimorphite locally shows a higher-order interference color than pore-filling hemimorphite (hemimorphite-B). However, locally it appears to be intergrown with smithsonite and sauconite. In certain samples containing hemimorphite-A, the matrix was a little more friable than smithsonite-rich samples.

Hemimorphite-B occurs as pore-filling tabular hemimorphite (Figure 3.5A and B). It is locally altered to sauconite, and hemimorphite precipitation is followed by calcite cement in some samples. It is also found on the outer edge of smithsonite as a single or

several crystals. Cell parameters for selected hemimorphite-I from XRD analyses are 8.370, 10.719, and 5.120 Å, which is close values to 8.365 (8), 10.711 (6), and 5.116 (8) Å, reported by Aversa et al. (2002).

Calcite

Petrography of several non-mineralized portions from the Smithsonite Manto was carried out. Bivalve and coral fragments are common with other fossil fragments. The size of fossils and fossil fragments, such as bivalves and corals, varies ranging from several micrometers to millimeters (Figure 3.6). Fossil fragments up to 4 mm are more common than complete fossils (Figures 3.6C). Late calcite after NSZ mineralization is common (Figure 3.7). Fracture porosity in ore-bearing limestone is partially or completely filled with bladed calcite, and most of pore spaces are completely filled with isopachous or blocky calcite (Figure. 3.7A). In addition, a few grains of barite have been observed in limestone and occur with hemimorphite precipitated along fracture (Sample SM08-01). Locally, smithsonite and hemimorphite are formed between calcite grains (Figure3.6 D).

Late calcite is found in various forms and habits with most non-sulfide Zn minerals as a secondary mineral (Figure 3.7). It is associated with hemimorphite, smithsonite and barite, and paragenetically later than supergene Zn minerals. Calcite shows blocky, scalenohedral, and rhombohedral crystal habits (Figure 3.7), and generally it does not exceed cm in size. It occurs locally as fracture-fillings (Figure 3.7B). Calcite cement is more common in hemimorphite-rich samples, such as SM08-11, SM08-27 and SM08-28 that include no smithsonite and are rich in sauconite and Mn oxides.

Occurrences of Zn clays and Mn minerals with smithsonite and hemimorphite

In most Smithsonite Manto samples studied, varieties of Zn clays have been observed with smithsonite and hemimorphite. K-bearing Zn clays were identified, but other types of clays were not detected. Tentative identification was performed using SEM/EDS in order to characterize its relationship with other Zn-bearing minerals. Sauconite is the Zn-bearing clays of the smectite group (Ross, 1946). Another common Zn clay in non-sulfide Zn deposits is fraipontite $(\text{Zn,Al})_3(\text{Si,Al})_2\text{O}_5(\text{OH})_4$ that belong to the kaolinite-serpentine group. Zn content in sauconite derived from the supergene alteration of sphalerite, while K-feldspar can be the major source of aluminum and silica (Boni et al., 2009). The abundance of sauconite might be related to arid climates as at Skorpion and Accha non-sulfide Zn deposits because the formation of sauconite from aluminosilicates can depend on Al and Si in relatively closed alkaline environments (Boni et al., 2009).

In hand specimens, it is friable and usually shows pink, white, ivory, and bright brown colors with powdery texture. It is difficult to identify exact clay types due to the various properties of clays even with observation of hand specimens, thin section petrography, and acquisition of SEM-EDS spectrum and due to unsuccessful powder X-ray diffraction analyses in this study. EDS spectra are mostly acquired at 20 keV. Due to the elemental peak overlap between Na and Zn, it is difficult to resolve the relative intensities of Na from Zn. Thin section petrography and SEM-EDS analyses reveals that hemimorphite and smithsonite have been locally replaced by Zn clays (sauconite).

Figures 3.8A and 3.8D show scalenohedral smithsonite that has been replaced by Zn clays and Mn-minerals (arrows in Figure 3.8D and E) which may have grown on Zn clay matrix. These types of replacement by sauconite could be found in many samples, including SM08-01, SM08-02, SM08-19, SM08-22, and SM08-26. Some of these Zn/Mn

clays usually show different morphological types and EDS patterns from sample to sample. Some Zn-clay layers appears to be intergrown with smithsonite (Figure 3.9D), but locally Zn clays appear to be clasts within karst detritus fill (Figure 3.1B). Also, smithsonite has grown on the brecciated fragments of sauconite and smithsonite (Figure 3.13D).

In Figure 3.9, secondary electron images of different types of authigenic Zn clays are shown. White Zn clays show Zn, Si, and Al elemental peaks without a Mn elemental peak (Figure 3.10A). Pink to brown Zn clays also show a Mn peak (Figures 3.8 and 3.10C). Relative intensity of Al and Si elemental peaks is different as well (Figure 3.8).

Other associated minerals

Barite is relatively common in trace amounts in the Smithsonite Manto. A typical barite occurrence can be seen in Figure 3.11A and B. Microcrystalline quartz is present, but rare. Mn/Pb-bearing minerals and oxides are also present (Figure 3.11D). K-(Mg)-bearing Zn clays are locally present (Figure 3.11C). Identification of these clays is tentative due to its extremely fine-grained and intermixed nature with other mineral phases.

Characteristics of cave-fill sediments

Mineralogical and elemental compositions of sediments in cave-fills are analyzed using SEM and SEM/EDS. Zn mineralization occurs as clasts, cement, pore-filling in karst detritus. These sedimentary materials are composed of friable fine-grained sediments and clay fragments (Figure 3.1B). In thin section views (Figure 3.11E and F), cave-fill sediments consists of clay-sized materials and contains Zn clays (sauconite) and Mn/Fe-oxides locally cemented by hemimorphite or calcite. Vugs are filled with hemimorphite, smithsonite, calcite, Zn clays, Fe oxides, and various Mn and Pb oxides.

The size of the breccias ranges from millimeters to a few centimeters. Hemimorphite and smithsonite are often altered to Zn clays as in Figure 3.9E and F. However, sauconite appears to have intergrown with smithsonite in some samples (Figure 3.9D). In these sedimentary materials, euhedral hemimorphite is more common as pore-fillings than smithsonite. The fragmented materials are usually one of the Zn clays later cemented by hemimorphite, smithsonite or calcite.

MAJOR ELEMENT ANALYSES OF CARBONATES

Methodology

Quantitative WDS analyses using electron probe microanalyzer (JEOL JXA-8200) were performed in order to obtain information on smithsonite composition in samples from Sierra Mojada. Elements included are MgO, FeO, MnO, CaO, and ZnO. Dolomite, siderite, and sphalerite were used as standards. Analyses were performed with an accelerating voltage of 15 keV, a probe current of 15~16 nA, and a spot size of 10 μm . Detailed analytical conditions are shown in Appendix D. Three types of smithsonite have been included for the analysis: massive and colloform smithsonite, pore-filling smithsonite, and microcrystalline smithsonite.

Massive and colloform smithsonite includes zoned smithsonite and smithsonite without distinct zonation under BSE images (Figure 3.12), which grows in vugs and usually banded. The thickness of banded colloform smithsonite analyzed ranges from 1 cm to 10 cm. This type of smithsonite was associated with late-stage calcite and hemimorphite. Although their colors and habits are slightly different from each other, they are grouped together because they share similar mineral habits like occurring as thick massive layers in vugs. Distinct compositional zonings under the backscattered

electron images are observed in some samples, including SM03-09, SM08-05 and SM08-09.

Scalenohedral smithsonite occurs in pore spaces (Figures 3.13), and banded smithsonite with scalenohedral crusts is included (Figure 3.13B) as scalenohedral smithsonite. Some of pore-filling scalenohedral smithsonite also shows compositional layering under BSE views, which is less visible under a polarizing microscope. Smithsonite in the matrix (Figure 3.14) has been analyzed, which is closely associated with sauconite.

Early and late calcites are included for WDS analyses. Early calcite occurs in limestone. Late calcite is found in various forms with most NSZ minerals as a secondary mineral.

Results

Metal content of Zn as ZnO ranges between 61 and 65 wt % (Table 3.2) (64.9 wt % ZnO for stoichiometric smithsonite (Boni et al., 2009)). Small amounts of Ca and Mg are present. The amount of MgO is from 0.1 to 3.5 wt %, and CaO is 0.1 to 2.8 wt %. Trace amount of FeO and MnO is detected in some samples. Overall, smithsonite analyzed in this project has no considerable amount of Mn or Fe.

Banded colloform smithsonite

The results are listed in Table 3.2. ZnO values range from 60.9 to 65.9 wt %. Minor amounts of CaO are detected ranging from 0.8 to 2.8 wt %. MgO, FeO, and MnO are only in trace amounts. Most FeO contents show no detectable amounts (<0.01 wt %). Figure 3.12C shows a difference in smithsonite composition. Figure 3.12C displays compositional layering in smithsonite alternating dark gray and light gray layers. Figure 3.12B and D shows a homogeneous phase in back-scattered electron images. The layers

result from compositional variations between the relatively lighter elements, such as Ca and Mg, and the heavier Zn. In darker zones, Ca ranges from 1.6 to 3.0 mole % with Mg of 0.1 to 0.2 mole %. In Zn-rich lighter areas, Ca ranges from 0.5 to 2.4 mole % and Mg ranges from 0.03 to 0.08 mole %.

Scaleno-hedral Smithsonite

This type of smithsonite is usually found in vugs and pores, and it is usually free from Zn clays and Mn/Fe oxides. The amount of ZnO ranges from 60.1 to 66.8 wt % (Table 3.3). This type of smithsonite is close to stoichiometric smithsonite. The MgO and CaO are detected. Most scaleno-hedral smithsonite does not show compositional variations (Figure 3.13B) except the sample, SM08-02 (Figure 3.13A). Fine dark zones are alternating with lighter layers. These darker zones are excluded when lighter areas are analyzed. In this scaleno-hedral smithsonite with distinct dark outer rim zonation, Mg is 5.3 mole % of and Ca is 0.2 mole %. The Zn-rich, lighter zone only shows 0.3 mole % Mg and 0.2 mole % of Ca. MnO and FeO are present in trace amounts. Only a small amount of hemimorphite is observed with smithsonite, which seems to have precipitated later than smithsonite.

Matrix Smithsonite

The composition of matrix smithsonite is analyzed in four samples (Table 3.4). It is intermixed or closely associated with Zn clays and Mn oxides (Figure 3.14). The matrix materials (Figure 3.14B) consist of Zn clays, smithsonite, and pores (Figure 3.14A). The amount of ZnO ranged from 62.0 to 65.9 wt % (47.9 to 49.5 in mole %). The average values of MgO and CaO are 0.4 and 0.6 wt %, respectively. Smithsonite in SM08-18A shows a slightly higher amount of MgO and CaO, and smithsonite in SM08-22B shows the relatively highest amount of CaO.

Calcite

Late-stage calcite includes minor amounts of Zn (Table 3.5). The average weight percent of CaO ranges from 53.2 to 57.6 wt %. The amount of MgO is in the range of 0.1 and 0.4 wt %. Late-stage calcite in the sample, SM08-26, shows the highest Zn content up to 2.0 wt % (1.3 mole %), compared to other calcite samples. FeO and MnO are generally below detection limit (<0.01 wt %).

CONCLUSION

In the Smithsonite Manto, the main NSZ minerals are smithsonite, hemimorphite, and sauconite. Other associated minerals include calcite, barite, Mn- and Fe- bearing minerals, and traces of microcrystalline silica. Smithsonite shows various mineral habits and is associated with hemimorphite, sauconite, and Fe/Mn oxides. Smithsonite can be divided into four major textural types: scalenohedral, rhombohedral, massive crystals of banded, colloform smithsonite, and matrix smithsonite. Smithsonite has been partially replaced and crosscut by hemimorphite, but locally it has intergrown with hemimorphite-A and sauconite. Scalenohedral and rhombohedral smithsonites partially or completely fill open spaces. Massive smithsonite occurs as irregular or colloform banding with a thickness varying from a minimum of a few millimeters to centimeters filling vugs.

Hemimorphite-A has replaced or intergrown with smithsonite, whereas tabular hemimorphite (hemimorphite-B) displays pore-filling and pore-lining features locally crosscutting smithsonite. Sauconite is commonly found with smithsonite and hemimorphite, which may indicate a sufficient amount of Si and Al was present in mineralizing fluids. Sauconite contains variable Mn in its structure. From the common presence of Mn/Fe oxides in a few samples, oxidizing conditions at the time of ore formation can be expected. Late-stage calcite cement only occurs in a few samples as the phase after NSZ mineralization. These late-stage calcite crystals appeared to be

precipitated only at the bottom of open space where smithsonite has grown around the pore space. This might have been related to changes in the water table after NSZ formation.

WDS analyses are performed on smithsonite and calcite. Matrix smithsonite shows higher Fe content, and both scalenohedral and matrix smithsonite show higher Mg contents than banded, colloform smithsonite (Figure 3.15). Different types of smithsonite do not show apparent differences in major chemical compositions and they have the near-stoichiometric smithsonite compositions. It is more likely that the amount of trace elements could vary between different types and generations of smithsonite.

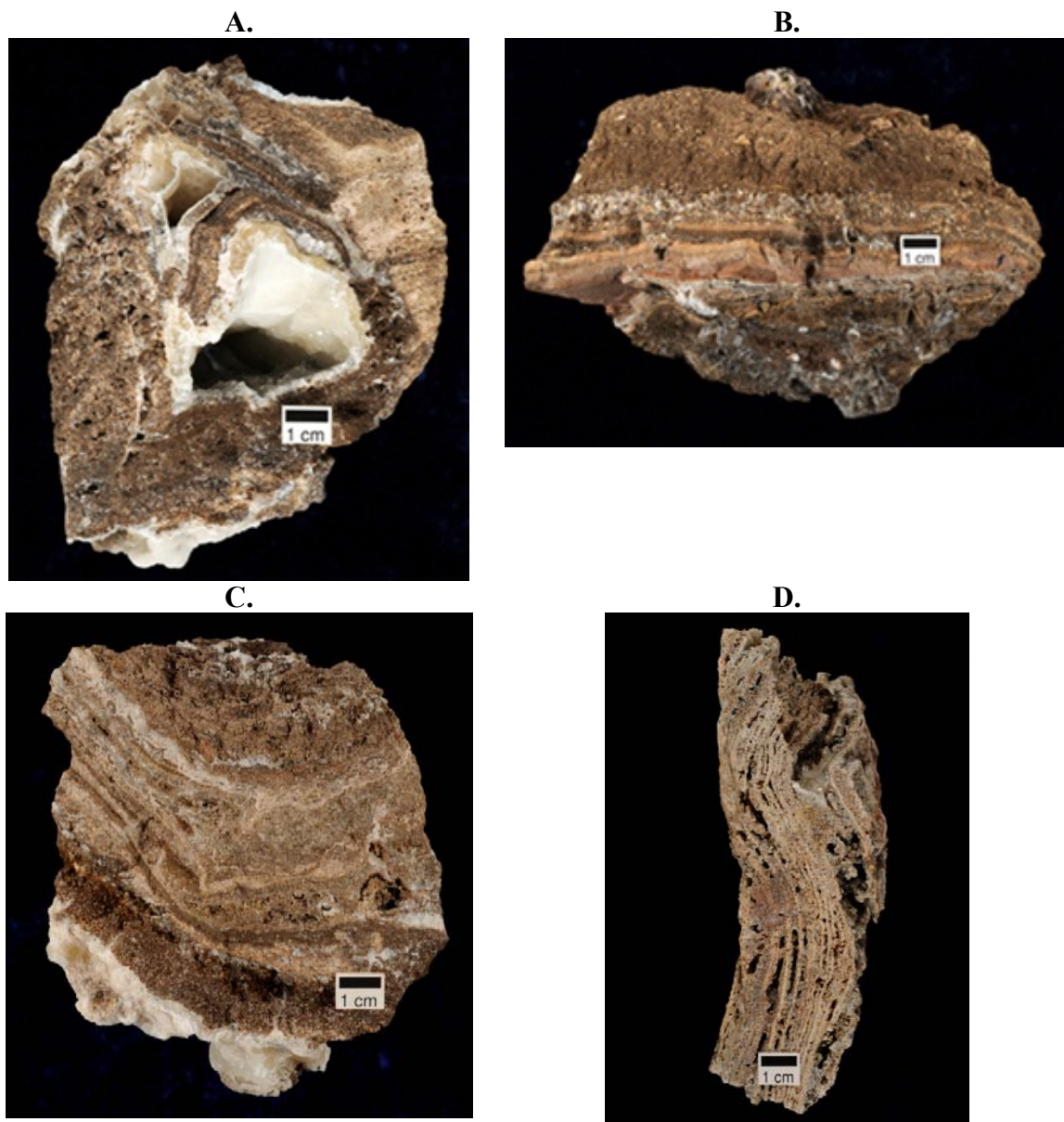


Figure 3.1. Hand samples from the Smithsonite Manto.

A. Botryoidal smithsonite and hemimorphite in vuggy cave fill. Sample SM08-22. **B.** Fragments and layers of Zn clay (pink to pale brown colors) cemented by Zn-bearing minerals and calcite. Sample SM08-28. **C.** Laminated Zn minerals and pendant smithsonite at the bottom. Sample SM08-24. **D.** Vertically banded smithsonite ore consisting of pale brown Zn clays and pore-filling scalenohedral smithsonite followed by calcite cement. Sample SM08-02.

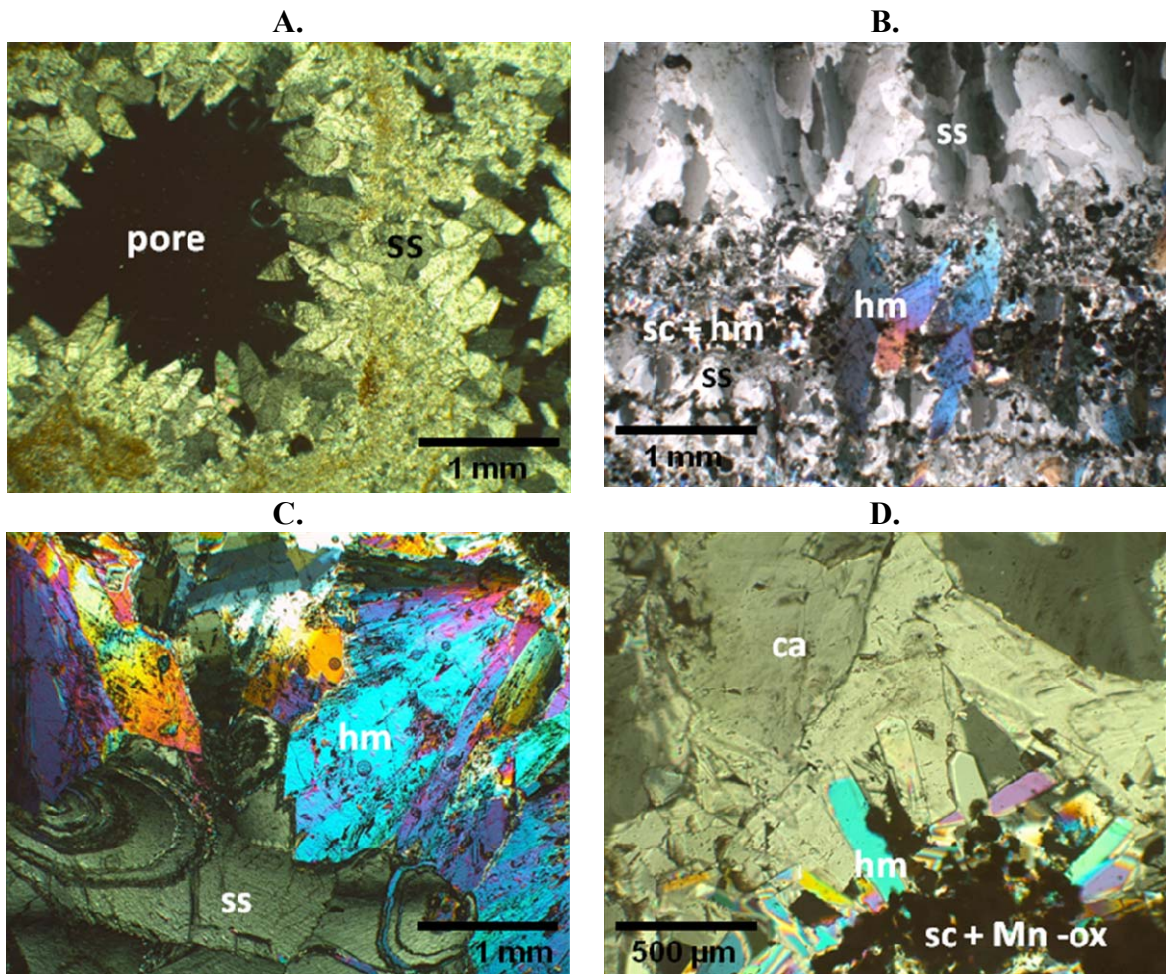


Figure 3.2. Photomicrographs of NSZ minerals.

A. Pore-filling scalenohedral smithsonite. XPL. Sample SM08-17. **B.** Hemimorphite and sauconite alternating with smithsonite. XPL. Sample SM08-22. **C.** Fan-shaped hemimorphite replacing smithsonite. XPL. Sample SM08-22. **D.** Tabular pore-filling smithsonite and late calcite cement. XPL. Sample SM08-11.

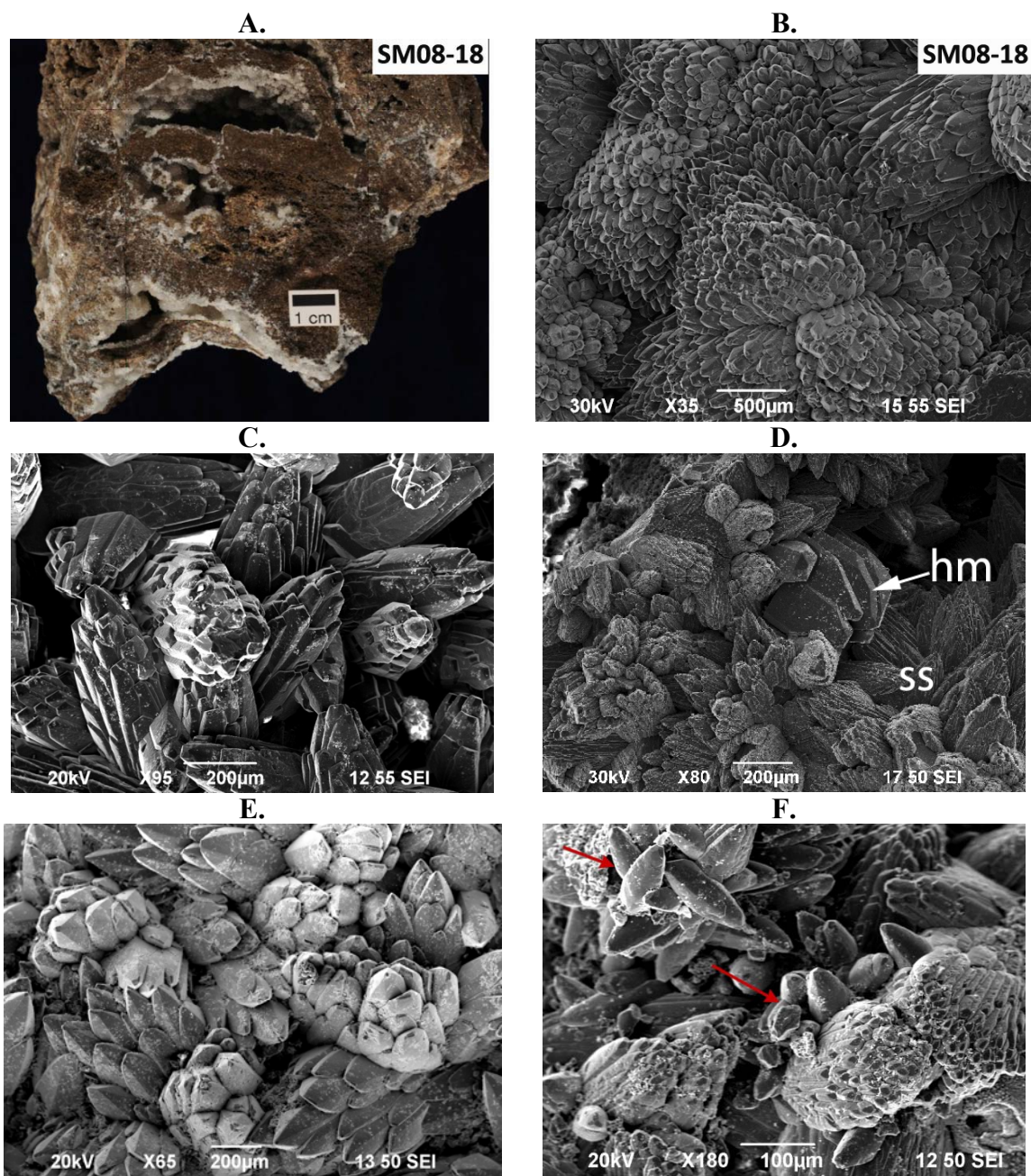


Figure 3.3. Scalenohedral smithsonite.

A. White smithsonite in vugs. **B.** Scalenohedral smithsonite of Figure 3.2.A. SEI. **C.** Aggregates of scalenohedral smithsonite. SEI. Sample SM08-16. **D.** Scalenohedral smithsonite and tabular hemimorphite. SEI. Sample SM08-02. **E.** Scalenohedral smithsonite. SEI. Sample SM03-09. **F.** Aggregates of scalenohedral smithsonite and single scalenohedral smithsonite crystal with curved faces (red arrows). Sample 08-01.

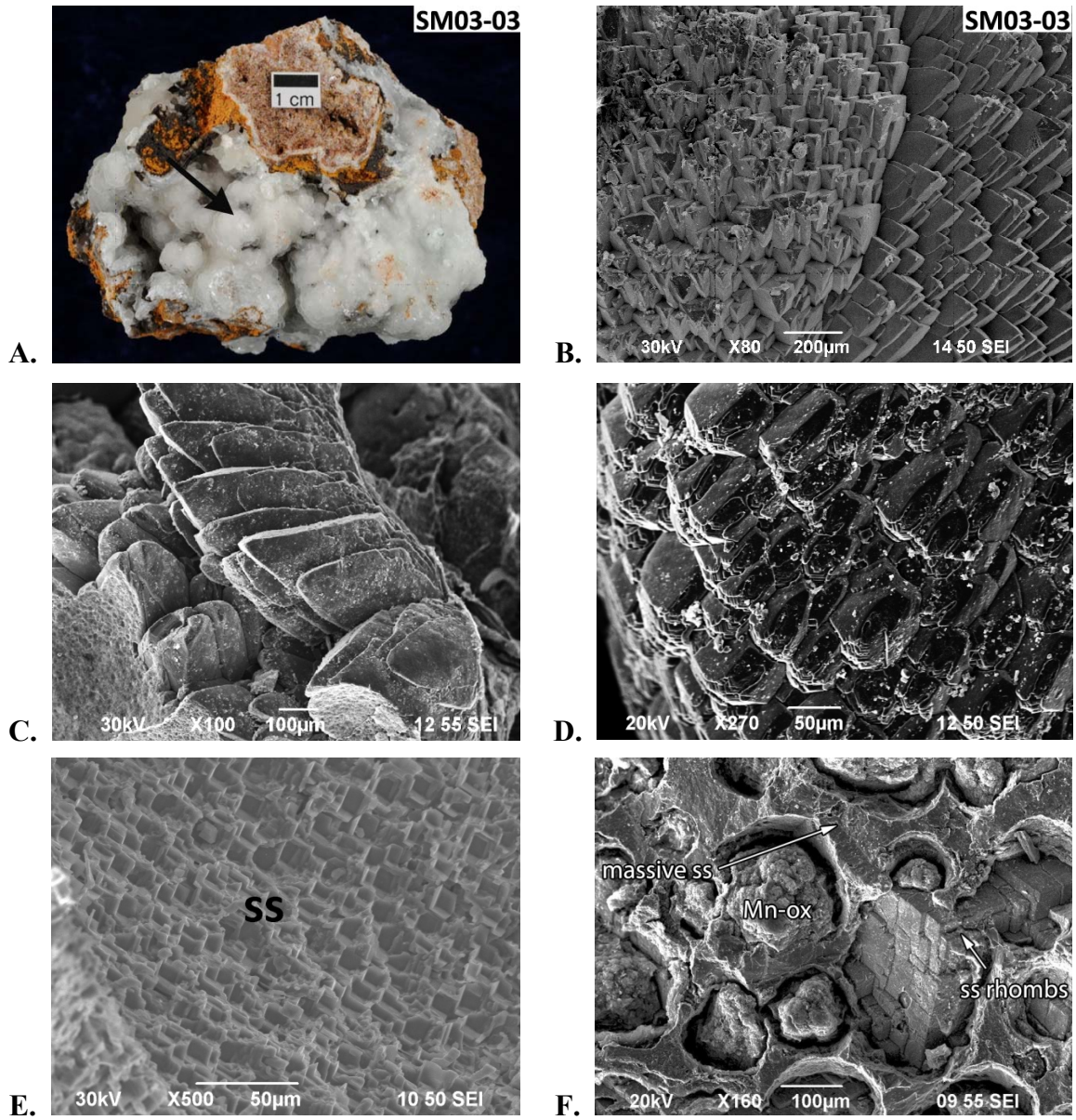


Figure 3.4. Typical smithsonite ores and SEM images.

A. Botryoidal smithsonite on matrix of Mn oxides and Zn clays. **B.** Smithsonite from Figure 3.2.B showing botryoidal concretion of smithsonite composed of individual rhombohedral crystals. SEI. **C.** Rhombohedral smithsonite. **D.** Idiomorphic, rhombohedral crystals. SEI. Sample SM08-04. **E.** Microcrystalline, rhombohedral . SEI. Sample SM08-24. **F.** Rhombic smithsonite and globular Mn-oxides in massive smithsonite. SEI. Sample SM08-06.

Table 3.1. Morphological types of smithsonite.

Comparison of Sierra Mojada smithsonites to morphological types of smithsonite as single crystals or aggregates (Boni et al. (2003), Balassone et al. (2007)). ****: abundant; ***: common; **: quite common; *: rare.

Morphological types	Abundance
Type I — rhombohedral, distinct idiomorphic, commonly zoned crystals	*
Type II — tiny subhedral crystals with curved and slightly rounded faces	
Type III — rice grain shaped	
Type IV — roughly rounded to one-dimensional clusters showing well-developed rhombohedral faces	
Type V — botryoidal aggregate, with more or less indiscernible crystal terminations	
Type VI — vuggy to drusy scalenohedral crystals	****
Matrix smithsonite (Sierra Mojada)	***
Massive crystals of banded, colloform (zoned) crystals (Sierra Mojada)	****

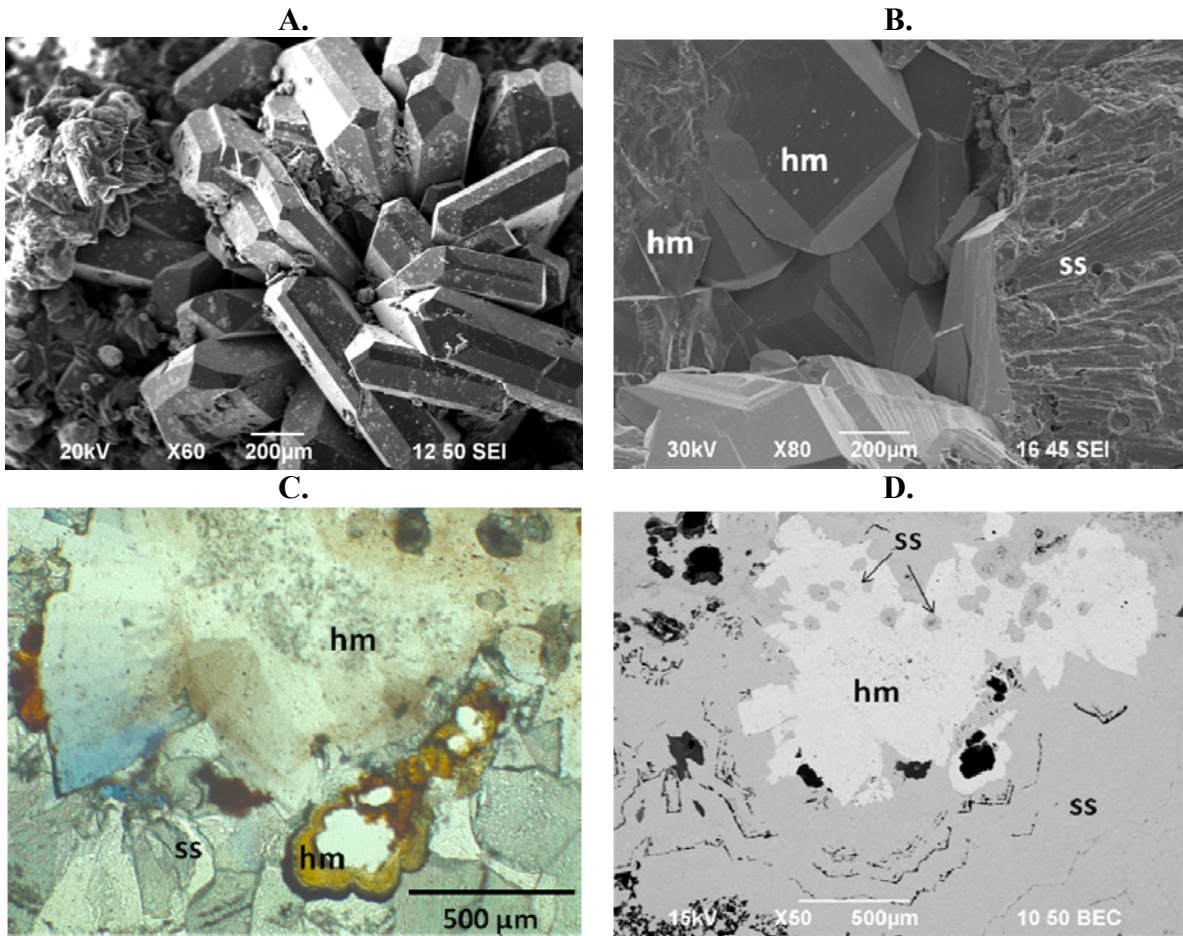


Figure 3.5. Occurrences of hemimorphite in the Smithsonite Manto.

A. Tabular hemimorphite. SEI. Sample SM08-24. **B.** Tabular, massive (left), and zoned (middle bottom) hemimorphite and smithsonite. SEI. Sample SM08-19. **C.** Colloform brownish hemimorphite, fan-shaped hemimorphite, and zoned smithsonite. XPL. Sample SM08-06. **D.** A same image of Figure 3.5C under BEI.

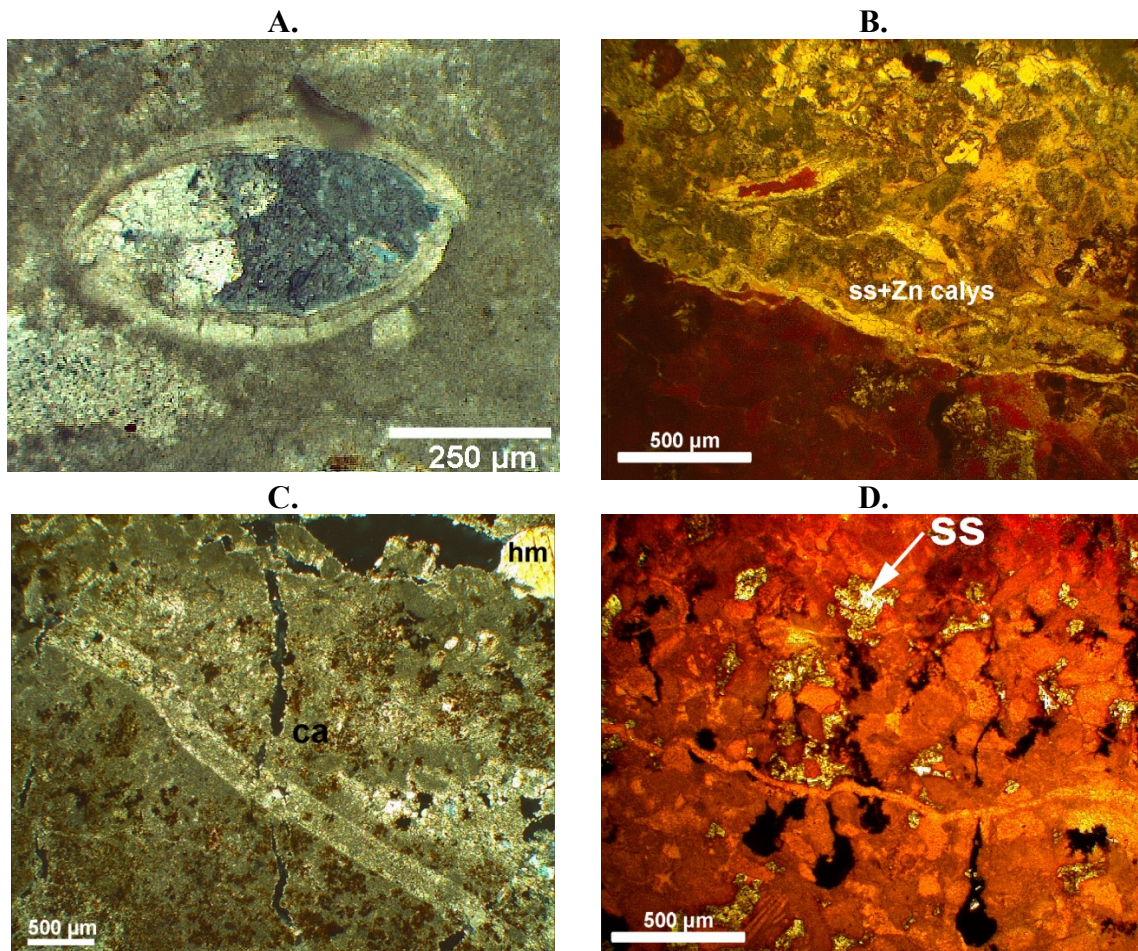


Figure 3.6. Characteristics of Aurora limestone.

A. Micrites and bivalves. XPL. Sample. SM08-03. **B.** Limestone contact with mineralized zone. PPL. Sample SM08-13 (calcite stained section). **C.** Micrite with a few grains of hemimorphite along fracture. XPL. Sample SM08-03. **D.** Limestone and microcrystalline smithsonite in pore space. PPL. Sample SM08-13 (calcite stained section).

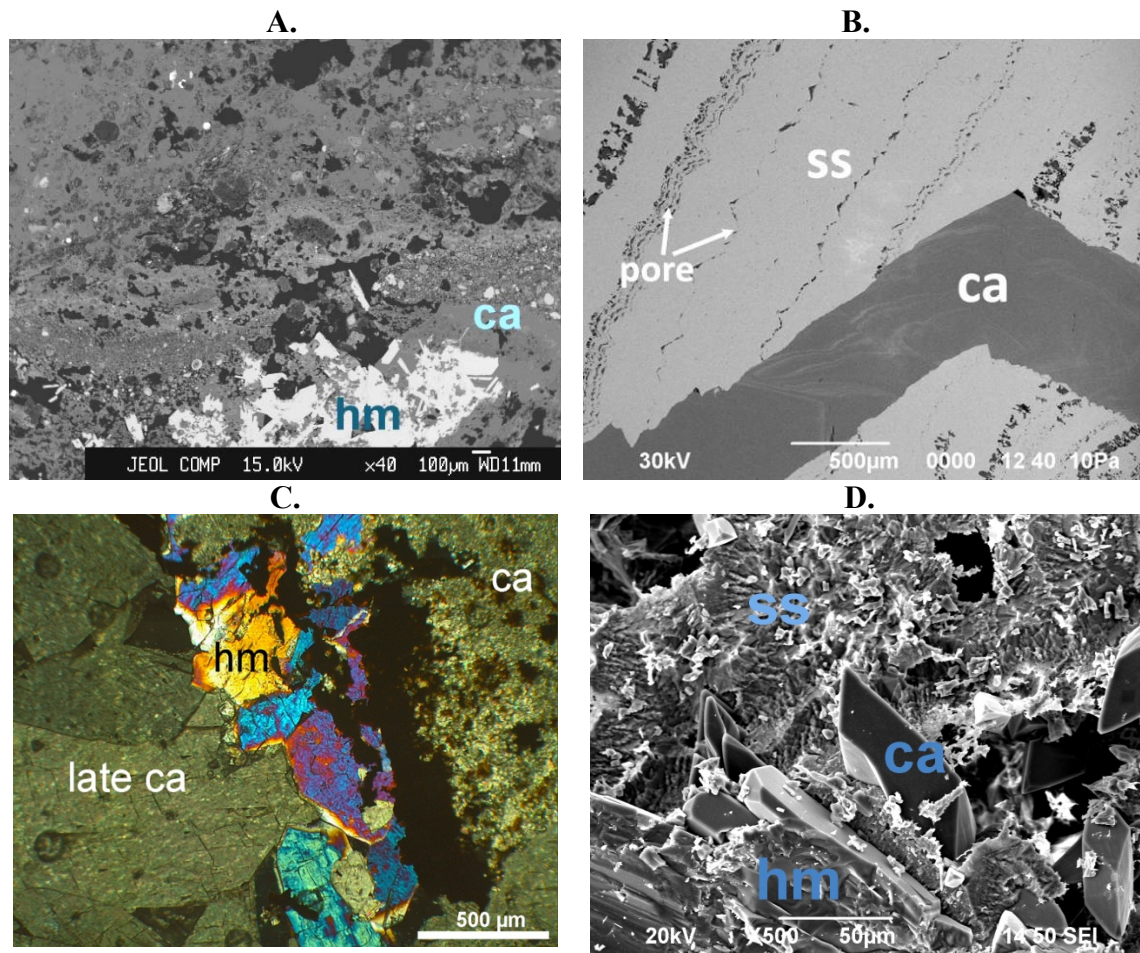
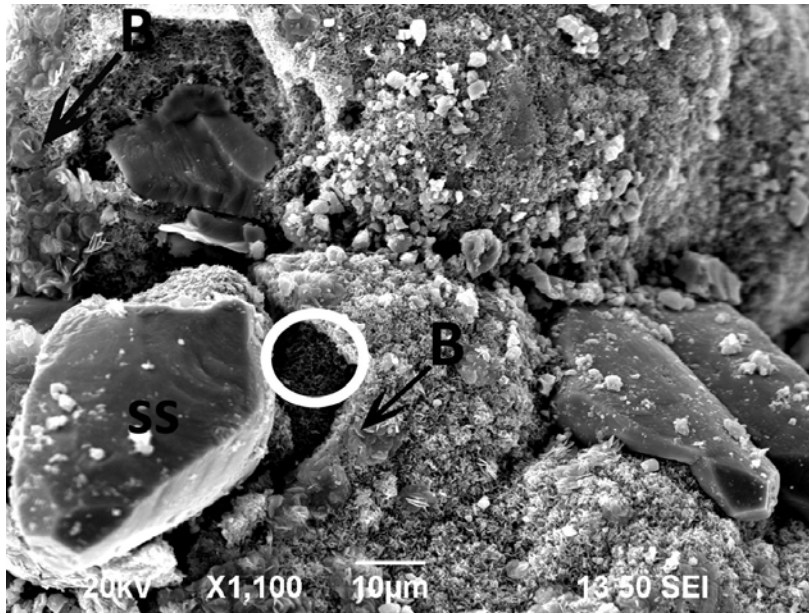


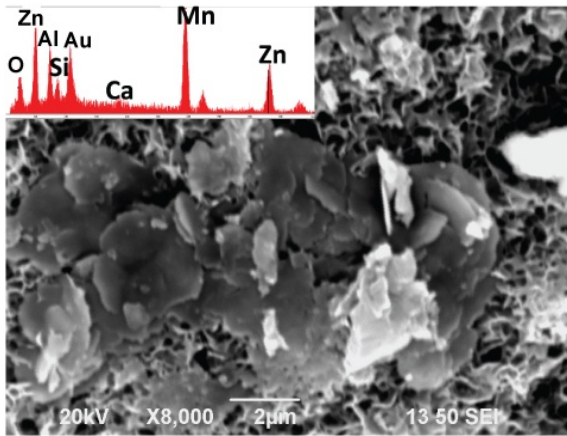
Figure 3.7. Occurrences of late-stage calcite.

A. Hemimorphite and calcite cement in the matrix of Zn clays and Pb/Mn oxides. BEI. Sample SM08-11. **B.** Late-stage calcite filling fracture in smithsonite. BEI. Sample SM03-22. **C.** Anhedral hemimorphite and the late-stage calcite on microcrystalline calcite. XPL. Sample SM08-01. **D.** Late-stage calcite and hemimorphite on smithsonite. SEI. Sample SM08-03.

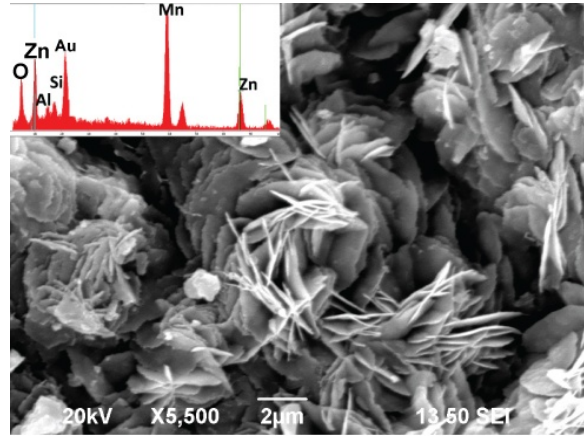
A.



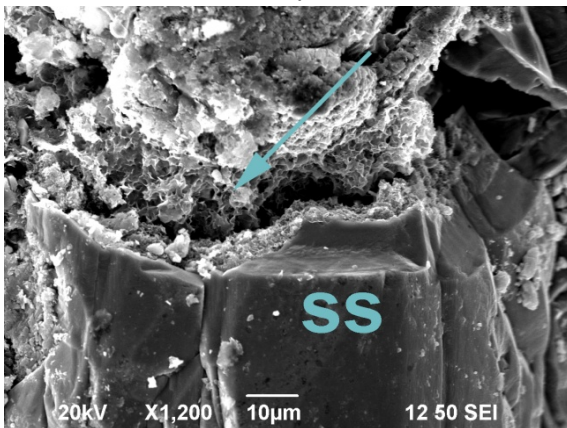
B.



C.



D.



E.

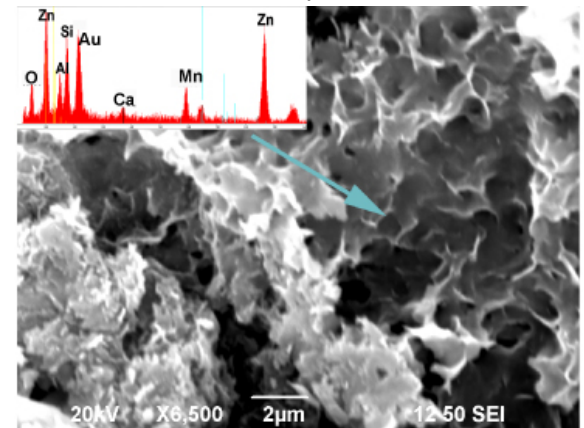


Figure 3.8. Occurrences of Zn clays.

Sample SM08-01. **A.** Smithsonite and authigenic Zn clays and Mn minerals. **B.** Mn minerals on sauconite (indicated as B in Figure 3.7A) and an inset image showing EDS spectra. **C.** Mn-rich Zn clay showing rosette patterns. An inset image of EDS spectra **D.** Smithsonite and locally altered to Zn clays. **E.** A magnified view of the left image indicated by a blue arrow. Different EDS patterns and morphology from Zn clays of the Figure 3.12.B. and 3.12.C. An inset map of EDS spectra.

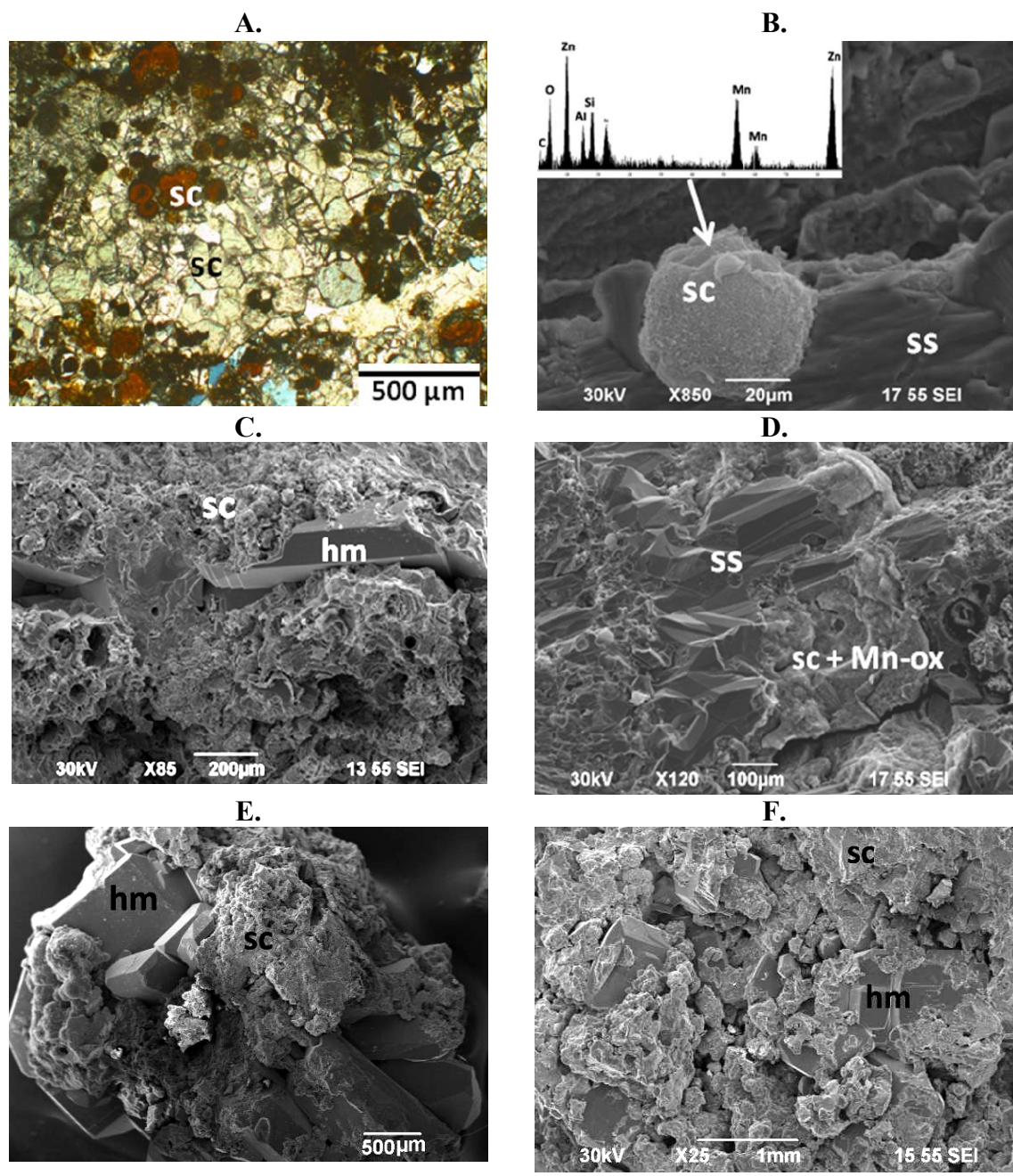


Figure 3.9. Alteration of smithsonite and hemimorphite into Zn clays.

A. Smithsonite and globular Zn clay. XPL. Sample SM08-19. **B.** Globular Zn clay. Sample SM08-19. SEI. Sample SM08-19. **C.** Hemimorphite altered to Zn clays. SEI. Sample SM08-17. **D.** Colloform smithsonite altered by Zn clays and Mn oxides. SEI. Sample SM08-19. **E.** Tabular hemimorphite and Zn clays (sauconite). SEI. Sample SM08-15. **F.** Tabular hemimorphite mostly altered to sauconite. SEI. Sample SM08-26.

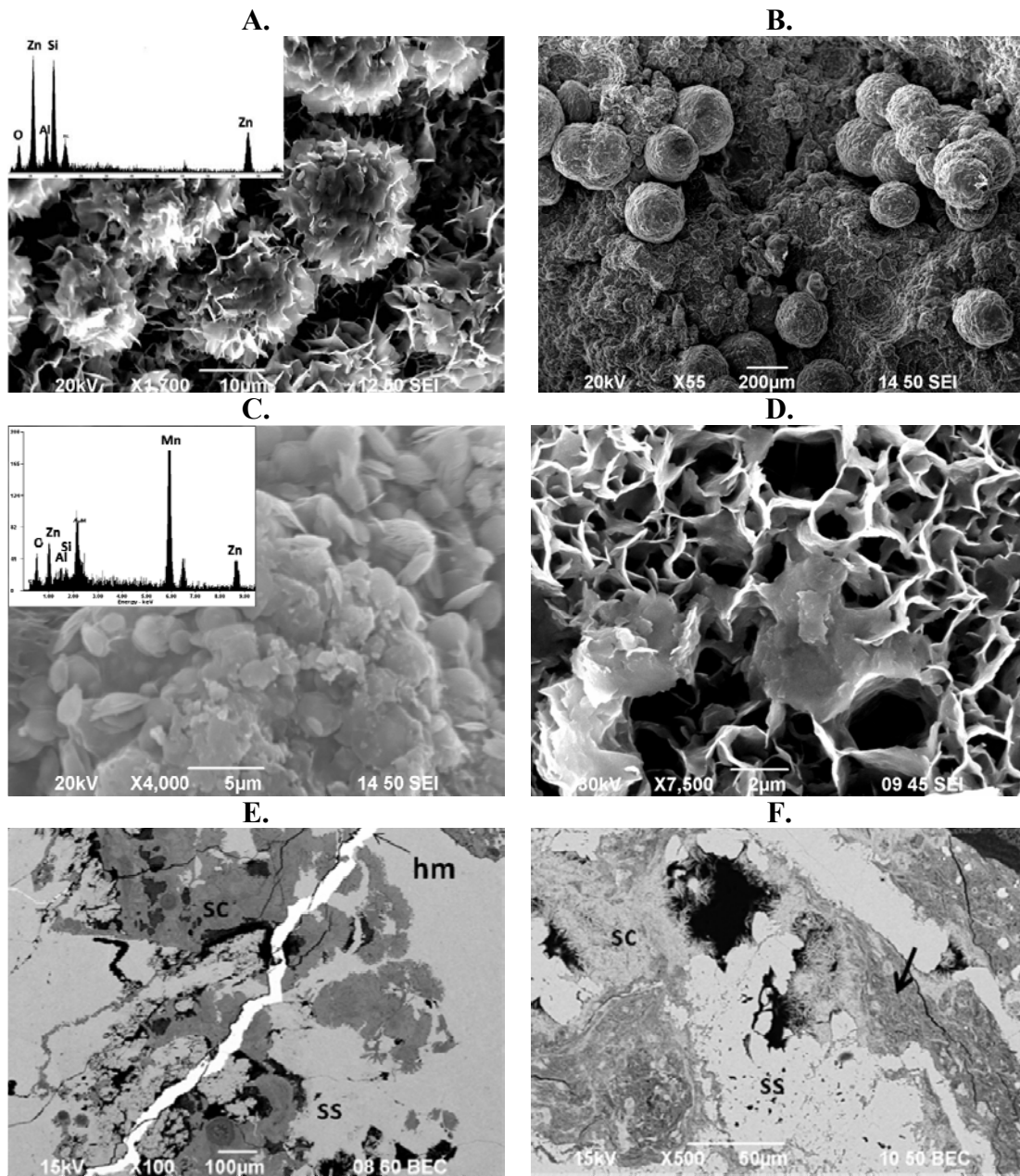


Figure 3.10. Occurrences of Zn clays and Mn minerals.

A. Results of ivory sauconite and an inset image of EDS spectrum. SEI. Sample SM08-27. **B.** Globular Mn mineral (white) on matrix of matrix (pink). SEI. Sample SM08-15. **C.** Results of pink Zn clays and an inset image of EDS spectrum. SEI. Sample SM08-15. **D.** Ivory Zn clays. SEI. Sample SM08-24. **E.** Globular sauconite crosscut by hemimorphite. SEI. Sample SM08-22. **F.** Sauconite grown in pores in smithsonite. K-bearing Zn clays are indicated by an arrow. SEI. Sample SM08-06.

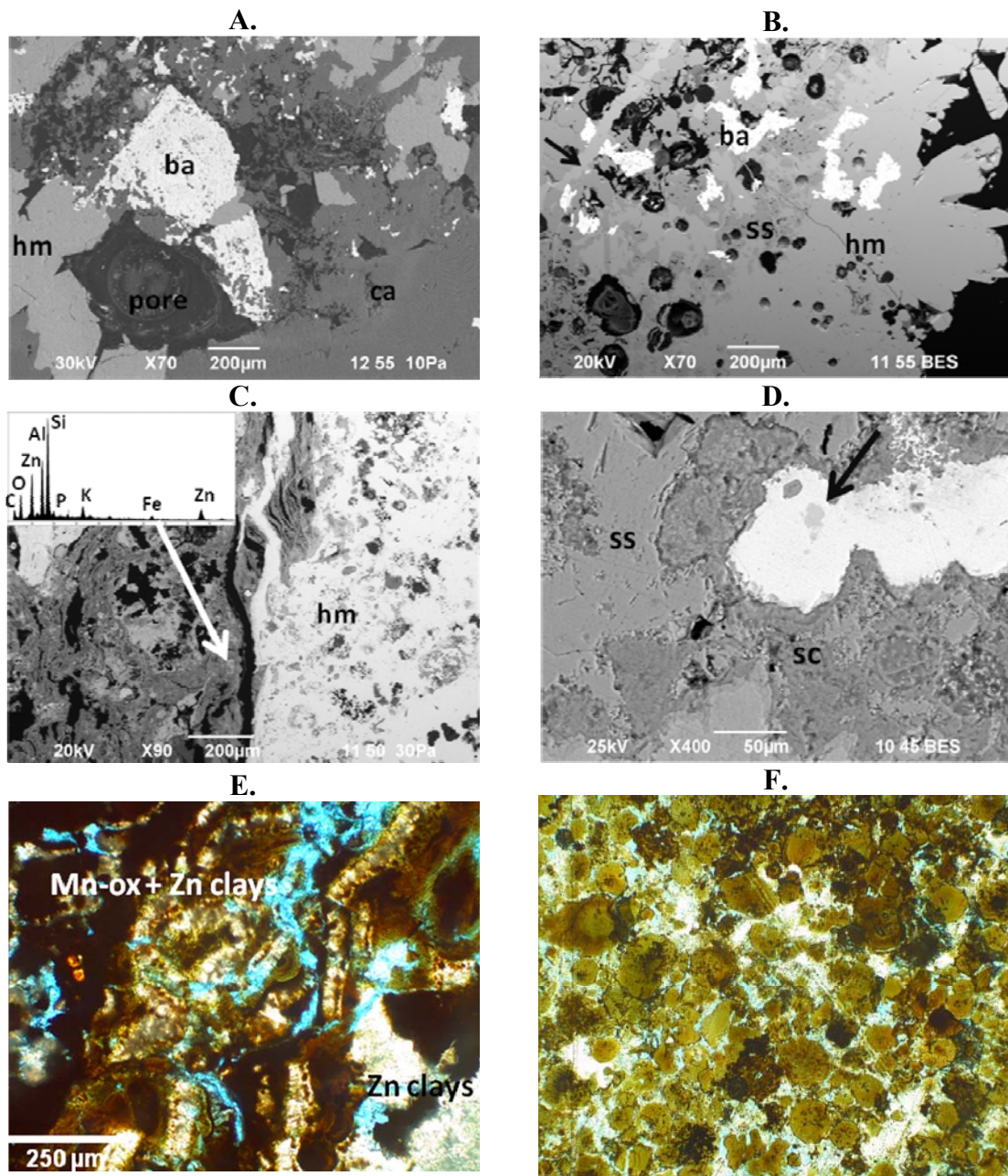


Figure 3.11. Other associated minerals in the Smithsonian Manto.

A. Barite, hemimorphite, and early calcite. BEI. Sample SM08-01. **B.** Dominantly hemimorphite with minor late barite crystals and smithsonite. BEI. Sample SM08-26. **C.** K-bearing Zn clays indicated by an arrow. BEI. Sample SM08-11. **D.** A Mn/Pb-bearing mineral indicated by an arrow surrounded by sauconite. Sample SM08-26. **E.** Sample SM08-27. **F.** Zn clays and Mn-oxides. FOV = 1 mm. Sample SM08-21.

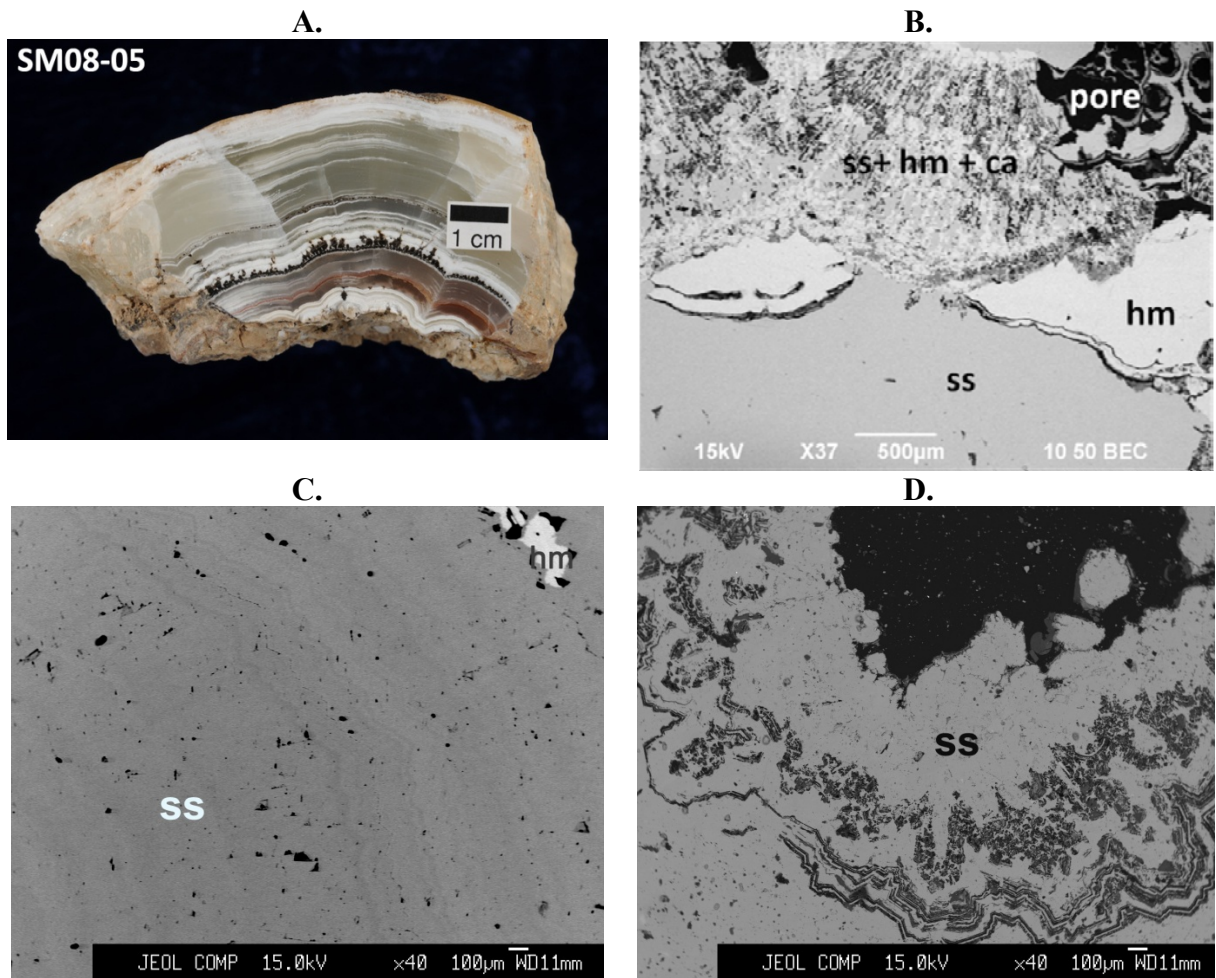


Figure 3.12. Occurrences of botryoidal, colloform smithsonite.

A. Hand sample of white banded smithsonite with Mn-oxides dendrites. **B.** Smithsonite and colloform hemimorphite. White bands in the left image consist of smithsonite, hemimorphite, calcite, and pores. BEI. Sample SM08-05. **C.** Compositional layering in smithsonite. BEI. Sample SM03-09. **D.** A backscattered electron image of smithsonite with no compositional variations. BEI. Sample SM08-10.

Table 3.2. Quantitative WDS results for banded, colloform smithsonite.

A. Mass percent of banded, colloform smithsonite.

Sample ID	MgO	FeO	MnO	CaO	ZnO	CO ₂ *	Total	Description
SM03-09	0.05	0.00	0.02	0.79	64.38	35.51	100.76	SM03-09 colloform ss (avg)
	0.10	0.01	0.01	1.48	63.50	35.63	100.73	SM03-09 Ca-Mg-rich layer
	0.02	0.00	0.03	0.45	64.82	35.45	100.77	SM03-09 Zn-rich layer
SM08-04	0.06	0.01	0.02	0.89	65.87	36.41	103.25	SM08-04 colloform ss
SM08-05	0.05	0.00	0.01	2.17	63.11	35.90	101.25	SM08-05 Ca-Mg rich layer
	0.14	0.00	0.00	2.77	62.03	35.87	100.81	SM08-05 Zn rich layer
	0.06	0.01	0.01	2.52	62.47	35.84	100.90	SM08-05 banded ss with no zonation
	0.07	0.01	0.01	2.50	62.51	35.86	100.96	SM08-05 ss average
SM08-06	0.07	0.01	0.01	1.74	60.88	34.38	97.09	SM08-06 coarse zoned banded ss with rhomb cleavages
SM08-08	0.07	0.01	0.01	1.28	64.62	36.04	102.04	SM08-08 Ca-Mg rich layer
	0.05	0.01	0.02	0.86	65.12	35.97	102.03	SM08-08 Zn rich layer
	0.05	0.01	0.02	0.83	60.88	35.98	102.07	SM08-08 ss average
SM08-10	0.03	0.03	0.02	0.25	60.88	34.14	97.13	SM08-10 pale purple ss

Values in wt %.

*: calculated from stoichiometry

B. Mole percent of banded, colloform smithsonite.

Sample ID	Mg	Fe	Mn	Ca	Zn	Description
SM03-09	0.07	0.00	0.02	0.87	49.03	SM03-09 colloform ss (avg)
	0.16	0.01	0.01	1.63	48.20	SM03-09 Ca-Mg-rich layer
	0.03	0.00	0.03	0.49	49.45	SM03-09 Zn-rich layer
SM08-04	0.10	0.00	0.02	0.96	48.93	SM08-04 colloform ss
SM08-05	0.21	0.00	0.00	3.03	46.76	SM08-05 Ca-Mg rich layer
	0.08	0.00	0.01	2.37	47.54	SM08-05 Zn rich layer
	0.09	0.01	0.01	2.75	47.14	SM08-05 banded ss with no zonation
	0.11	0.00	0.01	2.73	47.14	SM08-05 ss average
SM08-06	0.11	0.01	0.01	1.99	47.88	SM08-06 coarse zoned banded ss with rhomb cleavages
SM08-08	0.13	0.00	0.01	1.81	48.04	SM08-08 Ca-Mg rich layer
	0.08	0.01	0.01	0.94	48.96	SM08-08 Zn rich layer
	0.11	0.01	0.01	1.40	48.47	SM08-08 ss average
SM08-10	0.04	0.03	0.02	0.28	49.63	SM08-10 pale purple ss

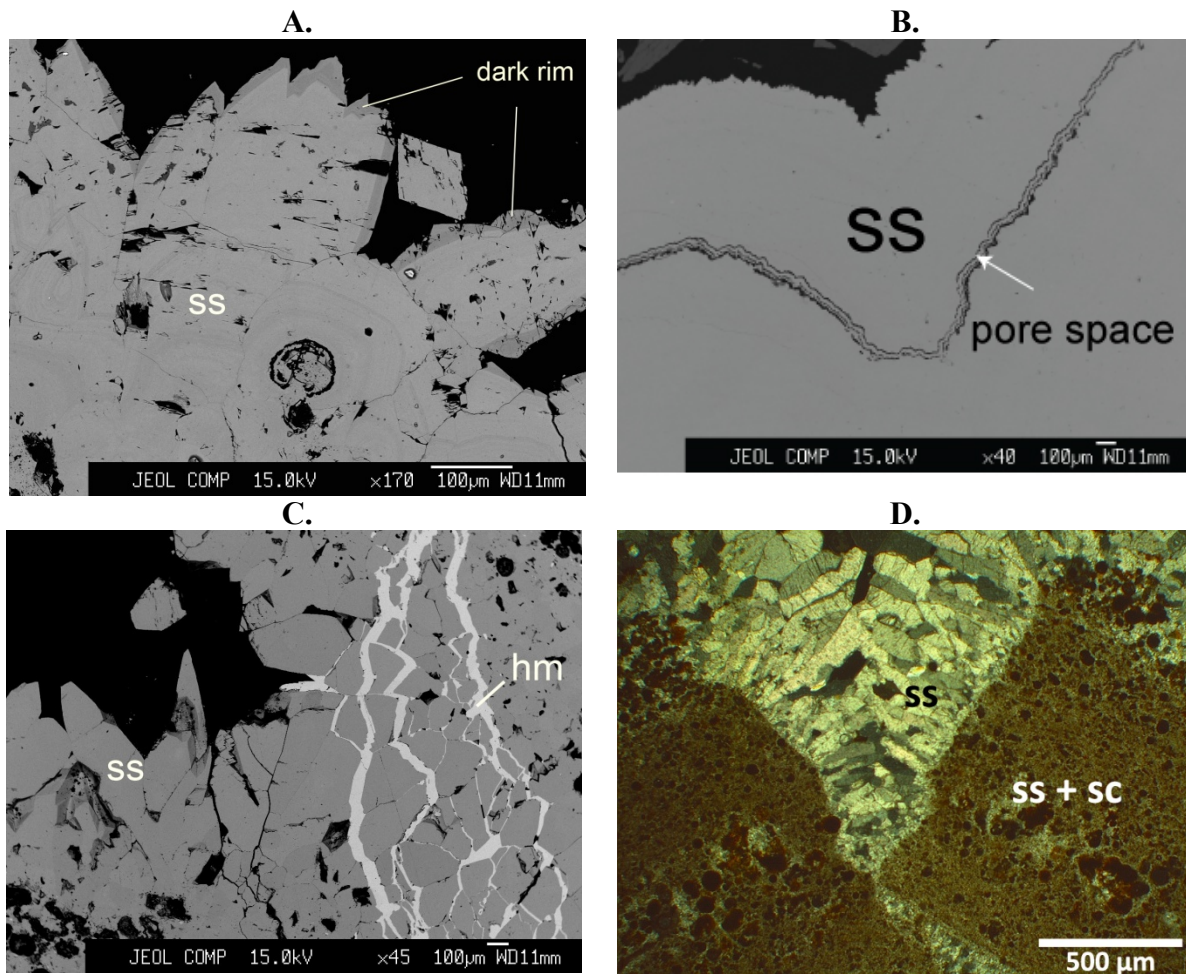


Figure 3.13. Scalenohedral smithsonite.

A. Scalenohedral (dog-tooth) smithsonite showing compositional zonation. BEI. Sample SM08-02. **B.** Banded smithsonite with the scalenohedral crust with the fairly homogeneous composition. BEI. Sample SM08-22A. **C.** Pore-filling scalenohedral smithsonite and fracture-filling hemimorphite. BEI. Sample SM08-23. **D.** Smithsonite intergrown with sauconite followed by late smithsonite growing into open space. XPL. Sample SM08-23.

Table 3.3. Quantitative WDS results for scalenohedral smithsonite.

A. Pore-filling smithsonite.

Sample ID	MgO	FeO	MnO	CaO	ZnO	CO2*	Total	Description
SM08-02	0.43	0.01	0.02	0.17	64.64	35.58	100.84	pore scalenohedral ss
	3.52	0.03	0.01	0.19	60.05	36.49	100.29	Zn poor scalen-ss
	0.22	0.01	0.02	0.14	63.89	34.92	99.20	Zn rich scalen-ss
SM08-17	0.59	0.02	0.02	0.25	66.84	37.02	104.75	scalen-ss
SM08-18A	0.12	0.02	0.02	0.10	64.31	35.01	99.57	scalen-ss in pore
SM08-18B	0.35	0.01	0.02	0.11	63.98	35.08	99.54	scalen-ss in pore
SM08-22B	0.16	0.04	0.01	0.17	64.24	35.08	99.69	scalen-ss
SM08-23	0.1	0.0	0.0	0.1	64.2	34.9	99.4	pore-filling scalen-ss
SM08-23	0.17	0.02	0.01	0.08	64.08	34.92	99.27	pore-lining scalen-ss on Zn clay
SM08-26	0.11	0.01	0.02	0.19	65.25	35.58	101.16	scalen-ss

B. Banded smithsonite layer with scalenohedral crust.

Sample ID	MgO	FeO	MnO	CaO	ZnO	CO2*	Total	Description
SM08-18B	0.19	0.01	0.02	0.20	64.01	35.00	99.41	ss layer
SM08-22A	0.15	0.01	0.03	0.84	64.86	35.94	101.84	ss bands
SM08-22B	0.19	0.00	0.01	0.45	63.30	34.81	98.77	bands
SM08-23	0.09	0.03	0.02	0.51	63.29	34.76	98.69	pale gray banded layer

Values in wt %.

*: calculated from stoichiometry

C. Compositions of scalenohedral pore-filling smithsonites shown in mole percents.

Sample ID	Mg	Fe	Mn	Ca	Zn	Description
SM08-02	0.66	0.01	0.02	0.18	49.14	pore scalenohedral ss
	5.27	0.02	0.01	0.20	44.50	Zn poor scalen-ss
	0.34	0.01	0.02	0.16	49.48	Zn rich scalen-ss
SM08-17	0.87	0.01	0.02	0.26	48.83	scalen-ss
SM08-18A	0.19	0.02	0.02	0.11	49.67	scalen-ss in pore
SM08-18B	0.54	0.00	0.01	0.12	49.32	scalen-ss in pore
SM08-22B	0.24	0.03	0.01	0.19	49.53	scalen-ss
SM08-23	0.15	0.02	0.02	0.10	49.72	pore-filling scalen-ss
SM08-23	0.27	0.01	0.01	0.09	49.62	pore-lining scalen-ss on Zn clay
SM08-26	0.17	0.01	0.02	0.20	49.60	scalen-ss

D. Compositions of banded smithsonite layer with scalenohedral crusts in mole percents.

Sample ID	Mg	Fe	Mn	Ca	Zn	Description
SM08-18B	0.29	0.00	0.01	0.22	49.47	ss layer
SM08-22A	0.23	0.01	0.03	0.92	48.81	ss bands
SM08-22B	0.30	0.00	0.01	0.51	49.18	bands
SM08-23	0.14	0.03	0.02	0.58	49.24	pale gray banded layer

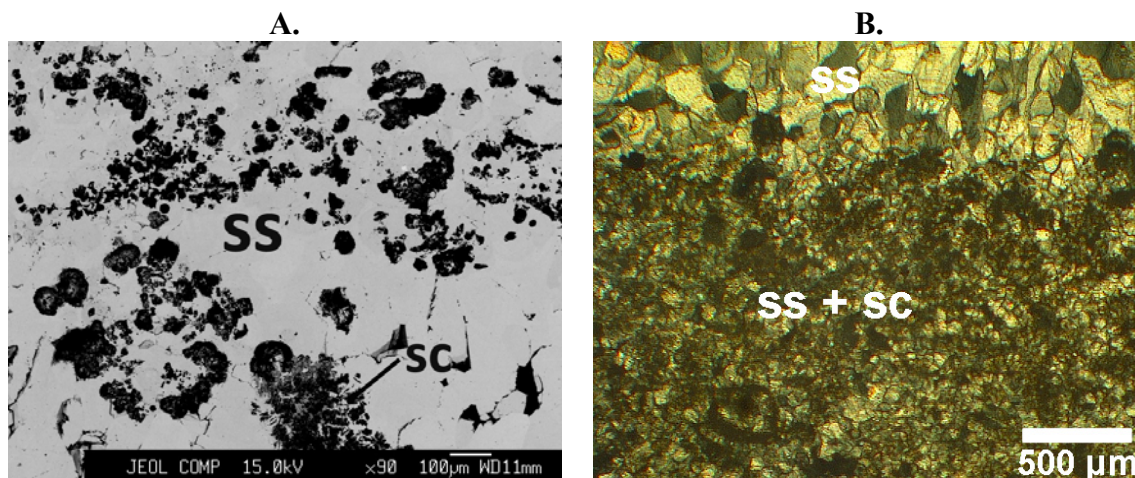


Figure 3.14. Matrix smithsonite.

A. Matrix smithsonite with pores (black) and Zn clays. BEI. Sample SM08-18B. **B.** Microcrystalline smithsonite in the matrix with sauconite. XPL. Sample SM08-22B

Table 3.4. Quantitative WDS results for matrix smithsonite.

A. Matrix smithsonite shown as weight percents.

Sample ID	MgO	FeO	MnO	CaO	ZnO	CO ₂ *	Total
SM08-17	0.36	0.29	0.02	0.58	65.89	36.68	103.82
SM08-18A	0.84	0.03	0.02	0.69	61.96	35.00	98.53
SM08-18B	0.19	0.01	0.02	0.14	63.64	34.76	98.76
SM08-22B	0.21	0.03	0.01	1.15	62.43	34.92	98.75

Values in wt %.

*: calculated from stoichiometry

B. Matrix smithsonite shown as mole percents.

Sample ID	Mg	Fe	Mn	Ca	Zn
SM08-17	0.54	0.23	0.01	0.62	48.59
SM08-18A	1.31	0.02	0.02	0.77	47.88
SM08-18B	0.30	0.01	0.02	0.16	49.52
SM08-22B	0.33	0.03	0.01	1.29	48.34

Table 3.5. Quantitative WDS results for late-stage calcite.

A. Mass percent of late calcite

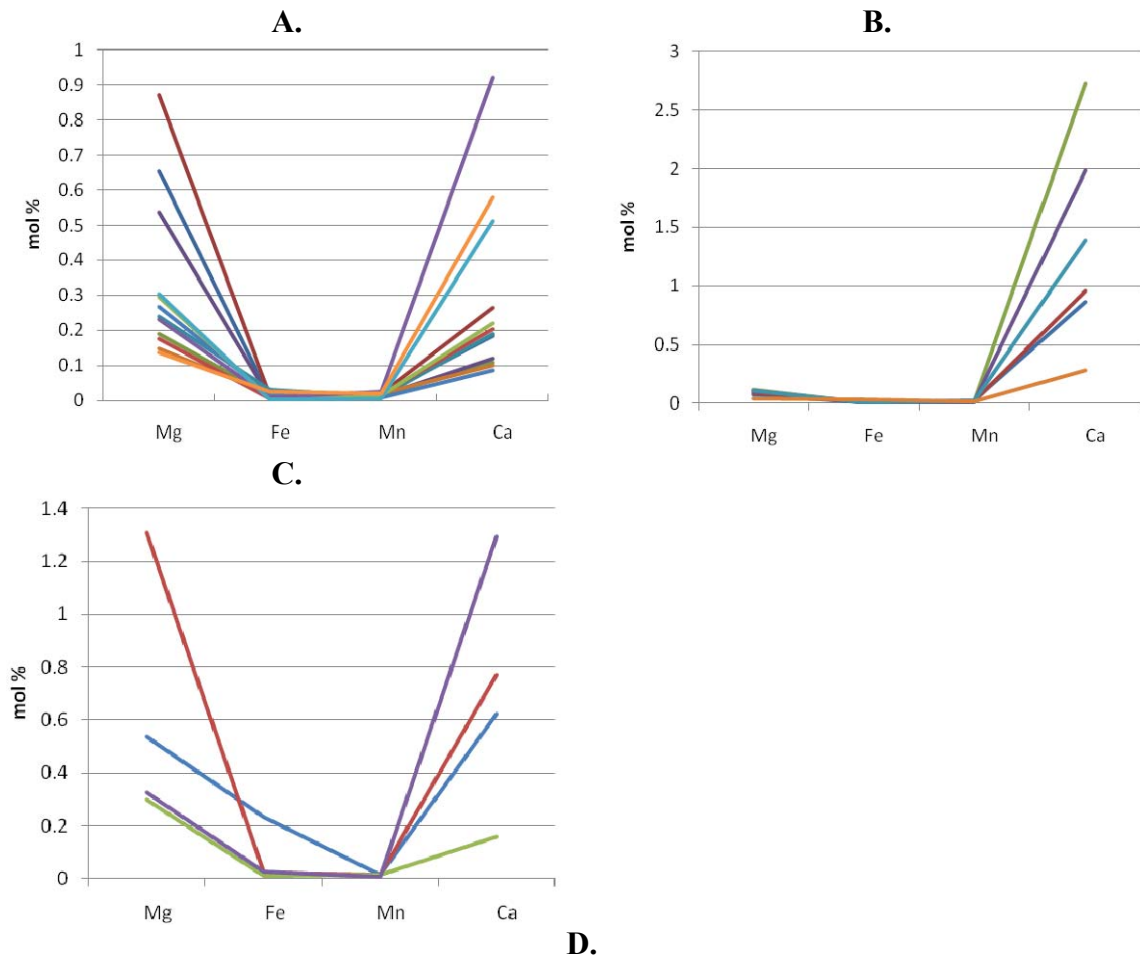
Sample ID	MgO	FeO	MnO	CaO	ZnO	CO2*	Total	Description
SM08-01	0.09	0.01	0.01	55.29	0.14	43.57	99.11	SM08-01 late ca
SM08-01	0.25	0.06	0.07	55.07	0.15	43.66	99.26	SM08-01 ca in ls
SM08-11	0.39	0.01	0.02	56.57	0.96	45.36	103.31	SM08-11 ca cement in the matrix
SM08-11	0.25	0.01	0.03	57.61	0.22	45.62	103.73	SM08-11 sparry late ca
SM08-11b	0.25	0.01	0.03	56.66	0.39	44.96	102.29	SM08-11b late ca
SM08-18A	0.14	0.01	0.02	53.19	0.97	42.44	96.78	SM08-18A late ca
SM08-26	0.15	0.01	0.01	54.27	2.03	43.86	100.32	SM08-26 late ca

Values in wt %.

*: calculated from stoichiometry

B. Mole percent of calcite

Sample ID	Mg	Fe	Mn	Ca	Zn	Description
SM08-01	0.11	0.01	0.01	49.79	0.08	SM08-01 late ca
SM08-01	0.32	0.04	0.05	49.50	0.10	SM08-01 ca in ls
SM08-11	0.47	0.01	0.01	48.94	0.57	SM08-11 ca cement in the matrix
SM08-11	0.30	0.01	0.02	49.55	0.13	SM08-11 sparry late ca
SM08-11b	0.30	0.01	0.02	49.44	0.24	SM08-11b late ca
SM08-18A	0.19	0.01	0.01	49.17	0.63	SM08-18A late ca
SM08-26	0.19	0.00	0.00	48.53	1.27	SM08-26 late ca



	Location	Mg	Fe	Mn	Ca	Zn
rhombohedral crystals (100 μm)	SSM	not determined				
scalenohedral crystals (100 μm -400 μm)	SSM	0.69	0.01	0.02	0.27	49.01
massive crystals consisting of banded, colloform bands (thickness of bands up to 15 cm)	SSM	0.09	0.01	0.01	1.37	48.51
matrix smithsonite (<10 μm - 100 μm)	SSM	0.62	0.07	0.01	0.71	48.58

Figure 3.15. Textural types of smithsonite and minor element compositions.

A. Scalenohedral smithsonite. **B.** Colloform, banded smithsonite. **C.** Matrix smithsonite. **D.** Smithsonite morphologies and average minor element composition in mole percent.

Chapter 4. Petrography and Mineralogy of the Iron Oxide Manto

The Iron Oxide Manto is located south of the San Marcos fault beneath the Polymetallic Manto (Figure 2.4A). It is strata-bound within the basal dolostone unit at the basal part of the Aurora formation. It dominantly consists of pore-filling hemimorphite and smithsonite in Fe-oxides matrix. Distinct red to orange color of ores are due to the content of Fe-oxides. In general, Fe-oxides with red color are due to hematitic (α -Fe₂O₃) contents and with orange color due to goethitic (α -FeOOH) contents. Some portions of the Iron Oxide Manto with high Zn concentrations are cave-fill deposits, partly containing cobble and boulder conglomerates cemented by zinc-bearing iron-oxide sandstone. However, this part of the Iron Oxide Manto is not included in this study. In the Iron Oxide Manto, hemimorphite is more abundant than smithsonite, and Zn mineralization is followed by late stage calcite.

SAMPLING AND METHODS

Samples analyzed are hand specimens collected from underground exposures from the Encantada mine and San Salvador mine, and a few core samples provided by the Metalline Company. Based on hand specimen analyses, identification of major mineral and their textures is performed using the optical microscope, SEM and SEM-EDS analyses, and microprobe.

HOST ROCK DESCRIPTION AND PETROGRAPHY

White pore-filling hemimorphite is hosted by red iron oxides matrix. Typical ore features are illustrated in Figure 4.1. These host rocks contain the various types of Fe oxides of either microcrystalline or amorphous Fe oxides. Primary dolostone is mostly oxidized. Most hemimorphite and calcite seem to precipitate in tabular vugs in Fe-oxide host rocks (Figure 4.1C and D). A smithsonite-bearing ore in oxidized limestone can be

seen in Figure 4.1B, which contains smithsonite intermixed with calcite and less amounts of Fe/Mn oxides.

SEM and SEM-EDS qualitative analyses are performed on several Fe-oxides samples in order to investigate their relationship with hemimorphite, smithsonite, and calcite. Abundance of Fe-oxides is a distinctive feature of the Iron Oxide Manto. Fe-oxides can be formed from direct reprecipitation from Fe^{2+} to Fe^{3+} , dissolution and reprecipitation or solid state transformation (Cornell, 2003). Secondary electron imaging reveals that most Fe oxides are massive, extremely fine-grained, or amorphous (Figures 4.2 and 4.3). Locally, hemimorphite seems to be corroded or replaced by Fe-oxides (Figure 4.3C, D and Figure 4.4E). Zn sorption onto Fe-oxides (goethite) has been reported in Ankomah, 1992. Zn mobility and bioavailability in aqueous settings are influenced by Fe-oxides (Ankomah, 1992; Trivedi et al., 2001; McPhail et al., 2006), although it is unclear how Fe-oxides influence the mobility of Zn with the presence of other aqueous ions, such as Ca, Mg, and Mn in the Iron Oxide Manto. Typical features of Fe-oxides are shown in Figure 4.2. Backscattered electron images of Fe oxides show that some of primary dolomite textures appear to be preserved (Figure 4.2A). Fe oxides also display concentric, colloform features (Figure 4.5E) without relict calcite or dolomite grains.

Tentative phase identification of Fe-oxides was attempted using SEM/EDS. EDS spectra were acquired from Fe-oxides on several samples ($n = 12$) (Figure 4.3) selected for variation in their color. Peaks shown in Figure 4.3 are obtained at 20 keV for comparison except Figure 4.3D, and acquisition time varies from 20 sec to 60 sec. Samples, EN1-3 and EN1-5, are characterized by distinct dark red color (Figure 4.1C), while SS4-3 shows orange color (Figure 4.1D). However, it should be noted that locally red and orange colored layers of Fe-oxides are alternating each other. EDS analyses

reveal that both hematitic and goethitic Fe-oxides usually display a C, O, FeL α peak (next to an O peak), and FeK α peak as well. The relative intensity of O is slightly different, but it does not confirm the differences between dark red Fe-oxides and orange color Fe-oxides. Also, it was not possible to distinguish Fe³⁺ from Fe²⁺ using EDS. They usually contain some amounts of Zn, Si and Al. It may be due to matrix effects from Zn-bearing minerals, or variable amounts of Zn may be absorbed in their structure. Ba and Pb are detected in some of the Fe-oxides samples, but it is relatively uncommon.

MINERALOGY OF MAJOR MINERALS

Hemimorphite

Hemimorphite in the Iron Oxide Manto shows tabular crystal habits in vugs and open spaces. The size of pore-filling hemimorphite ranges from 200 μm to 1 cm. Some hemimorphite has distinct crystal faces, whereas others showing rounded crystal edges overgrown by Fe-oxides or late calcite (Figure 4.4E). Subhedral to anhedral hemimorphite is closely associated with Fe-oxides or late calcite. It appears to be corroded or replaced by Fe-oxides (Figure 4.5A and B). Late-stage calcite partially or completely fills pores or coats hemimorphite (Figures 4.4 and 4.5). Locally, hemimorphite seems to be corroded or entirely coated by fine-grained Fe oxides (Figures 4.2C, 4.3C and D). Backscattered electron imaging combined with EDS analyses of some hemimorphite crystals reveals that it contains variable amounts of Ca. Under a backscattered electron image, the surface of hemimorphite (Figure 4.5A) is porous and shows slight compositional variations, which seems to be influenced by different fluids passing through this deposit after hemimorphite formation. Small grains of argentite have been observed in a hemimorphite crystal in goethitic Fe-oxides (Figure 4.4D).

Smithsonite

Smithsonite is much less common than hemimorphite in the Iron Oxide samples collected for this project. It is detected in dark red Fe-oxides and in pale orange limestone (SS8), but it has not been found in orange colored Fe-oxides. Smithsonite in dark red Fe oxides occurs as rhombic and platy microcrystals with a size ranging from 10 μm to 100 μm (Figure 4.6). Globular smithsonite aggregates consisting of platy smithsonite microcrystals have grown on Fe-oxides followed by large tabular crystals of hemimorphite (Figure 4.6A and B), and microcrystals of rhombohedral smithsonite have grown in pores on Fe-oxides (Figure 4.6E). The size of individual smithsonite crystals ranges from 50 μm to 100 μm and each cluster was about 200 μm . Also, smithsonite is finely intergrown with Fe-oxides (Figure 4.6), and it contains some amount of Fe in its structure. In pale orange colored massive limestone, smithsonite fills fractures (Figure 4.7C) or grows in open space. This smithsonite shows distinct compositional variations under backscattered electron images (Figure 4.7A).

Major elements of smithsonite in the limestone sample, SS8, were analyzed using microprobe. Analytical conditions were the same as those used for carbonates from the Smithsonite Manto. A section is cut perpendicular to the oriented direction of the rock sample. Figure 4.7C illustrates fine-grained smithsonite precipitated along fractures in brecciated chert along with fine-grained calcite. Three different smithsonite types are analyzed: rhombic smithsonite in pores, zoned smithsonite, and microcrystalline smithsonite associated with calcite. The results in weight percents and mole percents are listed in Table 4.1A. Rhombic smithsonite crystals intermixed with calcite are sometimes less than five μm , and these spots were avoided due to the beam diameter (10 μm). In rhombic smithsonite (Figure 4.7B), the amount of ZnO ranges from 44 to 58 wt % with the average value of 55.2 wt %. The average value of FeO is 3.5 wt % and the highest

FeO value is up to 13.5 wt %. In addition, this type of smithsonite contains 3.4 wt % of MgO and 0.4 wt % of MnO. Zoned smithsonite in pores (Figure 4.7A) shows a metal content between 55 and 64 wt % of ZnO. The amount of ZnO in microcrystalline smithsonite ranges from 54 and 62 wt %. FeO and MnO and is commonly present in all of these smithsonite and MgO and CaO as well. Zoned smithsonite in pores and microcrystalline smithsonite show nearly stoichiometric smithsonite compositions about $(\text{Ca,Mg,Fe,Mn})_{0.1}\text{Zn}_{0.9}\text{CO}_3$, and rhombohedral smithsonite has $(\text{Ca,Mg,Fe,Mn})_{0.2}\text{Zn}_{0.8}\text{CO}_3$.

Calcite

Late pore-filling calcite associated with hemimorphite is common in most samples collected from the Iron Oxide Manto (Figure 4.3.). It completely or partially cements pore space around hemimorphite (Figures 4.2. and 4.3.). WDS quantitative analyses on calcite are carried out in two samples (SS8 and SS11-2DS), and the result for quantitative analyses can be seen in Table 4.1B. The CaO content ranges from 53.7 to 55.5 wt %. MgO, FeO, and MnO seemed to occur only in trace amounts. Both calcites have nearly stoichiometric compositions. Early microcrystalline calcite in massive limestone shows slightly higher ZnO and MgO than other two late-stage calcite. The late-stage calcite in the sample, SS11-2DS, associated with hemimorphite, partially or completely cements open space around hemimorphite. It contains minor amount of Zn and Mg, and other elements are only in trace amounts. It is close to stoichiometric calcite.

Other secondary minerals

Barite is common in minor amounts in the Iron Oxide Manto samples collected for this project. It shows a euhedral habit of a size ranging from 50 μm to 100 μm growing on Fe/Mn-bearing carbonates (Figure 4.8A) and precipitated along fractures as a

secondary mineral after smithsonite (Figure 4.7C). Colloform Pb/Mn-bearing minerals with Zn are locally present with Fe-oxides (Figure 4.8B). However, their occurrence is relatively rare.

CONCLUSION

The Zn mineralization associated with the Iron Oxide Manto is dominantly hemimorphite and minor smithsonite growing within a Fe oxide matrix. Sauconite has not been found in samples collected for this study. Evidence of primary sulfides has not been found although some textural remnants in Fe-oxides suggest replacement features after sulfides and carbonate rocks. Hemimorphite occurs as pore-fillings with anhedral to euhedral crystal habits. Smithsonite is relatively common in samples containing dark red Fe-oxides and massive limestone. It usually displays micro-to-fine grained rhombic and platy crystals. Minor element distribution in smithsonite is shown in Figure 4.9. Rhombohedral smithsonite in pores shows higher Mg and Fe contents and it shows higher Mn contents than smithsonites from the Smithsonite Manto. Late-stage calcite is common in most ore samples associated with Zn-bearing minerals. It commonly coats hemimorphite or filled open spaces. This late calcite includes trace amounts of Zn. It is interpreted that calcite precipitation is after non-sulfide Zn mineralization. Sulfide minerals are rare except for the argentite occurrence in hemimorphite grain. Minor colloform Mn/Pb-bearing minerals are detected with Fe-oxide matrix in pores.

The character of fluids that deposited the high amount of hemimorphite might have contained the significant amount of aqueous silica along with Zn amounts in acidic fluids. It may be expected that the Iron Oxide Manto received more flux of aqueous silica than the Smithsonite Manto. In addition, the abundance of hemimorphite in carbonates can indicate silica was mobile during supergene alteration (Boni et al., 2003) and slightly reducing conditions (Hitzman et al., 2003) (Figure 1.3). The pH value would not have

been strongly acidic because hemimorphite became more soluble below pH 3 and Zn would be transported away (Takahashi, 1960). Acidic to slightly basic fluids generated from oxidation and buffered by carbonate host rocks might have been ideal for hemimorphite precipitation. Precipitation of smithsonite appears to take place with Fe oxides. The abundance of Fe-oxides with smithsonite, hemimorphite, and less amounts of Mn-oxides are characteristic of the Iron Oxide Manto compared to the Smithsonite Manto.

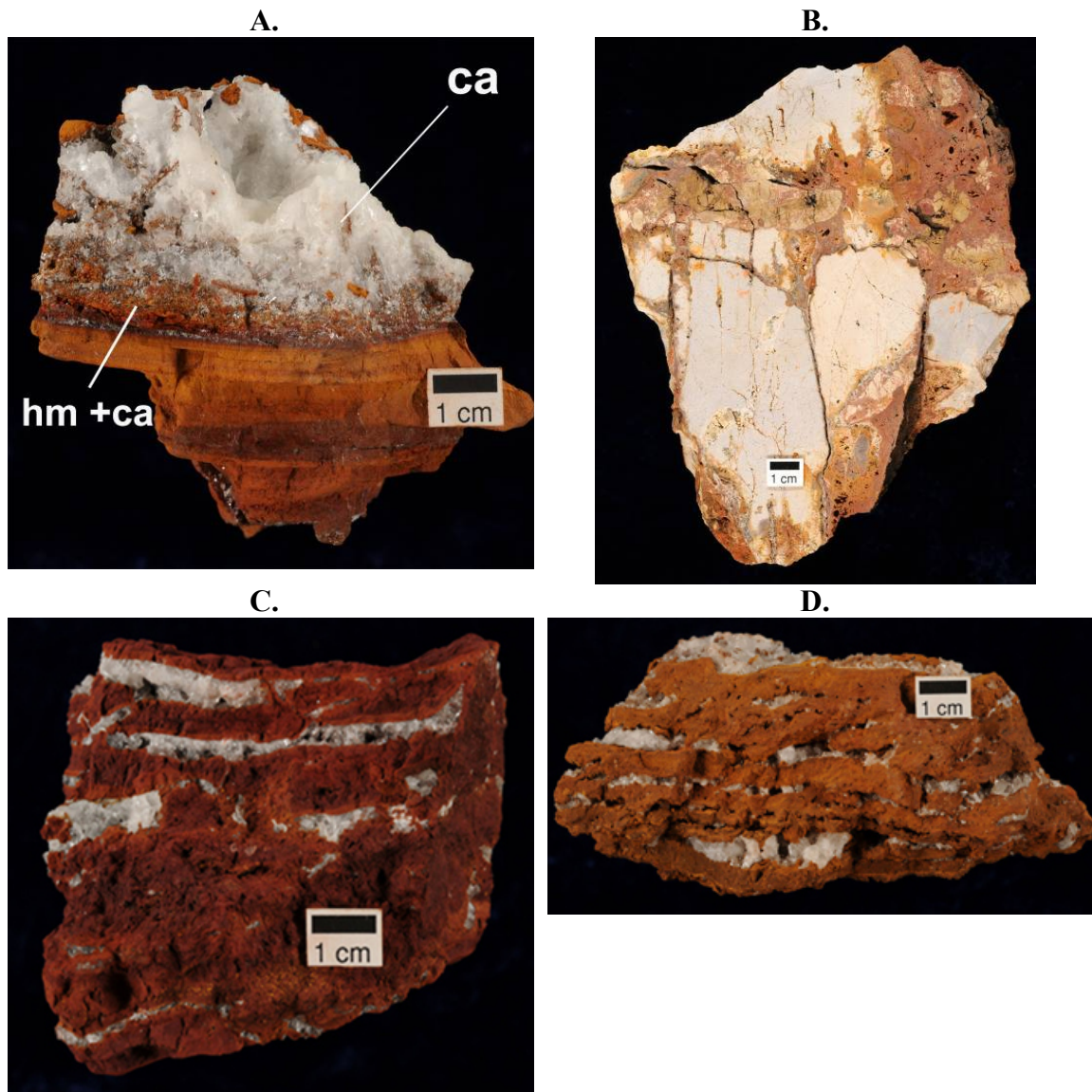


Figure 4.1. Hemimorphite and smithsonite ores in the Iron Oxide Manto.

Photographs of **A.** Hemimorphite and calcite on laminated Fe-oxides. Sample SS11-2DS. **B.** Smithsonite ore intermixed with late calcite in fracture-fills. Sample SS8 (oriented). **C.** Hematitic Fe-oxides with white hemimorphite and calcite crystals. Sample EN1-3. **D.** Pore-filling hemimorphite and calcite cement in goethitic Fe-oxides. Sample SS4-4.

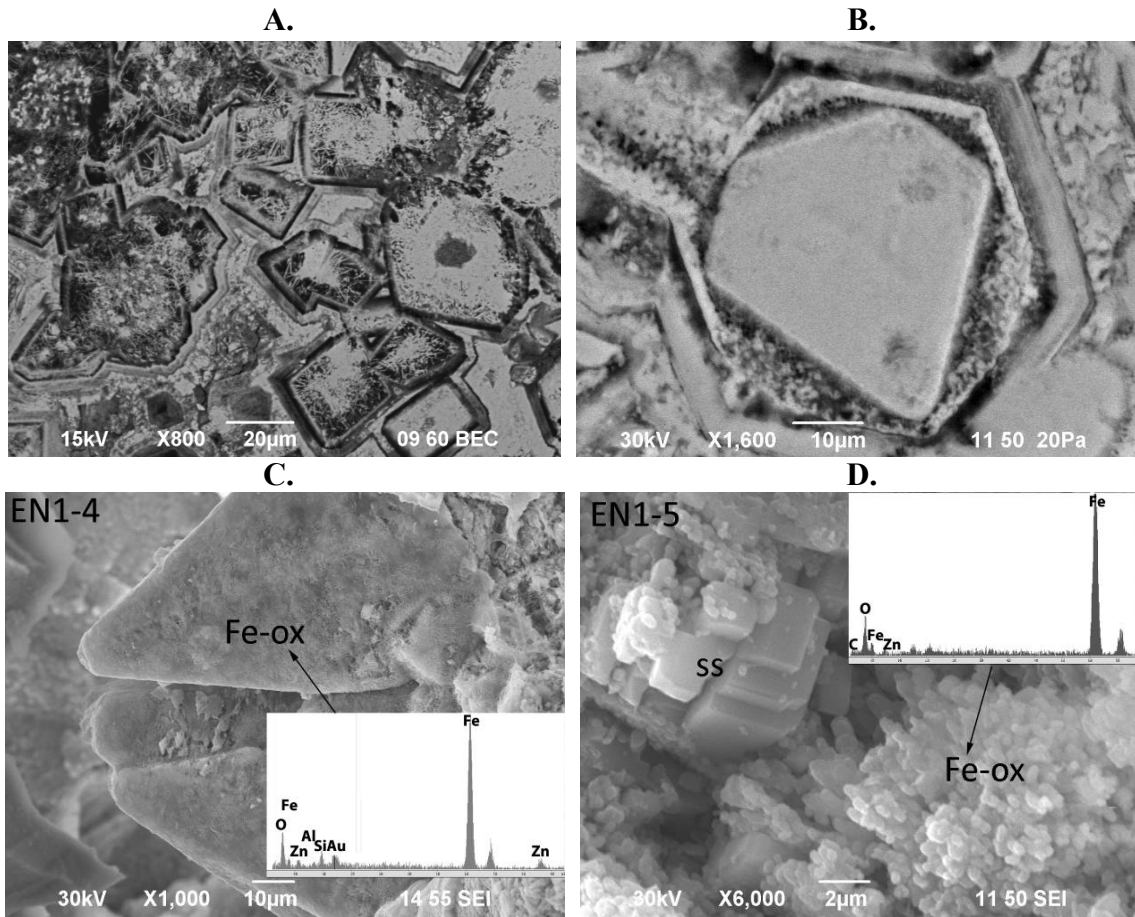


Figure 4.2. Occurrences of Fe-oxides.

A. Dark red Fe oxide matrix. BEI. Sample EN1-2. **B.** Fe-oxides after pyrite? Sample EN1-4. **C.** Fine-grained hematitic Fe-oxides covering hemimorphite. An inset image of EDS spectra of Fe-oxides. SEI. **D.** Fe-oxides and rhombohedral smithsonite. An inset image of EDS spectra. SEI.

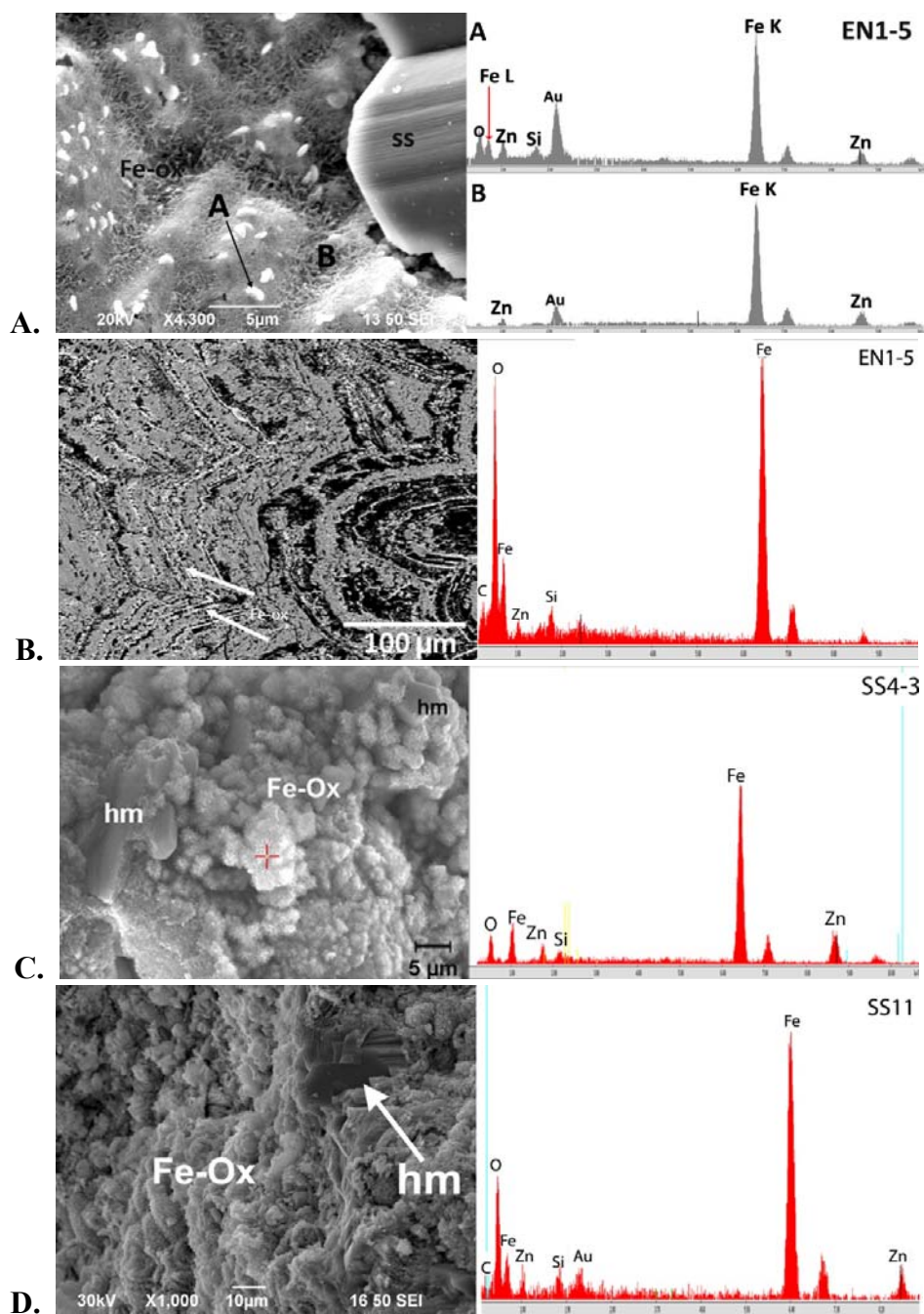


Figure 4.3. SE images and EDS spectra of Fe-oxides.

A. Bright grains of hematitic Fe-oxides (A) and fibrous grains of Fe-oxides (B). **B.** Smithsonite intergrown with Fe-oxides (indicated by arrows). EDS spectra obtained at 20 keV. **C.** Acicular fine-grained Fe-oxides and hemimorphite. EDS spectra obtained at 20 keV. **D.** Orange colored goethitic Fe-oxides and remnant of hemimorphite crystal. SEI.

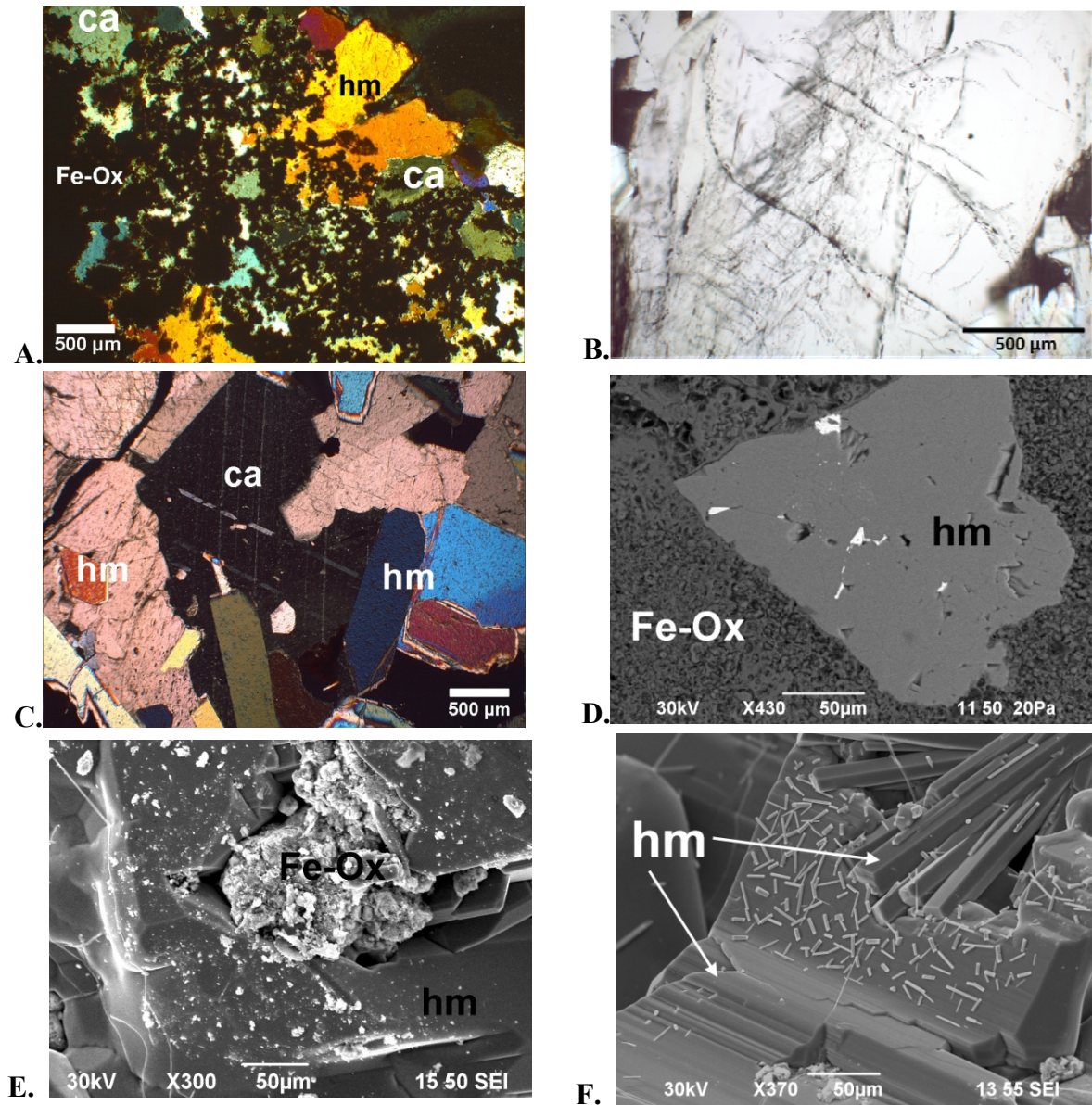


Figure 4.4. Occurrences of pore-filling hemimorphite in the Iron Oxide Manto.

A. Late-stage pore-filling hemimorphite and calcite locally corroded by Fe-oxides. XPL. Sample SS11-1. **B.** Fractures and fluid inclusions in hemimorphite. PPL. Sample EN2-1C. **C.** Tabular hemimorphite and late calcite. XPL. Sample SS11-2DS. **D.** A hemimorphite grain and argentite (bright white grains) in Fe-oxides. BEI. Sample SS4-1. **E.** Hemimorphite corroded by Fe-oxides. SEI. Sample SS11. **F.** Different generations of hemimorphite and cerussite (small white minerals on hemimorphite). SEI. Sample SS11-2DS.

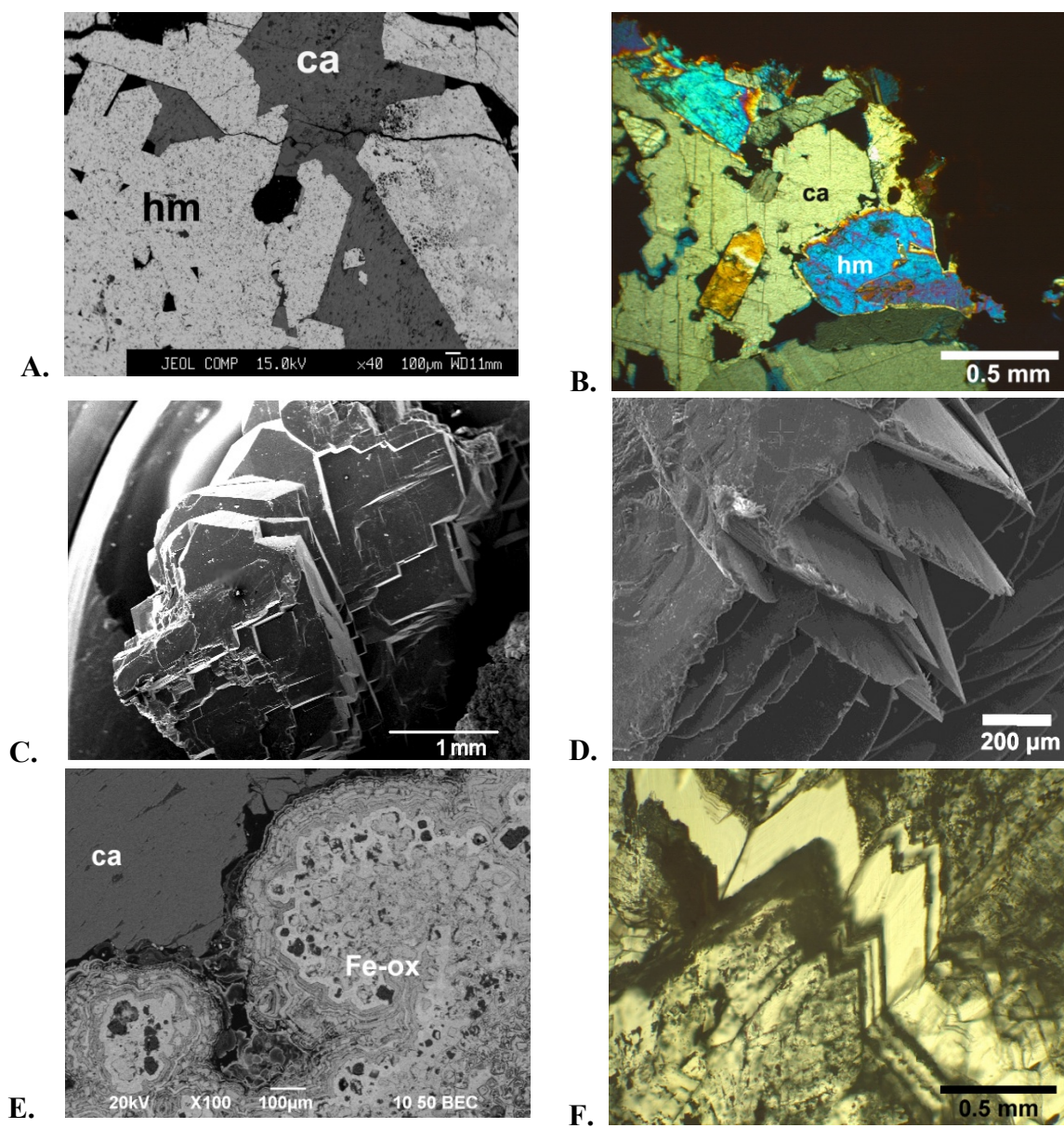
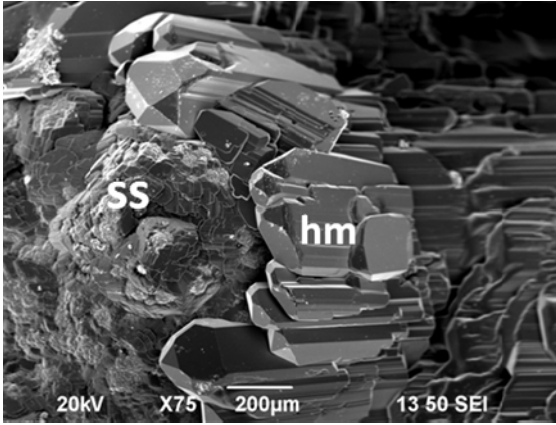


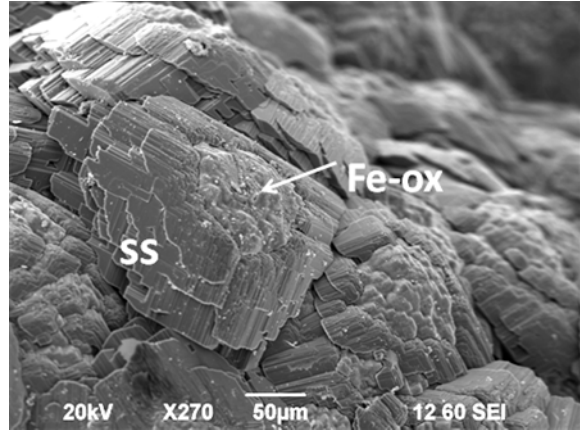
Figure 4.5. Altered hemimorphite and late-stage calcite.

A. Tabular hemimorphite and late calcite cement filling pores. BEI. Sample SS11-2DS. **B.** Tabular to anhedral hemimorphite and calcite cement. Sample BEI. EN1-2. **C.** Typical calcite coatings over hemimorphite. SEI. Sample SS4-4 (etched with 1% HCl for one minute). **D.** Commonly found calcite coatings over hemimorphite. SEI. Sample SS11-1DS. **E.** The Fe-oxide matrix and late calcite. BEI. Sample EN1-2. **F.** Zoned calcite. PPL. Sample SS11-2.

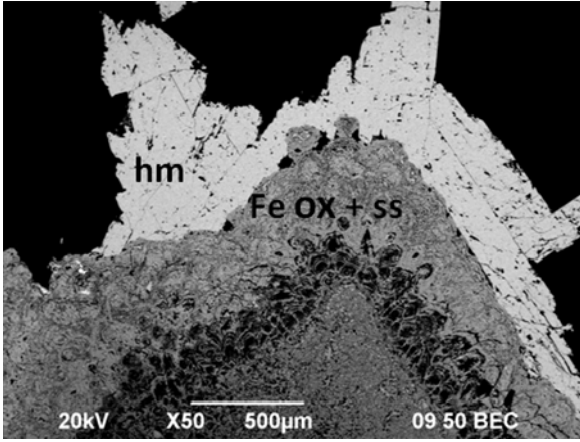
A.



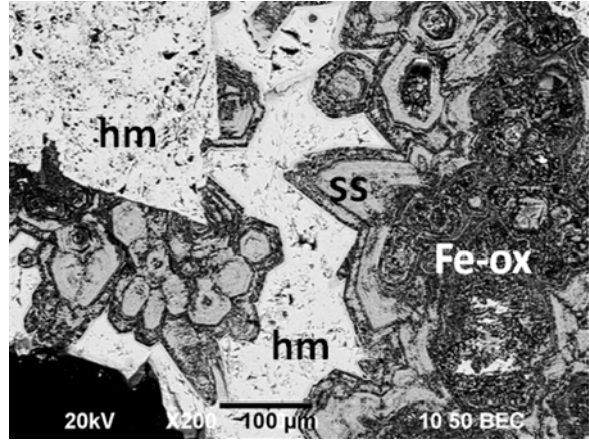
B.



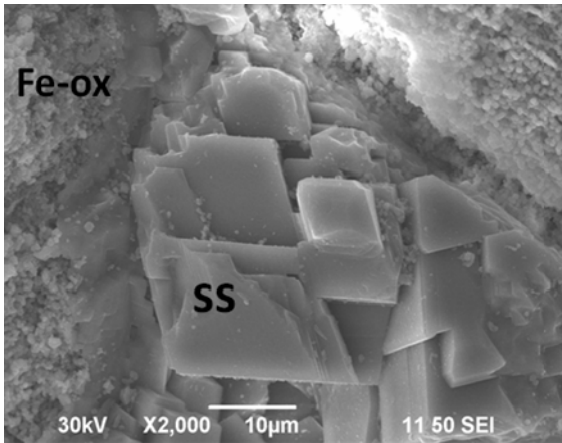
C.



D.



E.



F.

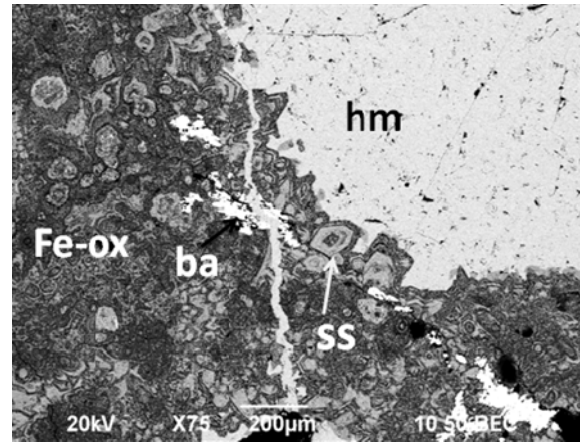


Figure 4.6. Smithsonite in the Iron Oxide Manto.

A. Aggregates of platy smithsonite on Fe-oxides and hemimorphite grown over smithsonite. SEI. Sample EN1-5. **B.** A magnified view of platy smithsonite aggregates. SEI. Sample EN1-5. **C.** Smithsonite finely intergrown with Fe oxides on matrix of Fe-oxides followed by hemimorphite. BEI. Sample EN1-5. **D.** Smithsonite (light gray) on Fe oxides cemented by hemimorphite. BEI. Sample EN1-3. **E.** Rhombohedral smithsonite in Fe-oxides. SEI. Sample EN1-5. **F.** Smithsonite intergrown with Fe-oxides (dark gray) and pore-filling hemimorphite (right top) and partially fracture-filling smithsonite matrix. Sample EN1-3.

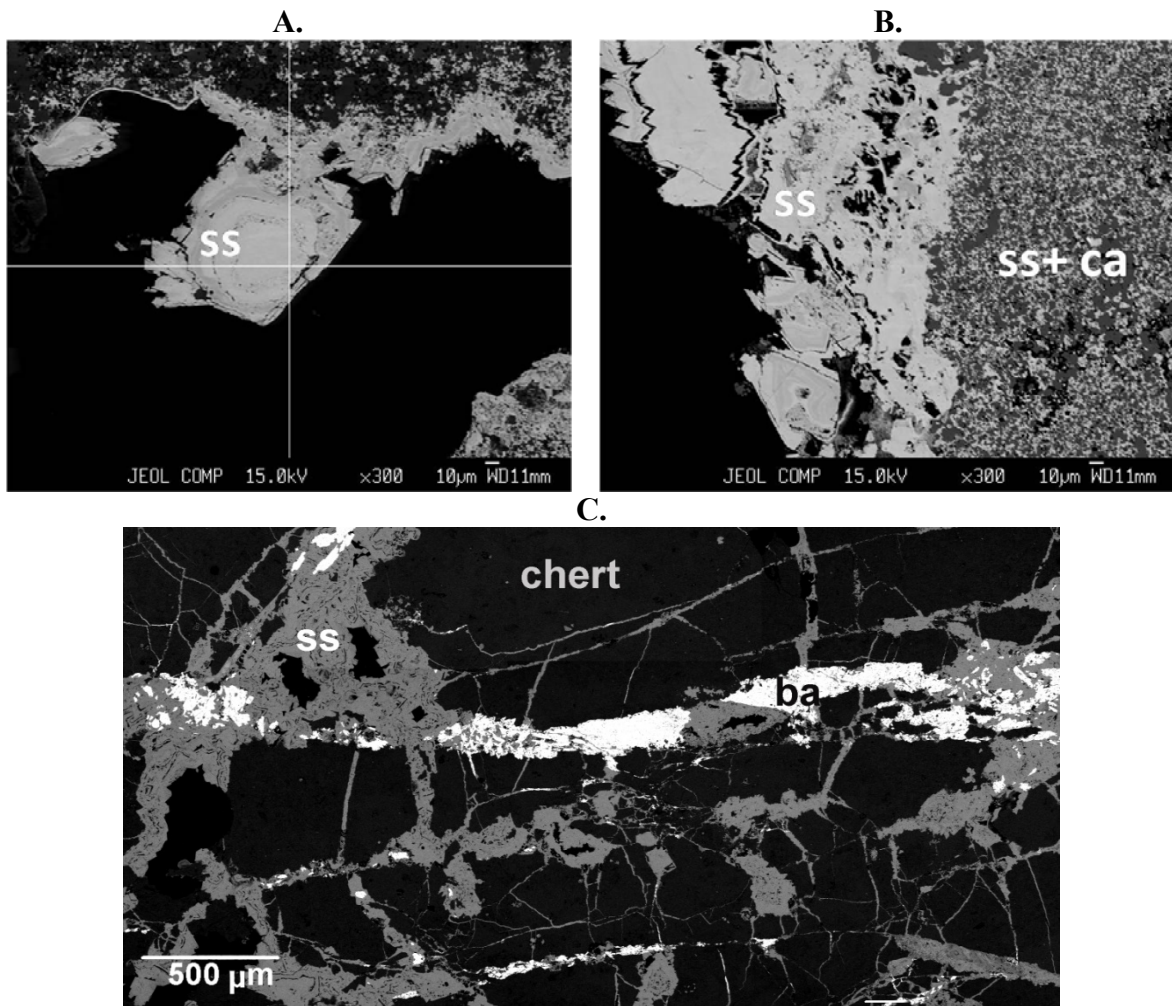


Figure 4.7. Smithsonite in the Iron Oxide Manto.

A. Zoned smithsonite in a pore. BEI. **B.** Smithsonite in vugs and disseminated microcrystalline calcite and smithsonite. BEI. **C.** A mosaic of several BSE images showing rhombohedral smithsonite in pores and late-stage barite in chert breccias. BEI. Sample SS8.

Table 4.1. WDS results of smithsonite and calcite.

A. Composition of smithsonite.

MgO	FeO	MnO	CaO	ZnO	CO ₂	Total	Sample ID/Description
1.47	0.76	0.11	0.73	61.20	35.81	100.07	SS8 zoned ss in pore
3.42	3.50	0.43	0.60	55.16	36.46	99.58	SS8 rhombic ss
2.92	1.14	0.06	0.59	58.34	35.95	99.01	SS8 ss in the matrix

Values in wt %.

*: calculated from stoichiometry

Smithsonite composition shown in mole %.

MgO	FeO	MnO	CaO	ZnO	Sample ID/Description
2.19	0.64	0.10	0.80	46.27	SS8 zoned ss in pore
5.08	2.98	0.37	0.65	40.92	SS8 rhombic ss
2.73	0.73	0.09	0.76	45.70	SS8 ss in the matrix

B. Composition of calcite.

Sample ID	MgO	FeO	MnO	CaO	ZnO	CO ₂	Total	Description
SS8	0.18	0.13	0.13	55.48	0.10	43.94	99.95	Late calcite vein
SS8	0.38	0.23	0.10	53.98	1.21	43.64	99.54	Early microcrystalline calcite
SS11-2DS	0.12	0.02	0.02	53.71	0.27	42.45	96.59	Late calcite

Values in wt %.

*: calculated from stoichiometry

Calcite composition shown in mole %.

Sample ID	Mg	Fe	Mn	Ca	Zn	Description
SS8	0.22	0.09	0.09	49.53	0.06	Late calcite vein
SS8	0.48	0.16	0.07	48.54	0.75	Early microcrystalline calcite
SS11-2DS	0.16	0.01	0.02	49.64	0.17	Late calcite

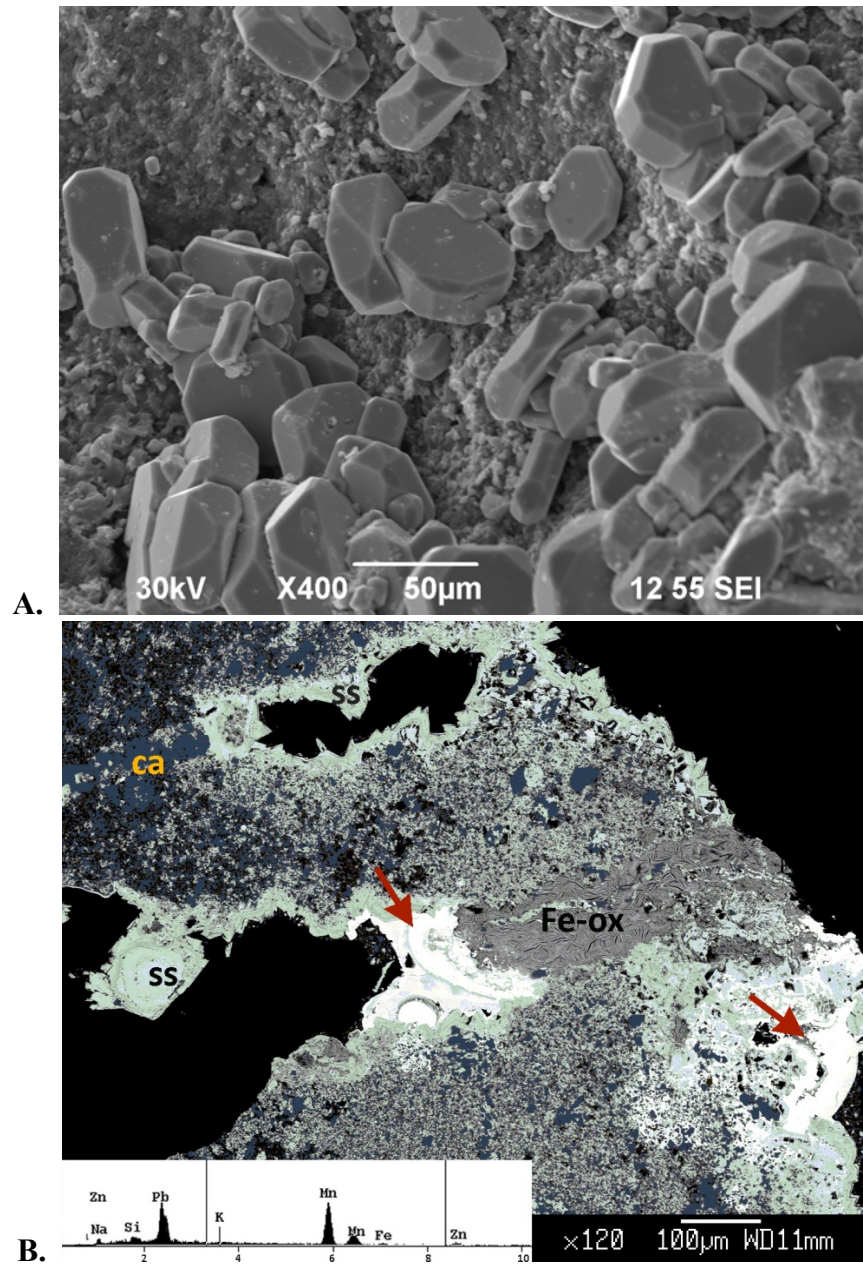
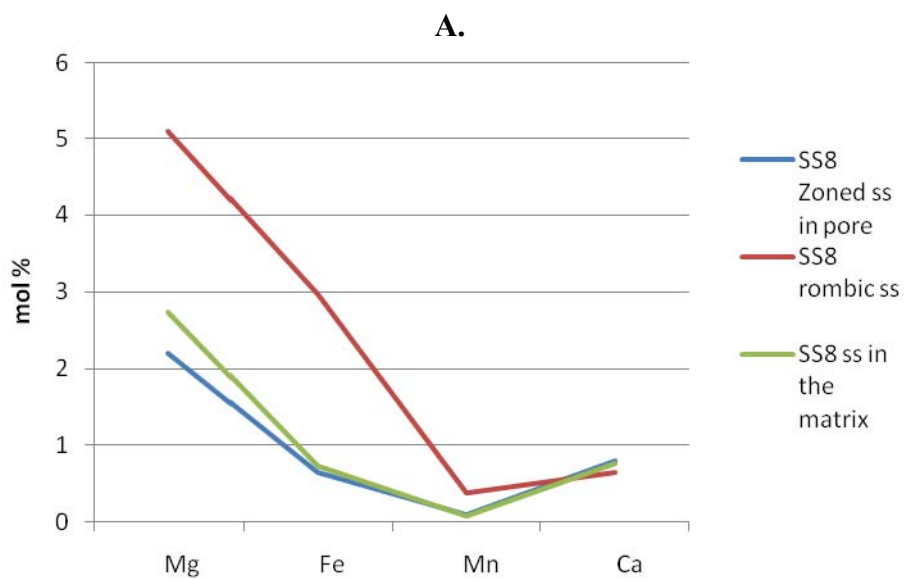


Figure 4.8. Barite and Mn-bearing minerals.

A. Euhedral barite crystals on oxidized carbonates. SEI. Sample SS4th. **B.** Pb/Mn-bearing minerals showing colloform features (red arrows) and an inset image showing EDS spectra. BEI. False color applied to a gray scale image. Sample SS8.



B.

	Sample ID.	Mg	Fe	Mn	Ca
rhombohedral crystals (10 μm - 50 μm)	EN1-5	Not determined			
rhombohedral crystals (10 μm - 50 μm)	SS8	3.64	1.81	0.24	0.72

Figure 4.9. Textural types of smithsonite and minor element compositions.

A. A plot showing minor element variations in rhombohedral smithsonite. **B.** Smithsonite morphologies and average minor element composition in mole percent.

Chapter 5. Stable Carbon and Oxygen Isotopes of Carbonates

ANALYTICAL METHOD

Carbon and oxygen isotope measurements were obtained from smithsonite and calcite samples from the Smithsonian Manto and calcite from the Iron Oxide Manto. Smithsonite and calcite samples were prepared as separates based on petrography. These samples consist of limestone, late-stage pore-filling calcite cement from both deposits and calcite speleothem from the Smithsonian Manto, banded, colloform and scalenohedral smithsonite, and one cerussite sample. Separation of different zones within smithsonite and calcite band was attempted in five smithsonite samples and one calcite sample. Separates were prepared sequentially from the inner zone to the outer zone according to their differences in color and mineral habits (Figure 5.1). Isotopic measurements were performed in the stable isotope laboratory of Museum für Naturkunde, Berlin, Germany (Dr. U. Struck, analyst). Methods applied for the isotope analyses were provided by Dr. H. Albert Gilg as follows: the CO₂ was extracted from 100 to 400 µg of carbonate by reaction with anhydrous phosphoric acid at 72°C for about 1.5 hours using a Thermo Finnigan GASBENCH II coupled online with a Thermo Finnigan DELTA V isotope ratio mass spectrometer in a continuous He flow mode. Isotope value is reported in the conventional delta-notation in permil (‰) relative to VSMOW for oxygen and VPDB for carbon. Reproducibility of replicate measurements of lab standards (limestone) is generally better than 0.10‰ (one standard deviation). The phosphoric acid fractionation factor for smithsonite and cerussite were applied as reported in Gilg et al. (2003).

RESULTS

Calcite

Sample description and results of the C-O isotopes for calcite are shown in Table 5.1. The isotopic composition of host limestone is clearly distinct from late calcite (Figure 5.2). Two limestone samples show relatively restricted $\delta^{13}\text{C}$ values of 3.2 and 3.8 ‰ and $\delta^{18}\text{O}$ values of 24.0 and 24.1 ‰. Late calcite associated with Zn ore minerals is paragenetically later than smithsonite and hemimorphite. Average oxygen isotope values of late-stage related calcite in the Smithsonite Manto are 21.7 ± 0.4 ‰ and the $\delta^{13}\text{C}$ values show the average of -6.3 ± 0.7 ‰ (n= 8).

Two types of calcite have been measured in the Sample, SM08-11: calcite cements in breccias associated with pore-filling hemimorphite and scalenohedral calcite on the top (Figure 5.1B). Carbon isotope values are slightly different by 1.2 ‰, but oxygen isotope values are similar. Carbon and oxygen isotope measurements from interior to exterior zones (separates from A to C) are measured in another calcite sample (SM08-12) (Figure 5.1A), and changes in the isotope value are illustrated in Figure 5.2A. The $\delta^{18}\text{O}$ values increase from A to B, but it remains relatively constant from B to C, and the $\delta^{13}\text{C}$ values are relatively close ranging from -6.6 to -7.2 ‰. The C-O isotope values of late calcite crystals on smithsonite (SM03-24-B, SM08-22-C and SM09-10-C) are within the ranges of other late calcite (Figure 5.2A).

Four calcite samples from the Iron Oxide Manto are included for the carbon and oxygen isotope measurements (Table 5.1). This calcite also appears to be formed after Zn mineralization. The average carbon and oxygen isotope values are -6.6 ± 1.9 ‰ and 21.0 ± 0.8 ‰ (n = 4), respectively. The results are shown in Figure 5.2A indicating a wider range of both C-O isotope values than those values of calcite from the Smithsonite Manto (Figure 5.2A).

Compared to C-O isotope values of Cretaceous marine carbonates (avg. of 27.7 and 2.36 ‰ for $\delta^{18}\text{O}_{\text{VSMOW}}$ and $\delta^{13}\text{C}_{\text{PDB}}$, respectively) in Veizer and Hoefs (1976), the carbon isotope values of limestone in the district are slightly heavier, but oxygen isotope values are slightly lighter. The C isotope measurements are compared to Lower Cretaceous carbonates at the Sierra Acatita of the Coahuila block in northeastern Mexico (Lehmann et al., 1999) and to late calcite of other NSZ deposits from Boni et al. (2003) and Gilg et al. (2008). Deposited during Aptian through Albian time on the Coahuila block, Acatita Formation is composed of cyclic, interbedded carbonates and evaporites (Lehmann et al., 1999). A diagram for this comparison is shown in Figure 5.2B. The $\delta^{13}\text{C}$ values of the Sierra Mojada limestone are within the range of carbonates from the Sierra Acatita. Most of carbon isotope values of late calcite in the Sierra Mojada district are slightly heavier than those of other NSZ deposits (Boni et al., 2003). The $\delta^{18}\text{O}$ values of Sierra Mojada calcite are lower than those calcite (24.7 ~ 25.6 ‰) of low temperature meteoric origin in Boni et al. (2003).

Smithsonite

The $\delta^{18}\text{O}$ values of smithsonite from the Smithsonite Manto show the average of 21.9 ± 0.5 ‰ (n= 31) and the carbon isotope values vary from -8.4 to 1.1 ‰ with an average of -1.6 ± 2.0 ‰. Smithsonite-A and -B were included for the isotope measurements. The description and results are listed in Table 5.1B. Smithsonite-A includes banded scalenohedral crystals without distinct zonation under an optical microscope. Smithsonite-B is characterized by banded or colloform mineral habits. Five smithsonite samples of smithsonite-B, including SM03-09, SM03-27, SM08-06, SM09-09, and SM09-10, are measured from several different points in the smithsonite bands and examples for a sampling method can be seen (Figure 5.1C and D). Results of smithsonite-A and smithsonite-B are presented in Figure 5.3A.

Smithsonite-A shows the average carbon isotope value of 0.3 ± 0.7 ‰ and the average oxygen isotope value of 21.5 ± 0.3 ‰ (n=4). Smithsonite-B smithsonite shows the average $\delta^{18}\text{O}$ values and the $\delta^{13}\text{C}$ values of 22.0 ± 0.5 ‰ and -1.9 ± 1.9 ‰, respectively.

Smithsonite-A is relatively ^{13}C -enriched with the carbon isotope values around 0 ‰, whereas the oxygen isotope values are close to smithsonite-B. The C-O isotope values of smithsonite-B vary from the inner zone to the outer zone. Figure 5.3B and C show variations in C-O isotope values. Inner zones of SM03-09 and other zones of SM09-10 display heavier carbon isotope values, while the oxygen isotope values remain within the range of the other smithsonite-B. SM09-10A and B showed both positive $\delta^{13}\text{C}$ values (Figure 5.3B). In the sample, SM03-27, where four different points are analyzed (Figure 5.3B), the $\delta^{18}\text{O}$ values are close each other ($21.4 \sim 22.3$ ‰) and the $\delta^{13}\text{C}$ values varied from -5.1 to -1.8 ‰. Figure 5.3C shows the C-O isotope variations in the sample, SM08-06 suggesting a series of minor temperature change during smithsonite precipitation. However, the systematic isotope variations might not be clearly defined in these measurements probably because sampling was performed in coarse scale. A pale purplish banded smithsonite sample (SM08-10) shows the lowest carbon isotope value (-8.4 ‰), but the oxygen isotope value was similar to others.

DISCUSSION

The isotopic patterns of smithsonite show a relatively wide range of the carbon isotopes and restricted values of the oxygen isotopes. The oxygen isotope values of calcite are within the same range of smithsonites, but the carbon isotope values are lower than those smithsonite. The C-O isotope values of smithsonite are compared to those from other non-sulfide Zn deposits (Figure 5.4). Data used for comparison is found in Boni et al. (2003 and 2007), and Gilg et al. (2008) (Figure 5.4). Carbon isotope values

from smithsonite are characteristic for supergene smithsonite, whereas oxygen isotope values are slightly lower than those reported in most supergene non-sulfide deposits, which range from 26 to 31 ‰ (Gilg et al., 2008). The oxygen isotope results might indicate that Sierra Mojada smithsonites were formed at slightly elevated temperature, at least during some stages of smithsonite mineralization and/or that oxidizing waters were isotopically much lighter than in the other studied areas (Gilg, written comment). $\delta^{18}\text{O}_{\text{VSMOW}}$ values for hypogene smithsonite in the Angouran deposit are more variable ranging from 18.3 to 23.6 ‰, and their carbon isotope values (3.2 to 6.0 ‰) are heavier than supergene smithsonites (Boni et al., 2007) (Figure 5.4).

Carbon isotopes

Carbon isotope values of smithsonite from the Smithsonite Manto shows a range of 9.5 ‰ (from -8.4 to 1.1 ‰). The carbon isotope values of late-stage calcite from the Smithsonite Manto are 1.9 ‰ and are 4.6 ‰ from the Oxide Manto. Calcite samples from the Iron Oxide Manto show the relatively wide ranges of both carbon and oxygen isotope values compared to the C-O values of calcite from the Smithsonite Manto. This calcite associated with Zn minerals shows negative $\delta^{13}\text{C}$ values as well as most of smithsonite samples are depleted in ^{13}C , but a few smithsonite samples show heavier carbon isotope values around 0 ‰. In most carbonate-hosted base metal deposits, the carbon isotope values of smithsonite vary more than about 10 ‰, indicating that there have been two different carbon sources (Gilg et al., 2008).

The differences in carbon isotope values in Sierra Mojada smithsonites and calcites suggest they might have been formed from different CO_2 sources, presumably by mixing several sources, including heavy carbonate wall rocks and organic matters. The ^{13}C -depleted component could be related to the soil CO_2 from the vegetation activities from C_3 plants or to oxidation of sulfide-oxidizing bacteria in sulfide bodies as a result of

a decreasing water table (Gilg et al., 2008). Trees of C₃ species are mostly common in arid or semi-arid climates, whereas C₄ plants do not exist where night temperature drops below 8 °C (Cerling, 1984). C₃ grasses show lower $\delta^{13}\text{C}$ values (-27.1 ‰) than C₄ grasses (-12.7 ‰), and CAM plants (Crassulacean Acid Metabolism) are in between these values (Cerling, 1984). The present flora of Sierra Mojada consists of variety of Yucca family, including the palms and lechuguilla (*Agave lechuguilla*); the cacti, and the mesquite (*Prosopis glandulose*), which is uncommon in the immediate surrounding area (Riley, 1936). The Yucca family plants and cactus belong to CAM species, and the mesquite is C₃ plants.

The ¹³C-enriched components (around 0 ‰) in smithsonite can originate from three possible sources: CO₂ generated from carbonate wall rocks, atmospheric CO₂ and soil CO₂ from C₄ plants decomposition (Gilg et al., 2008). However, the most probable source for enrichment in ¹³C in supergene environment for smithsonite could be from the CO₂ release from isotopically heavy wall rock carbonates and high values in supergene smithsonites can be expected (Gilg et al., 2008).

Oxygen isotopes

The $\delta^{18}\text{O}$ values of calcite and smithsonite are within the close range (20.5 ~ 23.3 ‰). The $\delta^{18}\text{O}$ values of smithsonite of SMj district are lower by about 6.2 ‰ than other supergene smithsonite and their average formational temperatures are 20 ± 5 °C (Gilg et al., 2008) (Figure 5.4). Formational temperatures for hypogene smithsonites in the Angouran deposit are much more variable ranging from 15 to 40 °C. Formational temperatures of smithsonite can be expected from oxygen isotope equilibrium curves between smithsonite and water (Gilg et al., 2008) if the $\delta^{18}\text{O}$ value of paleometeoric water is known. Although local paleometeoric water composition is unavailable for the Sierra Mojada district, adjacent modern groundwater can be used as an estimate of the

$\delta^{18}\text{O}$ water value. If the mineralizing fluids similar oxygen isotope composition of about -8 ‰ (VSMOW) as modern high elevation (2350 m) recharge groundwaters at Cuatro Ciénegas, Coahuila (Johannesson et al., 2004 and Wassenaar et al., 2009) have an oxygen isotope composition of about -8 ‰ (VSMOW) that might serve as a representative value for the Sierra Mojada NSZ-mineralizing waters. Cuatro Ciénegas is located in 26.59°N and 102.03°W. The pH of this groundwater is 6.94 with the temperature of 26.2 °C (Johannesson et al., 2004). Using this isotopic composition of water, formational temperatures for smithsonite were calculated. The oxygen isotope fractionation equation for smithsonite below 100 °C (Gilg et al., 2008):

$$1000\ln\alpha_{\text{smithsonite-water}} = 3.10(10^6/T^2) - 3.50 \quad (5-1)$$

In order to estimate temperature of late calcite formation, the equation for the oxygen isotope fractionation between calcite and water in O'Neil et al. (1969) was used:

$$1000\ln\alpha_{\text{calcite-water}} = 2.78(10^6/T^2) - 3.39 \quad (5-2)$$

The estimated formational temperature for smithsonite-A is 33.5 ± 1.2 °C and for smithsonite-B is 31.1 ± 2.2 °C. If the average oxygen isotope value of smithsonites is considered (21.9 ‰), the approximate formational temperature is about 35 °C. Using the same oxygen isotope composition of water, lower temperatures of 14 to 19 °C (average = 17 °C) are calculated for late calcite in the Smithsonite Manto. A temperature range of calcite from the Iron Oxide Manto is from 15 to 23 °C (average = 20 °C).

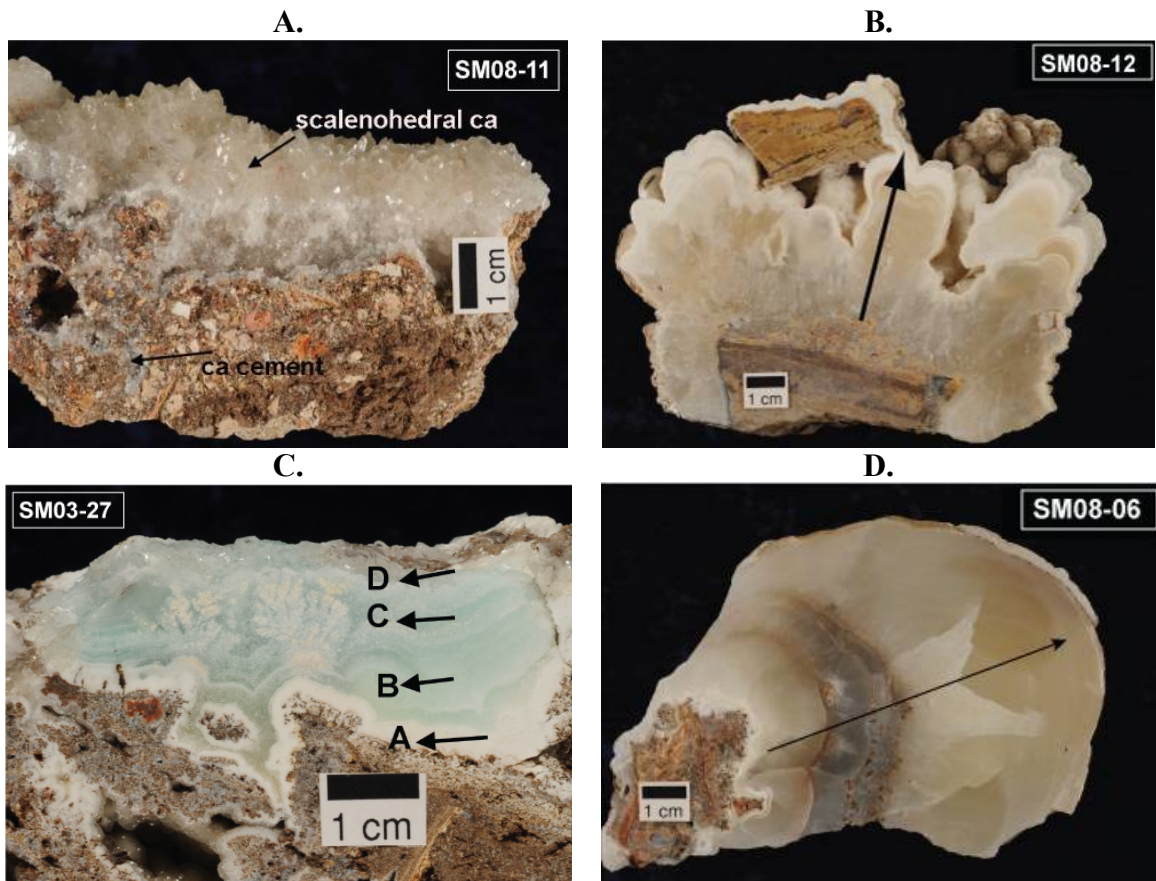


Figure 5.1. Samples for the C-O isotope measurements.

A. Fracture-fill calcite and scalenohedral calcite. **B.** Calcite speleothem. **C.** Banded smithsonite (ss-B). Alphabet letters indicate sampling locations. **D.** Coarsely zoned smithsonite (ss-B). Direction of an arrow indicates sampling sequence.

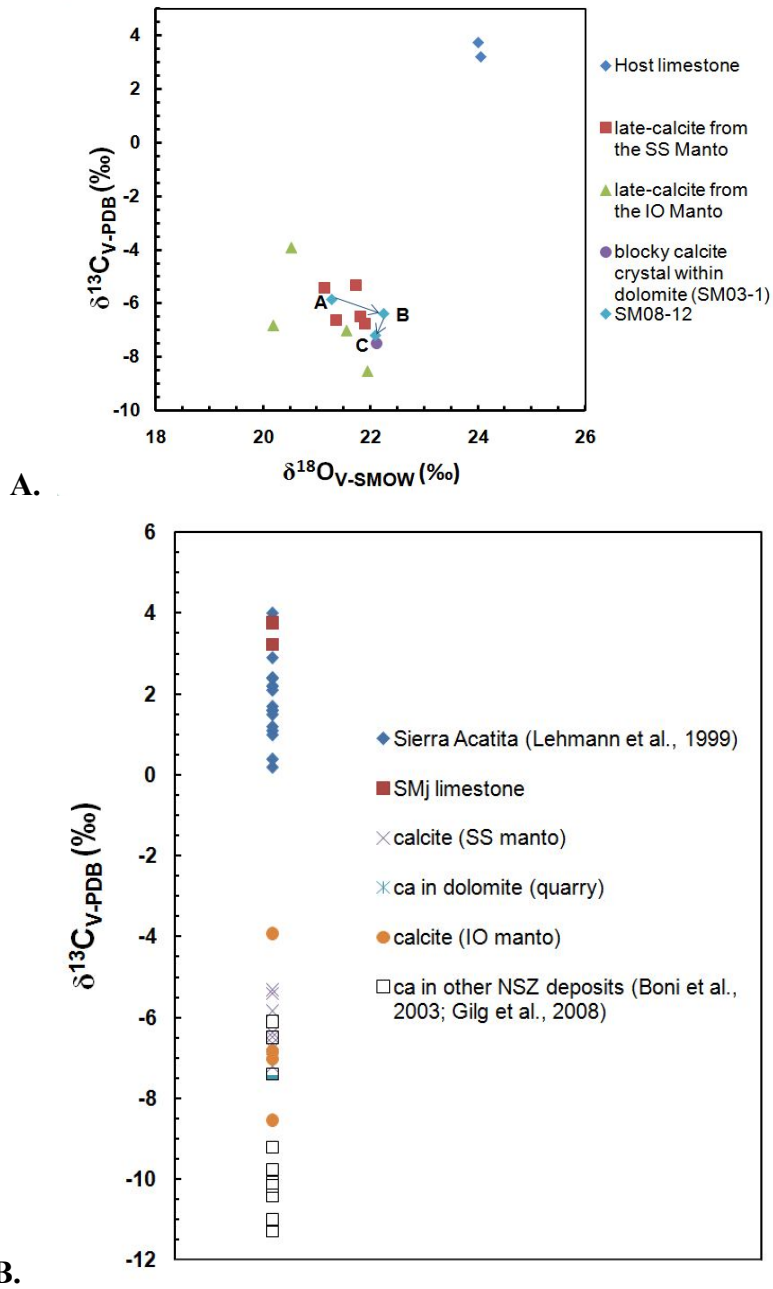


Figure 5.2. Diagrams of carbon and oxygen isotope composition of calcite.

A. Carbon and oxygen isotope values of calcite from the Smithsonite Manto and the Iron Oxide Manto and two limestone samples. Isotope variations of the sample, SM08-12. A (an inner zone) to C (an outermost part). **B.** Carbon isotope data of carbonates from Lehmann et al. (1999) and of calcite associated with NSZ from Gilg et al. (2008). The C-O values of Sierra Mojada as well.

Table 5.1. Carbon and Oxygen stable isotope values of carbonates.

A. Calcite

Sample ID	Mineral	Location	$\delta^{18}\text{O}_{\text{VSMOW}}$	stdev	$\delta^{13}\text{C}_{\text{VPDB}}$	stdev	Description
D9090307-23.5	ca		24.0	0.1	3.2	0.1	host limestone
D9090307-58	ca		24.0	0.1	3.8	0.2	host limestone
SM03-1	ca	quarry	22.1	0.3	-7.5	0.5	blocky ca crystals within Aurora dolomite
SM03-24-B	ca	SSM	21.1	0.2	-5.4	0.1	ca crystal on ss
SM08-11-A	ca	SSM	21.7	0.1	-5.3	0.1	fracture fill ca
SM08-11-B	ca	SSM	21.8	0.1	-6.5	0.1	scalenohedral ca fracture fill
SM08-12-A	ca	SSM	21.3	0.1	-5.8	0.1	interior radiating amber ca
SM08-12-B	ca	SSM	22.2	0.1	-6.4	0.1	white banded ca
SM08-12-C	ca	SSM	22.1	0.2	-7.2	0.2	5-mm colorless outer rind ca
SM08-22-C	ca	SSM	21.9	0.1	-6.8	0.1	5-mm ca on ss
SM09-10-C	ca	SSM	21.4	0.2	-6.6	0.4	ca-filled fracture
SM-DD1	ca	SSM	20.2	0.1	-6.8	0.1	colorless ca on late fracture
SMj-DD3	ca	IOM	21.9	0.0	-8.5	0.0	pore-fill ca mass
EN1-2	ca	IOM	20.5	0.2	-3.9	0.6	ca crystals
SS11-2	ca	IOM	21.5	0.1	-7.0	0.1	ca mass

B. Smithsonite

Sample ID	$\delta^{18}\text{O}_{\text{VSMOW}}$	stdev	$\delta^{13}\text{C}_{\text{VPDB}}$	stdev	Type	Description
SM08-22 A	21.6	0.1	0.8	0.2	ss-A	botryoidal bands
SM08-24	21.6	0.4	1.1	0.2	ss-A	pendulous pale gray smithsonite
SM08-22 B	21.1	0.1	-0.3	0.4	ss-A	scalen crust on mass ss
SM08-26	21.5	0.1	-0.2	0.2	ss-A	white ss frc-fill and masses
SM03-07	22.1		1.0		ss-B	multiple bands of white and colorless ss
SM03-09	21.8		0.9		ss-B	dark gray and green ss
SM03-09-A	21.9	0.1	0.6	0.1	ss-B	Interior colloform dark gray green
SM03-09-B	21.4	0.1	-0.8	0.2	ss-B	Exterior colloform white bands
SM03-27-A	23.3	0.0	-3.0	0.1	ss-B	colorless crystals
SM03-27-B	21.4	0.1	-5.1	0.3	ss-B	inner chalky band
SM03-27-C	22.3	0.1	-1.9	0.1	ss-B	5 mm bluish band
SM03-27-D	22.3	0.0	-1.8	0.2	ss-B	8 mm bluish band with minor white ss
SM08-06-2	22.3	0.1	-1.8	0.1	ss-B	outer 5 mm massive dark ss
SM08-06-3A	21.8	0.1	-2.5	0.1	ss-B	chalky ss
SM08-06-3B	20.9	0.1	-3.8	0.1	ss-B	Interior of 5-mm smithsonite band
SM08-06-4A	21.9	0.1	-3.2	0.0	ss-B	Exterior of 12 to 15-mm gray band
SM08-06-4B	21.9	0.0	-2.4	0.1	ss-B	Interior of gray ss band
SM08-06-4C	21.6	0.1	-2.4	0.2	ss-B	Exterior of gray ss band
SM08-06-5A	22.0	0.1	-1.4	0.0	ss-B	Interior 8-mm of ~40-mm ss band
SM08-06-5B	21.8	0.0	-1.7	0.0	ss-B	8-16 mm zone
SM08-06-5C	21.7	0.0	-2.1	0.1	ss-B	16-24 mm zone
SM08-06-5D	21.8	0.1	-1.9	0.1	ss-B	24-32 mm zone
SM08-06-5E	21.6	0.0	-2.6	0.1	ss-B	Exterior 8-mm of ~40-mm ss band
SM08-06-6	22.3	0.1	-1.3	0.1	ss-B	Interior of 12 to 15-mm gray band
SM09-10-A	23.2	0.0	0.2	0.1	ss-B	purple ss vug-fill crust
SM09-10-B	22.4	0.1	0.3	0.1	ss-B	late green ss crust intergrown with Mn-ox
SM09-9-A	22.4	0.0	-0.5	0.1	ss-B	Interior green yellow zone over Mn-ox
SM09-9-B	22.1	0.3	-3.3	1.9	ss-B	4 mm dark yellow green band
SM09-9-C	21.9	0.1	-1.9	0.2	ss-B	next 3-mm inner band
SM09-9-D	22.1	0.1	-1.6	0.1	ss-B	outer 5- mm yellow band
SM08-10	21.8	0.1	-8.4	0.3	ss-B	pale purplish bands

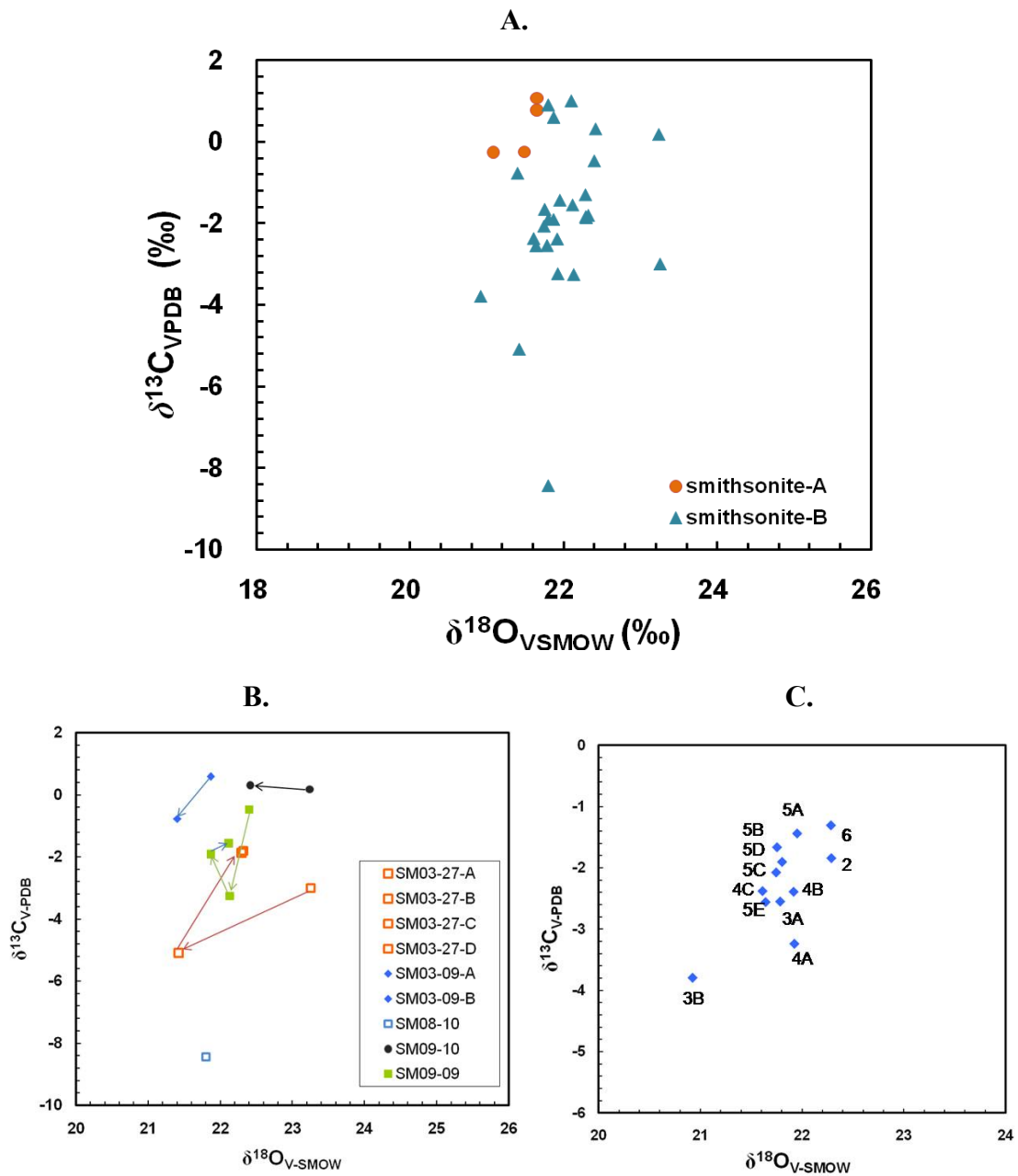


Figure 5.3. Carbon and oxygen stable isotope values of smithsonite.

A. C-O isotope values of the early smithsonite-A and the late smithsonite-B. **B.** Results of C-O isotope variations in smithsonite-B. **C.** Results of C-O isotope variations of smithsonite-B from the inner to outer zones indicated by numbers in ascending orders. Sample ID. SM08-06.

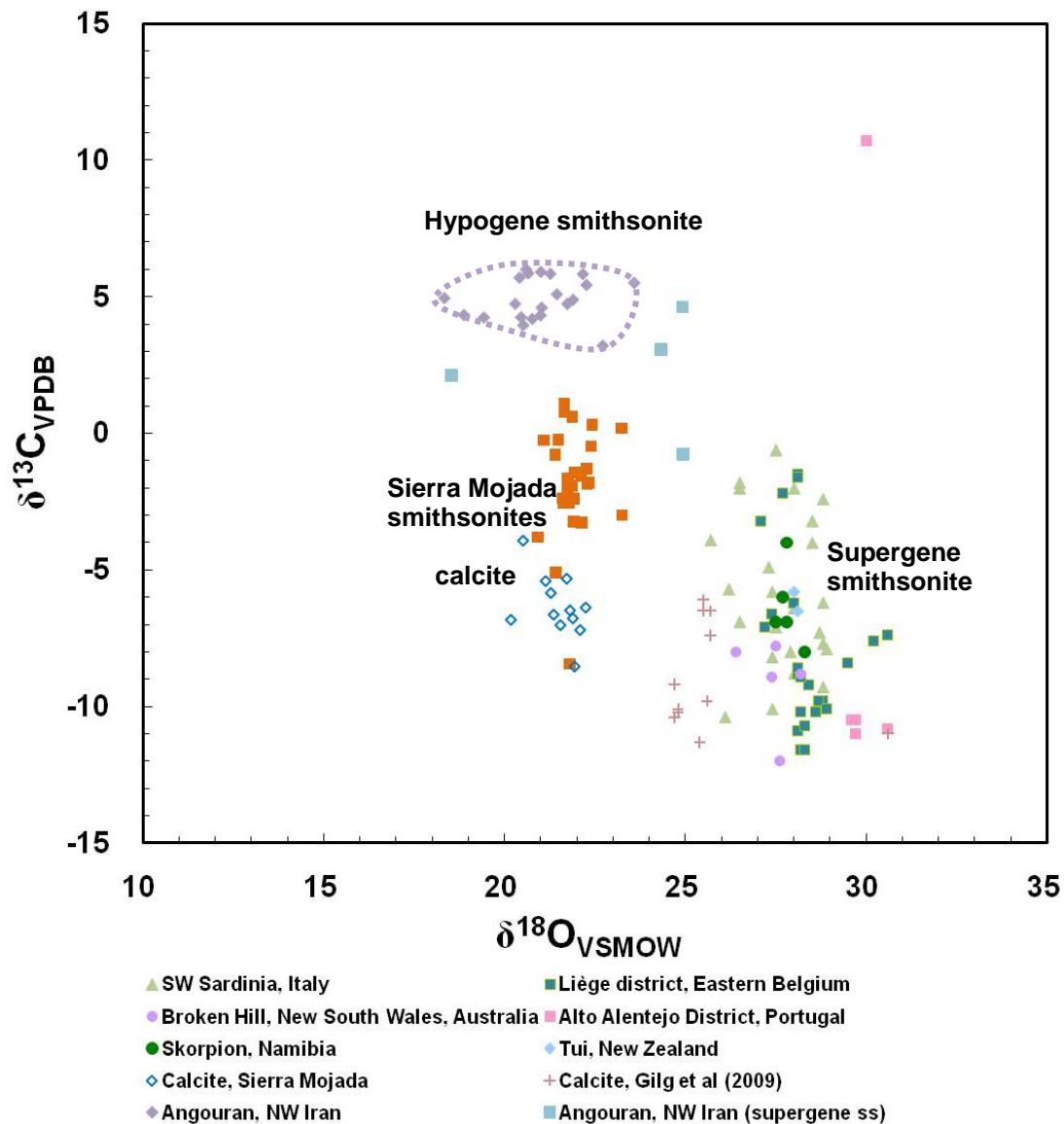


Figure 5.4. Comparison of the C-O isotope values.

Smithsonite and calcite of Sierra Mojada compared to other supergene smithsonites and calcite (Boni et al., 2003 and Gilg et al., 2008), and hypogene smithsonite at Angouran, NW Iran (Boni et al., 2007).

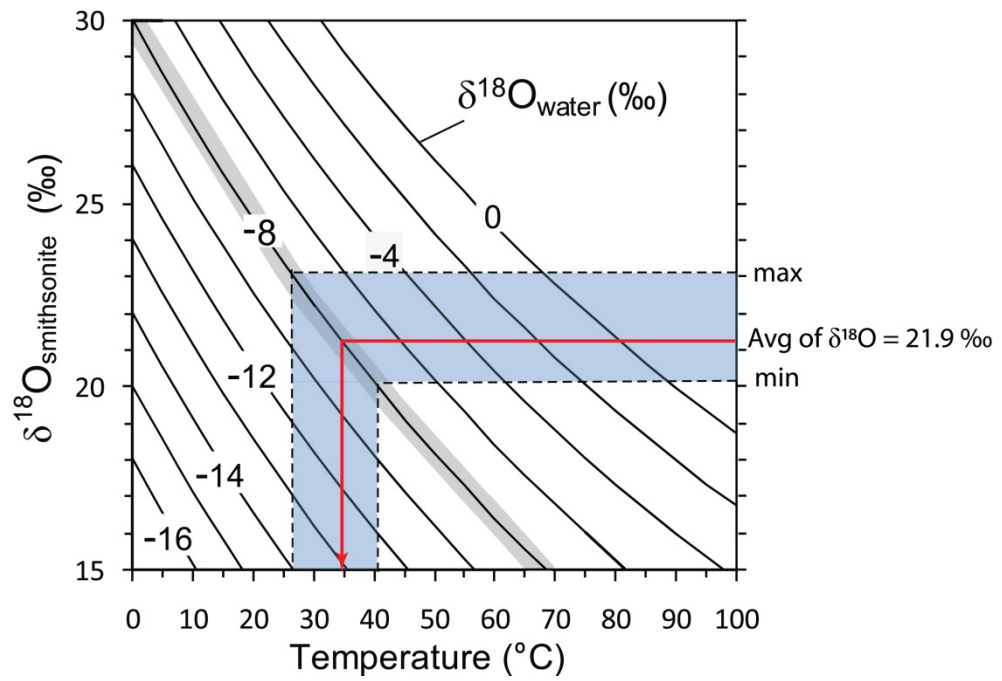


Figure 5.5. Oxygen equilibrium curves between smithsonite and water.

After Gilg et al. (2008). A shaded area shows the ranges of the oxygen isotope composition of smithsonite in SMj district.

Chapter 6. Pb Isotope Compositions

METHODS

Galena, cerussite, and smithsonite were measured for their Pb isotope composition to evaluate the possible genetic relations among the sulfide and non-sulfide ore bodies. Seven galena samples from the sulfide deposit, one cerussite, and one smithsonite from the non-sulfide Zn deposits were handpicked to measure Pb isotope compositions. Detailed methods are listed in Appendix E.

RESULTS AND DISCUSSION

Pb isotope results are shown in Table 6.1. The results are plotted on $^{207}\text{Pb}/^{204}\text{Pb}$ versus $^{206}\text{Pb}/^{204}\text{Pb}$ diagram and $^{208}\text{Pb}/^{204}\text{Pb}$ and $^{206}\text{Pb}/^{204}\text{Pb}$ diagram in Figures 6.1 and 6.2. The S-K line refers to the average crustal growth curve from Stacey and Kramer (1975). Galena samples have $^{206}\text{Pb}/^{204}\text{Pb}$ ratios between 18.634 and 18.700 (average = 18.679), $^{207}\text{Pb}/^{204}\text{Pb}$ between 15.631 and 15.662 (average = 15.644), and $^{208}\text{Pb}/^{204}\text{Pb}$ between 38.495 and 38.633 (average = 38.563). The Pb isotope compositions of galena, cerussite, and smithsonite are similar (within analytical error) except one galena sample (Figures 6.1 and 6.2). Data for most samples except the smithsonite plot above the average crustal Pb growth curves of Stacey and Kramers (1975) in the $^{207}\text{Pb}/^{204}\text{Pb}$ versus $^{206}\text{Pb}/^{204}\text{Pb}$ diagram (Figure 6.1), but most samples plot below in the $^{208}\text{Pb}/^{204}\text{Pb}$ versus $^{206}\text{Pb}/^{204}\text{Pb}$ diagram (Figure 6.2). The similarity of Pb isotope ratios of the smithsonite sample from the non-sulfide Zn deposits and the cerussite sample from the Lead Manto to the Pb isotopic compositions of the sulfide samples suggest that the source of the metals of the non-sulfide deposits appear to be derived from the sulfide deposits at Sierra Mojada.

The Pb isotope character of the Sierra Mojada mineralization is similar to polymetallic carbonate replacement deposits in northern Mexico at Naica (James and Henry, 1993) and at nearby (unpubl. Data, this study). However, these data are more radiogenic than the carbonate replacement deposits at Santa Eulalia, Dos Marias, and Plomosas, as well as the skarn deposit at Santa Eulalia, Dos Marias, and Plomosas, as well as the skarn deposit at San Carlos (James and Henry, 1993). The Pb isotope character of all the northern Mexico polymetallic deposits are distinctly different from the Laramide porphyry Cu-associated carbonate replacement deposit at Shafter in contiguous Texas, as well as the epithermal veins in mid-Tertiary Chinati Caldera (James and Henry, 1993).

Table 6.1. Pb isotope compositions of galena, cerussite, and smithsonite.

Sample ID	$^{206}\text{Pb}/^{204}\text{Pb}$	$^{207}\text{Pb}/^{204}\text{Pb}$	$^{208}\text{Pb}/^{204}\text{Pb}$
Galena			
SM03-4	18.676	15.638	38.551
SM-S3-Pb	18.693	15.642	38.559
D7080226-25.5	18.687	15.636	38.534
SM08-Pb01	18.697	15.648	38.575
D9090317-13	18.634	15.631	38.495
DRMT08-1	18.691	15.65	38.593
DRMT08-2	18.7	15.662	38.633
Cerussite			
SMj-PbC-1	18.692	15.647	38.575
Smithsonite			
SM03-09	18.686	15.623	38.491

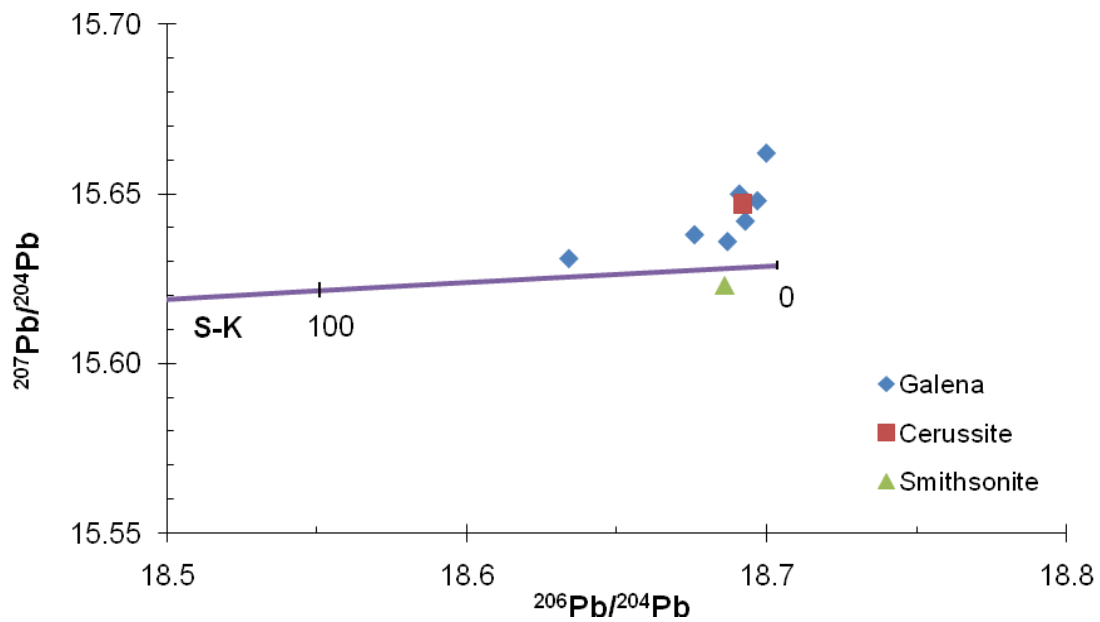


Figure 6.1. A plot of $^{207}\text{Pb}/^{204}\text{Pb}$ versus $^{206}\text{Pb}/^{204}\text{Pb}$.

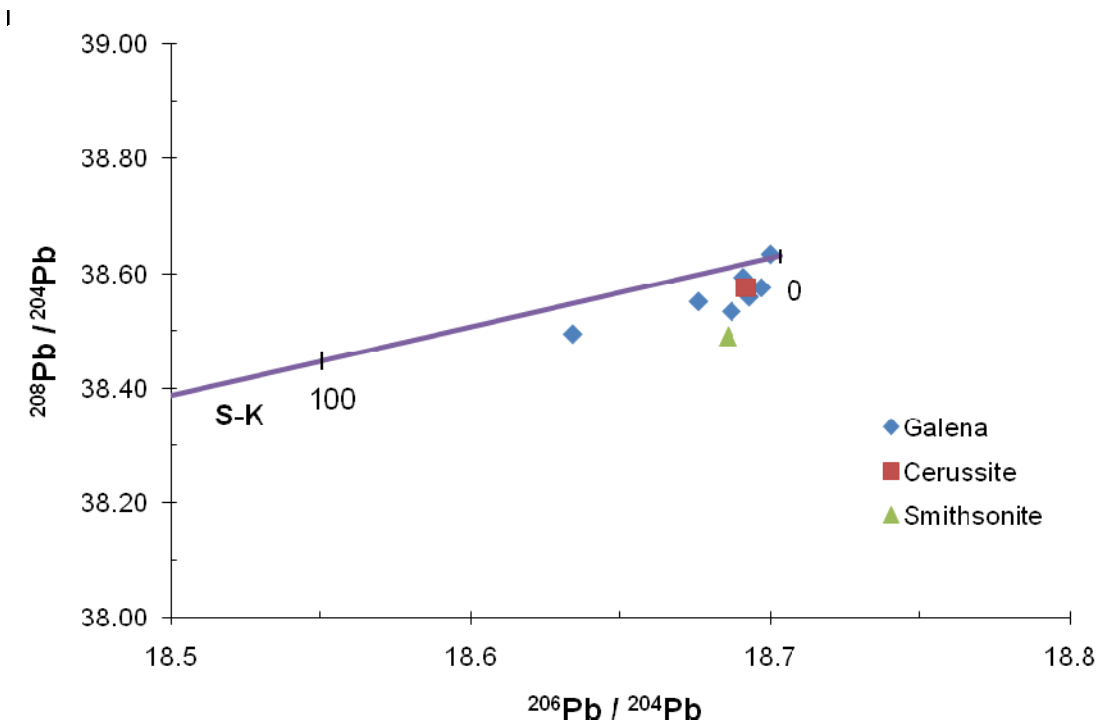


Figure 6.2. A plot of $^{208}\text{Pb}/^{204}\text{Pb}$ versus $^{206}\text{Pb}/^{204}\text{Pb}$.

Chapter 7. CL Investigations and Trace Element Distribution in Smithsonite

INTRODUCTION

There has been considerable amount of cathodoluminescence studies on carbonate minerals, particularly on calcite and dolomite. The causes of luminescence of common carbonate minerals have been well-known in various publications (Habermann et al., 1998; Ritcher et al., 2003; Boggs, 2006). Cathodoluminescence, one of the visible radiation emissions, is caused when photons are emitted by the bombardment of electrons at the surface of materials and the cathode is the source of electrons. Interaction of the electron beam with the solid material is converted to secondary electrons of weaker energies, X-rays, back-scattered electrons of higher energy, and some Auger electrons. Other energies produced by the beam cause the delocalized electrons to move from a ground state to an excited state. These excited electrons encounter traps in a band gap between the valency energy and conduction energy bands shortly before they are back into a lower energy level. The presence of traps, called luminescence center, can result in cathodoluminescence. When there are no traps present, electrons falling directly to the valence state emits photons in an ultraviolet range of wavelengths (Boggs, 2006).

There are two types of luminescence: intrinsic and extrinsic luminescence centers. The intrinsic luminescence implies that it is related to the lattice properties of minerals, which is always present in minerals without the influence of the trace elements. “Extrinsic” or impurity luminescence is more common in natural settings and is caused by trace elements that serve as activators or quenchers of luminescence, Mn^{2+} and Fe^{2+} , respectively. Additionally, trivalent REE elements can be activators in carbonate minerals (Habermann et al., 1998). Intrinsic luminescence can be improved by nonstoichiometry, structural imperfections, and impurities (Marshall, 1988). Extrinsic centers are often

included in a crystal from a mineralizing melt or fluid (Boggs, 2006). Doubly charged Mn ions, as a trace impurity, have been known to cause the most significant CL behavior and Cu and Fe play an opposite role to the activator in most carbonate minerals acting as quenchers. Also, quenching can occur when activators exceeds a certain limit of concentration, which is called self-quenching. Some other ions acting as neither activators nor quenchers are called sensitizers, such as Pb in carbonates, capable to absorb energy and transfer this energy to activators (Boggs, 2006).

CL and Geologic Influences

Formations of most carbonate minerals can be influenced by various geologic factors, such as properties of fluids, temperature, and tectonic processes. Also, changes in properties of mineral-forming fluids may cause different concentrations of major and trace elements in minerals. CL studies have been used to analyze in various fields, such as diagenesis and recrystallization of carbonate rocks and movement of mineralizing fluids in some of MVT environments (Boggs, 2006, pp. 133-139). Because Mn and Fe are always present in natural waters, it has been considered that the oxidizing and reducing characteristics of the fluids are related to chemical species of these elements (Marshall, 1988). Some studies concluded that CL intensity can be related to the pH, redox potential, and the total sulfur contents of pore fluids (Marshall, 1988). There might be controlling factors of Mn and Fe concentrations of carbonates, and several studies also show that the CL intensity of carbonate minerals could indicate varying factors caused by the water table movement (Marshall, 1988) in the later process of initial carbonate diagenesis. Various factors, including fluid composition, porosity, permeability, pore space shapes, and kinetics of mineral formation or growth rate (Marshall, 1988) would add more complicated variables to trace element concentration and distribution. It is also

concluded that Fe and Mn contents in a solid phase are not influenced by later diffusion processes of Mn after the original mineral formed (Marshall, 1988).

Causes of cathodoluminescence zoning in carbonate rocks may be related to multiple factors of different CL intensity. Although there are several factors that cause some trace elements partition into a crystal as stated above, a general agreement is that its intensity is related to Mn^{2+} as an activator and Fe^{2+} as a quencher in carbonate cement (Boggs, 2006). Several studies done on influences on CL caused by concentration of Mn and Fe as trace elements in carbonate rocks indicate that a divalent Mn ion can increase CL intensity, but show self-quenching effects at higher concentration and a divalent Fe ion acts as a quencher.

Carbonate minerals and cements are less likely to show luminescence if they are formed in shallow marine environment and vadose zones because Mn^{4+} and Fe^{3+} ions would be more prevalent in the oxygenated environment (Boggs, 2006). However, as the pore is filled with water, Mn^{2+} and Fe^{3+} ions are more common in fluids and luminescence would be bright unless Fe^{2+} concentrations are high (Boggs, 2006). CL colors and intensity can be related to fluid characters, including redox conditions of mineralizing fluids.

Previous CL study of Carbonates

The different cathodoluminescence colors can be an indicator of the various trace element amounts possibly implying the formational environment at the time of mineral growth. As similar cases in other carbonates, including calcite and dolomite, Mn and Fe are main elements affecting CL behaviors in smithsonite. Mn of 0.1 wt % has been known as a lower luminescence limit in carbonate minerals (Gillause et al., 2000).

Quantitative CL study of smithsonite by Götte and Richter (2004) indicates CL in smithsonite is caused by Mn and Fe like other carbonates. Cu may have a quenching

effect, but no clear influence of other elements, such as Ca, Pb. In their study, blue luminescence smithsonite (Mn-poor smithsonite) are related to the intrinsic spectra (400 and 510 nm) generally dominated by the 400 nm band, which is influenced by lattice defects and stoichiometry. The pink and red zones show an additional broad band at 660 nm. Mn^{2+} shows the linear relationship with the Mn emission intensities when Mn is below 1000 ppm. However, when there are significant amounts of substituting elements, such as Fe and Cu, in smithsonite, the linear correlation deviates significantly because these elements are also influencing the CL behavior in smithsonite. The observed intensity is lower when concentrations of Mn, Fe, and Cu are exceeding 1000 ppm, 2000 ppm, and 1500 ppm, respectively due to the quenching effects. Bright pink and red colors caused by Mn contents in smithsonite, but self-quenching by an energy transfer between Mn ions occurs when Mn^{2+} concentration exceeds 1000 ppm.

Colloform smithsonite can also exhibit distinct blue CL colors with several zonings and other types of zoned smithsonite show bright red and purple colors under CL (Boni, 2007 and 2009).

PURPOSE

Optical-CL is an excellent tool to image microtextures, growth zonings, and paragenetic relationships that cannot be seen under transmitted-light microscopy. CL study was carried out in order to characterize major Zn minerals and several calcite samples, which could offer additional information to morphologies of smithsonite and its paragenetic relationships. Also, CL studies were expected to provide paragenesis of NSZ minerals and possible formational environment of smithsonite. LA-ICP-MS was used to quantify the distribution of trace elements in smithsonite in order to constrain the trace element distribution in smithsonite and its relationship with the optical-CL response.

METHODS

CL investigations were attempted using Environmental Scanning Electron Microscope-CL. However, detailed and clear zonation patterns in smithsonite and other carbonates in the Sierra Mojada district were more visible in an optical microscope-CL. Detailed analytical methods are shown in Appendix F.

RESULTS

Early calcite samples in limestone show dull orange, orange, bright red luminescence, and non-luminescence. Sauconite and hemimorphite were non-luminescence. Fossil fragments generally showed dull luminescence and microcrystalline calcite showed orange and bright red CL colors (Figure 7.1). Several calcite veins showed dark red color and some fractures were non-luminescence. Late calcite paragenetically followed after Zn-bearing minerals occasionally shows no luminescence. Dolomite shows purple CL color cemented by calcite showing dark blue CL (Figure 7.1).

Smithsonite in the SMj district displays several CL colors from bright pink, red, dull red, violet and blue. Smithsonite samples from the SSM have CL colors ranging from pink to red hues. Smithsonite-A usually show blue luminescence, whereas colloform or massive smithsonite (ss-B) generally shows red and pink luminescence with complex zonation patterns (Figures 7.3F and 7.4A~D). Smithsonite in the matrix (ss-A) is opaque under plan polarized light, but it also displays same blue luminescent color as scalenohedral smithsonite under CL (Figure 7.3B), and also pink or dull luminescence. Hemimorphite is non-luminescent (Figures 7.1A and 7.3E) and sauconite shows no luminescence (Figures 7.2D and 7.3F). In colloform banded smithsonite type (ss-B), dark bands under a polarized microscope correspond to bright pink luminescence areas (Figure 7.3A~D). Dark patches of Mn oxides with Zn clay matrix occasionally are non-

luminescent. Scalenohedral smithsonite (ss-A) always shows blue luminescence either dark or bright blue hues, while colloform, massive smithsonite (ss-B) displays rather complex color patterns, which is not visible under a polarizing microscope.

At least two generations of smithsonite are found in one smithsonite sample from the IOM. Rhombohedral crystals in open pore space show very dull blue luminescence (Figure 7.1D), but the earlier generation of inclusion-rich (or impurity?) smithsonite shows bright red luminescent. In the microprobe analyses of smithsonite (Table 4.1 and Figure 4.9), smithsonite with weak blue luminescence only contains 0.1 wt % of Mn whereas red luminescent smithsonite shows 0.4 wt % of Mn. Fe content is lower in weak blue CL smithsonite. However, it should be noted that data points during microprobe analyses might not exactly match to smithsonite type of these two different luminescent.

The early stage of smithsonite (smithsonite-A), including microcrystals, scalenohedral crystals, matrix smithsonite, shows blue to bright blue luminescence colors without no or less observable CL zonation patterns.

SEMIQUANTITATIVE ELEMENTAL ANALYSIS OF SMITHSONITE

Method

Follow-up trace element analyses using LA-ICP-MS was attempted to constrain luminescent cause based on trace element concentration of smithsonites of selected samples. NIST 610 was chosen for normalization because it contained the highest Zn (456 ± 19 ppm) among the LA-ICP-MS standards available. There are currently no certified smithsonite LA-ICP-MS standards commercially available. However, evaluating quantitative accuracy was unlikely due to the extremely higher concentration of Zn (>1100 Zn) in smithsonite compared to Zn concentration in NIST610. Data in this project

is therefore considered semiquantitatively as trace element intensity ratios with ^{66}Zn . Detailed analytical methods are shown in Appendix F.

Results

The Mn^{55} and Zn^{66} intensity as ratio is plotted in Figure 7.4. In blue luminescence zones, the $\text{Mn}^{55}/\text{Zn}^{66}$ is generally lower than zoned pink to red luminescence zones. Some of bright pink luminescence zones correspond to the higher Mn intensity (represented with blue lines), but locally those bright pink zones does not match with the highest Mn. This might be due to the different composition of these bright pink zones (darker growth zones under plane polarized light in Figure 7.4) consisting smithsonite microcrystals, pores, and minor amounts of calcite. The Fe^{57} , Co^{59} , Rb^{85} , Sr^{88} , Cd^{111} , Ba^{137} were not shown here due to its low signal compared to the Zn^{66} signal. Intensity ratios of Mg^{25} , Ca^{44} , Cu^{63} , and Pb^{208} over Zn^{66} on the same laser line scan as in Figure 7.4 are illustrated in Appendix F. The Pb and Cu signals over the Zn signal appeared to show similar trends along the line scan (Table F2 in Appendix F).

Conclusions

Smithsonite-A showing blue colors without observable CL zonings would indicate that this smithsonite was formed without major variations in trace metal chemistry of ore-forming fluids. It has lower Mn and Fe concentrations compared to smithsonite-B. The late stage smithsonite (smithsonite-B), including colloform or massive smithsonite, displayed complex zonations with varying CL colors presumably due to the concentration changes in Mn. The $\text{Mn}^{55}/\text{Zn}^{66}$ from the LA-ICP-MS line scan revealed that the amount of Mn was mostly correlated with CL colors in smithsonite (Figure 7.4). This variation indicate that there was a change in fluid chemistry after precipitation of smithsonite-A. The Fe signal from the LA-ICP-MS line scan was very

low. Changes in Fe and Cu concentrations are assumed to be related the CL color and intensity, but quantitative analyses of trace elements would be necessary to see how trace elements influence CL in smithsonite.

These changes of trace elements, such as Mn and Fe, could reflect constant changes in redox conditions of groundwater and fluid compositions due to weathering conditions and climate changes, but quantification of these trace elements with C-O isotope measurement in micoroscale would be necessary to find the relationships between trace element chemistry and CL characteristics during smithsonite precipitation if it is related to climate changes.

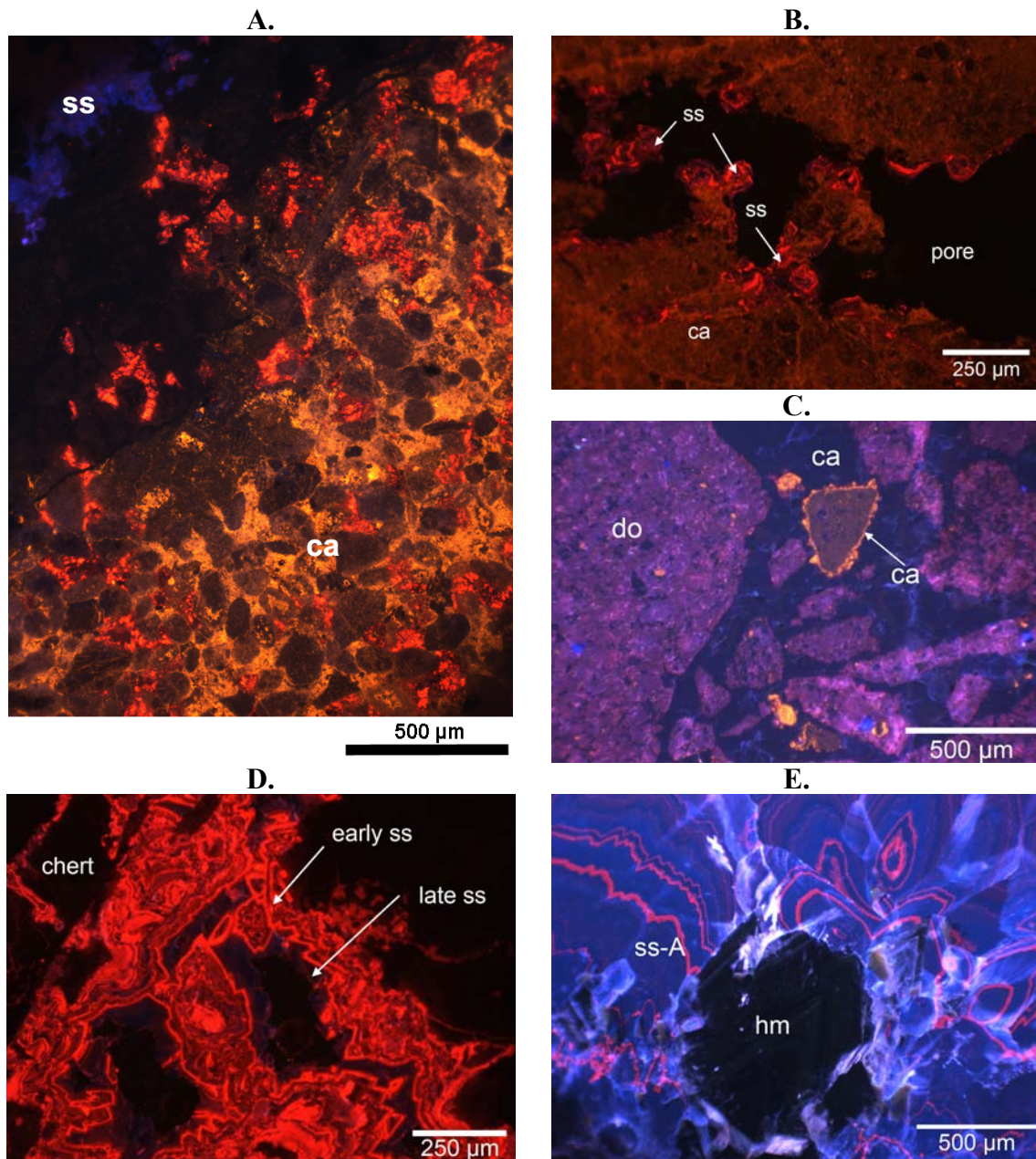


Figure 7.1. CL images of carbonates and hemimorphite.

A. Aurora limestone in contact with smithsonite. CL. Oriented. Sample SM08-13. **B.** Dark red luminescent calcite and smithsonite grown in pore spaces. Sample SS8. **C.** Dolomite and two stages of calcite cement (orange and blue). Sample JLF? **D.** Early red luminescent smithsonite and late pore-filling dull blue luminescent smithsonite. Sample SS8. **E.** Blue luminescent smithsonite-A with pink zonation and non-luminescent hemimorphite. Sample SM08-22.

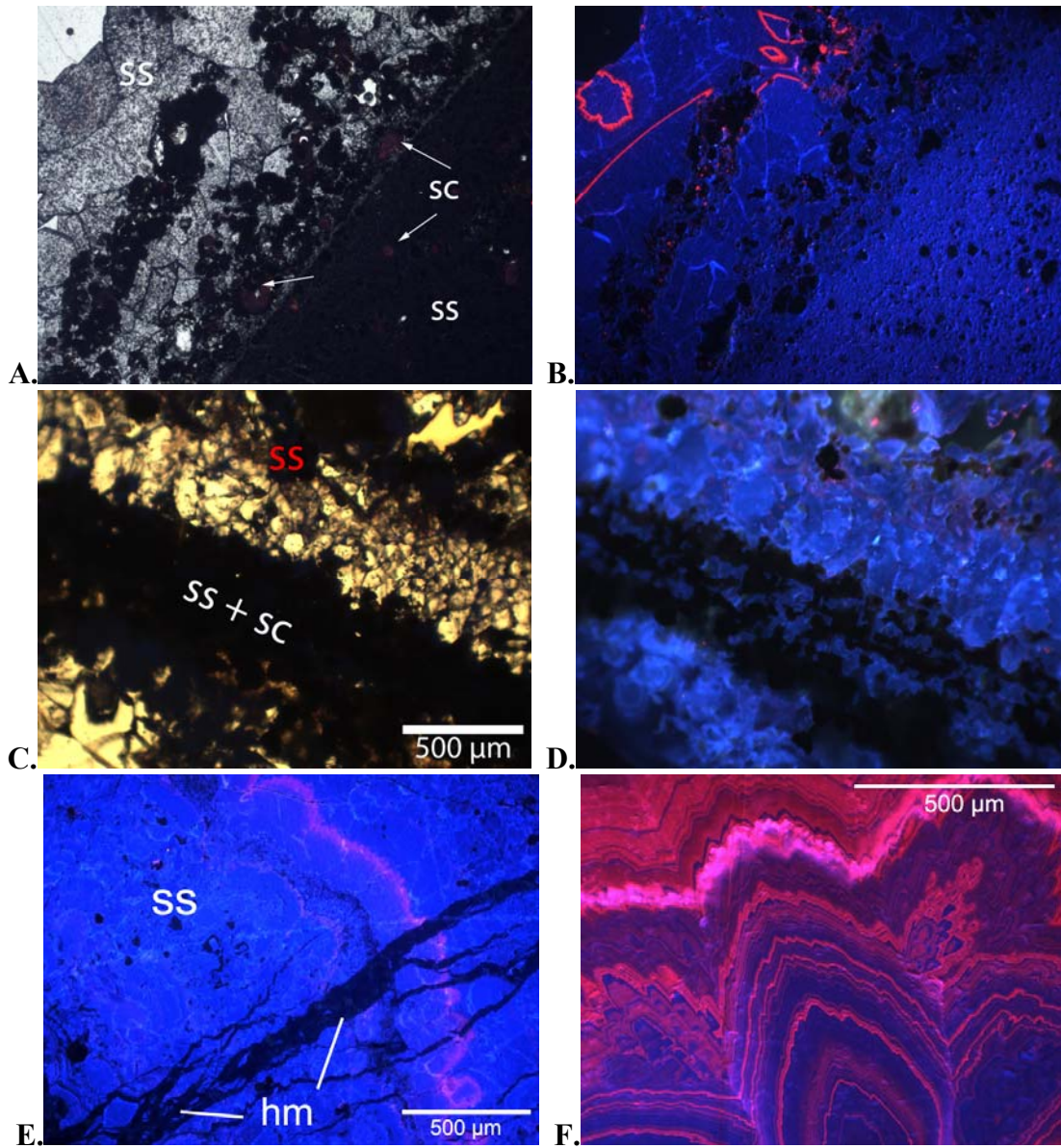


Figure 7.2. CL images of smithsonite.

A. Scalenohedral smithsonite grading into microcrystalline smithsonite with minor sauconite showing blue luminescence. PPL. Sample SM08-23. **B.** A CL image of Figure 5.3A. **C.** Microcrystalline smithsonite and matrix of smithsonite and sauconite. PPL. Sample SM08-22. **D.** A CL image of Figure 5.3C. **E.** Banded smithsonite showing blue luminescence and hemimorphite cross-cutting smithsonite. CL. Sample SM08-26. **F.** Complex zonings in smithsonite-B. CL. Sample SM03-09.

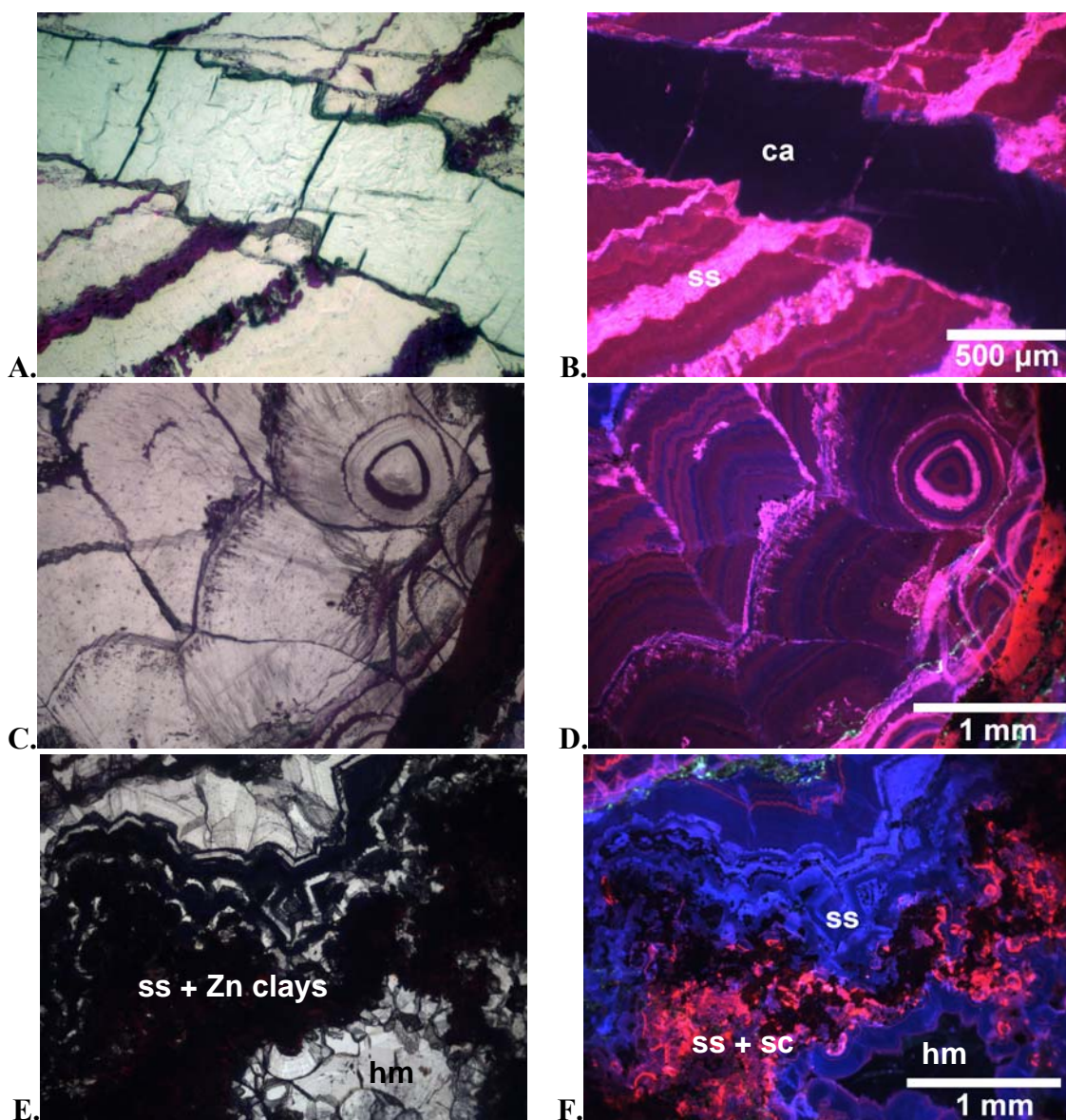


Figure 7.3. CL images of smithsonite, calcite, and hemimorphite.

A. A petrographic image of smithsonite-B. Plane polarized light. Sample SM03-22. **B.** A CL image of A. Nearly non-luminescent late calcite vein cutting smithsonite. Sample SM03-22. **C.** Smithsonite-B. Plane polarized light. Sample SM03-25. **D.** A CL image of same view as C showing complex growth zones. Sample SM03-25. **E.** Smithsonite-A intermixed with Zn clays in the matrix. Plane polarized light. Sample SM03-25. **F.** A same view as E. Smithsonite-A showing blue luminescence and red luminescence in the matrix, and non-luminescent pore-filling hemimorphite. Sample SM03-25.

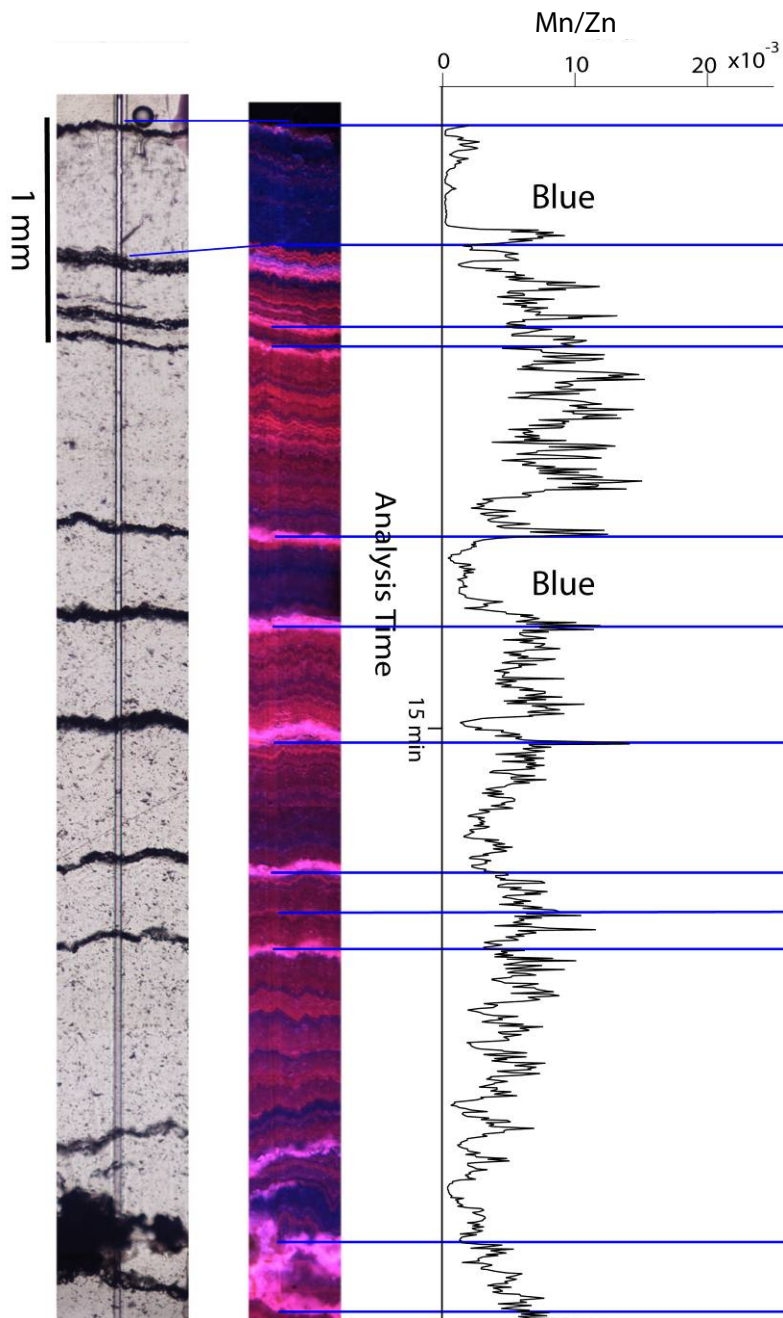


Figure 7.4. A plot of the ratio of the Mn over Zn signals in smithsonite.

The left image taken under polarized light and the right image under CL. The laser ablation linescan can be seen in both images.

Chapter 8. Reconnaissance Fluid Inclusions Studies

METHODS AND PROCEDURES

Petrography and inclusion studies were carried out on five doubly-polished thick (~100 μm) sections. Freezing runs were carried out to obtain fluid composition of primary inclusions and secondary inclusions in hemimorphite. Due to the single character of fluid inclusions, obtaining homogenization temperature was not possible using conventional methods, but single-phase inclusions are generally viewed as indicative of entrapment at low temperature ($<70\text{ }^{\circ}\text{C}$) (Roedder, 1981). There is a new technique that is able to nucleate vapor bubbles in such inclusions by using femtosecond laser pulses (Krüger et al., 2007).

Hemimorphite and calcite samples were selected. Fluid inclusions appear to be well preserved in hemimorphite and late calcite than smithsonite. Only a small number of single phase and two-phase inclusions of primary origin were observed in hemimorphite and calcite. The two-phase liquid-rich inclusions (Figure 8.1) and the more common single-phase aqueous inclusions (Figure 8.2) were cooled as low as $-180\text{ }^{\circ}\text{C}$, and warming and cooling were performed to form vapor bubbles. Slow heating was repeated at least three or four times to observe the final melt temperature. Measuring homogenization temperatures was avoided due to the different vapor and liquid ratio (Roedder, 1984). A few secondary two-phase inclusions were analyzed to see if it was comparable to primary inclusions. Detailed methods with sample description and fluid inclusion data are listed in Appendix G.

The objective of the fluid inclusion study is to determine the composition of fluid inclusions and homogenization temperatures from primary inclusions. Thus, composition of fluid inclusions could provide additional information to the genetic interpretation of

the formation of supergene Zn-bearing minerals at Sierra Mojada. Unfortunately, suitable fluid inclusions for study were not observed in smithsonite.

RESULTS

In some of single-phase inclusions in hemimorphite, bubbles were nucleated after freezing, but most did not form bubbles. Although still uncommon, more fluid inclusions are hosted in hemimorphite and calcite. Primary inclusions were rare, but secondary inclusions were abundant. Secondary fluid inclusions included two-phase (liquid + vapor) inclusions, single-phase (liquid) inclusions, and darker gas-rich inclusions. For this analysis, only the last ice-melting temperatures (T_m) were measured due to the difficulty of observing the eutectic point during freezing. Ice crystals were not observed. Inclusions only showed changes in bubbles during freezing, so the last ice-melting was measured when the bubbles went back to an original shape and location upon heating. During freezing, other types of solids did not form.

Microthermometry data and sample descriptions are shown in Table 8.1. The last ice-melting temperature for one primary two-phase inclusion on hemimorphite indicates salinities of 1.2 wt. % NaCl equivalent (Figure 8.1). Salinities of other primary inclusions range from 0 to 1.6 wt. % NaCl equivalent. Salinities of secondary single-phase inclusions in hemimorphite were between 0 and 6.3 wt. % NaCl equivalent. Two-phase (liquid + vapor) inclusions in calcite, if primary, showed salinities between 0 and 1.1 wt. % NaCl equivalent. Because these two-phase inclusions in both hemimorphite and calcite appeared to be stretched, homogenization temperatures were not measured.

Table 8.1. Sample description and microthermometry data of fluid inclusions.

Abbreviations: L = liquid; V = vapor; P = primary; S = secondary; T_m= the last ice-melting temperature.

Sample	Mineral	Paragenetic position	Location	Type	Size (µm)	T _m (°C)	Salinity (wt %)	Remarks
EN2-1C	hm	pore-fillings	IO manto	L+V	45	- 0.7	1.2	P
EN2-1C1	hm	pore-fillings	IO manto	L	45	0	0	P?
EN2-1C1	hm	pore-fillings	IO manto	L+V	10	0	0	P (stretched)
EN2-1C1	hm	pore-fillings	IO manto	L+V	25	0	0	P (stretched)
EN2-1C1	hm	pore-fillings	IO manto	L	10	0	0	S
EN2-1C1	hm	pore-fillings	IO manto	L	20	0	0	S
EN2-1C1	hm	pore-fillings	IO manto	L	10	0	0	S
EN2-1C1	hm	pore-fillings	IO manto	L	10	- 0.1	0.2	S
EN2-1C2	hm	pore-fillings	IO manto	L	15	0	0	S
SM08-11	ca	later than hm	SS Manto	L+V	10	0	0	P
SM08-22	hm	intergrown with ss	SS Manto	L	25	0	0	P
SM08-22	hm	intergrown with ss	SS Manto	L	10	- 0.4	0.7	P
SM08-22	hm	intergrown with ss	SS Manto	L	10	- 0.5	0.9	P
SM08-22	hm	intergrown with ss	SS Manto	L+V	10	- 0.9	1.6	P
SM08-22	hm	intergrown with ss	SS Manto	L+V	5	- 0.1	0.2	P
SMDD4-B	hm	pore-fillings	IO manto	L	60	- 3.2	5.3	S?
SMDD4-B	hm	pore-fillings	IO manto	L	10	- 3.2	5.3	S?
SMDD4-B	hm	pore-fillings	IO manto	L	30	- 2.8	4.6	S
SMDD4-B	hm	pore-fillings	IO manto	L	25	- 2.8	4.6	S
SMDD4-B	hm	pore-fillings	IO manto	L+V	10	- 3.9	6.3	S
SS11-2	hm	pore-fillings	IO manto	L	20	- 0.1	0.2	P?
SS11-2	hm	pore-fillings	IO manto	L	30	- 0.7	1.2	P?
SS11-2	ca	later than hm	IO manto	L+V	10	- 0.1	0.2	P (stretched)
SS11-2	ca	later than hm	IO manto	L+V	10	- 0.1	0.2	P (stretched)
SS11-2	ca	later than hm	IO manto	L+V	25	- 0.6	1.1	P (stretched)
SS11-2	ca	later than hm	IO manto	L+V	30	- 0.0	0	P (stretched)

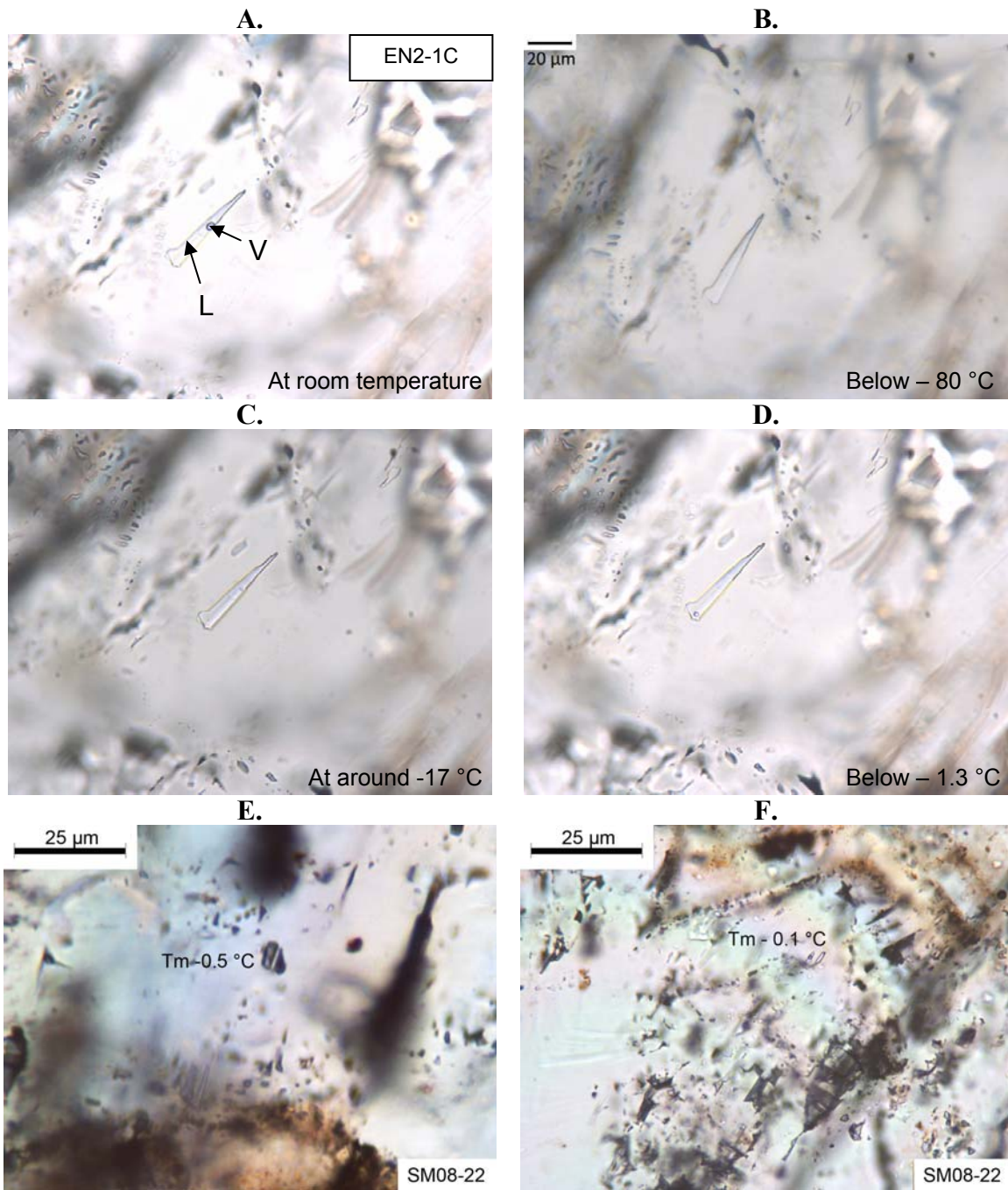


Figure 8.1. Primary inclusions in hemimorphite.

A~D. A two-phase inclusion in hemimorphite showing changes after freezing. E. A single-phase inclusion showing the final-melting temperature at $-0.5\text{ }^{\circ}\text{C}$. F. A two-phase inclusion with the final-melting temperature at $-0.1\text{ }^{\circ}\text{C}$.

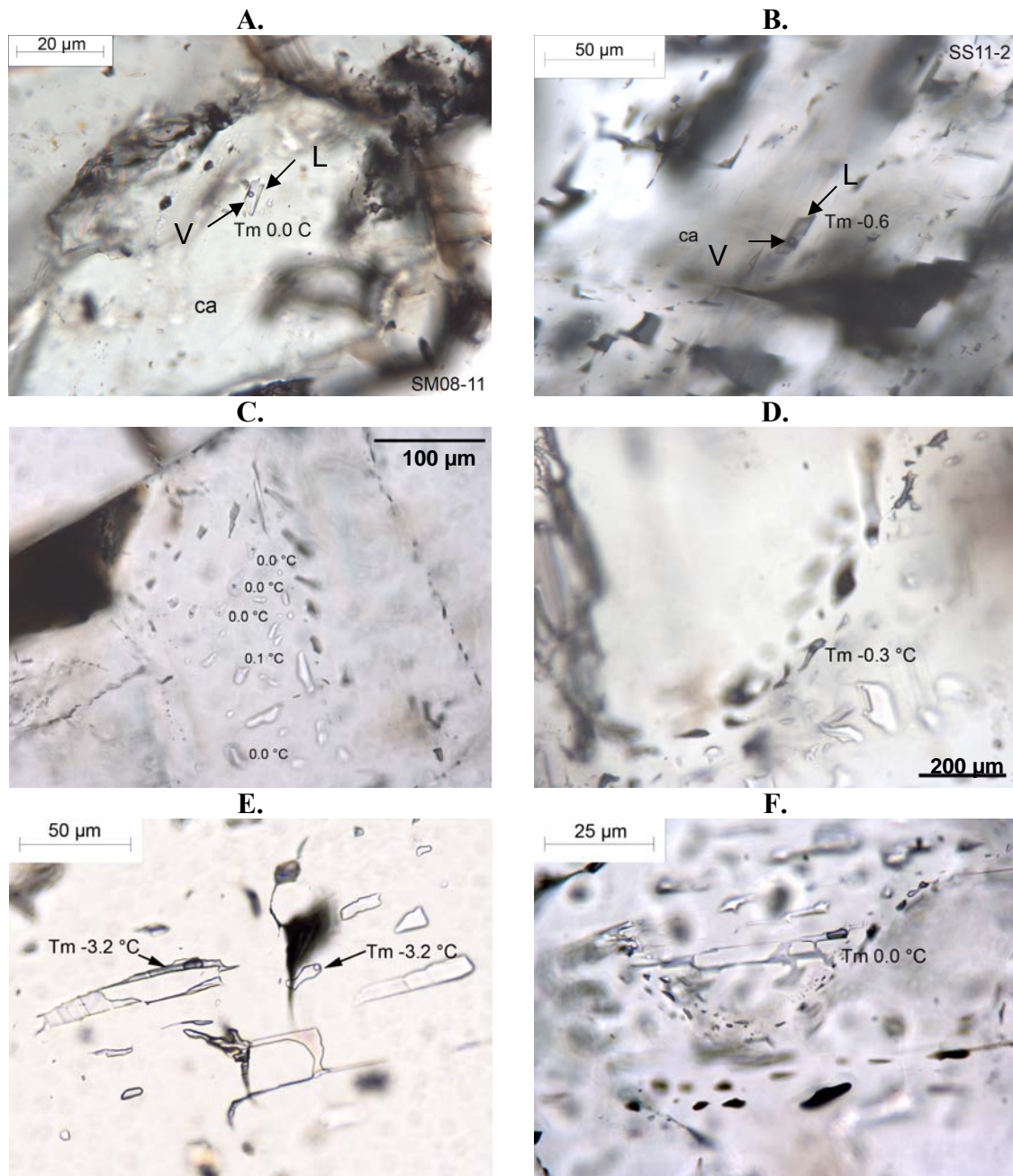


Figure 8.2. Fluid inclusions in calcite and hemimorphite.

A and **B**. Two-phase primary inclusions in late calcite. **C**. (Secondary) aqueous inclusions in hemimorphite, formed bubbles after freezing. Sample ID. EN2-1C. **D**. Two-phase (L+V) secondary inclusions in hemimorphite. Sample ID. EN2-1C. **E** and **F**. Secondary inclusions in hemimorphite. Sample SMDD4-B and EN2-1C1.

Chapter 9. Discussion

PARAGENETIC SEQUENCE

Paragenetic relationships of the non-sulfide Zn minerals and associated minerals were investigated by their textural relationships. The paragenetic sequence for the Smithsonite Manto and for the Iron Oxide Manto is shown in Table 9.1 and the description of thin sections is listed in Appendix B.

Petrographic analyses reveal that smithsonite was first precipitated and grew in pore spaces as scalenohedral crystals in the Smithsonite Manto. Hemimorphite (hemimorphite-A), sauconite, and Mn-oxides locally alternate with early smithsonite in the matrix. However, it is not clear that hemimorphite-A precipitated earlier than smithsonite-A. These minerals might have formed during the early stage of mineralization with smithsonite. Sauconite is abundant as fragmented or laminated with smithsonite and hemimorphite in karst-fills, and occurs as globular forms with smithsonite and hemimorphite. Also, sauconite occurs on smithsonite-A and hemimorphite-B indicating they were altered to sauconite. Sauconite displays various mineral habits, including globular, fibrous, rosette, and massive forms.

Smithsonite-A is characterized by blue luminescence under CL. Later tabular pore-filling hemimorphite-B (up to 800 μm in length) precipitated in open spaces and filled some of fractures crosscutting smithsonite-A, smithsonite-B and sauconite. It appears to happen during the late stage of ore formation. Hemimorphite-B also replaced smithsonite. Calcite occurs on hemimorphite or smithsonite indicating it formed after the major non-sulfide Zn mineralization. Pore-filling hemimorphite crosscuts subhedral barite grains indicating barite precipitated at least before late hemimorphite.

In the Iron Oxide Manto, smithsonite and hemimorphite are hosted in Fe-oxides. Smithsonite is finely intergrown with Fe-oxides indicating it precipitated during the early stage of mineralization. Tabular hemimorphite (1 μm to 3 mm in length) precipitated on Fe-oxides or smithsonite, and it locally filled fractures crosscutting smithsonite and Fe-oxides, and barite. Pb minerals (Pb oxides and Pb carbonates) were found on hemimorphite, but it was rare. Calcite cement appears to precipitate after NSZ mineralization and is commonly associated with hemimorphite. Mn-oxides occur in minor amounts showing colloform mineral habits. Barite is found with Fe-oxides or fracture-filling smithsonite as anhedral crystals, but euhedral barite also occurs on oxidized limestone.

Takahashi (1960) explained why hemimorphite is not often observed as the earliest supergene Zn mineral in three ways: the buffering capacity of limestone would not decrease pH less than 6.2; the Zn sulfate concentration may be so low that a pH less than 6.2 is unlikely when ground water circulates well; hemimorphite is soluble in strongly acidic fluids (pH = 3). In most natural waters with a pH between 6 and 8, smithsonite is more stable than hemimorphite; thus, the early formation and abundance of smithsonite in most secondary Zn deposits (Takahashi, 1960).

MINERALIZING FLUIDS AND SOURCE OF METALS

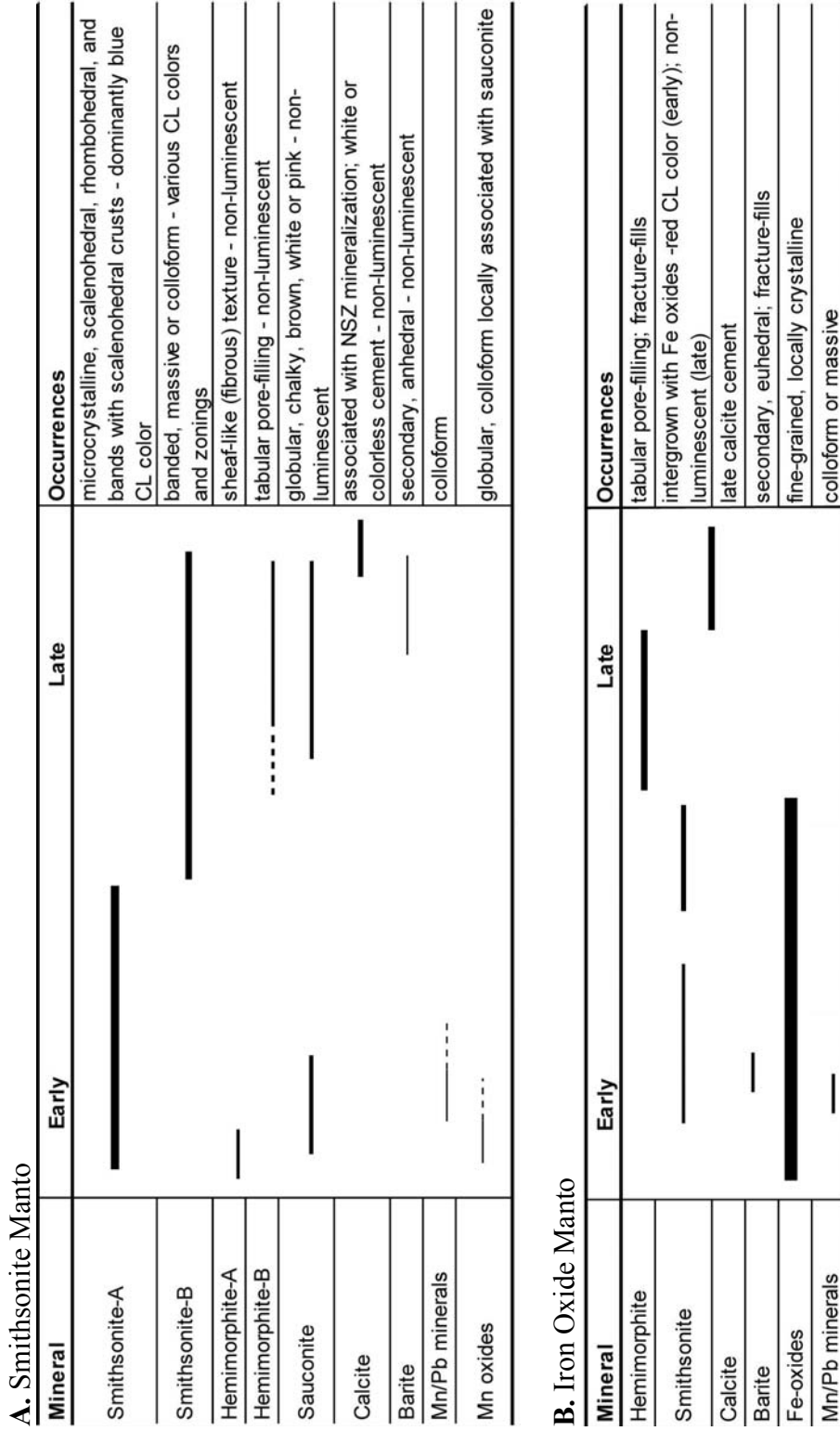
Meteoric waters appear to be responsible for precipitation of NSZ minerals in an evolving karst system at Sierra Mojada. The oxygen isotope values of smithsonite at Sierra Mojada is slightly lower than most supergene smithsonites (Figure 5.4) suggesting that the formational temperature for Sierra Mojada smithsonite could be as high as 35 °C. These somewhat elevated ground water temperatures could be related to the regional tectonic structure of northern Mexico with the active extensional basin possibly providing

the heat to the region. Lower temperatures were calculated for late calcite associated with smithsonite and hemimorphite, which may indicate temperature changes after NSZ mineralization.

Presumably, NSZ mineralization at Sierra Mojada might be related to precipitation of Zn from warm groundwater that might have transported a significant amount of Zn derived from the oxidation of primary sulfide deposits. Preliminary fluid inclusion studies of hemimorphite and calcite provide supporting evidence for low temperature aqueous solutions with salinities less than 2 wt. % NaCl equivalent.

The similarity of the Pb isotope composition of smithsonite to that of galena samples suggests that the sulfide deposits of the Sierra Mojada may have been the source of metals in NSZ mineralization.

Figure 9.1. Paragenetic sequence of NSZ minerals and other common minerals.



Chapter 10. Conclusions

The Sierra Mojada NSZ mineralization is considered to be the result of Zn mobilization by groundwater and precipitation in an evolving karst system in Cretaceous carbonates. Smithsonite and hemimorphite commonly occur as euhedral crystals, which have grown in open spaces, such as secondary pores, vugs, and fractures. Karst features include internal sediments and cavity-fills. In the Smithsonite Manto, the major NSZ minerals include smithsonite, hemimorphite, and sauconite associated with Mn and Fe oxides, barite, and calcite. Hemimorphite and smithsonite associated with Fe-oxides are main NSZ minerals in the Iron Oxide Manto. Smithsonite occurs in four major morphological forms, but the relationship between textural types of smithsonite and its elemental composition is unclear. Smithsonite displays complex CL zonings. The presence of Mn/Fe oxides with smithsonite and hemimorphite may indicate that Sierra Mojada NSZ minerals were precipitated under oxidizing conditions.

The oxygen isotope composition of smithsonite is relatively constant, but lower than most supergene smithsonites. The estimated temperature for smithsonite precipitation is about 35 °C and lower temperature (~20 °C) for late calcite have been calculated. Slightly deeply circulating meteoric water appears to be a possible reason for higher formational temperature for smithsonite than other supergene smithsonites. Alternatively, increased temperatures could be due to exothermic oxidation reactions in the vadose zone. The earlier generation of smithsonite-A show relatively heavier carbon isotope values, and the later generation of smithsonite-B varies from -1.9 to -8.4‰. Carbon isotope values for calcite were lighter than most smithsonite values. It may indicate that ¹³C-enriched sources, such as carbonate wall rocks, were more involved in smithsonite precipitation.

The characteristics of fluid inclusions in hemimorphite and calcite are compatible with the formation of the NSZ deposits at Sierra Mojada from low temperature groundwater. The Pb isotopic signatures suggest that the metals in NSZ deposits may be sourced from the sulfide deposits in the district.

As the timing of the NSZ mineralization at Sierra Mojada is uncertain, important studies are in progress to obtain age information by using radiogenic isotopes, such as $^{40}\text{Ar}/^{39}\text{Ar}$ on K-bearing Mn minerals.

Appendix A: Sample Description

28 samples were collected from underground exposures of the Smithsonite Manto and 20 samples were collected from underground exposures of the Iron Oxide Manto in 2008. Six samples, SMj03-20, SMj03-21, SMj03-22, SMj03-25, and SMj03-27 were collected from the Smithsonite Manto by Dr. J. Richard Kyle in 2003. Drill core samples, SM-DD4, SM-DD5, SM08-1, SM08-2, D26-25.5, and D26-26.3 were provided by the Metalline Company. Abbreviations used in Appendix A can be seen in Table 2.1. Sample descriptions are shown in Table A1 and Table A2.

Table A1. Samples collected from the Smithsonite Manto.

Sample ID	Formation	Rock Type	Description
SM03-03	Aurora	smithsonite ore	white botryoidal ss on orange Mn oxides
SM03-20	Aurora	smithsonite ore	white colloform ss
SM03-21	Aurora	smithsonite ore	2-cm colloform banded ss with Mn-Fe oxides
SM03-22	Aurora	smithsonite ore	3-cm banded ss; locally fracture filling calcite cross-cutting ss; fragmented Fe-rich dolostone cemented by ss
SM03-25	Aurora	smithsonite ore	banded white ss with Mn dendrites on red clay-looking materials
SM03-27	Aurora	smithsonite ore	zoned pale green ss alternating with white chalky ss on vuggy grey dolostone; botryoidal ss growing on vugs
SM08-01	Aurora	Fossiliferous limestone (mudstone)	Unmineralized limestone contact with mineralized banded ss and hm; late ca covering hm
SM08-02	Aurora	banded smithsonite	vertically banded porous dolostone with ss, hm and sc
SM08-03	Aurora	fossiliferous limestone (coral-bivalves mudstone)	bivalves and corals; microcrystalline ca
SM08-04	Aurora	smithsonite ore	zoned white botryoidal crust of smithsonite (~2cm) with colloform banding on porous matrix with Mn and Fe oxides
SM08-05	Aurora	smithsonite ore	Botryoidal ss with dendrites of Mn oxides; locally hm near the ss crust
SM08-06	Aurora	smithsonite ore	coarse zoned ivory white ss with hm near the matrix of sc and other Zn clays
SM08-08	Aurora	smithsonite ore	pale gray and pale red coarse zoned smithsonite
SM08-09	Aurora		3 cm of late ca
SM08-10	Aurora	smithsonite ore	pale purple colloform ss in vug
SM08-11	Aurora	brecciated sedimentary materials	brecciated materials with size of less than 1 mm to 2 cm; hm on open space in the matrix of fine-grained, reddish brown, Mn-oxides and Clay-rich sediments; various size of late-stage ca (as cement and as open-space growing calcite)
SM08-11B	Aurora	brecciated sedimentary materials	brecciated materials (Iron oxides) with hm and ca filling open space between breccias
SM08-12	Aurora	calcite	ca speleothem with laminated internal sediments; ca on the matrix of sedimentary materials
SM08-13	Aurora	fossiliferous limestone (coral-bivalves wackestone)	bivalves and corals; brown or black hydrocarbon residue usually associated with other carbonates (dol)

Sample ID	Formation	Rock Type	Description
SM08-14	Aurora	smithsonite ore, cave-fills	laminated and porous ss and sc at contact
SM08-15	Aurora	sediments of red zone	fine brown colored sediments
SM08-16	Aurora	smithsonite ore, cave-fills	laminated ss and sc
SM08-17	Aurora	smithsonite ore, cave-fills	laminated sc and ss (hemimorphite)
SM08-18	Aurora	smithsonite ore, cave-fills	botryoidal ss in vugs
SM08-19	Aurora	smithsonite ore, cave-fills	banded ss and sc
SM08-21	Aurora	internal sediments	detrital, internal sediments; fine brown colored sediments
SM08-22	Aurora	smithsonite ore, cave-fills	botryoidal ss in vugs with banded ss and hm; sc in the matrix
SM08-23	Aurora	smithsonite ore, cave-fills	banded ss
SM08-24	Aurora	smithsonite ore, cave-fills	banded ss with 2 cm pendulous white ss
SM08-25	Aurora	sediments	clay and Mn oxide-rich sediments
SM08-26	Aurora		(vertical) banded ss, hm, and sauconite infilling sediments, including Mn oxides
SM08-27	Aurora	cave-fill, sediments	sediments with Mn oxides, Zn clays, and hm
SM08-28	Aurora	cave-fill	laminated cave-fill; brecciated materials (size: <1mm-5mm) and pore-filling hemimorphite
SM08-29	Aurora	sediments	laminated sediments with ss
SM08-30	Aurora	hemimorphite	white hm crystals (1~1.5 cm); hm and sc in the matrix

Table A2. . Samples collected from the Iron Oxide Manto.

Sample ID	Formation	Rock Type	Description
EN1-2	Aurora	Fe-oxides	vuggy goethitic/jarpsotoc Fe-oxides; hemimorphite partially filled pore space; blocky and thin platy calcite crystals (1mm-3mm) coated over hemimorphite in open space
EN1-3	Aurora	Fe-oxides	vuggy goethitic/jarpsotoc Fe-oxides; hemimorphite partially filled pore space; blocky and thin platy calcite crystals (1mm-3mm) coated over hemimorphite in open space
EN1-4	Aurora	Fe-oxides	
EN1-5	Aurora	Fe-oxides	hemimorphite with vuggy hematitic Fe-oxides; locally globular-shaped smithsonite
EN2-1C	Aurora	Fe-oxides	hemimorphite (3 mm) grown on open space
SS3-E	Aurora	Fe-oxides	Iron oxide dolostone; fossil remains
SS3-20	Aurora	Fe-oxides	
SS4	Aurora	Fe-oxides	hemimorphite (1mm-2mm) filling open space; locally calcite coated over hemimorphite
SS4-1	Aurora	Fe-oxides	vuggy dark red dolostone; hemimorphite grown along vugs
SS4-3	Aurora	Fe-oxides	hemimorphite in pore space
SS4-4	Aurora	Fe-oxides	hemimorphite and calcite filling open space as layers
SS8	Aurora	Fe-oxides	matrix of orange color calcite and several calcite veins (<1 mm) in oxidized carbonates
DS A2	Aurora	Fe-oxides	
Drill base A	Aurora	Fe-oxides	thin flat platy calcite coatings; hemimorphite mineralization along layers
SS4th L	Aurora	Fe-oxides	Reddish oxidized carbonates
SS4th level DS2	Aurora	Fe-oxides	less tabular hemimorphite with bladed calcite coatings
SS11	Aurora	Fe-oxides	
SS11-1	Aurora	Fe-oxides	vuggy, Fe-oxide (dark red) dolostone; two stages of hemimorphite formation
SS11-1DS	Aurora	Fe-oxides	hemimorphite in Fe dolostone with bladed calcite coatings over hemimorphite

Appendix B. Petrography

Thin sections were made from most Zn-bearing rocks in the Smithsonite Manto and the Iron Oxide Manto. Transmitted-light microscope petrography was carried out on petrographic thin sections and polished thin sections. 43 thin sections from the Smithsonite Manto samples and 21 thin sections from the Iron Oxide samples were included. Table B1 includes identified minerals, volume percentages, and descriptions for samples from the Smithsonite Manto, and Table B2 contains petrographic observation of the thin sections from the Iron Oxide Manto and dolomite samples from the Dolomita Quarry location.

Table B1. Thin section petrography of the Smithosnite Manto.
Shown as a volume percentage of each mineral and descriptions

Sample ID	ss	hm	sc	ca	ba	do	Mn-ox	Fe-ox	qz	sl	Mn/Pb minerals	Note
SMj03-20	90>		<5									colloform ss; locally ss altered to Zn clays ; Mn oxides dendrites
SMj03-21	70	5~10	10		<5		<5	<5			<3	mostly banded ss; colloform Zn clay (sauconite)+ Fe oxides (early); hm on crusts of ss; subhedral ba (late stage); colloform Mn/Pb minerals; goethite grains
SMj03-22	70	10	<5	20	<2		5					colloform ss with Mn oxides; 1 mm calcite vein cutting non-sulfide Zn minerals (hm and ss); late-stage fracture-filling hm in ss; hm and ca alternating with ss
SMj03-25	80	5~10			<1		<5			<1 ?	<5	colloform banded ss with Fe-oxides; pores filled with ss and later by hm
SMj03-27	60	<10	20	<1	5		~10					late ca and ba, pore-filling hm in banded ss (some pore is completely filled with hm); ss with globular Zn/Mn clays
SM03-08	65	15	<15	<5								laminated (layered) ss and sheaflike hm found in the matrix with Zn clays (sauconite); yellowish brown hm (in ppl view) rim on matrix ss
SM03-09	>85		15									thick banded ss (about 1 mm in thickness) and the matrix of ss and sc; yellowish brown hm (in ppl view) rim on matrix ss
SM08-01		<5	<5	85	<5							early stage ca and late blocky ca cement partially filling vugs; tabular hm along fracture and some of them was altered Zn clays; early barite
SM08-01_1		<5	<5	<90	<1							several ca veins and late stage ca
SM08-02	85	<5	10									mostly microcrystalline matrix ss where sc is abundant; rhombohedral/scalenoedral ss along pore space; tabular hm partially grown on pore space

Sample ID	ss	hm	sc	ca	ba	do	Mn-ox	Fe-ox	qz	sl	Mn/Pb minerals	Note
SM08-03				90			10					bivalves, corals, skeletal fragments; several generations of calcite veins (10-100 μm); hydrocarbon residues?
SM08-04 (XB03)	80	<10					<5					Euhedral (tabular) hm showing fan-shaped aggregates and massive colloform ss; locally showing rhombohedral cleavages; ss and hm layers near the crust
SM08-05 (XB01)	75	10		5			<5					hm grown along certain layers of ss and euhedral hm and late ca on outer layer of smithsonite; sc occurring in a ss layer; ss appearing to be grown on Mn-oxides and colloform hm
SM08-06	85	10	5									fan-shaped hm occurring with sauconite and fracture-filling hm; colloform ss near hm and sc; secondary pore in ss masses
SM08-08 (XB02)	80	10										columnar smithsonite; hm only in certain layers of smithsonite; Mn oxides
SM08-09b				90								clear and inclusion-rich sparry calcite
SM08-10				>90								secondary calcite
SM08-11		10	20	40	<5		<10	<10			5	tabular pore-lining hemimorphite cemented by zoned calcite cement
SM08-11A		10	20	50			<10	<10				zoned calcite
SM08-11B		15		45				40				sparry ca cement, some inclusion-rich; tabular pore-filling (completely or partially) hm locally corroded by Mn/Fe oxides and Zn clays
SM08-13		<1	<1	90			10					mostly calcite; several generations of ca veins; bivalves, corals, echinoderms fossil fragments;
SM08-14 (ps)	80	15	5									sheaflike hm replacing ss; tabular pore-filling hemimorphite over the pore-filling ss
SM08-16	45	<10	40	5								zoned scalenohedral smithsonite alternating with Zn clays; a few grains of hm and late-stage calcite cement (common at the up (oriented))

Sample ID	ss	hm	sc	ca	ba	do	Mn-ox	Fe-ox	qz	sl	Mn/Pb minerals	Note
SM08-17	85	5	5	3								microcrystalline ss with sauconite in the matrix; scalenohedral smithsonite (up to 50 µm) grown on them; some pores partially filled or some completely filled
SM08-18A	80	<10	10									microcrystalline ss with sauconite in the matrix; scalenohedral smithsonite grown on them; fracture-filling hemimorphite; scalenohedral ss in vugs
SM08-18-1	80	<5	10	10								0.5mm length smithsonite grown on open space; some smithsonite altered to sauconite; rather anhedral smithsonite
SM08-18-2		<10	15									Rhomohedral smithsonite (4 mm); microcrystalline (anhedral) smithsonite; hemimorphite locally crosscutting or replacing smithsonite
SM08-18B	80	10	10									
SM08-19		20	10	15~20								pore-filling subhedral hemimorphite associated with microcrystalline ss; smithsonite fracture-filling hm; scalenohedral ss in pore space; Zn clays altering hm and ss
SM08-21			50		1		10~15					globular Mn/Zn/Fe clays and oxides; mostly Zn clays, some of them high in Mn content; euhedral smithsonite in pore space; no hemimorphite; barite (10-100 µm)
SM08-22 b	60		30									
SM08-22-1(A)	85	5	~10									2~3mm smithsonite layer; hemimorphite locally cross-cutting smithsonite or sheaflike hm replacing ss; tabular hm on ss; scalenohedral ss in pores and microcrystalline ss in matrix with Zn clays
SM08-22-2 (B)	85	~10		5								ss layer 5 mm; microcrystalline ss in the matrix with Zn clays; hm cutting ss along certain boundaries of ss layer or sheaflike hm replacing ss

Sample ID	ss	hm	sc	ca	ba	do	Mn-ox	Fe-ox	qz	sl	Mn/Pb minerals	Note
SM08-23	90		10						<1			5 mm ss layer; (1cm*0.3mm) brown blocks of the matrix of Zn clays and ss; subhedral ss grains; elongated ss on brown blocks
SM08-25			20				30					globular Zn clays and Mn oxides mixture (>90%)
SM08-26-1		35~40	15	10								late stage calcite; 5 mm ss layer; sheaflike hm locally replacing ss and hm replacing ss along certain boundaries of ss crystals; hm in fracture of ss; ca rombs showing zonations; na earlier than hm
SM08-26-2	55	35	5	5								slightly banded smithsonite; hm locally replacing or cross-cutting ss
SM08-26-3	45	20	15	5	<5		<5		<1			banded ss layer (4mm); hemimorphite locally cross-cutting ss
SM08-26	40	45	10									scalen-ss, fracture-filling hm replacing ss; pore-filling hm
SM08-27		~5	~10				70					subhedral to anhedral hemimorphite, Zn clays abundant; colloform Mn-oxides and Zn clays; altered hm intermixed with Zn clays and Mn/Fe oxides
SM08-28A		40	40~50				~20					(oriented) sc-rich layer and altered hm at the top of the thin section; anhedral and sheaflike hm occurring in the middle layer; tabular hm abundant at the bottom
SM08-28B		~40	40									(oriented) fine-grained hm with sc at the upper part of the thin section; tabular pore-filling hm (locally pore-lining); smaller and less tabular hm toward the bottom of the thin section
SM08-30	20	>60	>10									bladed (Tabular) hemimorphite (1~1.5 mm) on the matrix of Zn clays

Table B2. Thin section petrography of the Iron Oxide Manto.
Shown as a volume percentage of each mineral and descriptions

Sample ID	ss	hm	sc	ca	ba	do	Mn-oxides	Fe oxides	qz	Mn/Pb minerals	ag	Note
EN1-2	5	15		5	0	0	5	70				tabular hm (1~ 4 mm) in Fe oxides; Fe-oxides showing concentric features; hm appears to be corroded and locally replaced by Fe-oxides; ca cement filling pore space
EN1-3	10	10			5			75				elongated hm crystals locally corroded by Fe-oxides; host rocks replaced by ss occurring with Fe-ox
EN1-4		40		5				55				tabular hm (1~ 4 mm) with late-stage ca
EN1-5	10	10						80				Subhedral to anhedral hemimorphite locally corroded by Fe-oxides
EN2-1C		10						85				elongated thin hemimorphite crystals (2-4 mm) on Fe-oxides
SM-DD4		10		10				80				pore-filling hemimorphite later cemented almost completely by calcite and locally replaced by Fe-oxides; anhedral to subhedral hemimorphite rim along Fe-oxides and calcite cement
SM-DD4-A		10		10				75				hm(subhedral) rim on Fe-oxides; late calcite over hm
SM-DD4-B		10		10				75				hm(subhedral) rim on Fe-oxides; late calcite over hm
SM-DD4-C		10		10				75				hm(subhedral) rim on Fe-oxides; late calcite over hm
SM-DD4-D		5						85				
SM-DD5		10						85				
SS4		10						80				Fe-oxides showing rhombic features;
SS4-1		10		5		5		85			1	Dark red Fe oxides and hemimorphite (~100 μm) occurring locally in pore space; colloform Mn minerals (~100 μm); Fe-oxide matrix showing concentric, colloform, rhombic, and hexagonal features ; argentite inclusions in hemimorphite grain;
SS4-3		10			5			80				hemimorphite corroded and replaced by Fe-oxides
SS4-4		10		10				80	0	0	0	
SS4th		0		5				85	0	0	1	

Sample ID	ss	hm	sc	ca	ba	do	Mn-oxides	Fe oxides	qz	Mn/Pb minerals	ag	Note
SS8	24	8		30	5	0	5	20	5	3		ss replacing carbonates; precipitating along angular chert breccias; sparsely fossiliferous calcite micrite consisting of fine-grained skeletal particles and pore-filling ss and hm
SS11-1		15		0				85				subhedral hemimorphite locally replaced by Fe-oxides
SS11-1B		15		0				85				
SS11-2		10		10				80				sparry calcite cement s and euhedral hemimorphite in Fe-oxides
SS11-2 DS (ps)		15		2				80				sparry calcite; hemimorphite (100-500 μm) filling open space, locally replaced by Fe-oxides; pore-filling hemimorphite (~1mm) locally replaced by Fe-oxides; small fractures (100 μm) filled by hemimorphite and calcite

Appendix C. SEM-EDS Analyses

Analytical Techniques

In order to characterize non-sulfide Zn minerals in the Smithsonite and Iron Oxide Manto, SEI (Secondary Electron Imaging), and BEI (Backscattered Electron Imaging) were carried out using Scanning Electron Microscope (JEOL JSM-6490 LV) and mineral identification were aided by the EDS (Energy Dispersive Spectroscopy) detector in the Jackson School of Geosciences, Department of Geological Sciences at the University of Texas at Austin. An Accelerating voltage and spot size were adjusted depending on materials of interest. Samples from the Iron Oxide Manto and the Smithsonite Manto were included and sulfides samples as well. List of samples and identified minerals are listed in Table C1 and C2. Table C3 contains descriptions about smithsonite and hemimorphite morphologies. Table C4 includes typical EDS spectra acquired during EDS analyses. Minerals included are smithsonite, hemimorphite, sauconite, Fe-oxides, Mn-oxides, barite, calcite, dolomite, and Mn/Pb minerals.

Table C1. List of samples and identified minerals using SEM/EDS.

Sample ID	ss	hm	sc	Fe-ox	Mn-ox	Pb/Mn min	ba	ca	do	qz
SM03-03	o				o					
SM03-08	o		o							
SM03-20	o	o	o		o					
SM03-21	o									
SM03-22	o									
SM03-25	o									
SM08-27	o	o	o	o	o					
SM08-01	o	o	o		o		o	o		
SM08-02	o	o	o					o		
SM08-03	o	o						o		
SM08-04	o	o	o							
SM08-13	o	o	o							
SM08-15		o	o		o					
M08-16	o		o							
SM08-18	o	o	o	o	o		o	o		
SM08-19	o	o	o	o	o			o		
SM08-20			o		o					
SM08-22	o	o	o							
SM08-23	o	o	o					o		o
SM08-26		o	o				o			o
SM08-26-3	o	o	o			o	o	o	o	
SM08-27			o			o		o		

Table C2. List of the Iron Manto samples and sulfide samples and identified minerals using SEM.

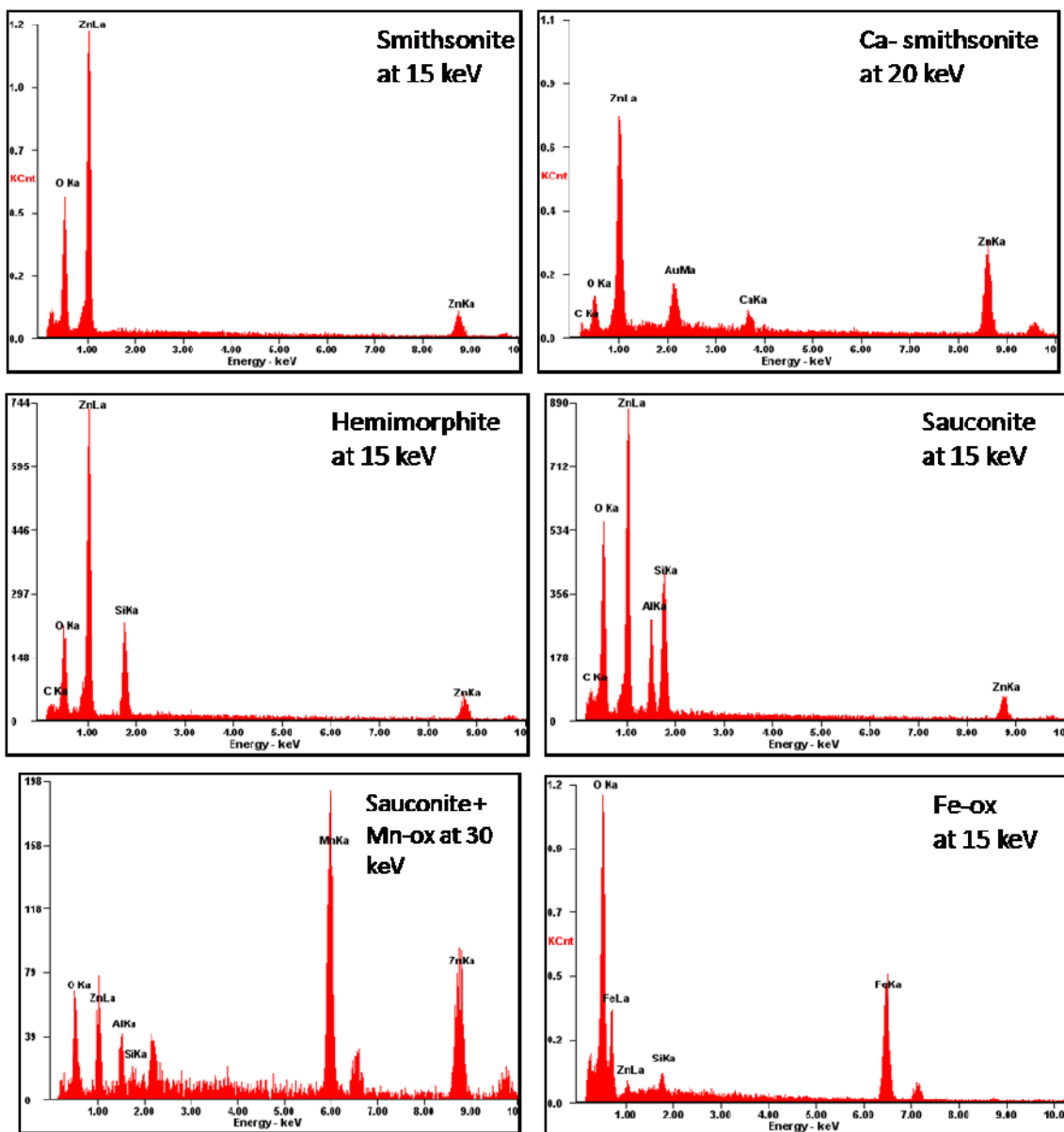
Sample ID	ss	hm	sc	Fe-ox	Mn-ox	Pb/Mn min.	ba	ca	do	qz	ga	ce	an	sl	py	tn	as
EN1-4		o		o													
EN1-5	o	o		o													
SS4-4		o						o									
SS8	o			o		o	o	o									
SS11		o		o								o					
SS11-1DS		o		o				o				o					
SMj-DD1				o													
JLF								o	o								
D26-25.5										o	o		o	o			o
D26-26.3									o	o	o		o	o	o	o	o
SM08-1		o		o							o	o					o
SM08-2				o					o		o						
SMj-PbC1									o		o						

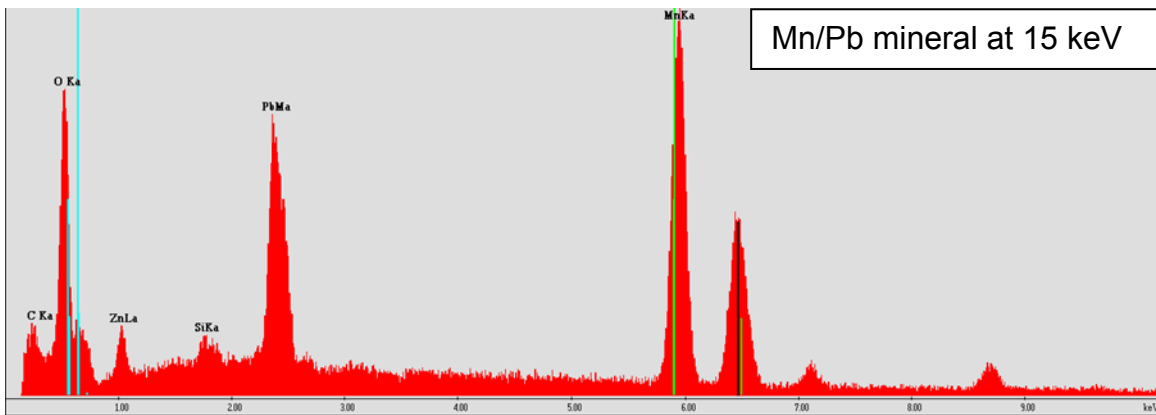
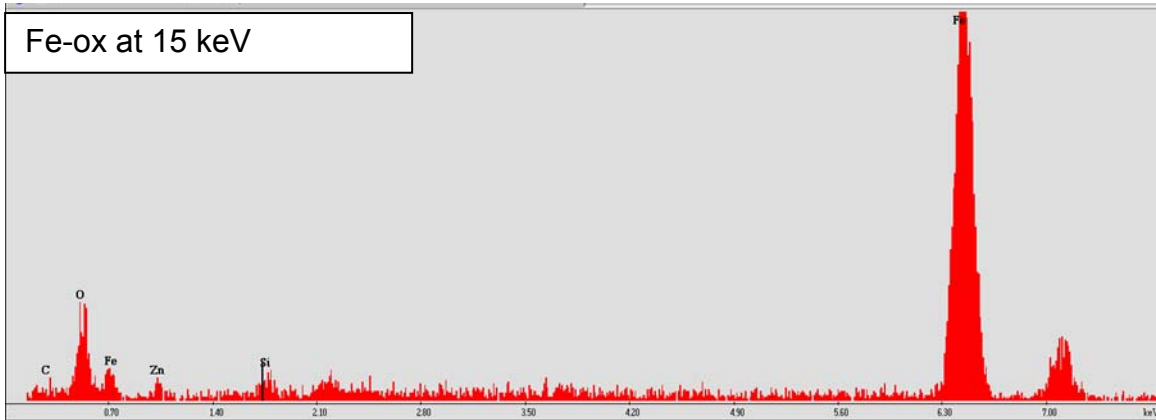
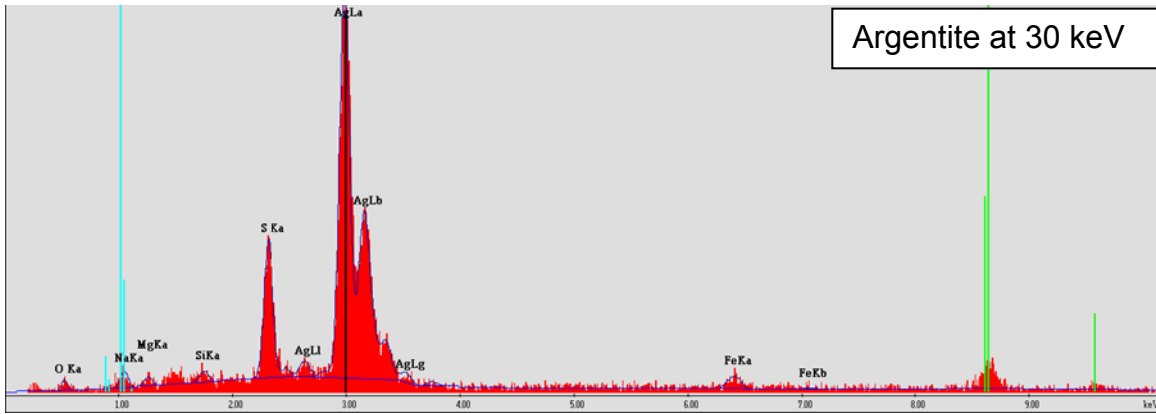
Table C3. Description of smithsonite and hemimorphite morphologies.

Sample ID	Smithsonite	Hemimorphite
SM03-08	elongated scalenohedral (100 - 200 μm); scalenohedral aggregates containing scalenohedral microcrystals (200 - 400 μm)	
SM08-01	aggregates of scalenohedral crystals (150 ~ 300 μm) ; small grains of rounded scalenohedral crystals (50 μm)	tabular hemimorphite (100 μm -250 μm ; sometimes 900 μm)
SM08-02	aggregates of scalenohedral smithsonite forming flower-like features (200 μm) on zoned smithsonite	tabular hemimorphite (250 μm -300 μm)
SM08-03	massive smithsonite with rhombohedral calcite	tabular hemimorphite (250 μm -300 μm)
SM08-04	globular aggregates of rhombohedral smithsonite (100 μm) showing cleavage faces	tabular hemimorphite (300 μm -400 μm)
SM08-06	botryoidal smithsonite showing massive (microcrystalline) surface; smithsonite included within botryoidal smithsonite showing distinct cubic cleavage faces	
SM08-13	aggregates of rounded scalenohedral crystals (200 μm)	tabular hemimorphite (200 μm -300 μm) with clays (sauconite)
SM08-16	aggregates of scalenohedral smithsonite displaying distinct cleavage faces, showing zonation (200 - 400 μm)	
SM08-18	distinct scalenohedral smithsonite (100 - 200 μm) in aggregates	Irregular shapes of hemimorphite with sauconite; massive hemimorphite
SM08-19	distinct rhombohedral smithsonite showing flower-like features (100 - 200 μm)(radiating?); elongated scalenohedral smithsonite with sauconite; massive;	tabular (500 μm) locally altered to sauconite; massive, partially altered to sauconite (abundant);
SM08-22	distinct scalenohedral smithsonite (200 - 400 μm); massive; rhombic (up to 50 μm)	tabular (200 -800 μm)
SM08-23	less distinct (rounded) scalenohedral smithsonite (50 - 100 μm in diameter)	
SM08-26	massive	tabular (200 -400 μm) with sauconite
SM08-28		tabular (100 -800 μm) locally altered to sauconite
EN1-4		elongated tabular hm locally corroded by Fe oxides
EN1-5	globular smithsonite of platy smithsonite microcrystals growing on Fe-oxides and displaying clear rhomb cleavage faces at the surface (type IV)	elongated tabular shape (as large as 3 mm) covering smithsonite; microcrystalline hemimorphite (~ 1 μm); elongated 400-500 μm
SS4-3		elongated tabular hm locally corroded by Fe oxides(niddle-like less than 1 μm); hemimorphite (~200 μm);
SS4-4		anhedral hemimorphite locally replaced by Fe-oxides

Sample ID	Smithsonite	Hemimorphite
SS11		Fe-oxides locally corroding or replacing hemimorphite; hemimorphite mostly showing subhedral shapes; small Pb minerals (~10 μm) precipitating on hemimorphite
SS11-1DS		aggregates of subhedral hemimorphite; elongated hexagonal hemimorphite (~300 μm in length and 10-50 μm in width) inclusions in large tabular-shaped hemimorphite crystal (>400 μm); cerussite crystals (less than 10 μm) on hemimorphite
SSA-2		less tabular shaped hm with calcite coatings
SM09-10	platy smithsonite locally covered by Mn oxides; rhombohedral smithsonite (300 μm); also some massive forms	

Table C4. EDS spectra of NSZ minerals and other major minerals.





Appendix D. Microprobe Analyses

Analytical Techniques

Mineral composition of carbonates in the Smithsonite Manto and the Iron Oxide Manto was analyzed using the JEOL 8200 Electron Microprobe (JXA-8200) in the Jackson School of Geosciences, Department of Geological Sciences at the University of Texas at Austin. An accelerating voltage of 15 kV and the probe current of 15 nA with the probe diameter of 10 μm were used. A dwell time was 20 seconds on the standards and the unknowns for each element. The weight percent of each element was obtained as oxides.

Table D1. List of samples and minerals analyzed using microprobe.

Table D2. Microprobe conditions during analysis and composition of standards used for carbonate minerals.

Table D3. Microprobe analyses of carbonates from the Smithsonite Manto.

Table D4. Microprobe analyses of carbonates from the Iron Oxide Manto.

Table D1. List of samples and minerals analyzed using microprobe.

Sample ID	smithsonite	calcite	occurrence
SM03-09	O		SM
SM08-01	O	O	SM
SM08-02	O		SM
SM08-04	O		SM
SM08-05	O		SM
SM08-06	O		SM
SM08-08	O		SM
SM08-10	O		SM
SM08-11		O	SM
SM08-11-B		O	SM
SM08-17	O		SM
SM08-18A	O	O	SM
SM08-18B	O		SM
SM08-22A	O		SM
SM08-22B	O		SM
SM08-23	O		SM
SM08-26	O	O	SM
SS8	O	O	IO
SS11-2DS		O	IO

Abbreviations: SM= Smithsonite Manto; IO= Iron Oxide Manto

Table D2. Microprobe conditions during analysis and composition of standards used for carbonate minerals.

Element	X-ray	Crystal	Channel	Element	Standard name
Mg	Ka	TAP	2	MgO	dolomiteT64
Fe	Ka	LIFH	3	FeO	sideriteTT66
Mn	Ka	LIFH	4	MnO	sideriteTT66
Ca	Ka	PETJ	5	CaO	dolomiteT64
Zn	Ka	LIF	5	ZnO	sphalerite

Mineral/Element	CaO	MgO	FeO	MnO	CO2	Zn	Fe	S	Total
Siderite			59.08	2.95	37.88				99.91
Dolomite	30.56	22.04			46.93				99.53
Sphalerite						67.1	2	32.9	100

Table D3. Probe data of carbonates from the Smithsonite Manto.

SM03-09 ss	MgO	FeO	MnO	CaO	ZnO	CO2	Total
SM03-09 Ca-Mg rich layer	0.02	0.00	0.04	0.38	64.88	35.43	100.74
SM03-09 Ca-Mg rich layer	0.00	0.02	0.03	0.20	64.26	34.95	99.48
SM03-09 Ca-Mg rich layer	0.00	0.00	0.06	0.16	65.27	35.46	100.94
SM03-09 Ca-Mg rich layer	0.13	0.00	0.00	1.16	64.15	35.75	101.19
SM03-09 Ca-Mg rich layer	0.00	0.01	0.00	0.27	66.11	35.98	102.37
SM03-09 Zn rich layer	0.02	0.00	0.00	0.30	65.62	35.74	101.68
SM03-09 Zn rich layer	0.03	0.00	0.07	0.93	64.67	35.78	101.48
SM03-09 Zn rich layer	0.13	0.00	0.03	1.71	63.18	35.67	100.72
SM03-09 Zn rich layer	0.08	0.00	0.00	1.42	63.16	35.37	100.03
SM03-09 Zn rich layer	0.13	0.01	0.00	2.37	63.03	36.09	101.63
SM03-09 Zn rich layer	0.01	0.00	0.05	0.47	63.93	34.99	99.45
SM03-09 Zn rich layer	0.06	0.01	0.03	0.48	64.14	35.15	99.86
SM03-09 Zn rich layer	0.00	0.00	0.02	0.68	64.62	35.49	100.80
SM03-09 Zn rich layer	0.05	0.02	0.03	0.73	63.99	35.27	100.10
SM03-09 Zn rich layer	0.06	0.00	0.00	0.60	64.68	35.52	100.85
						AVG	100.76

	MgO	FeO	MnO	CaO	ZnO	CO2	Total
SM08-01 late ca	0.09	0.03	0.00	56.54	0.30	44.65	101.61
SM08-01 late ca	0.07	0.00	0.00	55.10	0.18	43.41	98.76
SM08-01 late ca	0.32	0.00	0.00	56.19	0.23	44.57	101.31
SM08-01 late ca	0.17	0.02	0.00	53.85	0.50	42.72	97.25
SM08-01 late ca	0.14	0.14	0.01	53.40	0.32	42.32	96.33
SM08-01 late ca	0.15	0.04	0.00	54.27	0.23	42.90	97.58
SM08-01 late ca	0.11	0.04	0.00	54.76	0.18	43.22	98.31
SM08-01 late ca	0.17	0.00	0.01	54.51	0.09	43.01	97.79
SM08-01 late ca	0.12	0.01	0.05	54.96	0.33	43.48	98.96
SM08-01 late ca	0.06	0.00	0.00	55.07	0.17	43.38	98.68
SM08-01 late ca	0.09	0.00	0.00	55.30	0.39	43.70	99.48
SM08-01 late ca	0.08	0.02	0.05	55.60	0.00	43.77	99.52
SM08-01 late ca	0.01	0.00	0.00	55.96	0.07	43.97	100.02
SM08-01 late ca	0.01	0.00	0.00	55.69	0.15	43.80	99.65
SM08-01 late ca	0.14	0.00	0.00	55.54	0.08	43.78	99.53
SM08-01 late ca	0.04	0.00	0.03	54.38	0.14	42.81	97.40
SM08-01 late ca	0.03	0.03	0.02	54.99	0.00	43.23	98.31
SM08-01 late ca	0.10	0.04	0.00	54.61	0.00	42.99	97.74
SM08-01 late ca	0.02	0.00	0.00	55.35	0.13	43.53	99.03
SM08-01 late ca	0.25	0.04	0.00	54.96	0.21	43.54	99.00
SM08-01 late ca	0.04	0.00	0.00	55.22	0.03	43.39	98.67
SM08-01 late ca	0.07	0.05	0.02	55.44	0.00	43.63	99.22
SM08-01 late ca	0.03	0.00	0.00	55.75	0.06	43.82	99.66
SM08-01 late ca	0.11	0.01	0.01	55.65	0.05	43.82	99.64
SM08-01 late ca	0.07	0.00	0.00	55.71	0.12	43.86	99.75
SM08-01 late ca	0.07	0.00	0.00	56.00	0.11	44.08	100.26
SM08-01 late ca	0.07	0.00	0.03	55.82	0.00	43.90	99.82
SM08-01 late ca	0.04	0.00	0.00	55.66	0.08	43.76	99.54
SM08-01 late ca	0.09	0.00	0.01	56.67	0.19	44.69	101.66
SM08-01 late ca	0.06	0.00	0.07	56.62	0.00	44.54	101.29
SM08-01 late ca	0.07	0.01	0.02	56.32	0.06	44.33	100.81
SM08-01 late ca	0.07	0.00	0.00	56.27	0.01	44.24	100.59
SM08-01 late ca	0.09	0.00	0.01	56.15	0.25	44.31	100.81
SM08-01 late ca	0.11	0.00	0.00	55.18	0.16	43.51	98.95
SM08-01 late ca	0.08	0.00	0.00	56.28	0.13	44.33	100.82
SM08-01 late ca	0.11	0.01	0.00	54.54	0.16	43.02	97.85
SM08-01 late ca	0.02	0.02	0.02	54.15	0.15	42.62	96.99
SM08-01 late ca	0.04	0.01	0.00	54.22	0.13	42.67	97.07
SM08-01 late ca	0.03	0.05	0.00	54.34	0.10	42.76	97.28
SM08-01 late ca	0.02	0.00	0.00	54.66	0.00	42.91	97.59
						AVG	99.11

SM08-01	MgO	FeO	MnO	CaO	ZnO	CO2	Total
SM08-01 ca in ls	0.31	0.10	0.09	54.64	0.23	43.45	98.82
SM08-01 ca in ls	0.20	0.06	0.00	55.54	0.11	43.89	99.80
SM08-01 ca in ls	0.24	0.03	0.05	55.53	0.11	43.95	99.91
SM08-01 ca in ls	0.35	0.09	0.07	54.78	0.25	43.60	99.14
SM08-01 ca in ls	0.28	0.00	0.03	55.33	0.01	43.75	99.39
SM08-01 ca in ls	0.52	0.09	0.01	54.68	0.10	43.60	99.01
SM08-01 ca in ls	0.13	0.08	0.02	54.08	0.19	42.74	97.24
SM08-01 ca in ls	0.26	0.00	0.00	55.20	0.00	43.60	99.06
SM08-01 ca in ls	0.20	0.11	0.12	53.08	0.56	42.32	96.39
SM08-01 ca in ls	0.26	0.04	0.00	54.23	0.55	43.16	98.24
SM08-01 ca in ls	0.05	0.05	0.03	55.94	0.22	44.12	100.40
SM08-01 ca in ls	0.27	0.05	0.00	54.37	0.13	43.07	97.89
SM08-01 ca in ls	0.27	0.03	0.06	55.02	0.08	43.56	99.01
SM08-01 ca in ls	0.20	0.21	0.27	55.11	0.04	43.79	99.63
SM08-01 ca in ls	0.05	0.05	0.08	56.08	0.22	44.27	100.74
SM08-01 ca in ls	0.48	0.01	0.06	55.76	0.08	44.37	100.76
SM08-01 ca in ls	0.29	0.00	0.08	55.97	0.00	44.30	100.64
SM08-01 ca in ls	0.50	0.01	0.00	55.54	0.00	44.14	100.18
SM08-01 ca in ls	0.05	0.00	0.00	55.52	0.00	43.63	99.20
SM08-01 ca in ls	0.21	0.14	0.36	55.03	0.20	43.83	99.75
						AVG	99.26

SM08-02	MgO	FeO	MnO	CaO	ZnO	CO2	Total
SM08-02 ss in pore	3.16	0.00	0.00	0.10	59.17	35.53	97.95
SM08-02 ss in pore	0.29	0.00	0.00	0.58	62.50	34.58	97.96
SM08-02 ss in pore	0.47	0.02	0.00	0.16	63.47	34.98	99.10
SM08-02 ss in pore	0.25	0.00	0.02	0.12	64.37	35.19	99.93
SM08-02 ss in pore	0.29	0.01	0.00	0.55	63.63	35.17	99.65
SM08-02 ss in pore	0.70	0.01	0.02	0.07	64.50	35.72	101.03
SM08-02 ss in pore	0.32	0.00	0.01	0.11	65.11	35.66	101.22
SM08-02 ss in pore	0.44	0.00	0.00	0.24	65.39	36.04	102.11
SM08-02 ss in pore	0.25	0.01	0.06	0.24	65.28	35.81	101.66
SM08-02 ss in pore	0.12	0.00	0.00	0.02	66.60	36.17	102.91
SM08-02 ss in pore	0.90	0.00	0.04	0.02	66.07	36.75	103.77
SM08-02 ss in pore	0.38	0.00	0.00	0.17	66.14	36.33	103.03
SM08-02 ss in pore	0.46	0.01	0.00	0.10	66.60	36.60	103.76
SM08-02 ss in pore	0.39	0.01	0.00	0.21	66.19	36.41	103.22
SM08-02 ss in pore	0.83	0.02	0.00	0.11	66.11	36.76	103.82
SM08-02 ss in pore	0.15	0.07	0.10	0.19	64.52	35.31	100.34
SM08-02 ss in pore	0.25	0.03	0.00	0.08	64.29	35.13	99.77
SM08-02 ss in pore	0.55	0.02	0.03	0.07	64.82	35.74	101.22
SM08-02 ss in pore	0.07	0.01	0.00	0.13	66.39	36.09	102.69
SM08-02 ss in pore	0.53	0.00	0.02	0.11	64.92	35.78	101.35
SM08-02 ss in pore	0.14	0.00	0.04	0.06	64.04	34.87	99.16
SM08-02 ss in pore	0.24	0.00	0.00	0.21	65.48	35.84	101.77
SM08-02 ss in pore	0.37	0.03	0.02	0.27	66.89	36.82	104.39
SM08-02 ss in pore	0.35	0.01	0.00	0.39	63.54	35.06	99.36
SM08-02 ss in pore	0.39	0.00	0.06	0.13	64.32	35.35	100.25
SM08-02 ss in pore	0.20	0.00	0.09	0.19	62.50	34.23	97.21
SM08-02 ss in pore	0.15	0.00	0.00	0.10	63.75	34.72	98.71
SM08-02 ss in pore	0.07	0.00	0.00	0.06	63.71	34.58	98.41
SM08-02 ss in pore	0.43	0.01	0.03	0.19	63.34	34.90	98.89
SM08-02 ss in pore	0.10	0.00	0.02	0.04	66.07	35.88	102.10
SM08-02 ss in pore	0.24	0.01	0.00	0.27	63.53	34.84	98.88
SM08-02 ss in pore	0.24	0.00	0.05	0.05	65.40	35.70	101.43
						AVG	100.84
SM08-02 Zn-poor ss	3.70	0.00	0.03	0.22	59.58	36.45	99.98
SM08-02 Zn-poor ss	3.35	0.04	0.00	0.16	60.36	36.45	100.36
SM08-02 Zn-poor ss	3.52	0.03	0.00	0.18	60.21	36.57	100.51
						AVG	100.29
SM08-02 Zn-rich ss	0.35	0.00	0.00	0.17	63.68	34.96	99.16
SM08-02 Zn-rich ss	0.44	0.03	0.00	0.24	62.92	34.71	98.33
SM08-02 Zn-rich ss	0.23	0.05	0.04	0.08	64.57	35.29	100.26
SM08-02 Zn-rich ss	0.06	0.01	0.00	0.05	64.15	34.81	99.08
SM08-02 Zn-rich ss	0.20	0.00	0.00	0.06	65.53	35.70	101.48
SM08-02 Zn-rich ss	0.22	0.01	0.00	0.09	63.04	34.42	97.78
SM08-02 Zn-rich ss	0.13	0.00	0.11	0.19	63.42	34.66	98.51
SM08-02 Zn-rich ss	0.09	0.00	0.00	0.26	63.80	34.81	98.96
						AVG	99.20

SM08-04	MgO	FeO	MnO	CaO	ZnO	CO2	Total
SM08-04 colloform ss	0.02	0.02	0.00	0.80	65.00	35.82	101.66
SM08-04 colloform ss	0.03	0.01	0.00	0.81	64.82	35.73	101.40
SM08-04 colloform ss	0.06	0.03	0.00	0.76	66.05	36.41	103.31
SM08-04 colloform ss	0.04	0.00	0.01	1.58	64.49	36.17	102.28
SM08-04 colloform ss	0.03	0.00	0.00	1.30	65.25	36.35	102.94
SM08-04 colloform ss	0.06	0.00	0.01	1.84	65.50	36.95	104.36
SM08-04 colloform ss	0.03	0.00	0.00	0.63	67.04	36.79	104.49
SM08-04 colloform ss	0.03	0.00	0.02	1.59	65.17	36.53	103.34
SM08-04 colloform ss	0.04	0.00	0.00	0.95	64.80	35.84	101.62
SM08-04 colloform ss	0.09	0.00	0.00	1.28	66.17	36.90	104.45
SM08-04 colloform ss	0.06	0.00	0.00	1.00	66.54	36.84	104.43
SM08-04 colloform ss	0.01	0.00	0.04	0.63	66.59	36.54	103.80
SM08-04 colloform ss	0.03	0.00	0.02	0.69	66.31	36.44	103.48
SM08-04 colloform ss	0.02	0.00	0.06	0.34	67.00	36.56	103.97
SM08-04 colloform ss	0.15	0.00	0.00	1.55	64.11	36.06	101.87
SM08-04 colloform ss	0.02	0.00	0.04	0.18	67.03	36.43	103.69
SM08-04 colloform ss	0.06	0.02	0.03	0.73	65.58	36.13	102.55
SM08-04 colloform ss	0.05	0.01	0.00	0.69	65.71	36.14	102.59
SM08-04 colloform ss	0.08	0.01	0.01	0.70	66.03	36.35	103.17
SM08-04 colloform ss	0.10	0.00	0.08	0.79	65.59	36.26	102.82
SM08-04 colloform ss	0.05	0.00	0.09	0.90	66.60	36.84	104.48
SM08-04 colloform ss	0.12	0.00	0.03	0.61	65.70	36.17	102.63
SM08-04 colloform ss	0.09	0.00	0.04	0.41	66.19	36.24	102.97
SM08-04 colloform ss	0.00	0.02	0.04	0.79	65.81	36.25	102.91
SM08-04 colloform ss	0.07	0.00	0.00	1.37	66.08	36.89	104.40
SM08-04 colloform ss	0.04	0.00	0.05	1.03	66.22	36.69	104.03
SM08-04 colloform ss	0.01	0.00	0.00	0.73	65.37	35.93	102.04
SM08-04 colloform ss	0.03	0.02	0.02	0.45	66.32	36.27	103.10
SM08-04 colloform ss	0.04	0.01	0.02	0.51	67.00	36.69	104.27
SM08-04 colloform ss	0.04	0.01	0.00	0.65	66.63	36.60	103.93
SM08-04 colloform ss	0.03	0.00	0.04	0.26	66.76	36.38	103.47
SM08-04 colloform ss	0.04	0.01	0.02	0.87	66.90	36.93	104.77
SM08-04 colloform ss	0.04	0.00	0.02	0.77	66.65	36.70	104.17
SM08-04 colloform ss	0.08	0.00	0.00	1.02	66.37	36.78	104.25
SM08-04 colloform ss	0.02	0.00	0.00	0.45	65.21	35.65	101.33
SM08-04 colloform ss	0.07	0.03	0.05	1.58	63.21	35.55	100.49
SM08-04 colloform ss	0.04	0.01	0.00	1.08	67.58	37.45	106.16
SM08-04 colloform ss	0.01	0.02	0.01	0.54	66.48	36.40	103.45
SM08-04 colloform ss	0.01	0.00	0.02	0.49	67.37	36.85	104.74
SM08-04 colloform ss	0.03	0.00	0.05	1.24	66.21	36.84	104.36
SM08-04 colloform ss	0.04	0.00	0.02	0.31	67.23	36.65	104.24

SM08-04	MgO	FeO	MnO	CaO	ZnO	CO2	Total
SM08-04 colloform ss	0.14	0.00	0.00	1.83	64.85	36.67	103.49
SM08-04 colloform ss	0.12	0.01	0.01	0.81	66.47	36.73	104.16
SM08-04 colloform ss	0.05	0.00	0.00	1.18	66.57	36.99	104.80
SM08-04 colloform ss	0.19	0.01	0.01	0.60	64.49	35.57	100.87
SM08-04	MgO	FeO	MnO	CaO	ZnO	CO2	Total
SM08-04 colloform ss	0.16	0.01	0.00	0.86	64.57	35.78	101.37
SM08-04 colloform ss	0.26	0.00	0.01	1.03	64.94	36.21	102.44
SM08-04 colloform ss	0.08	0.00	0.09	0.60	63.93	35.19	99.88
SM08-04 colloform ss	0.11	0.00	0.01	1.29	66.12	36.91	104.44
SM08-04 colloform ss	0.05	0.00	0.00	0.54	67.01	36.72	104.32
SM08-04 colloform ss	0.17	0.00	0.03	0.89	65.61	36.39	103.08
SM08-04 colloform ss	0.03	0.02	0.00	1.14	65.86	36.57	103.62
SM08-04 colloform ss	0.14	0.00	0.00	1.61	64.67	36.39	102.81
SM08-04 colloform ss	0.04	0.01	0.02	0.80	65.21	35.96	102.05
						AVG	103.25

SM08-05	MgO	FeO	MnO	CaO	ZnO	CO2	Total
SM08-05 Zn rich layer	0.14	0.00	0.00	2.83	61.48	35.62	100.05
SM08-05 Zn rich layer	0.16	0.00	0.00	2.73	61.84	35.77	100.50
SM08-05 Zn rich layer	0.16	0.00	0.00	2.95	61.77	35.90	100.78
SM08-05 Zn rich layer	0.10	0.00	0.00	2.56	63.06	36.22	101.93
SM08-05 Zn rich layer	0.14	0.00	0.00	2.77	62.03	35.87	100.81
						AVG	100.81
SM08-05 Ca-Mg rich layer	0.09	0.00	0.05	2.90	61.99	35.94	100.97
SM08-05 Ca-Mg rich layer	0.01	0.00	0.00	1.11	64.62	35.83	101.57
SM08-05 Ca-Mg rich layer	0.05	0.00	0.00	2.10	62.72	35.63	100.50
SM08-05 Ca-Mg rich layer	0.06	0.00	0.00	2.58	63.11	36.23	101.98
SM08-05 Ca-Mg rich layer	0.05	0.00	0.01	2.17	63.11	35.90	101.25
						AVG	101.25
SM08-05 banded ss with no zonation	0.02	0.00	0.01	2.42	62.42	35.69	100.56
SM08-05 banded ss with no zonation	0.08	0.01	0.03	2.99	62.25	36.13	101.48
SM08-05 banded ss with no zonation	0.09	0.00	0.00	3.06	62.56	36.34	102.06
SM08-05 banded ss with no zonation	0.03	0.00	0.00	2.43	62.61	35.81	100.88
SM08-05 banded ss with no zonation	0.04	0.01	0.00	2.26	62.78	35.78	100.87
SM08-05 banded ss with no zonation	0.07	0.00	0.02	2.56	61.96	35.61	100.22
SM08-05 banded ss with no zonation	0.07	0.00	0.00	2.37	61.86	35.40	99.70
SM08-05 banded ss with no zonation	0.07	0.02	0.00	2.20	62.27	35.50	100.05
SM08-05 banded ss with no zonation	0.06	0.03	0.00	2.57	62.12	35.70	100.48
SM08-05 banded ss with no zonation	0.04	0.02	0.00	2.48	62.51	35.82	100.87
SM08-05 banded ss with no zonation	0.06	0.00	0.02	2.35	63.84	36.46	102.74
SM08-05 banded ss with no zonation	0.06	0.01	0.01	2.52	62.47	35.84	100.90
						AVG	100.90

SM08-06	MgO	FeO	MnO	CaO	ZnO	CO2	Total
SM08-06 ss	0.05	0.01	0.00	1.51	60.90	34.19	96.66
SM08-06 ss	0.10	0.00	0.00	1.82	60.23	34.11	96.25
SM08-06 ss	0.15	0.00	0.02	2.43	59.09	34.04	95.72
SM08-06 ss	0.19	0.01	0.00	1.95	60.04	34.21	96.40
SM08-06 ss	0.02	0.00	0.01	1.24	63.14	35.14	99.54
SM08-06 ss	0.06	0.00	0.00	1.88	60.74	34.40	97.08
SM08-06 ss	0.06	0.00	0.00	2.10	59.47	33.88	95.50
SM08-06 ss	0.07	0.00	0.05	2.47	61.97	35.56	100.12
SM08-06 ss	0.03	0.01	0.04	1.41	61.15	34.25	96.89
SM08-06 ss	0.01	0.02	0.00	1.95	60.45	34.25	96.68
SM08-06 ss	0.05	0.03	0.00	0.97	62.53	34.66	98.24
SM08-06 ss	0.06	0.02	0.01	1.19	60.81	33.92	96.02
						AVG	97.09

SM08-08	MgO	FeO	MnO	CaO	ZnO	CO2	Total
SM08-08 Ca-Mg rich layer	0.15	0.00	0.00	2.25	63.49	36.27	102.16
SM08-08 Ca-Mg rich layer	0.06	0.00	0.04	1.87	64.53	36.46	102.95
SM08-08 Ca-Mg rich layer	0.06	0.00	0.00	1.50	63.70	35.69	100.94
SM08-08 Ca-Mg rich layer	0.00	0.00	0.01	0.26	66.00	35.90	102.17
SM08-08 Ca-Mg rich layer	0.11	0.00	0.01	1.71	63.97	36.07	101.87
SM08-08 Ca-Mg rich layer	0.05	0.02	0.05	1.17	64.02	35.63	100.93
SM08-08 Ca-Mg rich layer	0.13	0.02	0.02	1.92	62.86	35.66	100.59
SM08-08 Ca-Mg rich layer	0.17	0.01	0.00	2.01	64.07	36.42	102.69
SM08-08 Ca-Mg rich layer	0.09	0.00	0.02	1.38	65.24	36.49	103.22
SM08-08 Ca-Mg rich layer	0.10	0.02	0.00	2.05	63.39	36.02	101.58
SM08-08 Ca-Mg rich layer	0.10	0.02	0.00	2.59	63.60	36.55	102.86
SM08-08 Ca-Mg rich layer	0.02	0.00	0.02	1.37	64.38	35.93	101.72
SM08-08 Ca-Mg rich layer	0.14	0.00	0.00	1.52	64.67	36.32	102.65
SM08-08 Ca-Mg rich layer	0.10	0.00	0.00	1.93	64.75	36.65	103.44
SM08-08 Ca-Mg rich layer	0.20	0.01	0.00	2.42	62.67	36.01	101.30
SM08-08 Ca-Mg rich layer	0.15	0.02	0.00	1.18	64.88	36.19	102.41
SM08-08 Ca-Mg rich layer	0.04	0.00	0.00	1.29	65.15	36.30	102.78
SM08-08 Ca-Mg rich layer	0.03	0.00	0.00	1.78	62.96	35.48	100.26
SM08-08 Ca-Mg rich layer	0.01	0.00	0.02	0.90	65.01	35.89	101.83
SM08-08 Ca-Mg rich layer	0.12	0.00	0.02	2.28	63.70	36.39	102.51
SM08-08 Zn rich layer	0.04	0.03	0.04	1.58	63.80	35.83	101.32
SM08-08 Zn rich layer	0.07	0.02	0.00	1.68	63.73	35.87	101.36
SM08-08 Zn rich layer	0.04	0.00	0.01	0.50	65.36	35.80	101.72
SM08-08 Zn rich layer	0.04	0.00	0.04	0.26	65.78	35.85	101.96
SM08-08 Zn rich layer	0.01	0.01	0.00	1.32	64.56	35.96	101.85
SM08-08 Zn rich layer	0.04	0.00	0.03	0.23	66.07	35.97	102.34
SM08-08 Zn rich layer	0.18	0.00	0.01	1.01	65.02	36.16	102.38
SM08-08 Zn rich layer	0.00	0.01	0.00	0.90	65.37	36.07	102.35
SM08-08 Zn rich layer	0.01	0.01	0.02	1.37	65.41	36.49	103.31
SM08-08 Zn rich layer	0.01	0.00	0.01	0.66	65.32	35.85	101.84
SM08-08 Zn rich layer	0.06	0.03	0.00	0.78	64.87	35.78	101.51
SM08-08 Zn rich layer	0.02	0.02	0.01	0.58	64.96	35.62	101.21
SM08-08 Zn rich layer	0.20	0.00	0.00	1.24	64.60	36.12	102.15
SM08-08 Zn rich layer	0.01	0.00	0.03	0.29	64.83	35.33	100.50
SM08-08 Zn rich layer	0.04	0.02	0.05	0.47	65.80	36.04	102.43
SM08-08 Zn rich layer	0.03	0.02	0.00	0.65	65.31	35.88	101.89
SM08-08 Zn rich layer	0.05	0.00	0.02	0.55	65.50	35.93	102.05
SM08-08 Zn rich layer	0.03	0.00	0.05	0.65	66.35	36.47	103.56
SM08-08 Zn rich layer	0.15	0.03	0.00	1.71	64.54	36.43	102.86
						AVG	102.04

SM08-10	MgO	FeO	MnO	CaO	ZnO	CO2	Total
SM08-10 pale purple ss	0.05	0.04	0.00	0.26	61.75	33.68	95.78
SM08-10 pale purple ss	0.09	0.05	0.02	0.18	62.47	34.07	96.87
SM08-10 pale purple ss	0.00	0.03	0.00	0.27	63.66	34.66	98.62
SM08-10 pale purple ss	0.03	0.05	0.11	0.05	61.93	33.67	95.83
SM08-10 pale purple ss	0.00	0.08	0.00	0.54	62.24	34.14	97.00
SM08-10 pale purple ss	0.00	0.01	0.02	0.27	63.19	34.40	97.89
SM08-10 pale purple ss	0.01	0.04	0.07	0.30	64.42	35.16	100.01
SM08-10 pale purple ss	0.03	0.00	0.00	0.20	62.04	33.75	96.02
SM08-10 pale purple ss	0.02	0.03	0.00	0.22	62.71	34.13	97.12
SM08-10 pale purple ss	0.03	0.00	0.00	0.17	62.15	33.79	96.14
						AVG	97.13

SM08-11	MgO	FeO	MnO	CaO	ZnO	CO2	Total
ca cement in the matrix	0.43	0.03	0.00	56.37	0.92	45.22	102.98
ca cement in the matrix	0.45	0.01	0.01	56.22	1.13	45.23	103.05
ca cement in the matrix	0.34	0.02	0.00	56.60	0.59	45.11	102.66
ca cement in the matrix	0.35	0.00	0.01	56.21	0.90	44.99	102.46
ca cement in the matrix	0.30	0.01	0.00	56.89	0.46	45.22	102.88
ca cement in the matrix	0.18	0.00	0.10	56.88	0.65	45.25	103.05
ca cement in the matrix	0.53	0.01	0.09	56.54	0.75	45.42	103.33
ca cement in the matrix	0.51	0.03	0.01	56.69	1.04	45.63	103.91
ca cement in the matrix	0.31	0.00	0.04	56.66	0.88	45.31	103.20
ca cement in the matrix	0.52	0.02	0.00	57.06	0.84	45.81	104.24
ca cement in the matrix	0.18	0.00	0.00	56.43	1.05	45.05	102.72
ca cement in the matrix	0.54	0.00	0.00	56.45	1.36	45.63	103.98
ca cement in the matrix	0.36	0.01	0.00	56.90	1.13	45.66	104.06
ca cement in the matrix	0.28	0.03	0.00	56.34	1.04	45.10	102.79
ca cement in the matrix	0.45	0.00	0.00	56.72	1.23	45.66	104.05
ca cement in the matrix	0.59	0.02	0.08	56.03	1.27	45.37	103.36
ca cement in the matrix	0.20	0.02	0.00	56.77	0.89	45.26	103.13
ca cement in the matrix	0.10	0.04	0.00	57.63	0.50	45.63	103.89
ca cement in the matrix	0.51	0.05	0.00	56.31	1.30	45.47	103.62
ca cement in the matrix	0.44	0.00	0.00	56.05	1.33	45.18	102.99
ca cement in the matrix	0.53	0.04	0.00	56.37	1.07	45.41	103.42
ca cement in the matrix	0.68	0.02	0.08	56.00	1.17	45.38	103.33
ca cement in the matrix	0.47	0.00	0.00	55.96	1.05	44.99	102.45
ca cement in the matrix	0.32	0.02	0.00	56.02	1.12	44.93	102.41
ca cement in the matrix	0.37	0.00	0.00	56.85	1.07	45.59	103.88
ca cement in the matrix	0.36	0.01	0.03	56.97	0.96	45.64	103.95
ca cement in the matrix	0.62	0.02	0.00	56.66	0.69	45.53	103.52
ca cement in the matrix	0.42	0.01	0.09	56.83	0.68	45.49	103.53
ca cement in the matrix	0.34	0.00	0.00	56.59	0.84	45.24	103.01
ca cement in the matrix	0.15	0.00	0.04	57.04	0.77	45.36	103.36
						AVG	103.31

SM08-11	MgO	FeO	MnO	CaO	ZnO	CO2	Total
sparry ca	0.19	0.00	0.10	58.54	0.12	46.27	105.22
sparry ca	0.20	0.00	0.05	58.41	0.22	46.21	105.09
sparry ca	0.41	0.01	0.00	57.98	0.41	46.18	104.99
sparry ca	0.16	0.02	0.04	57.53	0.14	45.44	103.33
sparry ca	0.15	0.00	0.01	58.01	0.17	45.79	104.13
sparry ca	0.01	0.00	0.00	58.10	0.08	45.65	103.83
sparry ca	0.15	0.01	0.00	57.44	0.11	45.30	103.00
sparry ca	0.20	0.01	0.00	55.94	0.24	44.26	100.66
sparry ca	0.49	0.03	0.00	57.43	0.24	45.75	103.93
sparry ca	0.19	0.04	0.05	57.50	0.21	45.51	103.50
sparry ca	0.20	0.01	0.00	57.70	0.48	45.76	104.15
sparry ca	0.29	0.02	0.11	57.72	0.23	45.82	104.19
sparry ca	0.38	0.01	0.00	56.95	0.33	45.29	102.94
sparry ca	0.00	0.00	0.00	58.00	0.00	45.52	103.52
sparry ca	0.15	0.00	0.00	57.52	0.05	45.33	103.05
sparry ca	0.12	0.00	0.00	57.87	0.13	45.62	103.74
sparry ca	0.55	0.00	0.00	57.13	0.45	45.68	103.82
sparry ca	1.03	0.01	0.06	56.90	0.28	45.97	104.25
sparry ca	0.15	0.00	0.00	57.59	0.09	45.41	103.24
sparry ca	0.00	0.00	0.02	57.69	0.33	45.47	103.51
sparry ca	0.27	0.00	0.10	57.84	0.23	45.88	104.32
						AVG	103.48

SM08-18A	MgO	FeO	MnO	CaO	ZnO	CO2	Total
SM08-18A scalenohedral ss in pores	0.22	0.00	0.01	0.08	62.97	34.37	97.66
SM08-18A scalenohedral ss in pores	0.08	0.04	0.00	0.11	62.13	33.80	96.15
SM08-18A scalenohedral ss in pores	0.21	0.02	0.08	0.23	62.70	34.39	97.62
SM08-18A scalenohedral ss in pores	0.09	0.03	0.02	0.01	64.59	35.07	99.80
SM08-18A scalenohedral ss in pores	0.13	0.00	0.00	0.05	62.74	34.11	97.02
SM08-18A scalenohedral ss in pores	0.05	0.00	0.00	0.04	64.18	34.81	99.08
SM08-18A scalenohedral ss in pores	0.06	0.01	0.05	0.08	64.70	35.16	100.05
SM08-18A scalenohedral ss in pores	0.29	0.00	0.00	0.12	68.10	37.24	105.75
SM08-18A scalenohedral ss in pores	0.25	0.05	0.01	0.38	63.98	35.20	99.86
SM08-18A scalenohedral ss in pores	0.08	0.00	0.00	0.07	64.92	35.25	100.31
SM08-18A scalenohedral ss in pores	0.10	0.05	0.07	0.07	65.66	35.74	101.68
SM08-18A scalenohedral ss in pores	0.10	0.06	0.00	0.03	66.22	35.99	102.40
SM08-18A scalenohedral ss in pores	0.09	0.00	0.07	0.07	64.85	35.27	100.35
SM08-18A scalenohedral ss in pores	0.09	0.04	0.00	0.06	62.98	34.22	97.38
SM08-18A scalenohedral ss in pores	0.08	0.05	0.00	0.04	65.04	35.33	100.54
SM08-18A scalenohedral ss in pores	0.04	0.00	0.00	0.09	65.59	35.59	101.31
SM08-18A scalenohedral ss in pores	0.13	0.00	0.02	0.06	62.63	34.08	96.92
SM08-18A scalenohedral ss in pores	0.15	0.04	0.00	0.08	64.65	35.21	100.13
SM08-18A scalenohedral ss in pores	0.10	0.00	0.02	0.05	63.78	34.65	98.60
SM08-18A scalenohedral ss in pores	0.04	0.04	0.02	0.19	62.16	33.85	96.30
SM08-18A scalenohedral ss in pores	0.20	0.03	0.00	0.22	61.30	33.57	95.32
SM08-18A scalenohedral ss in pores	0.05	0.02	0.00	0.06	64.50	35.00	99.62
SM08-18A scalenohedral ss in pores	0.12	0.00	0.00	0.13	65.43	35.61	101.29
SM08-18A scalenohedral ss in pores	0.25	0.00	0.00	0.09	62.26	34.02	96.62
SM08-18A scalenohedral ss in pores	0.15	0.00	0.05	0.11	64.67	35.25	100.23
SM08-18A scalenohedral ss in pores	0.11	0.00	0.00	0.08	65.17	35.43	100.79
SM08-18A scalenohedral ss in pores	0.10	0.01	0.01	0.05	66.99	36.40	103.56
SM08-18A scalenohedral ss in pores	0.09	0.00	0.05	0.05	65.73	35.73	101.65
						AVG	99.57
SM08-18A ss in the matrix	0.95	0.05	0.04	0.74	62.10	35.26	99.14
SM08-18A ss in the matrix	1.29	0.00	0.05	1.28	60.71	35.28	98.60
SM08-18A ss in the matrix	0.87	0.03	0.01	0.63	61.07	34.50	97.11
SM08-18A ss in the matrix	0.62	0.00	0.06	0.48	63.14	35.24	99.54
SM08-18A ss in the matrix	1.02	0.01	0.05	0.71	62.16	35.33	99.28
SM08-18A ss in the matrix	1.03	0.07	0.00	0.45	58.80	33.32	93.67
SM08-18A ss in the matrix	0.84	0.00	0.02	0.55	61.85	34.82	98.08
SM08-18A ss in the matrix	0.64	0.00	0.00	0.68	63.55	35.61	100.49
SM08-18A ss in the matrix	0.41	0.01	0.00	0.33	64.70	35.70	101.14
SM08-18A ss in the matrix	0.90	0.04	0.00	0.68	62.31	35.24	99.16
SM08-18A ss in the matrix	0.60	0.06	0.00	0.84	60.77	34.22	96.50
SM08-18A ss in the matrix	0.87	0.05	0.00	0.90	62.39	35.43	99.65
						AVG	99.27

SM08-18A	MgO	FeO	MnO	CaO	ZnO	CO2	Total
SM08-18A ca	0.14	0.00	0.03	54.47	0.38	43.12	98.13
SM08-18A ca	0.15	0.03	0.00	51.91	1.57	41.77	95.43
						AVG	99.15

SM08-18B	MgO	FeO	MnO	CaO	ZnO	CO2	Total
SM08-18B ss layer	0.03	0.01	0.02	0.07	64.41	34.93	99.45
SM08-18B ss layer	0.09	0.00	0.03	0.03	65.96	35.81	101.91
SM08-18B ss layer	0.13	0.01	0.03	0.07	64.98	35.37	100.58
SM08-18B ss layer	0.07	0.00	0.03	0.06	64.63	35.10	99.90
SM08-18B ss layer	0.20	0.00	0.00	0.24	64.77	35.43	100.64
SM08-18B ss layer	0.05	0.01	0.00	0.08	63.84	34.65	98.61
SM08-18B ss layer	0.05	0.00	0.00	0.08	64.45	34.97	99.55
SM08-18B ss layer	0.07	0.00	0.00	0.24	64.77	35.30	100.37
SM08-18B ss layer	0.26	0.00	0.00	0.28	63.44	34.82	98.80
SM08-18B ss layer	0.45	0.00	0.00	0.37	63.28	35.01	99.10
SM08-18B ss layer	0.32	0.02	0.08	0.30	62.89	34.67	98.28
SM08-18B ss layer	0.44	0.00	0.03	0.53	64.08	35.57	100.66
SM08-18B ss layer	0.15	0.00	0.00	0.22	62.29	34.03	96.69
SM08-18B ss layer	0.08	0.00	0.00	0.22	64.40	35.09	99.78
SM08-18B ss layer	0.15	0.00	0.04	0.15	63.60	34.71	98.65
SM08-18B ss layer	0.21	0.00	0.00	0.18	64.93	35.48	100.79
SM08-18B ss layer	0.47	0.04	0.03	0.21	61.52	33.99	96.26
						AVG	99.41
SM08-18B ss in the matrix	0.11	0.03	0.00	0.13	63.98	34.85	99.10
SM08-18B ss in the matrix	0.40	0.01	0.00	0.20	63.09	34.72	98.42
SM08-18B ss in the matrix	0.24	0.03	0.00	0.21	63.16	34.60	98.23
SM08-18B ss in the matrix	0.03	0.00	0.00	0.08	64.31	34.89	99.31
SM08-18B ss in the matrix	0.17	0.00	0.08	0.08	63.68	34.74	98.75
						AVG	99.27
SM08-18B scalenohedral ss	0.53	0.02	0.02	0.16	63.04	34.83	98.60
SM08-18B scalenohedral ss	0.49	0.01	0.00	0.15	63.67	35.09	99.41
SM08-18B scalenohedral ss	0.16	0.00	0.01	0.09	63.82	34.76	98.84
SM08-18B scalenohedral ss	0.54	0.00	0.00	0.11	63.06	34.79	98.50
SM08-18B scalenohedral ss	0.48	0.00	0.00	0.16	63.27	34.87	98.78
SM08-18B scalenohedral ss	0.27	0.00	0.00	0.12	64.78	35.43	100.60
SM08-18B scalenohedral ss	0.36	0.01	0.05	0.09	63.95	35.10	99.57
SM08-18B scalenohedral ss	0.48	0.00	0.07	0.10	64.66	35.62	100.93
SM08-18B scalenohedral ss	0.11	0.00	0.05	0.07	64.06	34.86	99.15
SM08-18B scalenohedral ss	0.54	0.00	0.00	0.14	65.00	35.86	101.54
SM08-18B scalenohedral ss	0.10	0.00	0.00	0.05	64.27	34.91	99.32
SM08-18B scalenohedral ss	0.09	0.01	0.00	0.05	64.21	34.87	99.23
						AVG	99.36

SM08-22A	MgO	FeO	MnO	CaO	ZnO	CO2	Total
SM08-22A scalenohedral ss in pore	0.07	0.10	0.00	0.91	64.22	35.58	100.87
SM08-22A scalenohedral ss in pore	0.40	0.10	0.01	0.82	61.15	34.23	96.71
SM08-22A scalenohedral ss in pore	0.26	0.20	0.17	0.85	63.20	35.36	100.04
SM08-22A scalenohedral ss in pore	0.01	0.04	0.01	0.41	63.57	34.75	98.79
SM08-22A scalenohedral ss in pore	0.32	0.06	0.00	0.45	65.03	35.91	101.76
SM08-22A scalenohedral ss in pore	0.23	0.07	0.02	0.94	65.05	36.22	102.52
SM08-22A scalenohedral ss in pore	0.01	0.11	0.01	0.72	64.56	35.57	100.98
SM08-22A scalenohedral ss in pore	0.00	0.14	0.08	0.92	63.67	35.30	100.11
SM08-22A scalenohedral ss in pore	0.15	0.07	0.05	1.22	63.47	35.53	100.50
SM08-22A scalenohedral ss in pore	0.10	0.13	0.00	0.23	64.01	34.99	99.46
SM08-22A scalenohedral ss in pore	0.20	0.01	0.00	0.43	65.23	35.84	101.70
						AVG	100.31
SM08-22A banded ss	0.00	0.01	0.00	0.81	65.72	36.18	102.72
SM08-22A banded ss	0.00	0.00	0.03	0.29	65.50	35.67	101.49
SM08-22A banded ss	0.00	0.00	0.06	0.32	65.51	35.72	101.61
SM08-22A banded ss	0.00	0.00	0.14	1.68	63.60	35.80	101.20
SM08-22A banded ss	0.17	0.03	0.11	1.24	65.39	36.61	103.55
SM08-22A banded ss	0.00	0.07	0.00	0.45	64.98	35.55	101.05
SM08-22A banded ss	0.00	0.01	0.00	0.51	65.89	36.05	102.47
SM08-22A banded ss	0.00	0.04	0.13	0.63	65.40	35.97	102.16
SM08-22A banded ss	0.25	0.00	0.00	0.72	65.92	36.49	103.37
SM08-22A banded ss	0.32	0.00	0.06	0.59	65.31	36.17	102.44
SM08-22A banded ss	0.01	0.00	0.02	0.58	65.18	35.74	101.54
SM08-22A banded ss	0.05	0.00	0.07	0.94	64.54	35.74	101.35
SM08-22A banded ss	0.22	0.00	0.00	0.73	62.96	34.86	98.77
SM08-22A banded ss	0.18	0.00	0.03	1.42	64.11	36.01	101.75
SM08-22A banded ss	0.38	0.00	0.07	0.66	65.37	36.33	102.80
SM08-22A banded ss	0.42	0.01	0.05	1.15	64.20	36.12	101.94
SM08-22A banded ss	0.45	0.00	0.00	1.02	63.64	35.71	100.81
SM08-22A banded ss	0.03	0.03	0.00	1.56	62.94	35.32	99.87
SM08-22A banded ss	0.20	0.00	0.02	1.50	65.09	36.62	103.44
SM08-22A banded ss	0.00	0.00	0.05	1.14	64.76	35.95	101.90
SM08-22A banded ss	0.22	0.01	0.00	1.23	64.04	35.86	101.37
SM08-22A banded ss	0.26	0.00	0.00	0.94	64.92	36.13	102.25

SM08-22A	MgO	FeO	MnO	CaO	ZnO	CO2	Total
SM08-22A banded ss	0.10	0.01	0.00	0.95	65.17	36.10	102.33
SM08-22A banded ss	0.13	0.01	0.00	0.93	65.23	36.16	102.46
SM08-22A banded ss	0.46	0.02	0.00	1.03	64.11	36.00	101.63
SM08-22A banded ss	0.08	0.01	0.00	0.84	65.40	36.13	102.45
SM08-22A banded ss	0.00	0.00	0.00	0.69	65.09	35.75	101.52
SM08-22A banded ss	0.14	0.00	0.05	0.65	64.65	35.66	101.16
SM08-22A banded ss	0.11	0.04	0.00	0.43	64.68	35.47	100.72
SM08-22A banded ss	0.15	0.00	0.15	0.43	65.64	36.10	102.46
SM08-22A banded ss	0.19	0.02	0.00	0.46	65.80	36.18	102.66
SM08-22A banded ss	0.09	0.00	0.00	0.46	64.85	35.53	100.93
SM08-22A banded ss	0.20	0.02	0.00	1.20	65.30	36.49	103.21
SM08-22A banded ss	0.34	0.00	0.02	0.99	64.07	35.81	101.22
						AVG	101.44

SM08-22B	MgO	FeO	MnO	CaO	ZnO	CO2	Total
SM08-22B colloform banded ss	0.08	0.00	0.02	0.08	64.87	35.25	100.30
SM08-22B colloform banded ss	0.08	0.00	0.00	0.02	64.60	35.04	99.74
SM08-22B colloform banded ss	0.27	0.00	0.00	0.22	62.30	34.17	96.96
SM08-22B colloform banded ss	0.28	0.00	0.02	0.12	65.23	35.70	101.35
SM08-22B colloform banded ss	0.15	0.00	0.00	0.11	63.21	34.44	97.91
SM08-22B colloform banded ss	0.04	0.00	0.01	0.03	63.74	34.54	98.35
SM08-22B colloform banded ss	0.31	0.00	0.00	0.11	62.35	34.14	96.91
SM08-22B colloform banded ss	0.12	0.00	0.00	0.11	63.77	34.71	98.71
SM08-22B colloform banded ss	0.35	0.00	0.00	0.29	63.45	34.94	99.04
SM08-22B colloform banded ss	0.32	0.00	0.01	0.36	58.90	32.50	92.09
SM08-22B colloform banded ss	0.28	0.01	0.02	0.17	62.36	34.18	97.02
SM08-22B colloform banded ss	0.10	0.00	0.00	0.10	65.38	35.55	101.13
SM08-22B colloform banded ss	0.13	0.00	0.01	0.18	64.16	34.99	99.48
SM08-22B colloform banded ss	0.32	0.00	0.00	0.35	63.60	35.02	99.29
SM08-22B colloform banded ss	0.27	0.00	0.00	0.25	66.72	36.57	103.80
SM08-22B colloform banded ss	0.23	0.00	0.05	0.14	64.07	35.04	99.53
SM08-22B colloform banded ss	0.28	0.03	0.00	0.24	64.03	35.14	99.72
SM08-22B colloform banded ss	0.21	0.00	0.00	0.76	63.44	35.14	99.54
SM08-22B colloform banded ss	0.20	0.02	0.01	0.17	63.58	34.76	98.74
SM08-22B colloform banded ss	0.22	0.00	0.03	0.88	61.84	34.40	97.37
SM08-22B colloform banded ss	0.06	0.00	0.00	0.39	62.45	34.15	97.05
SM08-22B colloform banded ss	0.25	0.01	0.00	0.88	61.92	34.46	97.51
SM08-22B colloform banded ss	0.12	0.03	0.00	0.45	64.72	35.50	100.82
SM08-22B colloform banded ss	0.11	0.00	0.00	0.43	63.49	34.79	98.82
SM08-22B colloform banded ss	0.20	0.00	0.00	1.00	62.31	34.71	98.22
SM08-22B colloform banded ss	0.09	0.00	0.00	0.90	61.88	34.27	97.14
SM08-22B colloform banded ss	0.18	0.00	0.03	1.72	61.66	34.92	98.51
SM08-22B colloform banded ss	0.20	0.02	0.02	1.47	63.91	35.96	101.58
SM08-22B colloform banded ss	0.24	0.00	0.00	1.24	61.49	34.50	97.47
SM08-22B colloform banded ss	0.06	0.00	0.00	0.57	62.48	34.31	97.43
SM08-22B colloform banded ss	0.23	0.01	0.00	0.32	64.48	35.38	100.42
						AVG	98.77
SM08-22B ss in the matrix	0.26	0.01	0.01	0.98	62.15	34.68	98.09
SM08-22B ss in the matrix	0.26	0.01	0.00	1.35	61.80	34.77	98.19
SM08-22B ss in the matrix	0.08	0.04	0.02	1.23	63.54	35.45	100.35
SM08-22B ss in the matrix	0.24	0.06	0.00	1.05	62.22	34.79	98.37
						AVG	98.77

SM08-22B	MgO	FeO	MnO	CaO	ZnO	CO2	Total
SM08-22B scalenohedral ss in pore	0.15	0.03	0.02	0.07	64.30	35.03	99.60
SM08-22B scalenohedral ss in pore	0.23	0.03	0.00	0.23	64.88	35.54	100.91
SM08-22B scalenohedral ss in pore	0.18	0.00	0.00	0.08	64.71	35.26	100.23
SM08-22B scalenohedral ss in pore	0.10	0.02	0.00	0.04	66.20	35.96	102.32
SM08-22B scalenohedral ss in pore	0.40	0.00	0.05	0.33	64.39	35.55	100.72
SM08-22B scalenohedral ss in pore	0.06	0.00	0.00	0.08	64.33	34.92	99.39
SM08-22B scalenohedral ss in pore	0.36	0.00	0.00	0.31	65.61	36.12	102.41
SM08-22B scalenohedral ss in pore	0.10	0.00	0.01	0.29	64.14	35.03	99.57
SM08-22B scalenohedral ss in pore	0.07	0.03	0.00	0.12	64.80	35.24	100.26
SM08-22B scalenohedral ss in pore	0.16	0.02	0.03	0.08	65.67	35.78	101.72
SM08-22B scalenohedral ss in pore	0.05	0.03	0.04	0.04	64.57	35.05	99.77
SM08-22B scalenohedral ss in pore	0.13	0.01	0.03	0.61	62.24	34.31	97.33
SM08-22B scalenohedral ss in pore	0.18	0.02	0.00	0.10	62.68	34.18	97.16
SM08-22B scalenohedral ss in pore	0.18	0.03	0.00	0.08	62.75	34.22	97.26
SM08-22B scalenohedral ss in pore	0.05	0.18	0.01	0.10	62.64	34.14	97.13
SM08-22B scalenohedral ss in pore	0.10	0.08	0.00	0.13	66.47	36.22	103.01
SM08-22B scalenohedral ss in pore	0.14	0.19	0.00	0.10	62.78	34.30	97.52
SM08-22B scalenohedral ss in pore	0.15	0.01	0.03	0.22	63.24	34.56	98.21
						AVG	99.07

SM08-26	MgO	FeO	MnO	CaO	ZnO	CO2	Total
SM08-26 ss in pore	0.08	0.00	0.00	0.03	63.40	34.40	97.91
SM08-26 ss in pore	0.11	0.00	0.00	0.16	63.14	34.40	97.81
SM08-26 ss in pore	0.07	0.00	0.00	0.36	63.79	34.86	99.07
SM08-26 ss in pore	0.09	0.00	0.02	0.22	64.57	35.20	100.10
SM08-26 ss in pore	0.14	0.00	0.00	0.19	67.51	36.81	104.64
SM08-26 ss in pore	0.10	0.02	0.00	0.12	66.96	36.43	103.63
SM08-26 ss in pore	0.10	0.00	0.01	0.12	67.36	36.64	104.24
SM08-26 ss in pore	0.08	0.02	0.06	0.28	66.72	36.44	103.60
SM08-26 ss in pore	0.10	0.00	0.01	0.67	66.29	36.50	103.57
SM08-26 ss in pore	0.12	0.00	0.00	0.22	67.08	36.58	104.01
SM08-26 ss in pore	0.13	0.00	0.01	0.08	66.41	36.13	102.75
SM08-26 ss in pore	0.10	0.00	0.03	0.02	64.98	35.28	100.41
SM08-26 ss in pore	0.21	0.01	0.02	0.11	63.77	34.82	98.94
SM08-26 ss in pore	0.20	0.00	0.02	0.09	64.92	35.41	100.64
SM08-26 ss in pore	0.11	0.01	0.04	0.20	64.93	35.42	100.71
SM08-26 ss in pore	0.16	0.00	0.04	0.31	62.43	34.21	97.16
SM08-26 ss in pore	0.20	0.01	0.00	0.07	65.47	35.68	101.43
SM08-26 ss in pore	0.06	0.00	0.00	0.06	63.92	34.69	98.73
SM08-26 ss in pore	0.05	0.00	0.04	0.11	65.03	35.33	100.56
SM08-26 ss in pore	0.09	0.01	0.00	0.15	65.74	35.78	101.78
SM08-26 ss in pore	0.14	0.09	0.11	0.10	67.27	36.73	104.44
SM08-26 ss in pore	0.08	0.01	0.03	0.44	63.84	34.98	99.37
						AVG	101.16
SM08-26 late ca near hm	0.24	0.00	0.00	49.25	6.35	42.35	98.19
SM08-26 late ca near hm	0.09	0.02	0.00	60.19	1.01	47.89	109.20
SM08-26 late ca near hm	0.05	0.02	0.02	55.72	1.40	44.57	101.78
SM08-26 late ca near hm	0.09	0.00	0.00	54.27	1.34	43.42	99.12
SM08-26 late ca near hm	0.09	0.00	0.00	54.66	1.68	43.91	100.34
SM08-26 late ca near hm	0.28	0.00	0.00	55.15	1.11	44.19	100.73
SM08-26 late ca near hm	0.08	0.00	0.01	54.96	0.71	43.61	99.36
SM08-26 late ca near hm	0.11	0.00	0.00	53.32	1.08	42.55	97.05
SM08-26 late ca near hm	0.24	0.02	0.01	56.27	1.53	45.27	103.35
SM08-26 late ca near hm	0.22	0.00	0.01	50.25	5.48	42.64	98.60
SM08-26 late ca near hm	0.17	0.00	0.00	53.71	1.18	42.97	98.02
SM08-26 late ca near hm	0.18	0.02	0.02	53.44	1.48	42.96	98.09
						AVG	100.87

Table D4. Microprobe analyses of carbonates from the Iron Oxide Manto.

SS8	MgO	FeO	MnO	CaO	ZnO	CO2	Total
SS8 Zoned ss in pore	0.53	0.10	0.09	1.07	63.65	35.97	101.41
SS8 Zoned ss in pore	0.00	0.12	0.05	0.74	64.04	35.32	100.28
SS8 Zoned ss in pore	0.16	0.10	0.10	0.66	64.15	35.51	100.68
SS8 Zoned ss in pore	0.65	0.12	0.00	0.89	64.18	36.21	102.06
SS8 Zoned ss in pore	0.85	0.25	0.28	0.89	62.04	35.50	99.81
SS8 Zoned ss in pore	0.17	0.10	0.04	1.13	64.69	36.14	102.26
SS8 Zoned ss in pore	0.73	0.08	0.15	0.84	62.30	35.29	99.39
SS8 Zoned ss in pore	2.86	3.98	0.24	0.71	57.34	37.28	102.41
SS8 Zoned ss in pore	3.49	1.64	0.13	0.50	58.15	36.74	100.65
SS8 Zoned ss in pore	1.62	5.27	0.40	0.69	55.21	35.64	98.82
SS8 Zoned ss in pore	4.61	0.35	0.03	0.75	58.15	37.30	101.18
SS8 Zoned ss in pore	5.08	0.37	0.07	0.86	57.82	37.76	101.96
SS8 Zoned ss in pore	1.62	4.39	0.33	0.70	56.00	35.50	98.53
SS8 Zoned ss in pore	4.57	0.29	0.00	0.88	57.72	37.08	100.54
SS8 Zoned ss in pore	0.98	0.15	0.03	0.66	60.59	34.47	96.89
SS8 Zoned ss in pore	1.16	0.15	0.13	0.52	62.37	35.58	99.91
SS8 Zoned ss in pore	0.50	0.12	0.04	0.41	62.37	34.70	98.14
SS8 Zoned ss in pore	1.01	0.10	0.01	0.63	61.90	35.14	98.79
SS8 Zoned ss in pore	0.57	0.09	0.11	0.64	63.22	35.44	100.06
SS8 Zoned ss in pore	0.69	0.08	0.08	0.75	61.93	34.93	98.45
SS8 Zoned ss in pore	1.08	0.09	0.11	0.79	62.70	35.83	100.60
SS8 Zoned ss in pore	0.48	0.07	0.11	0.48	63.15	35.17	99.46
SS8 Zoned ss in pore	1.16	0.07	0.11	0.52	62.88	35.79	100.52
SS8 Zoned ss in pore	0.62	0.06	0.05	0.77	62.33	35.07	98.91
						AVG	100.07

SS8 ss in the matrix	1.78	0.01	0.00	1.00	60.43	35.41	98.61
SS8 ss in the matrix	1.59	5.39	0.23	0.46	54.29	34.90	96.86
SS8 ss in the matrix	1.98	0.14	0.00	0.64	62.20	36.38	101.33
SS8 ss in the matrix	1.97	0.03	0.16	0.52	61.73	36.06	100.46
SS8 ss in the matrix	2.73	1.51	0.06	0.69	54.77	34.11	93.87
SS8 ss in the matrix	4.36	0.21	0.00	0.53	58.61	37.01	100.71
SS8 ss in the matrix	6.05	0.14	0.00	0.10	57.10	37.64	101.02
SS8 ss in the matrix	2.95	1.72	0.07	0.77	57.62	36.09	99.23
						AVG	99.01

SS8	MgO	FeO	MnO	CaO	ZnO	CO2	Total
SS8 rombic ss	4.86	1.56	0.25	0.77	55.98	37.29	100.70
SS8 rombic ss	2.60	13.52	0.55	0.57	44.67	36.08	98.01
SS8 rombic ss	3.04	1.34	0.60	0.51	58.14	36.35	99.97
SS8 rombic ss	1.60	2.55	0.52	0.58	57.78	35.34	98.38
SS8 rombic ss	1.57	4.47	0.81	0.70	56.21	35.90	99.66
SS8 rombic ss	3.68	2.67	0.40	0.47	52.73	34.78	94.73
SS8 rombic ss	4.57	1.39	0.24	0.76	57.19	37.52	101.67
SS8 rombic ss	5.48	0.52	0.10	0.45	58.60	38.41	103.56
						AVG	99.58

SS8 ca	0.46	1.13	0.19	47.75	8.25	43.25	101.04
SS8 ca	0.14	0.35	0.00	55.18	0.83	44.12	100.63
SS8 ca	0.24	0.52	0.44	51.50	4.36	43.63	100.68
SS8 ca	0.68	0.72	0.25	52.23	1.99	43.41	99.30
SS8 ca	0.73	0.03	0.05	55.05	0.35	44.24	100.44
SS8 ca	0.52	0.05	0.03	53.01	0.30	42.38	96.28
SS8 ca	0.02	0.04	0.00	54.87	0.23	43.23	98.39
SS8 ca	0.40	0.02	0.03	55.80	0.02	44.26	100.53
SS8 ca	0.17	0.00	0.00	56.54	0.09	44.61	101.41
SS8 ca	0.55	0.03	0.02	54.75	0.00	43.60	98.94
SS8 ca	0.38	0.13	0.11	54.24	0.11	43.19	98.16
SS8 ca	0.33	0.13	0.19	54.69	0.10	43.53	98.97
SS8 ca	0.13	0.00	0.00	54.96	0.19	43.39	98.68
SS8 ca	0.61	0.02	0.13	55.19	0.06	44.10	100.10
						AVG	99.54

SS8 calcite vein	0.26	0.11	0.17	55.92	0.01	44.35	100.83
SS8 calcite vein	0.03	0.04	0.10	55.67	0.24	43.93	100.01
SS8 calcite vein	0.19	0.07	0.07	55.57	0.11	43.96	99.96
SS8 calcite vein	0.25	0.10	0.13	55.39	0.05	43.91	99.83
SS8 calcite vein	0.23	0.19	0.08	54.94	0.13	43.59	99.15
SS8 calcite vein	0.38	0.13	0.23	55.32	0.12	44.12	100.30
SS8 calcite vein	0.17	0.47	0.12	54.60	0.17	43.49	99.02
SS8 calcite vein	0.03	0.10	0.08	56.09	0.14	44.23	100.67
SS8 calcite vein	0.14	0.05	0.11	56.05	0.03	44.26	100.64
SS8 calcite vein	0.24	0.19	0.18	54.91	0.05	43.61	99.19
SS8 calcite vein	0.24	0.05	0.24	55.00	0.00	43.60	99.12
SS8 calcite vein	0.03	0.09	0.00	56.25	0.10	44.28	100.73
						AVG	99.95

SS11-2DS	MgO	FeO	MnO	CaO	ZnO	CO2	Total
SS11-2DS ca cement	0.14	0.00	0.00	54.09	0.04	42.63	96.90
SS11-2DS ca cement	0.09	0.12	0.00	53.15	0.11	41.95	95.42
SS11-2DS ca cement	0.12	0.02	0.00	54.38	0.21	42.93	97.65
SS11-2DS ca cement	0.04	0.00	0.02	55.56	0.23	43.78	99.64
SS11-2DS ca cement	0.03	0.01	0.02	53.41	0.09	42.01	95.58
SS11-2DS ca cement	0.11	0.01	0.08	54.01	0.32	42.74	97.27
SS11-2DS ca cement	0.13	0.00	0.00	52.37	0.84	41.69	95.02
SS11-2DS ca cement	0.09	0.00	0.00	54.27	0.43	42.92	97.71
SS11-2DS ca cement	0.06	0.00	0.04	53.16	0.35	41.99	95.59
SS11-2DS ca cement	0.22	0.00	0.03	52.82	0.19	41.82	95.08
SS11-2DS ca cement	0.13	0.04	0.04	51.19	0.38	40.57	92.35
SS11-2DS ca cement	0.07	0.00	0.03	54.31	0.10	42.77	97.28
SS11-2DS ca cement	0.10	0.00	0.00	52.46	0.18	41.37	94.11
SS11-2DS ca cement	0.22	0.01	0.00	54.54	0.29	43.21	98.27
SS11-2DS ca cement	0.23	0.03	0.06	54.66	0.16	43.29	98.43
SS11-2DS ca cement	0.05	0.03	0.00	54.25	0.38	42.85	97.56
SS11-2DS ca cement	0.24	0.00	0.08	54.40	0.28	43.16	98.16
						AVG	96.59

Appendix E. Pb Isotope Analyses

Analytical Techniques

Pb isotope analyses on galena, cerussite, and smithsonite were performed in the Isotope Geochemistry Lab in the Jackson School of Geosciences, Department of Geological Sciences at the University of Texas at Austin. Pb isotopes were analyzed by Dr. Larry Mack, and analytical procedures were provided him as follows:

Analytical Procedure: Common Lead

Sample Preparation

I. Weigh and wash.

Galena sample weights: 0.4 to 8 mg.

Smithsonite weights: 100 to 220 mg.

Hemimorphite weights: 220 to 330 mg.

Cerussite weight: 150 mg.

Samples were transferred to cleaned Teflon vials, and rinsed two times in 0.05 M HCl.

II. Sample dissolution.

Galena samples were dissolved in 4 mL of hot 6 M HCl.

Smithsonite samples were dissolved in 4 mL of 5 M HCl.

Hemimorphite samples were dissolved in 2 mL of 6 M HCl plus 1 mL of concentrated HF, dried, redissolved in 2 mL of 6 M HCl, then dried again (to drive off fluoride), and finally redissolved in 2 mL of 6 M HCl.

Cerussite sample was dissolved in 1 mL of 6 M HCl.

An aliquot of dissolved sample estimated to contain ~100 ng of Pb was transferred to a separate Teflon vial then dried. (For the galena samples, an intermediate vial had to be employed to dilute an aliquot of the original sample.)

III. Pb separation.

Isolate Pb using 200 μL of Bio Rad AG 1-X8, 100-200 mesh, anion resin in a Teflon shrink-tube column. The smithsonite and hemimorphite samples were put through the column twice using 0.5 M HBr – 0.5 M HNO₃, then two more times using 1 M HBr- 2 M HCl – 6 M HCl. The cerussite sample was put through the column twice using the 1 M HBr-2 M HCl – 6 M HCl procedure. The galena samples were put through the columns only once using the 0.5 M HBr – 0.5 M HNO₃ procedure.

Mass Spectrometry

1. Load Pb onto outgassed Re filaments with silica gel and 0.3 M H₃PO₄.
2. Measure Pb isotope ratios in Thermo Triton TI thermal-ionization mass spectrometer in static-multicollection data-acquisition mode, at the Jackson School of Geosciences, The University of Texas at Austin. Filament temperature was 1200 °C. ²⁰⁸Pb signal intensity was < 20 mV for two of the hemimorphite samples; all other samples had intensities between 1 and 32 Volts. Between 80 and 140 ratios were measured. The linear fractionation “law” was used to correct for mass discrimination in the mass spectrometer. The magnitude of the fractionation correction is estimated by analyzing the NIST SRM 981 common Pb isotope standard multiple times under conditions identical to those for the samples. For these samples, the fractionation correction averaged 0.11% per amu. The true composition of the NIST SRM 981 standard is assumed to be that given by Galer and Abouchami (1998). Outliers are rejected from the data set

Analytical uncertainty is estimated to be +/- 0.05% per amu (2σ) (Luhr et al., 1995). This is equivalent to +/- 0.0004 for typical $^{207}\text{Pb}/^{206}\text{Pb}$ ratios, +/- 0.002 for $^{208}\text{Pb}/^{206}\text{Pb}$ ratios, +/- 0.02 for $^{206}\text{Pb}/^{204}\text{Pb}$ ratios, +/- 0.02 for $^{207}\text{Pb}/^{204}\text{Pb}$ ratios, and +/- 0.08 for $^{208}\text{Pb}/^{204}\text{Pb}$ ratios. The average reproducibility of 14 duplicate analyses of four different samples is 0.026% per amu, (worst-case value is 0.043%) suggesting that, in general, the true analytical uncertainty is somewhat better than the assumed value.

We monitor the amount of contamination introduced during sample processing and analysis by analyzing “blanks” along with the samples. The technique of “isotope dilution” is used to determine this quantity of Pb. For these samples, the lab procedural blanks were 11 and 23 pg of Pb for the smithsonite-hemimorphite samples, and 2 and 3 pg of Pb for the galena samples. Relative to the amount of Pb in the target sample, ~100 ng, this amount of contamination is insignificant, i.e. it does not measurably change the Pb isotope compositions of the analyzed samples.

References

Galer, S.J.G. and Abouchami, W., 1998, Practical application of lead triple spiking for correction of instrumental mass discrimination: Goldschmidt Conf., Toulouse. *Mineralogical Magazine*, v. 62A, p. 491-492.

Luhr, J.F., Aranda-Gómez, J.J., and Housh, T.B., 1995, San Quintín volcanic field, Baja California Norte, Mexico: Geology, petrology, and geochemistry: *Jour. of Geophysical Research*, v. 100, no. B7, p. 10353-10380.

Appendix F. CL and LA-ICP-MS

Analytical techniques

For cathodoluminescence imaging, several polished thin sections of smithsonite were selected to observe different CL colors and zonation using operating at 16~22 keV and 400~600 μA of an accelerating voltage and gun current, respectively. Samples were investigated under a Technosyn cold-cathode microscope instrument and images were taken with Olympus digital camera mounted on the luminoscope in the microbeam facilities at Jackson School of Geosciences, the University of Texas at Austin. As for acquiring photomicrographs, exposure times were between 960 μs and 1.90 seconds. Petrography using CL is listed in Table F1.

For LA-ICPMS analyses, a New Wave UP193FX laser with an Agilent 7500ce ORS ICP-MS in the ICP-MS lab at Jackson School of Geosciences, the University of Texas at Austin, was used. NIST 610 and NIST 612 glass standards were run before and after smithsonite linescan and spot analyses, and for this study the supercell was used. The supercell is a sample chamber designed to fit many samples by New Wave Research. Its geometry and gas-flow dynamics enable rapid evacuation of the laser generated aerosol (Electro Scientific Industries: www.esi.com). The elements and masses selected for this project include 25Mg, 44Ca, 55Mn, 57Fe, 59Co, 63Cu, 67Zn, 85Rb, 88Sr, 111Cd, 137Ba, and 208Pb. Zn was used as the internal standard element for quantification based on a weight fraction of Zn determined from microprobe analyses (0.51336009). NIST 610 was chosen for normalization. Polished thick sections (~100 μm) were used and CL images were taken before and after the measurement. Pre-ablation for spots were performed at 10 % laser power with a 50 μm spot, a 10 Hz repetition rate, and a 1 second dwell time. The ablation on spots was at 5 % laser power, a 25 μm spot, 7 Hz repetition rate, and 60 second dwell. The pre-ablation for line scans were performed at 10 % laser power, 35 μm line width, 25 $\mu\text{m}/\text{sec}$ line scan rate, and 10 Hz repetition rate.

For the ablation scans, 20 % laser power, a 25 μm line width, 10 Hz repetition rate, and 25 $\mu\text{m}/\text{sec}$ scan rate were used. Intensity ratios of Mg25, Ca44, Cu63, and Pb208 over Zn66 on the same laser linecane as in Figure 7.4 are illustrated in Table F2.

Table F1. Petrography using the optical-cathodoluminescence microscopy.

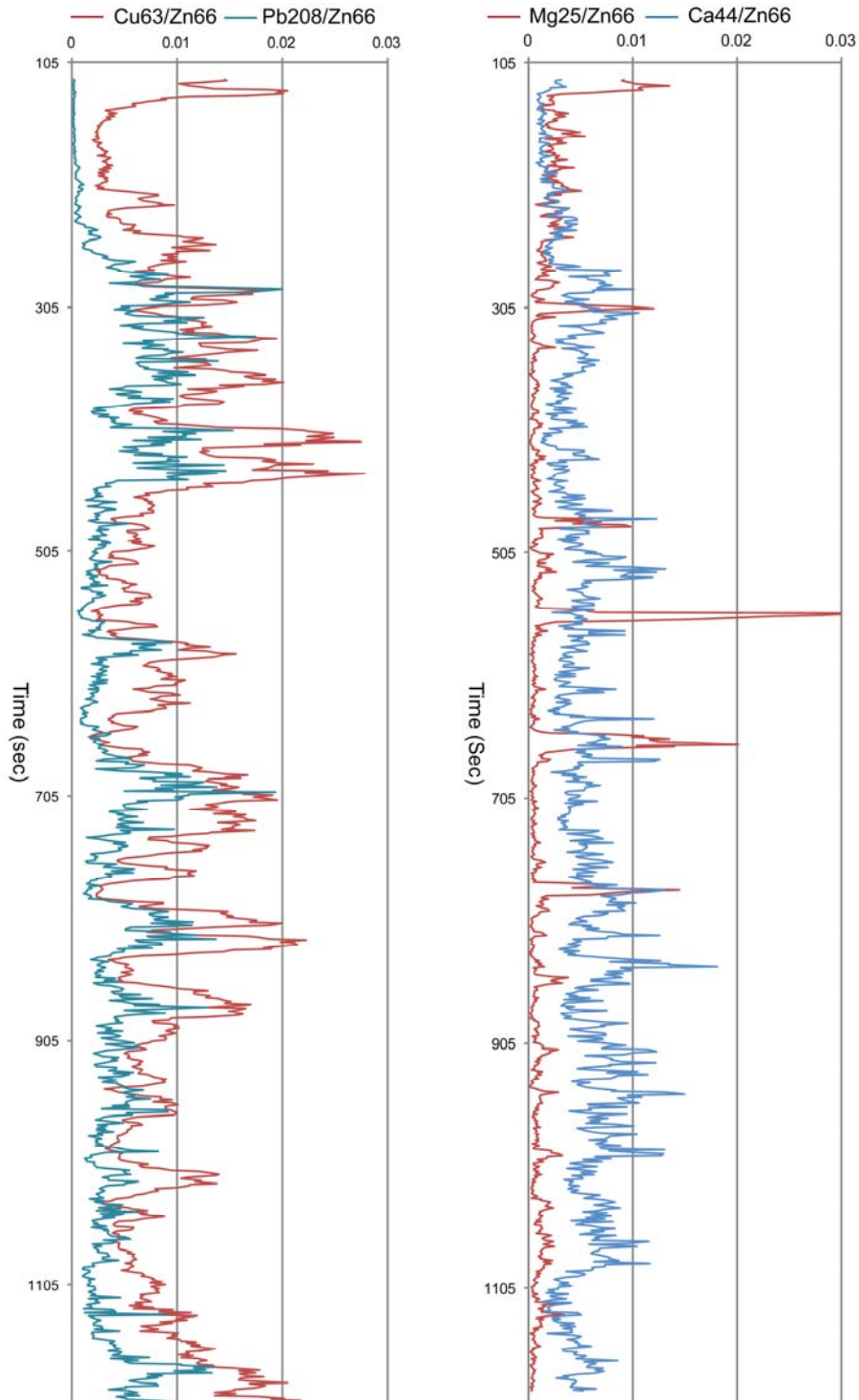
A. Smithsonite

Textural type	colloform, banded ss in vugs	pore-filling	matrix
SM03-09	zonations of bright pink, blue, and red	dull blue with red rims	blue with pink patches of sauconite + Mn oxides
SMj03-20	zonations of smithsonite represented by alternating pink, purple, and blue bands		
SMj03-22	zonations of bright pink and darker pink or alternating pink and blue color		
SMj03-25	zonations of alternating pink and blue	blue with bright red to pink rims	
SMj03-27	zonations alternating bright red. Dull red, and non-luminescence layers	blue/blue with red and pink rims and zonation patterns	
SM08-05	blue-dark blue-purple-bright pink- purple- blue		
SM08-06	red-blue		
SM08-10	red-blue		
SM08-22		blue	blue and bright pink
SM08-22C		blue; blue with bright pink rims	blue and bright pink
SM08-23		blue/ locally bright red rhombic or colloform rims	
SM08-26		blue w/ red rims around the edge of some smithsonite crystals	blue w/ red rims around the edge of some smithsonite crystals
SM09-9	red- (dull) blue		
SS8		dark red	

B. Calcite

Textural type	late pore-filling	late vein	micrite
SMj03-22		dark blue (nearly non-luminescence)	
SMj03-27	non-luminescence		
SM08-03		bright orange	orange to red
SM08-11	non-luminescence		
SM08-13		bright orange	orange to red
SS8		orange	orange-dull orange

Table F2. Intensity ratios of Cu63, Pb208, Mg55, and Ca44, over Zn66 from laser linescan in Figure 7.4. Sample ID. SM03-09.



Appendix G. Fluid Inclusion Microthermometry

Analytical Procedures

Evaluation of the suitability of samples for fluid inclusions was made on the five doubly polished plates, approximately 100 μm thick, containing hemimorphite and calcite to establish fluid compositions during NSZ mineral precipitation from groundwater. Hemimorphite from the Iron Oxide Manto occurs as pore-fillings followed by calcite. In the samples from the Smithsonite Manto, hemimorphite is intergrown with smithsonite. Late calcite is associated with pore-filling hemimorphite in the Smithsonite Manto. Fluid inclusion measurements were made on a modified USGS-design gas-flow heating-freezing stage mounted on an Olympus petrographic microscope equipped with a Olympus digital camera at the fluid inclusion lab at the Bureau of Economic Geology, the University of Texas at Austin. The precision of vapor homogenization and ice melting temperatures, based on reproducibility of data, varied according to the size and arrangement of the inclusion and its contained components, as well as the clarity of the host mineral.

References

- Ankomah, A. B., 1992, Magnesium and pH effect on zinc sorption by goethite: *Soil Science*, v. 154, p. 206-213.
- Balassone, G., M. Rossi, M. Boni, G. Stanley, and P. McDermott, 2008, Mineralogical and geochemical characterization of nonsulfide Zn-Pb mineralization at Silvermines and Galmoy (Irish Midlands): *Ore Geology Reviews*, v. 33, p. 168-186.
- Boggs, S., and D. Krinsley, 2006, *Application of Cathodoluminescence Imaging to the Study of Sedimentary Rocks*: New York, Cambridge University Press.
- Boni, M., 2003, Non-Sulfide Zinc Deposits: a new-(old) type of economic mineralization, *Society for Geology Applied to Mineral Deposits (SGA)*.
- Boni, M., 2005, Willemite in the Belgian non-sulfide zinc deposits; a fluid inclusion study, in V. Coppola, L. Dejonghe, and L. Fedele, eds., *Periodico di Mineralogia*, Italy, Bardi Editore : Rome, Italy, p. 87-100.
- Boni, M., 2009, The nonsulfide zinc deposit at Accha (southern Peru); geological and mineralogical characterization, in G. Balassone, V. Arseneau, and P. Schmidt, eds., *Economic Geology and the Bulletin of the Society of Economic Geologists*, United States, Economic Geology Publishing Company : Lancaster, PA, United States, p. 267-289.
- Boni, M., H. Gilg, G. Balassone, J. Schneider, C. Allen, and F. Moore, 2007, Hypogene Zn carbonate ores in the Angouran deposit, NW Iran: *Mineralium Deposita*, v. 42, p. 799-820.
- Boni, M., H. A. Gilg, G. Aversa, and G. Balassone, 2003, The "Calamine" of Southwest Sardinia: Geology, Mineralogy, and Stable Isotope Geochemistry of Supergene Zn Mineralization: *Economic Geology*, v. 98, p. 731-748.
- Borg, G., K. Karner, M. Buxton, R. Armstrong, and S. W. v. d. Merwe, 2003, Geology of the Skorpion Supergene Zinc Deposit, Southern Namibia: *Economic Geology*, v. 98, p. 749-771.
- Brugger, J., D. C. McPhail, M. Wallace, and J. Waters, 2003, Formation of Willemite in Hydrothermal Environments: *Economic Geology*, v. 98, p. 819-835.
- Campa, M. F., and P. J. Coney, 1983, Tectono-stratigraphic terranes and mineral resource distributions in Mexico: *Canadian Journal of Earth Sciences = Revue Canadienne des Sciences de la Terre*, v. 20, p. 1040-1051.

- Cerling, T. E., 1984, The stable isotopic composition of modern soil carbonate and its relationship to climate: *Earth and Planetary Science Letters*, v. 71, p. 229-240.
- Chavez-Cabello, G., J. J. Aranda-Gomez, M. Garza, T. Cossio-Torres, I. R. Arvizu-Gutierrez, and G. A. Gonzalez-Naranjo, 2007, The San Marcos Fault; a Jurassic multireactivated basement structure in northeastern Mexico: *Special Paper - Geological Society of America*, v. 422, p. 261-286.
- Chism, R. E., 1887, Sierra Mojada, Mex: *Transactions of the Society of Mining Engineers of American Institute of Mining, Metallurgical and Petroleum Engineers, Incorporated (AIME)*, p. 542-587.
- Chvez, G., J. Aranda, A. Iriondo, M. Aranda, R. Peterson, S. Eguiluz, and Anonymous, 2008, Evidence of basement inversion during the Laramide Orogeny in the Sabinas Basin area, Coahuila, Mexico: *Abstracts with Programs - Geological Society of America*, v. 40, p. 546.
- Chvez, G., M. Cerca, M. Valencia, and Anonymous, 2008, The Laramide Orogeny in Mexico: an updated revision: *Abstracts with Programs - Geological Society of America*, v. 40, p. 548.
- Coppola, V., M. Boni, H. Gilg, and B. Strzelska-Smakowska, 2009, Nonsulfide zinc deposits in the Silesia-Cracow district, Southern Poland: *Mineralium Deposita*, v. 44, p. 559-580.
- Coppola, V., M. Boni, H. A. Gilg, G. Balassone, and L. n. Dejonghe, 2008, The "calamine" nonsulfide Zn-Pb deposits of Belgium: Petrographical, mineralogical and geochemical characterization: *Ore Geology Reviews*, v. 33, p. 187-210.
- Cornell, R. M., Schwertmann, Udo., 2003, *The iron oxides: structure, properties, reactions, occurrences, and uses* Weinheim: Wiley-VCH, 2003.
- de Antunano, S. E., 2001, Geologic evolution and gas resources of the Sabinas Basin in northeastern Mexico: *AAPG Memoir*, v. 75, p. 241-270.
- Dyer, M. J., 2004, Sabinas Basin Lower Cretaceous to Jurassic production; comparison to south Texas equivalents, in C. Bartolini, ed., *Transactions - Gulf Coast Association of Geological Societies, United States, Gulf Coast Association of Geological Societies* : New Orleans, LA, United States, p. 169-184.
- Electro Scientific Industries (ESI): www.esi.com
- Gabriel Chávez-Cabello, J. J. A.-G., Roberto S. Molina-Garza, Tomás Cossío-Torres, Irving R. Arvizu-Gutiérrez and Gildardo A. González-Naranjo, 2007, The San Marcos fault: A Jurassic multireactivated basement structure in northeastern Mexico: *Geological Society of America Special Papers*, v. 422, p. 261-286.

- Gilg, H. A., 2004, Stable isotope compositions of Zn- and Pb-carbonates; their role in exploration of non-sulphide ores, in M. Boni, ed., Publication - Geology Department and Extension Service, University of Western Australia, Australia, University of Western Australia, Geology Department and Extension Service : Perth, West. Aust., Australia, p. 361-365.
- Gilg, H. A., M. Boni, R. Hochleitner, and U. Struck, 2008, Stable isotope geochemistry of carbonate minerals in supergene oxidation zones of Zn-Pb deposits: *Ore Geology Reviews*, v. 33, p. 117-133.
- Gilg, H. A., U. Struck, T. Vennemann, and M. Boni, 2003, Phosphoric acid fractionation factors for smithsonite and cerussite between 25 and 72°: *Geochimica et Cosmochimica Acta*, v. 67, p. 4049-4055.
- Gillhaus, A., D. Habermann, J. Meijer, and D. K. Richter, 2000, Cathodoluminescence spectroscopy and micro-PIXE: combined high resolution Mn-analyses in dolomites - First results: *Nuclear Instruments and Methods in Physics Research Section B: Beam Interactions with Materials and Atoms*, v. 161-163, p. 842-845.
- Goette, T., 2004, Quantitative high-resolution cathodoluminescence spectroscopy of smithsonite, in D. K. Richter, ed., *Mineralogical Magazine*, United Kingdom, Mineralogical Society: London, United Kingdom, p. 199-207.
- Goldhammer, R. K., 1991, Sequence stratigraphy and cyclostratigraphy of the Mesozoic of the Sierra Madre Oriental, northeast Mexico: a field guidebook Gulf Coast Section, Society of Economic Paleontologists and Mineralogists Foundation, 1991.
- González-Sánchez, F., A. Camprubí, E. González-Partida, R. Puente-Solís, C. Canet, E. Centeno-García, and V. Atudorei, 2009, Regional stratigraphy and distribution of epigenetic stratabound celestine, fluorite, barite and Pb-Zn deposits in the MVT province of northeastern Mexico: *Mineralium Deposita*, v. 44, p. 343-361.
- Gotze, J., and U. Kempe, 2008, A comparison of optical microscope- and scanning electron microscope-based cathodoluminescence (CL) imaging and spectroscopy applied to geosciences: *Mineral Mag*, v. 72, p. 909-924.
- Habermann, D., R. D. Neuser, and D. K. Richter, 1998, Low limit of Mn²⁺-activated cathodoluminescence of calcite: state of the art: *Sedimentary Geology*, v. 116, p. 13-24.
- Hitzman, M. W., N. A. Reynolds, D. F. Sangster, C. R. Allen, and C. E. Carman, 2003, Classification, Genesis, and Exploration Guides for Nonsulfide Zinc Deposits: *Economic Geology*, v. 98, p. 685-714.

- James, E. W., and C. D. Henry, 1993, Southeastern extent of the North American craton in Texas and northern Chihuahua as revealed by Pb isotopes: *Geological Society of America Bulletin*, v. 105, p. 116-126.
- Johannesson, K. H., A. Cort, and K. C. Kilroy, 2004, Reconnaissance isotopic and hydrochemical study of Cuatro Ciénegas groundwater, Coahuila, Mexico: *Journal of South American Earth Sciences*, v. 17, p. 171-180.
- Krüger, Y., P. Stoller, J. Rička, and M. Frenz, 2007, Femtosecond lasers in fluid-inclusion analysis: overcoming metastable phase states: *Eur J Mineral*, v. 19, p. 693-706.
- Large, D., 2001, The geology of non-sulphide zinc deposits; an overview: *Erzmetall*, v. 54, p. 264-274.
- Lehmann, C., D. A. Osleger, I. P. Montanez, W. Sliter, A. A. Vanneau, and J. Banner, 1999, Evolution of Cupido and Coahuila carbonate platforms, Early Cretaceous, northeastern Mexico: *Geological Society of America Bulletin*, v. 111, p. 1010-1029.
- Malcolmson, J. W., and S. F. Emmons, 1902, The Sierra Mojada, Coahuila, Mex., and its ore deposits (with discussion by S. F. Emmons): *Transactions of the Society of Mining Engineers of American Institute of Mining, Metallurgical and Petroleum Engineers, Incorporated (AIME)*, p. 100-139.
- Markham, N. L., 1960, The willemite-hemimorphite relationship: *Economic Geology*, v. 55, p. 844-847.
- Marshall, D. J., 1988, *Cathodoluminescence of geological materials*: Boston, Unwin Hyman.
- McPhail, D. C., E. Summerhayes, V. Jayaratne, A. Christy, and Anonymous, 2006, Hemimorphite solubility and stability of low-T zinc minerals: *Geochimica et Cosmochimica Acta*, v. 70, p. A414.
- McPhail, D. C., E. Summerhayes, S. Welch, and J. Brugger, 2003, The geochemistry and mobility of zinc in the regolith: *Advances in regolith; proceedings of the CRC LEME regional regolith symposia 2003*: Bentley, West. Aust., Cooperative Research Centre for Landscape Environments and Mineral Exploration, 287-291 p.
- Megaw, P. K. M., J. Ruiz, and S. R. Titley, 1988, High-temperature, carbonate-hosted Ag-Pb-Zn(Cu) deposits of northern Mexico: *Economic Geology*, v. 83, p. 1856-1885.
- Metalline Mining Company; www.metalin.com.

National Map Seamless Server: seamless.usgs.gov.

Pough, F. H., 1941, Occurrence of willemite: *American Mineralogist*, v. 26, p. 92-102.

Reichert, J., and G. Borg, 2008, Numerical simulation and a geochemical model of supergene carbonate-hosted non-sulphide zinc deposits: *Ore Geology Reviews*, v. 33, p. 134-151.

Riley, L. B., 1936, *Geology and ore deposits of Sierra Mojada, Coahuila, Mexico* Yale University, 343 p.

Roedder, E., 1981, Origin of fluid inclusions and changes that occur after trapping in Hollister, L.S. and Crawford, M.L. (editors), *Fluid Inclusions: Application to Petrology: Mineralogical Association of Canada Short Course Handbook*, v. 6, p. 101-137.

Roedder, E., 1984, Fluid Inclusions, *Reviews in mineralogy: Mineralogical Society of America*, v. 12, p. 644.

Ross, C. S., 1946, Sauconite, a clay mineral of the montmorillonite group: *American Mineralogist*, v. 31, p. 411-424.

Sangameshwar, S. R., and H. L. Barnes, 1983, Supergene processes in zinc-lead-silver sulfide ores in carbonates: *Economic Geology*, v. 78, p. 1379-1397.

Shaw, S. F., 1923, *The ore deposits of Sierra Mojada, Coahuila, Mexico (with discussion): Transactions of the American Institute of Mining, Metallurgical and Petroleum Engineers, Incorporated (AIME)*, v. 68, p. 556-586.

Smith, D. M., 1997, Sedimentary basins and the origin of intrusion-related carbonate-hosted Zn-Pb-Ag deposits: *Special Publication (Society of Economic Geologists (U. S.))*, v. 4, p. 255-263.

Stacey, J. S., and J. D. Kramers, 1975, Approximation of terrestrial lead isotope evolution by a two-stage model: *Earth and Planetary Science Letters*, v. 26, p. 207-221.

Takahashi, T., 1960, Supergene alteration of zinc and lead deposits in limestone: *Economic Geology*, v. 55, p. 1083-1115.

Titley, S. R., 1997, Characteristics of high temperature, carbonate-hosted replacement ores and some comparisons with Mississippi valley-type ores: *Special Publication (Society of Economic Geologists (U. S.))*, v. 4, p. 244-254.

Tritlla, J., G. Levresse, R. Corona-Esquivel, D. A. Banks, H. Lamadrid, J. Bourdet, and P. Julio Pinto-Linares, 2007, Epigenetic, low-temperature, carbonate-hosted Pb-

- Zn-Cu-Ba-F-Sr deposits in Mexico: A Mississippi Valley Type classification: Geological Society of America Special Papers, v. 422, p. 417-432.
- Trivedi, P., L. Axe, and J. Dyer, 2001, Adsorption of metal ions onto goethite: single-adsorbate and competitive systems: Colloids and Surfaces A: Physicochemical and Engineering Aspects, v. 191, p. 107-121.
- Van Horn, F. R., 1912, The occurrence of silver, copper, and lead ores at the Veta Rica Mine, Sierra Mojada, Coahuila, Mexico: Transactions of the Society of Mining Engineers of American Institute of Mining, Metallurgical and Petroleum Engineers, Incorporated (AIME), p. 867-881.
- Veizer, J. H., Jochen, 1976, The nature of $^{18}\text{O}/^{16}\text{O}$ and $^{13}\text{C}/^{12}\text{C}$ secular trends in sedimentary carbonate rocks: Geochimica et Cosmochimica Acta, v. 40, p. 1387-1395.
- Wassenaar, L. I., S. L. Van Wilgenburg, K. Larson, and K. A. Hobson, 2009, A groundwater isoscape (δD , $\delta^{18}\text{O}$) for Mexico: Journal of Geochemical Exploration, v. 102, p. 123-136.
- Wallén, C. C., 1955, Some Characteristics of Precipitation in Mexico: Geografiska Annaler, v. 37, p. 51-85.
- Williams, P. A., 1990, Oxide Zone Geochemistry: Ellis Horwood Series in Inorganic Chemistry: Ellis Horwood Limited, 286 p.

Vita

Hye In Ahn was born in Seoul, South Korea in 1981. After attending the Yeouido Girls' High School in Seoul, South Korea, Hye In studied Earth and Environmental Sciences at the Korea University, Seoul, South Korea in 2003. After graduating from college in 2006, she pursued her master's degree in Geological Sciences at the University of Texas at Austin in 2007.

Email: hahn117@gmail.com

This thesis was typed by the author.